Alongshore variability
of nourished and natural beaches

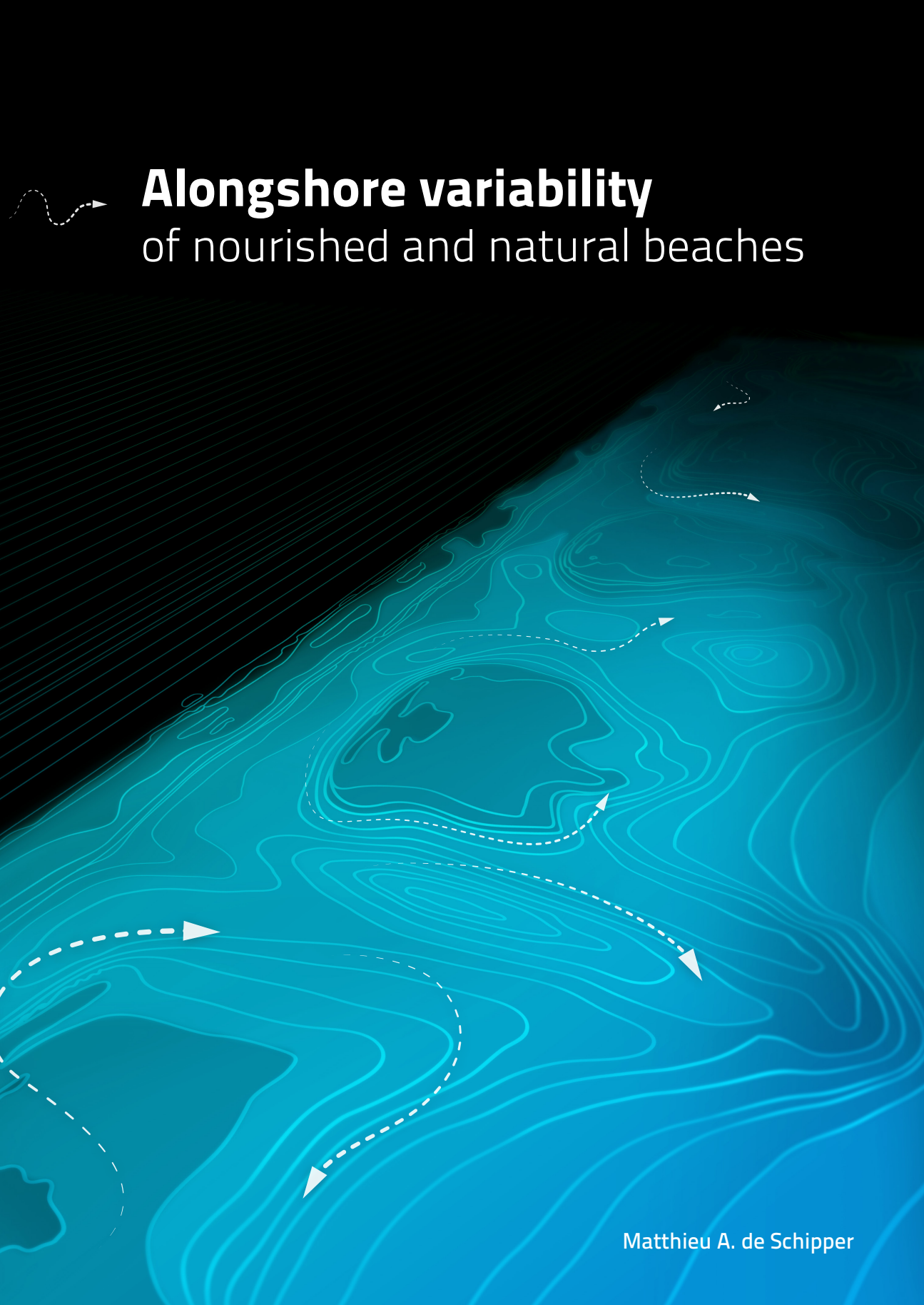

Matthieu A. de Schipper

Alongshore variability of nourished and natural beaches

Proefschrift

ter verkrijging van de graad van doctor
aan de Technische Universiteit Delft,
op gezag van de Rector Magnificus prof. ir. K.C.A.M. Luyben,
voorzitter van het College voor Promoties,
in het openbaar te verdedigen op
donderdag 16 januari 2014 om 15.00 uur

door Matthieu Andréas DE SCHIPPER
civiel ingenieur
geboren te Rotterdam

Dit proefschrift is goedgekeurd door de promotoren:
Prof.dr.ir. M.J.F. Stive
Prof.dr.ir. A.J.H.M Reniers

Copromotor:
Dr. R. Ranasinghe

Samenstelling promotiecommissie:

Rector Magnificus,	voorzitter
Prof.dr.ir. M.J.F. Stive,	Technische Universiteit Delft, promotor
Prof.dr.ir. A.J.H.M Reniers,	University of Miami, USA, promotor
Dr. R. Ranasinghe,	Technische Universiteit Delft, copromotor
Prof.dr. J.H. MacMahan,	Naval Postgraduate School, Monterey, USA
Prof.dr.ir. J.A. Roelvink,	Unesco-IHE Delft
Prof.dr. B.G. Ruessink,	Universiteit Utrecht
Dr. K.M. Wijnberg,	Universiteit Twente
Prof.dr.ir. W.S.J. Uijttewaal,	Technische Universiteit Delft, reservelid

This research has been supported by EcoShape / Building with Nature under project code NTW 3.2. The Building with Nature program is funded from several sources, including the Subsidieregeling Innovatieketen Water (SIW, Staatscourant nrs 953 and 17009) sponsored by the Dutch Ministry of Infrastructure and the Environment and partner contributions of the participants to the Foundation EcoShape. The program receives co-funding from the European Fund for Regional Development (EFRO) and the Municipality of Dordrecht.

Cover design: Alex Schreuders / MetInspiratie

ISBN 978-94-6186-247-1

Summary

Supplying additional sand to dunes, beach and shoreface by means of nourishments is a widely applied technique to mitigate coastal erosion. The implementation of these nourishments changes the topography of the beach and therefore impacts the nearshore coastal currents. One of the important coastal currents in this regard are horizontal flow circulation patterns as these affect the mixing of biota and nutrients in the coastal zone but can also cause distress to swimmers. Two phenomena inducing flow circulations are researched in this thesis; the alongshore variability in the topography and alongshore variability in wave forcing due to wave groups.

A prediction of these alongshore variability phenomena for a (Dutch) nourished beach is difficult as the behaviour is non-deterministic and data on these nourished beaches is scarce. Moreover, prior to this study the knowledge of the impact of the type of wave climate (swell vs wind sea) on the response was limited, and therefore is was unclear how the observations at natural, open ocean beaches could be translated to the Dutch coastal setting. To improve on predictability of these phenomena, the present research was aimed at collecting and analysing field observations of alongshore variability, preferably at nourished beaches, and elaborating further using conceptual numerical modelling. Special attention was paid to the effect of the 'wind sea' type of sea state at the Dutch coast, characterised by short wave periods, a wide spread in directions and frequencies of the incoming wave field and often accompanied by large angles of wave incidence.

The starting point for this research were data of emerging alongshore topographic variability at a nourished beach. Over 3 years of morphodynamic data were collected at Vlugtenburg beach, the Netherlands, after implementation of a large nourishment that covered all prior topographic variability. The detailed bathymetric surveys (38 in total) were executed nearly monthly using both jetski and GPS backpack surveys. These measurements showed in detail how the cross-shore profile of the beach transforms in the years after the nourishment was implemented. The first period just after implementation of the nourishment showed no different magnitude of variability than the total

period investigated, and therefore an apparent effect of the nourishment shape on the variability could not be discerned. Moreover, changes in topographic variability were found to be on the timescale of months, which is much slower than previous observations at the US east coast (Duck, NC) or Australian east coast (Palm Beach, Gold Coast).

The relation between incoming wave conditions and changing alongshore topographic variability on a beach was elaborated further in-depth, aiming to understand better the observed differences between beaches in different coastal settings. It was hypothesised that the formation time of alongshore variability is dependent on sea state (long crested swell waves or nearby generated wind sea). Unique data of a natural beach (Palm Beach, Australia) were examined since the variability at this site evolves rapid (on the timescale of days) and variability is removed several times a year by storms and subsequently regenerated. Four years of Argus video images and wave data were analysed with the primary objective of investigating the impact of wave height, period, angle and frequency bandwidth of the incoming wave field on the formation time T_v of post-reset alongshore variability. The results of the analysis showed that large T_v's (slow formation of variability) coincided with very oblique wave angles. The data analysis also suggested a previously unknown relationship between T_v and frequency bandwidth such that large (small) T_v's coincided with the prevalence of wide (narrow) banded sea (swell) wave conditions after resetting storms.

To test the individual impact of peak period, frequency spread and directional spread on formation time, a conceptual modelling study was undertaken for a schematised embayed beach bathymetry with a single bar. Results of the different scenarios showed different formation times of topographic variability, yet only if the wave period was varied substantially, i.e. from typical Dutch (T_{m01} =5 s) to Australian (T_{m01} =10 s) conditions. Modifications in the directional and frequency spread of the wave field had a negligible effect on the predicted formation time when tested separately. The findings of both model and field data combined confirm the hypothesised relation between sea state and formation time based on the impact of wave period and wave angle. This implies that open ocean coasts with shore-normal or moderately obliquely incident, swell waves represent preferential conditions for rapid development of topographic variability. In contrast, typical Dutch conditions with short wave periods and large angles of incidence yield slower development.

The effect of different sea states was further investigated by examining the effect of sea state on Very Low Frequency (VLF) surf zone velocity fluctuations. These (vortical) VLF surf zone motions are important for the mixing of the suspended material in the surf zone and the presence of transient rip cur-

rents. Moreover, it is previously suggested that these VLF motions contribute to the formation of alongshore variability in the topography.
A second hypothesis was postulated stating that the formation time of alongshore variability in topography is related to the magnitude of the VLF motions. To investigate this hypothesis, first a study was undertaken to examine what determines the magnitude of the VLF motions. Observations of vortical VLF motions measured during an extensive field campaign at Duck, NC, USA were re-analysed. The analysis showed that vortical VLF motions are stronger under long wave period or narrow frequency spread waves (i.e. swell conditions) as found at open-ocean beaches and vortical VLF motions are generally weaker if forced by wind sea conditions. Conceptual model simulations, in which the characteristics of the offshore wave forcing were varied independently, confirmed these field findings. Interestingly, additional computations with this conceptual model also revealed that the slope of the surf zone near the breakpoint largely determines the magnitude of the wave group driven VLF motions. This provides an explanation for the presence of VLF motions that were measured during this study at the nourished Vlugtenburg beach with its short period wind-sea climate, as the beach slope at the time of the campaign was very steep.

A comparison of morphodynamic simulations and the simulations of hydrodynamics alone showed that sea state scenarios with larger VLF motion magnitudes did not consistently coincided with larger (or smaller) formation times. Further investigation also showed that the contribution of VLF motions to sediment transport (fluctuations) is small, which led to the rejection of the hypothesis that the formation time of alongshore variability in topography is related to the magnitude of the VLF motions.

In summary, the present study shows implications of the implementation of a large nourishment on a beach. Measurements showed that, despite substantial changes in the cross-shore profile, the magnitude of topographic variability in the first year after implementation is not necessarily substantially different than a few years after implementation the nourishment. This emerging variability was found to evolve slowly, which can be partly explained by the typical 'wind sea' wave conditions at the Dutch coast (i.e. large wave angles and short wave periods). Also, in the first phase after implementation the initially steep cross-shore profile can result in stronger very low frequency fluctuations in surf zone flow.

Samenvatting

Het aanbrengen van extra zand op de duinen, strand en vooroever, het zogenaamde suppleren, is wereldwijd een veelgebruikte methode om kusten te beschermen tegen ongewenste erosie. Het aanbrengen van dergelijke suppleties verandert de bodemligging van het strand en de daarmee samenhangende stromingen in de ondiepe kustzone. Belangrijk aspect van deze kuststromingen zijn horizontale circulaties omdat deze het transport van biota in de kustzone beïnvloeden en zeewaartse stromingen kunnen opwekken die mogelijk gevaar voor badgasten opleveren. Dit proefschrift beschrijft onderzoek naar twee fenomenen die verantwoordelijk kunnen zijn voor horizontale stromingscirculaties; de variabiliteit van de bodemligging in kustlangse richting en de kustlangse variabiliteit in golf krachten door golf groepen.

Een voorspelling van deze kustlangse variabiliteiten voor een gesuppleerd strand (aan de Nederlandse kust) is moeilijk aangezien het gedrag niet deterministisch is en gedetailleerde metingen aan een gesuppleerd strand schaars zijn. Bovendien was voorafgaand aan deze studie de kennis over de invloed van het type golfklimaat (deining of windzee) op de respons beperkt, en derhalve was het onduidelijk hoe eerdere metingen aan natuurlijke stranden langs oceaan kusten kunnen worden vertaald naar de Nederlandse kustsituatie. Om de voorspelbaarheid van deze fenomenen te vergroten heeft het huidige onderzoek als doel gehad om allereerst meetgegevens van kustlangse variabiliteit te verzamelen en analyseren, bij voorkeur bij gesuppleerde stranden. Daarnaast zijn de bevindingen aan de hand van de gegevens verder uitgebreid met conceptuele numerieke modellering. Extra aandacht is uitgegaan naar het effect van het 'windzee' klimaat aan de Nederlandse kust, wat gekenmerkt wordt door korte golfperioden, een brede spreiding in richtingen en frequenties in het golfveld en vaak sterk schuin invallende golven.

Als startpunt van het onderzoek zijn gegevens verzameld van de ontwikkeling van kustlangse variabiliteit in bodemligging bij een recent gesuppleerd strand. Meer dan 3 jaar aan gegevens van de veranderende bodemligging zijn verzameld bij Slag Vlugtenburg te 's Gravenzande na het uitvoeren van een grote suppletie die alle bestaande variabiliteit in bodemligging had bedekt.

38 gedetailleerde metingen van de bodemligging zijn uitgevoerd met nagenoeg maandelijks interval met zowel jetski als GPS-rugzak apparatuur voor respectievelijk het droge en natte deel van het domein. Deze metingen lieten in detail zien hoe het kustdwarse profiel zich aanpast in de jaren na de aanleg van de suppletie. De eerste periode kort na de aanleg was de variabiteit van vergelijkbare grootte als de volledige periode, en er is derhalve geen effect waargenomen van de aanpassing van de suppletie op de kustlangse variabiliteit in de bodemligging. Bovendien vonden veranderingen in de variabiliteit in de bodemligging plaats op de tijdschaal van maanden. Dit is aanmerkelijk langzamer dan voorgaande waarnemingen aan de oostkust van de Verenigde Staten (bij Duck) of in Australië (bij Palm Beach, Gold Coast).

Er is vervolgens dieper ingegaan op de relatie tussen de eigenschappen van het inkomende golfveld en de veranderende variabiliteit in bodemligging, om de waargenomen verschillen tussen verschillende stranden beter te begrijpen. Een hypothese is opgesteld dat kustlangse variabiliteit afhankelijk is van het type zeegang (langkammige deining of nabij opgewekte windzee). Hiervoor zijn gegevens van een natuurlijk strand (Palm Beach, Australië) onderzocht aangezien de variabiliteit hier snel veranderd (op de tijdschaal van dagen) en variabiliteit enkele keren per jaar wordt verwijderd tijdens stormen om vervolgens weer te ontstaan. Vier jaar aan Argus video beelden en golf gegevens zijn geanalyseerd met als belangrijkste doel om het effect van de golfhoogte, -periode, -hoek en frequentie bandbreedte van inkomende golfveld te relateren aan de ontwikkelingstijd, T_v, van de kustlangse variabiliteit na de storm. De resultaten laten zien dat grote T_v waarden (langzame ontwikkeling van variabiliteit) gelijktijdig optreden met sterk schuin invallende golven. De data suggereren tevens relatie tussen T_v en de frequentie bandbreedte van het inkomende golfveld. Grote (kleine) T_v waarden lijken hierin samen te vallen met periodes waarbij het inkomende golfveld een wijde (smalle) bandbreedte in frequenties heeft.

Om het afzonderlijke effect van golf periode, frequentie bandbreedte en richtingsspreiding van het inkomende golfveld op de ontwikkelingstijd te onderzoeken is vervolgens een conceptuele modelstudie ondernomen met een vereenvoudigd strand met een enkel banksysteem. Resultaten van verschillende scenario's laten verschillende ontwikkelingstijden van de kustlangse variatie in bodemligging zien. Echter, deze verschillen treden enkel op als de golfperiode substantieel wordt gewijzigd, bijvoorbeeld van typisch Nederlandse waarden (T_{m01} =5 s) naar Australische waarden (T_{m01} =10 s). Wanneer enkel de bandbreedte van de frequenties of de spreiding in golfrichtingen van het inkomend golfveld afzondelijk werden gewijzigd had dit nauwelijks effect op de ontwikkelingstijd. De meetgegevens van Palm Beach en de resultaten van

het model bevestigen derhalve de hypothese dat er een relatie bestaat tussen het inkomende golfveld en de ontwikkelingssnelheid van bodempatronen maar enkel door het effect van golfperiode en golfrichting. Dit betekent dat kusten die grenzen aan grote oceaan bekkens met (nagenoeg) recht invallende deining gunstigere omstandigheden hebben voor een snelle ontwikkeling van de kustlangse variabiliteit in de bodemligging.

Het effect van verschillende zeegang is verder onderzocht door te observeren wat het effect is van het type zeegang op zeer laagfrequente fluctuaties in brandingsstroming (VLF's). Deze VLF (circulaties) zijn belangrijk voor de verspreiding van gesuspendeerd materiaal in de kustzone en het optreden van tijdelijke, niet plaatsvaste muistromen. Bovendien is eerder verondersteld dat deze VLF's aanzetten tot de vorming van kustlangse variabiliteit in de bodemligging.
Een tweede hypothese is geformuleerd, die stelt dat de ontwikkelingssnelheid van kustlangse variabiliteit in de bodemligging verband houdt met de sterkte van de VLF stromingsfluctuaties. Hiervoor zijn VLF stromingsfluctuaties onderzocht die gemeten zijn tijdens een uitvoerige meetcampagne bij Duck (Verenigde Staten). Een analyse laat zien dat VLF bewegingen sterker zijn ten tijde van inkomende golven met lange golfperiode en kleine spreiding in frequenties, kenmerkend voor deining langs stranden grenzend aan grote oceaan bekkens en zwakker als deze worden opgewekt door 'wind zee' omstandigheden. Conceptuele model simulaties, waarbij de karakteristieken van het inkomende golfklimaat afzonderlijk zijn getest bevestigen deze bevindingen. Opvallend genoeg laten simulaties met dit model ook zien dat de kustdwarse helling nabij het breekpunt van golven in grote mate de sterkte van de VLF bewegingen beïnvloedt. Dit geeft een mogelijke verklaring voor de waargenomen VLF stromingsfluctuaties bij Vlugtenburg gedurende deze studie onder windzee omstandigheden, aangezien vooroever steil was ten tijde van het experiment.

Desalniettemin laat een vergelijk van simulaties van de waterbeweging en de veranderende bodemligging zien dat omstandigheden met sterkere VLF stromingen niet systematisch leiden tot een snellere of langzamere ontwikkeling van patronen. Uitgebreider onderzoek laat tevens zien dat de bijdrage van VLF sstromingsfluctuaties aan het sediment transport klein is vergeleken met andere brandingsstromingen. Op basis van deze bevindingen is de hypothese dat de sterkte van de VLF stromingsfluctuaties verband houdt met de ontwikkelingssnelheid van kustlangse variabiliteit in de bodemligging verworpen.

Samenvattend toont het huidige proefschrift mogelijke gevolgen van een grote suppletie op een strand. Metingen tonen dat de grootte van de kustlangse variabiliteit in bodemligging in het eerste jaar na aanleg van een suppletie niet sterk hoeft te verschillen van variabiliteit in de navolgende jaren, ondanks de grote veranderingen in kustdwarse profiel die gelijktijdig plaats vinden. De kustlangse patronen van de variabiliteit laten een grote samenhang zien over de maanden, een teken dat patronen slechts langzaam veranderen. Een mogelijke verklaring voor het waargenomen trage gedrag is de grote hoek van golfinval en de korte golfperiode aan de Nederlandse kust. Tevens is gevonden dat na de aanleg het aanvankelijk steile profiel sterkere VLF stromingsfluctuaties tot gevolg kan hebben.

Contents

1 Introduction

Supplying additional sand to dunes, beach and shoreface by means of nourishments is nowadays a widely applied technique to mitigate coastal erosion (e.g. *Valverde et al.*, 1999; *Hanson et al.*, 2002; *Dean*, 2002). The implementation of these nourishments however not only modifies the topography of the beach but also impacts the nearshore coastal currents. One of the important coastal currents in this regard are the horizontal flow circulation patterns which affect the mixing of biota and nutrients in the coastal zone and also, on occasion, cause distress to swimmers (*McLachlan and Hesp*, 1984; *Talbot and Bate*, 1987; *Dalrymple et al.*, 2011, amongst others). These horizontal flow circulations can have different origins of which two are investigated in detail in this thesis; firstly the alongshore variability in bed level elevation that can induce mostly stationary flow circulation patterns and secondly, the transient circulations induced by temporal and alongshore variations in wave forcing. The overarching objective is to develop the capability to predict the magnitude and presence of alongshore topographic variability and resulting horizontal flow circulations.

1.1 Context

The coastal zone is increasingly under pressure, with growing population and economic value on the landward side and a foreseen sea level rise on the seaward side, increasing the risk of flooding. On the Dutch coast this 'coastal squeeze' is very prominent, with narrow dune rows and a densely populated hinterland below sea level, making this area highly vulnerable. Over the course of the last few centuries, large parts of the Dutch coast have been structurally eroding and several coastal towns have been lost and repositioned. Traditionally the continued erosion was mitigated by building coastal structures; strengthening the coastline locally with seawalls, breakwaters, or groynes amongst others. However, as these do not resolve the origin of sediment loss from a coastal cell, these measures have not provided a permanent solution to the coastal recession.

Using artificial shore nourishments, as an alternative way of mitigating erosion, was introduced in the middle of the 20^{th} century. In this approach sand is dredged offshore (i.e. 10 km offshore beyond the -20 m isobath in the Dutch case) and placed at a beach with a shortage of sediment. Although the sand can be eroded again and consequently nourishments often only provide a temporary solution, it has proven to be more cost effective to re-nourish every few years than to construct coastal structures (*Hanson et al.*, 2002; *Roelse*, 1996, 2002). Therefore, after successful initial projects, nourishments were adopted by the end of the last century as the preferential coastal erosion mitigation method by the Dutch Ministry of Infrastructure and the Environment (*Rijkswaterstaat*, 1990), and have been executed ever since at numerous locations (*Hanson et al.*, 2002).

The present day Dutch coastal policy states that the coastline has to be maintained seaward of its 1990 position, and no substantial coastal recession is to be allowed. To execute this policy the Dutch Ministry of Infrastructure and the Environment performs a yearly evaluation of the coastal profiles approximately every 250 m alongshore. A nourishment project is planned if the coastline trend indicates that the coastline position may migrate landward of the recorded 1990 position (*van Koningsveld and Mulder*, 2004). From the time this policy was adopted, the total annual nourishment volume along the Dutch coast has increased from 6 million m^3 per year in 1990 (*Hanson et al.*, 2002) to 12 million m^3 in 2012 (*Stive et al.*, 2013). Moreover, to compensate for the projected sea level rise, the annual nourishment volume is envisaged to increase to 40-80 million m^3 over the 21^{th} century (*New Delta Committee*, 2008).

Simultaneously, the design of coastal nourishments has changed over the

years from a direct beach/dune protection to a more indirect feeder approach. The first nourishments executed along the Dutch coast, starting in 1970 (*Hamm et al.*, 2002), were beach and dune nourishments. Sand is placed high up the profile, directly providing material to compensate for dune and beach erosion in case of a storm event (Figure 1.1, top). These nourishments are relatively expensive due to the effort required to reshape the sand high up the profile and moreover it's often necessary to temporarily close the beach affecting the beach amenity.

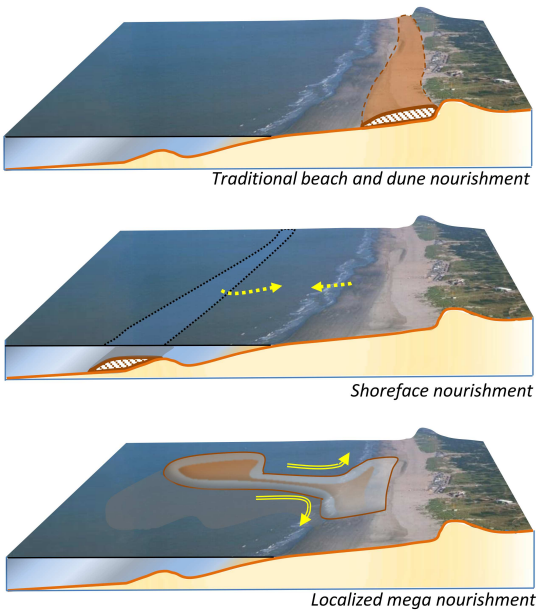

Figure 1.1: Conceptual overview of the different nourishment strategies. With the traditional beach and dune nourishments the sand is supplied on the coastal defense itself (top). Shoreface nourishments as introduced in the 1990's utilise marine processes to redistribute the sand in the cross-shore and create a wider coastal defense over time (middle). Concentrated mega nourishments, as recently introduced, account for both marine and aeolian processes to redistribute the sand both in cross and alongshore directions (bottom). *Modified from: Stive et al.* (2013).

From the 1990's onward the nourishment strategy and design shifted towards the use of shoreface nourishments (*Stive et al.*, 2013), placing the sediment a water depth of 4 to 6 m (Figure 1.1, *middle*) by bottom dumping or pumping the sand over the bow of the dredging vessel ('rainbowing'). As no reworking of the sand is necessary on the beach this method is less costly per disposed m^3 sand nor is it required to close off the beach. The safety against flooding increases from the sediment on the shoreface by means of two indirect effects: 1) the 'feeder' effect, where the sediment is redistributed from the nourishment mass to the beach and 2) the 'leeside-effect' where the nourishment acts as a berm with enhanced wave dissipation thus protecting the beach (*Grunnet et al.*, 2004). The latest development in nourishment strategy is the implementation of concentrated (mega) nourishments (Figure 1.1, *bottom*). Here a large volume of sand in placed at a single location with the intention to feed the adjacent coast. Under the combined wind, waves and tides the sediment is expected to be redistributed in along and cross-shore directions, hence enhancing the safety of a longer stretch of coast (*Waterman*, 2010). Inspired by the projected increase of nourishment volume of the *New Delta Committee* (2008) this concept is now being tested at the Dutch coast with the *Sand Engine* pilot project (*Stive et al.*, 2013).

The shift in nourishment design is partly driven by a more multi-disciplinary evaluation of coastal projects (*Roelse*, 1996). Rather than the longest (visible) lifetime for coastal protection or a cost-benefit analysis solely based on sediment balance, nourishment projects are now evaluated including ecology, recreational, safety and landscape values (*Aarninkhof et al.*, 2012). With the increasing size and sequencing of the nourishments these latter aspects have become more and more important (*Stive et al.*, 2013) and questions arise about the impact of nourishments on these other indicators. It is within this context that the current project is carried out.

One of the effects questioned is the impact that nourishments have on the alongshore topographic variability and horizontal hydrodynamic circulation patterns. The topography of a beach is often not perfectly uniform in alongshore direction but contains some variability. The presence of this alongshore variability can induce horizontal hydrodynamic circulations which are of importance for ecology and water quality, as hydrodynamic circulations play a key role in mixing of nutrients, organisms and other suspended matter (*Inman et al.*, 1971; *McLachlan and Hesp*, 1984; *Talbot and Bate*, 1987; *Smith and Largier*, 1995; *Grant et al.*, 2005; *Clarke et al.*, 2007; *Reniers et al.*, 2010, amongst others). Moreover, they can result in strong offshore directed flows (i.e. rip currents) and can therefore pose a threat to swimmers (*Shepard et al.*, 1941; *Johnson and Pattiaratchi*, 2004; *MacMahan et al.*, 2006; *Short*, 2007;

Dalrymple et al., 2011; *Brander and MacMahan*, 2011; *Austin et al.*, 2012, amongst others). As nourished beaches are often situated along the most heavily used coastal zones, a change in swimmer safety and ecology due to a nourishment (design) is of primary interest.

1.2 Problem definition & Research focus

The current prediction skill for the magnitude of alongshore topographic variability and horizontal hydrodynamic circulations after installation of a nourishment is limited, impeding the evaluation of ecology and recreational safety amongst others. This is due to two aspects, firstly a shortage in observations on nourished beaches giving little information from reference projects. Secondly, the processes generating topographic variability and horizontal hydrodynamic circulations are not fully understood, such that it's not clear why different beaches show different patterns and magnitude of variability, regardless of whether the beach is nourished or natural. This thesis is focused on addressing these issues, collecting and examining data gathered at a nourished beach as well as investigating two mechanisms of horizontal hydrodynamic circulations in detail; alongshore topographic variability and non-stationary flow circulations on the very low frequency timescale.

Figure 1.2: Alongshore variability of the intertidal topography at Katwijk, the Netherlands. Image: Beeldbank Rijkswaterstaat / Rens Jacobs.

Alongshore topographic variability

Alongshore topographic variability is here defined as the deviation of the bed elevation in alongshore direction from an alongshore uniform topography (Figure 1.2). This alongshore variability in topography on the coast can be observed near the shoreline (e.g. beach cusps) or in the intertidal and subtidal bar(s) (e.g. a bar-rip morphology).

In case of a bar-rip morphology the typical depth variations between the rip channels and shallow shoals are of O (1 m) (*Brander*, 1999; *MacMahan et al.*, 2006; *Winter et al.*, 2012), and alongshore spacing between the rip channels of $\sim$ 100 to 3000 m (*van Enckevort et al.*, 2004; *Holman et al.*, 2006). The presence of topographic variability results in alongshore variations in wave breaking and as a result a horizontal circulation pattern is generated in the surf zone, with onshore flow over the shallow shoals and offshore flow in the deeper rip channels (e.g. *Shepard et al.*, 1941; *Sonu*, 1972; *Brander*, 1999; *Reniers et al.*, 2001; *MacMahan et al.*, 2006, 2010a). The offshore flow velocities in these rip channels can reach 1.5 m/s (*MacMahan et al.*, 2006; *Dalrymple et al.*, 2011). Consequently these current patterns also have a feedback on the morphology, such that (small) topographic variability can grow over time by feedback (*Coco and Murray*, 2007) or existing topographic variability can be maintained (*Smit et al.*, 2010).

The generation of alongshore variability in nearshore bars (or rip generation) has been the subject of great scientific interest since the middle of the last century. Over the years, various rip generation mechanisms and models have been presented by different authors. These can be broadly categorised into 2 types: hydrodynamic template (forced) models and instability or self organization models.

The first category, hydrodynamic template models, are based on forced behaviour in which a permanent offshore forcing contains an alongshore length scale which is imposed on the topography. As such the alongshore topographic variability is a direct result of the forcing. Alongshore variation in wave height due to complex topography is the clearest example of a hydrodynamic template, such as found at offshore submarine canyons (*Long and Özkan-Haller*, 2005) or coupling with an offshore crescentic outer bar (*Castelle et al.*, 2010). For an alongshore uniform profile, a hydrodynamic template could be given by water level variations in the nearshore generated by intersecting wave trains (*Dalrymple*, 1975) or infragravity edge waves as proposed by *Bowen and Inman* (1971) and later extended by *Holman and Bowen* (1982) and *Symonds and Ranasinghe* (2000).

The second category, instability or self organization models, are based on small system perturbations (hydrodynamic or morphological). In this cate-

gory, the alongshore variable topography is created by interaction between the morphology and the feedback mechanisms in the fluid and sediment motion. Small or temporary perturbations in hydrodynamic forcing or topography can hence trigger instabilities that will result in the growth of specific preferred morphological length scales of O ($\sim$100 m) in these models. Linear and nonlinear stability models explore the growth rate of perturbations of different length scales revealing perturbations that are either dampened (negative feedback), or enhanced (positive feedback) by the mean flow. Fastest growing mode(s) are assumed to be representative for the final topography (e.g. *Hino*, 1974; *Deigaard et al.*, 1999; *Coco et al.*, 2002; *Calvete et al.*, 2005, 2007; *Falqués et al.*, 2008; *Garnier et al.*, 2008; *Thiebot et al.*, 2011). This self organization behaviour can also be simulated with process based 2DH (or Quasi3D) coastal area models. In this case the alongshore uniform topography is seeded with very small random bottom level perturbations of O (0.01 m) which trigger the development of rip shoal patterns (e.g. *Damgaard et al.*, 2002; *Castelle et al.*, 2006; *Drønen and Deigaard*, 2007; *Smit et al.*, 2008). Similarly, (small) variations in the forcing in process based simulations are also capable of starting the feedback and the development of realistic rip shoal patterns (*Reniers et al.*, 2004). Here, perturbations in the forcing are given by the temporal and spatial variations in wave groups thus containing distinct (non-random) length scales. Their work suggests that flow fluctuations on Very Low Frequency (VLF) timescale of O (10 min) trigger the development of rip channels.

Little is known on the observed magnitude of emergent topographic variability in case the cross-shore profile is substantially modified by the implementation of a nourishment. Most research into the subject either focuses on the length scales of variability (e.g. *Ojeda et al.*, 2008; *Ruessink et al.*, 2012) or uses simplified conceptual models to evaluate the matter (*Klein*, 2006). One of the aspects currently lacking is research observing the emerging and changing topographic variability in the years after installation of a nourishment, linking the overall behaviour of the nourishment to the evolution of alongshore variability, specifically whether the first period after implementation results in larger or smaller variability magnitude. The latter is of importance to asses if extra safety measures are necessary in the first period after implementation of the nourishment.

Non-stationary flow circulations on the Very Low Frequency timescale

The second type of horizontal flow circulations of interest are the non-stationary flow circulations that can be present even on a (nearly) alongshore uniform topography (Figure 1.3). Although such vorticity occurs on multiple scales, the focus here is on large scale features of O (100's m). As these have timescales

Figure 1.3: Large scale non-stationary horizontal flow circulations of the coast of Angola. Image: S. Ross / Boskalis

of the order of 10 minutes and they can be vortical (eddy-like) rather than wave-like motions, they are referred to as vortical Very Low Frequency motions (VLF's) (*MacMahan et al.*, 2004; *Reniers et al.*, 2007; *MacMahan et al.*, 2010b). As stated, previous findings of *Reniers et al.* (2004) suggests that these VLF motions trigger the development of rip channels and are thus an important process for the generation of alongshore variability in the topography. Velocity motions on the VLF timescale can be generated by the temporal alongshore variability in wave forcing originating from the natural spread in the wavefield (*Peregrine*, 1998; *MacMahan et al.*, 2004; *Spydell and Feddersen*, 2009; *MacMahan et al.*, 2010b), or from strong shear in the flow causing instabilities (*Oltman-Shay et al.*, 1989; *Aagaard and Greenwood*, 1995; *Haller et al.*, 1999; *Miles et al.*, 2002; *Noyes et al.*, 2005). *MacMahan et al.* (2010b) hypothesise VLF motions due to spread in the wavefield to be ubiquitous, and strong VLF related surf zone velocities of O (0.5 m/s) have been measured in absence of strong alongshore current at several open ocean beaches with medium to long wave periods (US East coast, *Smith and Largier* (1995); *MacMahan et al.* (2004), US west coast, *MacMahan et al.* (2010b) and Australia, *Johnson and Pattiaratchi* (2004)). However, at a beach with short wave periods (T of 3-6 s) on the Israeli Mediterranean coast, *Bowman et al.* (1988) find no VLF pulsations in their observations. Moreover, observations at a single beach show that the magnitude of vortical VLF velocity fluctuations can vary significantly from day to day and for a given offshore wave height at a single beach, the existing observations of VLF magnitude show a large scatter (*MacMahan et al.*, 2010b). Although these transient hydrodynamic circulations are ubiquitous

and potentially large, there is only limited knowledge on what determines the magnitude of the VLF motions, and whether they are sufficiently strong and persistent to generate alongshore variability in the nearshore zone.

Both alongshore variability in topography and VLF surf zone motions have been primarily researched at open ocean coasts (e.g. *Ranasinghe et al.*, 2004; *Holman et al.*, 2006; *Turner et al.*, 2007; *Price*, 2013; *MacMahan et al.*, 2010b; *Spydell and Feddersen*, 2009). The Dutch coast is however located on a shallow (20-80 m water depth) marginal sea. One of the differences between the two coastal settings is the type of wave conditions. Open ocean coasts located far from the wave generation area (i.e. storms) experience much longer crested waves (characterised as a 'swell' sea state) than locations closer to the storm generation area which show a more short-crested 'wind sea' sea state (see Figure 1.4).

Figure 1.4: Examples of different sea states. Top panel shows an aerial photograph taken at the Dutch coast, showing short wave crests and short period waves. Bottom panel shows longcrested long period waves arriving at the coast of New Zealand. Both images are to similar scale. Image data: Google, Aerodata, DigitalGlobe.

Observations at ocean coasts show that alongshore variability can change on short timescales, of the order of days (e.g. *Ranasinghe et al.*, 2004; *Holman et al.*, 2006; *Ranasinghe et al.*, 2012). Yet, observations at the Dutch coast show a more gradual change in alongshore variability (*van Enckevort and Ruessink*, 2003b). It is presently unknown whether the difference in wave conditions has an effect on the alongshore variability in topography and VLF motions.

1.3 Overall aim & Research objectives

The overall aim of the present study is to collect and examine data on alongshore variability in topography at a nourished beach and, more generally, to investigate the generation of alongshore topographic variability and Very Low Frequency motions under different wave forcing conditions. This research is separated into four different in-depth research objectives:

1. Examine the morphological development and emergent alongshore topographic variability at a beach after implementation of a nourishment with frequent topographic surveys.
Results provide quantitative values of topographic variability on the timescale of months to years. As data is obtained at a nourished beach, the frequent topographic surveys can be used to evaluate whether the evolution of alongshore variability in topography relates to the profile adaptation after the nourishment, the concurrent wave forcing over the months, or both.

A specific aspect of the emergence of alongshore variability, the formation time, is investigated further focussing on the impact of the characteristics of the wave forcing. The formation time, defined as the time it takes to evolve from a (nearly) alongshore uniform topography to an alongshore variable topography, shows how rapid the coastal system responds to the incoming wave forcing. For the current thesis it is hypothesised that *[H.1] different sea states (short wind sea or distant swell waves) yield different formation times of variability.*
This results in the second research objective:
2. Examine the impact of wave field characteristics (wind sea vs swell) on the emergence of alongshore topographic variability.
This part of the research examines to understand which conditions are favourable for a rapid generation of alongshore topographic variability at a specific beach.

Understanding the effect of the type of wave forcing is paramount to generalise findings from the Dutch coast.

Additionally, previous work by *Reniers et al.* (2004) shows that Very Low Frequency surf zone motions have the potential to generate alongshore topographic variability. Yet, these VLF motions can be of different magnitudes, as seen in previous field experiments. In line with the work of *Reniers et al.* (2004) it is hypothesised that *[H.2] VLF motion magnitude is important for the formation time of variability.* Combined with hypothesis *[H.1]* two further research objectives are regarded:
3. Examine the magnitude of Very Low Frequency surf zone motions under different sea states (wind sea vs swell) and profiles.
Investigation of the controls on the magnitude of VLF motions potentially clarifies under which conditions strong VLF motions can be expected. Besides their hypothesised role in the emergence of topographic variability, VLF motions can also yield substantial horizontal flows. This is important for mixing and transient rip currents even without the presence of topographic variability in the topography.
And:
4. Examine the relation between magnitude of Very Low Frequency surf zone motions and the formation time of topographic variability.
By examining conditions with different VLF motion magnitude and concurrent formation process of topographic variability, the final research objective confirms or refutes the hypothesis *[H.2]* on the importance of VLF motion magnitude for the formation time of variability.

In all, the proposed elements aim to provide new data and insight in how alongshore variability evolves at Dutch nourished beaches. Furthermore, results potentially show how results from beaches in different wave forcing environments can be translated based on wave forcing characteristics.

1.4 Outline

The thesis is organised in chapters following the objectives above. First the topographic observations of a nourishment case study at Vlugtenburg beach are discussed (Chapter 2). Analysis of monthly surveys after implementation of a nourishment elaborates on how an initially nearly alongshore uniform profile evolves over time into a more natural topography and associated evolution of the alongshore topographic variability. Chapter 3 addresses the formation

of alongshore variability in topography in more detail, investigating the effect of the type of wave conditions on the emergence speed of topographic patterns based on video data of a natural beach. Several transitional periods (in which the topography evolves from nearly alongshore uniform to alongshore variable) are examined in conjunction with the concurrent wave conditions to observe preferential conditions for which rapid development of variability occurs. Chapters 4 and 5 investigate the hypothesised effect of sea state and very low frequency surf zone (VLF) velocity fluctuations. Chapter 4 investigates the presence and magnitude of VLF motions for different sea states. Measurements of a field campaign are used to investigate the presence of VLF motions at a Dutch nourished beach. Further investigation into sea state dependency is performed using data collected at Duck NC, USA. Conceptual numerical modelling is executed to reveal how the magnitude of these motions may be dependent on the type of wave conditions and profile.
Chapter 5 elaborates on the emergence of variability under different sea states using conceptual morphodynamic modelling. Schematised cases show the difference between the (Dutch) wind sea climate and a (open ocean) swell wave climate on the formation of alongshore variability. Furthermore the suggested contribution of VLF motions for the formation of variability is evaluated.

The contents of this thesis is arranged as a compilation of research manuscripts with separate introductory sections and conclusions. In order to retain chapters that are legible individually, some parts are repeated. A one-page intermezzo between chapters provides an abstract of the upcoming chapter and discusses its coherence with other chapters.

Abstract Chapter 2
The morphodynamic evolution of a beach after implementation of a beach and shoreface nourishment is examined on the timescale of months, to investigate 1) the adaptation of the constructed profile towards a more natural profile and 2) the generation and evolution of alongshore variability in topography. The dataset consists of 38 surveys at Vlugtenburg beach, the Netherlands, containing both the sub-aqueous and sub-aerial beach and spanning 3.5 years in total.
Morphodynamic evolution is analysed first in terms of nourishment volume, shoreline changes and redistribution of sand in the cross-shore. Results show that the initially steep construction profile results in a large redistribution of nourished sand from high up the profile down and seaward to the subtidal zone, and resulting in a retreat of the initial shoreline. The evolution can be characterised by two periods, a first period of 6 to 12 months in which the largest losses of sediment volume are observed, of O (70 m^3/m alongshore/yr), and the steep foreshore slope is re-adjusting and a subtidal bar is formed. The following 2.5 to 3 years show a slower evolution and sediment losses in the area are limited, of O (15 m^3/m alongshore/year).
Furthermore, the emergence of a cyclic subtidal bar system is observed and its emerging alongshore variability is compared to environmental and topographic controls previously suggested as governing processes. This analysis shows that the variability at Vlugtenburg beach is evolving on a monthly timescale and much slower than previous observations at the US east coast (Duck, NC) or Australian coasts (Palm Beach, Gold Coast). Temporal variation in the magnitude of the alongshore topographic variability is found to be related to the incoming wave power offshore. In contrast to other beaches, storms do not remove the alongshore variability in topography. Instead, energetic storm events during winter result in a rapid increase in variability, which is then followed by a gradual decrease in alongshore variability during milder spring and summer wave conditions.

Novel items in Chapter 2 are:

- Detailed measurements of emerging alongshore variability after implementation of a large nourishment covering all pre-existing variability.
- Investigation of the evolution of alongshore variability based on measured depth variations in surveys rather than planform variability extracted from imagery data.
- The postulated relationship of increased initial losses at a nourished site with alongshore gradients in sediment transport due to the construction profile shape.

2

Alongshore topographic variability and morphological evolution at a nourished beach

2.1 Introduction

Beach and foreshore nourishments are nowadays widely applied worldwide (e.g. *Valverde et al.*, 1999; *Hanson et al.*, 2002; *Dean*, 2002). Often the primary objectives for nourishment projects are to enhance safety of the coastline against flooding or to widen the beach for recreational use. This chapter focuses on the medium term development (timescale of months to 4 years) of the beach and foreshore topography after implementation of a large nourishment. It discusses in part the overall changes in sediment balance at a nourished beach and the adjustment from a man made cross-shore profile. Special emphasis is on the alongshore variability in topography that emerges and evolves over time.

Alongshore topographic variability is the deviation of the bed height in alongshore direction from an alongshore uniform topography. It can be observed near the shoreline (e.g. beach cusps) or in the subtidal bar(s) (e.g. a bar-rip

morphology) amongst others. This variability in topography often coincides with horizontal hydrodynamic circulations and offshore directed flows, which provide mixing of nutrients but can also cause distress to swimmers (*McLachlan and Hesp*, 1984; *Talbot and Bate*, 1987; *Dalrymple et al.*, 2011, amongst others).

Alongshore variability and pattern formation on natural beaches has been a subject of vigorous research over the years (e.g. *Hom-ma and Sonu*, 1962; *Bowen and Inman*, 1971; *Hino*, 1974; *Wright and Short*, 1984; *Coco et al.*, 2002; *van Enckevort and Ruessink*, 2003b; *Reniers et al.*, 2004; *Ranasinghe et al.*, 2004; *Holman et al.*, 2006; *Smit*, 2010; *Splinter et al.*, 2011). Topographic variability on a natural beach is nowadays commonly thought to be originating from self-organisation; the intrinsic instability of the nearshore topography and its forcing causes small initial perturbations in the bed level into grow to large bed forms and patterns (e.g. *Hino*, 1974; *Falqués et al.*, 2000; *Coco and Murray*, 2007, and references therein). Moreover, detailed conceptual modelling has revealed that the magnitude and spacing of the variability is dependent on multiple parameters; on the one hand related to external forcing such as wave height, angle and period (e.g. *Deigaard et al.*, 1999; *Calvete et al.*, 2005; *Castelle et al.*, 2007; *Thiebot et al.*, 2011) and on the other hand dependent on the characteristics of the cross-shore profile such as bar volume and crest position (e.g. *Damgaard et al.*, 2002; *Calvete et al.*, 2007; *Smit et al.*, 2008). These relations are difficult to examine in nature, as often the signal is masked by antecedent morphology. Once a spatial pattern is developed, it can remain enforced by a variety of wave conditions (*Holman et al.*, 2006; *Smit et al.*, 2012), such that variability observed at a single instant does not need to be in balance with the concurrent conditions (*Plant et al.*, 2006).

Little is known on how nourishment design can influence the generation of topographic variability. Most nourishment evaluation is concentrated on the overall sediment balance and the cross-shore redistribution of the nourished sediment, being indicators of the performance of a nourishment project in terms of beach width and safety against flooding. In general, Dutch nourishment projects have a lifetime of 2 to 6 years (*de Sonneville and van der Spek*, 2012). Larger volume nourishments tend to have a longer lifetime, but the placement of the nourishment in the cross-shore is crucial. Nourishments placed high up on the profile (i.e. beach fills), are found to have a short lifetime of 1-2 years (e.g. *Yates et al.*, 2009; *van Rijn*, 2011).

As discussed by *van Duin et al.* (2004); *Grunnet and Ruessink* (2005); *Klein* (2006) and *Ojeda et al.* (2008), nourishments can interact with the pre-existing subtidal bars. The first readjustment of the nourishment to the bars is on the timescale of months (*Grunnet and Ruessink*, 2005). The autonomous bar

behaviour can be interrupted by the implementation of a nourishment, and nourishments have been reported to impede the bar migration cycle (*Grunnet and Ruessink*, 2005; *van Duin et al.*, 2004).

Based on isolated conceptual modelling, steep beach slopes (such as found after implementation of a nourishment) are thought to yield faster development of alongshore variability in topography as "cross-shore gradients in all processes are inversely scaled with the profile slope" leading to faster feedbacks (*Drønen and Deigaard*, 2007). Such findings have however not been reported in the field to date, and it is therefore unclear whether nourishment design can be adjusted to reduce (or promote) the alongshore variability. Only at a single site, Terschelling, the Netherlands, variability was reported to increase after a nourishment (*Grunnet and Ruessink*, 2005), whilst after nourishments at Noordwijk, the Netherlands, no effect was found on the variability (*Ruessink et al.*, 2012). Such intersite differences are, based on these first observations, suggested to be related to the positioning of the nourishment with respect to the pre-existing and surrounding bars (*Ruessink et al.*, 2012).

To avoid the interference with remnant and surrounding morphology it would be beneficial to investigate a nourishment project with complete regeneration of subtidal morphology. The objective of the current study is therefore to examine in detail the development of alongshore variability after implementation of a large beach and shoreface nourishment covering all subtidal bars and variability prior to the nourishment. Typically, alongshore variability in topography is examined over time using imagery data, showing in high temporal detail the alongshore length scales of the bar crest (rip spacing) and the planform variations in the bar or nourishment position from shore (e.g. *Ojeda et al.*, 2008; *Ruessink et al.*, 2012). Here a different approach is used, using frequent detailed bathymetric surveys to focus not only on the plan view variations in bar crest position but predominantly on the magnitude of the patterns (i.e. incorporating the vertical dimension). Special attention is paid to the temporal variations in alongshore variability and their relationship to the cross-shore profile evolution of the nourishment and wave forcing.

To evaluate the alongshore variability and morphological evolution this chapter is organised as follows. First the field site and investigated nourishment are discussed, followed by the methodology and observations of the topographic surveys and the wave forcing. Results are subsequently organised in five sections: The overall sediment budget (§ 2.4.1), the evolution of the shoreline position(§ 2.4.2), the cross-shore redistribution of the sediment within the profile (§ 2.4.3), the characteristics of the emerging subtidal bar (§ 2.4.4) and finally the alongshore variability in the topography (§ 2.4.5). Emergent alongshore variability is related to other extracted parameters (e.g.

shoreline migration and wave forcing) in the discussion section. Finally, main conclusions of this part of the study are summarised in Section 2.6.

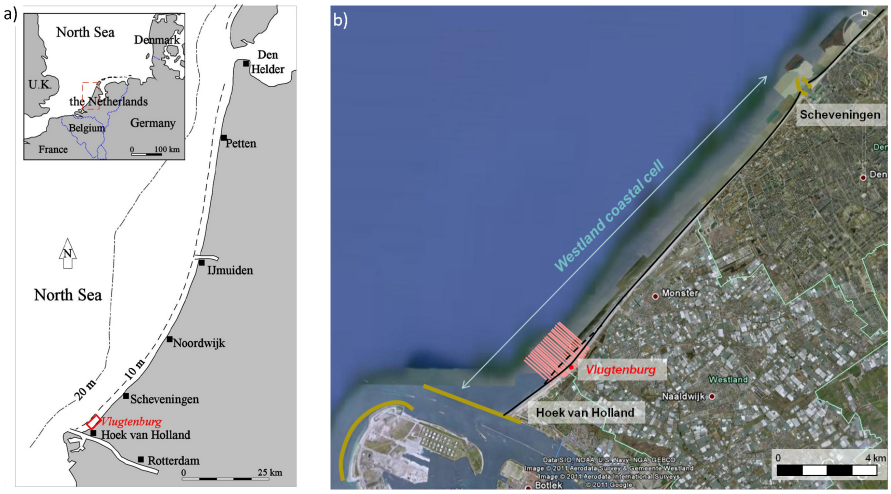

Figure 2.1: a) Location of Vlugtenburg beach on the Holland coast.
b) Satellite view of the Westland coast. Approximate coastline position prior (post) construction of the nourishment project at Vlugtenburg given by the solid (dashed) black line. Yellow lines indicate the harbourmoles of the port of Rotterdam (in the south) and port of the Hague (north). Survey profiles shown by the pink lines.

2.2 Study area

The studied beach, Vlugtenburg beach, is located in the 'Westland' coastal cell, a 17 km stretch of sandy coast between the harbourmoles of the Hague and Hoek van Holland on the southwest part of the Dutch coast (Figure 2.1). Vlugtenburg beach is situated at the south end of this Westland cell, 3 km north of the harbourmoles of Hoek van Holland. In 2008, prior to the nourishment investigated, the coastline at Vlugtenburg beach was slightly concave in planview (Figure 2.1). In cross-shore direction the beach profile was mildly sloping, with the slope between +3 and -5 m NAP and +3 and -10 being respectively 1:70 and 1:120 (see Figure 2.2 b). Towards the south end of the beach the slope at the deeper contours was slightly milder, leading towards the harbourmoles. This part of the coast is sandy and median grain size around

the shoreline in this area is O (250 μm). The profile on the Holland coast generally contains multiple nearshore subtidal bars, migrating offshore in cycles with return intervals of 4 to 16 years (*Ruessink et al.*, 2003). The location of the field site, at the southern end of the Holland coast, showed less prominent temporal behaviour over the decades before the project; generally only a single bar offshore of the groyne heads (*Wijnberg and Terwindt*, 1995). Possibly the less prominent bar behaviour and cyclic migration at this site was influenced by the presence of the groynes, and as there are no records of the coastal profile in the 1700's (before the groynes), it was unclear a priori what kind of profile and bar behaviour could be expected after completion of a large nourishment project.

The coastline angle at Vlugtenburg is 40 degrees with respect to North. Mean annual wave height and wave period are H_{m0}=1.4m and T_{m01}=5s and wave direction offshore is predominantly oblique from the south west and north sectors (85 counterclockwise and 50 degrees clockwise with respect to shore-normal) (*Wijnberg*, 2002). The site has a mean tidal range of 1.7 m and -due to the propagating character of the tidal wave at this coast- also a horizontal tide with an amplitude of O (0.5 m/s).

In the centuries prior to the construction of the nourishment, this part of the coast was characterised by rubble mound groynes around 250 m apart which were installed from the year 1791 onwards. Despite the presence of these groynes, the coast suffered from structural erosion and sand nourishments were implemented starting in 1971. Around the 1990's the nourishment frequency increased as a result of the new policy to arrest the coastline at its 1990 position. Since then an average about 1.10^6 m^3 of sand has been nourished per annum along the 17 km coastal stretch to preserve the current coastline position. Some locations herein were being frequented almost biennially[1]. Despite these nourishments the Westland cell was identified as a weak link in the coastal defence in 2006 and a large scheme of nourishments was initiated in 2008 (the *'Delflandse Kustversterking'* project) to strengthen the entire Westland coast with almost 12.10^6 m^3 of sand on shoreface, beach and dune (*Hoogheemraadschap van Delfland*, 2007).

2.2.1 Investigated nourishment project

The large *'Delflandse Kustversterking'* nourishments implemented from 2008 onwards covered all antecedent beach morphology and groynes to create a new

[1] RWS nourishment records between 1990-2007. In this period about 15.10^6 m^3 sand has been supplied over the coastal stretch.

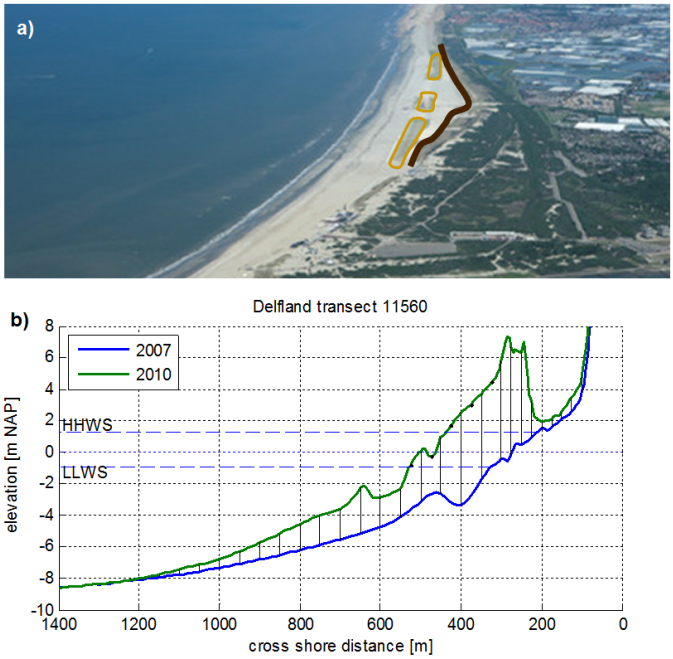

Figure 2.2: a) Aerial view of the Vlugtenburg field site after implementation of the nourishment project. The old dune (app. +10 m NAP) and new constructed foredune (app. +6 m NAP) are indicated by the dark brown and yellow lines, respectively. b) Coastal profiles of the Ministry of Infrastructure and the Environment ('JARKUS' profiles) prior to (blue) and post-construction (green) of the nourishment.

beach type. The investigated nourishment project at Vlugtenburg beach was particularly large, moving the cross-shore profile seaward by 300 meters with beach and shoreface nourishments. This reduced the planform concavity in the coastline and created a new artificial dunerow (Figure 2.2a). The new lens-shaped dunevalley of 35 hectares between the old and new artificial dunerow is proposed to serve as a nature reserve to compensate for the reduction in nature values attributed to a nearby port expansion. The nourished volume is large compared to other nourishments, about 2500 m^3 per meter alongshore in the middle of the field site (Figure 2.2b).

2.3 Observations & Methodology

2.3.1 Topographic surveys

The topography of the newly constructed area is surveyed approximately monthly since the completion of the construction in April 2009 resulting in 38 surveys spanning 3.5 years. Topography surveys contained both the sub-aerial and sub-aqueous beach, where both parts were measured almost concurrently (< 3 days apart). The main part of the nourishment project was subdivided in 22 transects roughly 80 m apart (Figure 2.3) resulting in an alongshore extent of the observed coastal cell of 1745 m centered around the beach entrance. In cross-shore direction the surveyed profiles extend 900 m offshore to approximately -9 m NAP[2]. Profile extent and distance are optimised such that the sub-aqueous part can be surveyed in a single high tide (~ 3 h). The total topography (sub-aqueous and sub-aerial parts) can be therefore be surveyed in a one-day lull between two storms. On the landward side the profiles are bound either by the dune foot of the new artificial dune (at ca. +5 m NAP) or at the crest of the old dunes (ca. +10 m NAP). Approximately half of the profiles extend beyond the new dune row through the dunevalley into the old dunes (Figure 2.3). Based on the 80 m transect spacing and the alongshore extent of the survey domain, emergent alongshore variability with length scales of O (200 - 1500 m) can be captured. As a reference, typical length scales on the Dutch coast are in the range 250 - 3000 m, where the larger length scales are observed in the (older) outer bar and the smallest length scales in the inner bar (*van Enckevort and Ruessink*, 2003a).

Surveys are executed using two techniques, walking and jetski (personal watercraft) surveys. Walking (RTK-GPS backpack) surveys for the sub-aerial part of the profile extend to the low water line and have an estimated accuracy of O (5 cm). The sub-aqueous part of the profile was surveyed using a jetski equipped with a single beam echo sounder and RTK-GPS, capable to obtain bed level measurements with accuracy in the order of 10 cm (*van Son et al.*, 2010). Vertical displacements of the jetski due to tide and waves are compensated for by subtracting the elevation of the jetski recorded by the (high quality) RTK-GPS. More detailed information on the survey equipment and the accuracy the reader is referred to appendix A.

Surveys are typically executed during spring tide resulting in maximum overlap of both techniques as jetski surveys are executed around high tide and backpack surveys around low tide. Transects of both jetski and walking

[2] *'Normaal Amsterdams Peil'* (NAP) is the Dutch datum, which is located at approximately mean sea level.

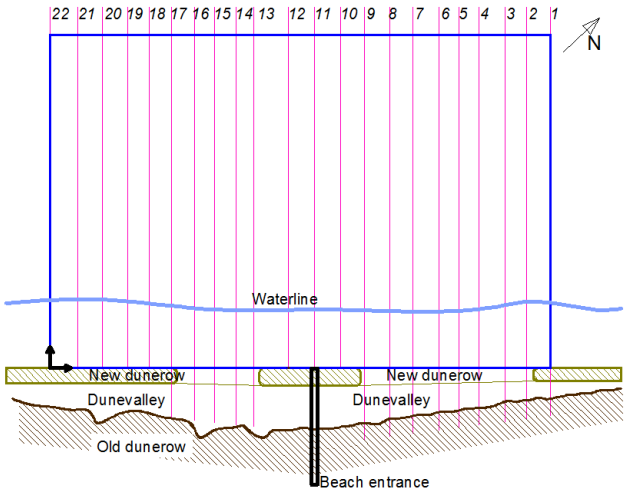

Figure 2.3: Schematised overview of the survey area. The 22 cross-shore survey transects are given by the magenta lines. Shaded areas indicate vegetated dunes. Results in this chapter are based on the beach and foreshore parts of the transects (i.e. within blue rectangle).

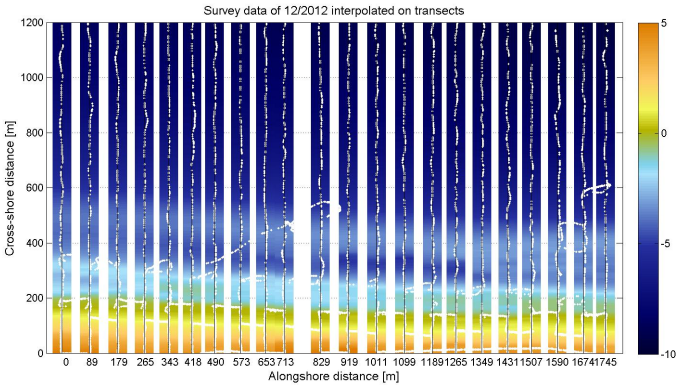

Figure 2.4: Survey data on the beach and shoreface (blue rectangle in Figure 2.3) for the December 2012 survey. Black lines show the predefined cross-shore survey transects, white dots the surveyed x, y, z point data. Colored bands show bottom elevation data on the transects in m NAP as interpolated from the surveyed point data.

surveys are in line and transect locations are identical for each survey since the beginning of the field campaign reducing the need of interpolation of the survey data over large distances.

Both walking and jetski surveys result in point data (in x, y, z) of the bottom elevation scattered around the 22 predefined survey lines. To obtain monthly profiles for comparison these scattered data are linearly interpolated to the shore-normal profiles with a cross-shore step size of 5 m (Figure 2.4).

An overview of the topographic survey data is shown for approximately every 3 months in Figure 2.5. The overview of the surveys shows large patterns in the topography which are slowly evolving such that surveys 3 months apart show a large resemblance. Shortly after construction the topography contains some alongshore irregularities and a small mound in the shoreface nourishment can be observed around the alongshore 1000 m and cross-shore 450 m location. Also, just after completion of the project in summer 2009, the profile was steep ($\sim$ 1:30) in the zone 0 to -4 m NAP, as a result of the construction method (pushing the sediment seaward from shore with bulldozers). Although no bar was present in the first surveys, a single subtidal bar was formed in about a year, which becomes alongshore variable over time.

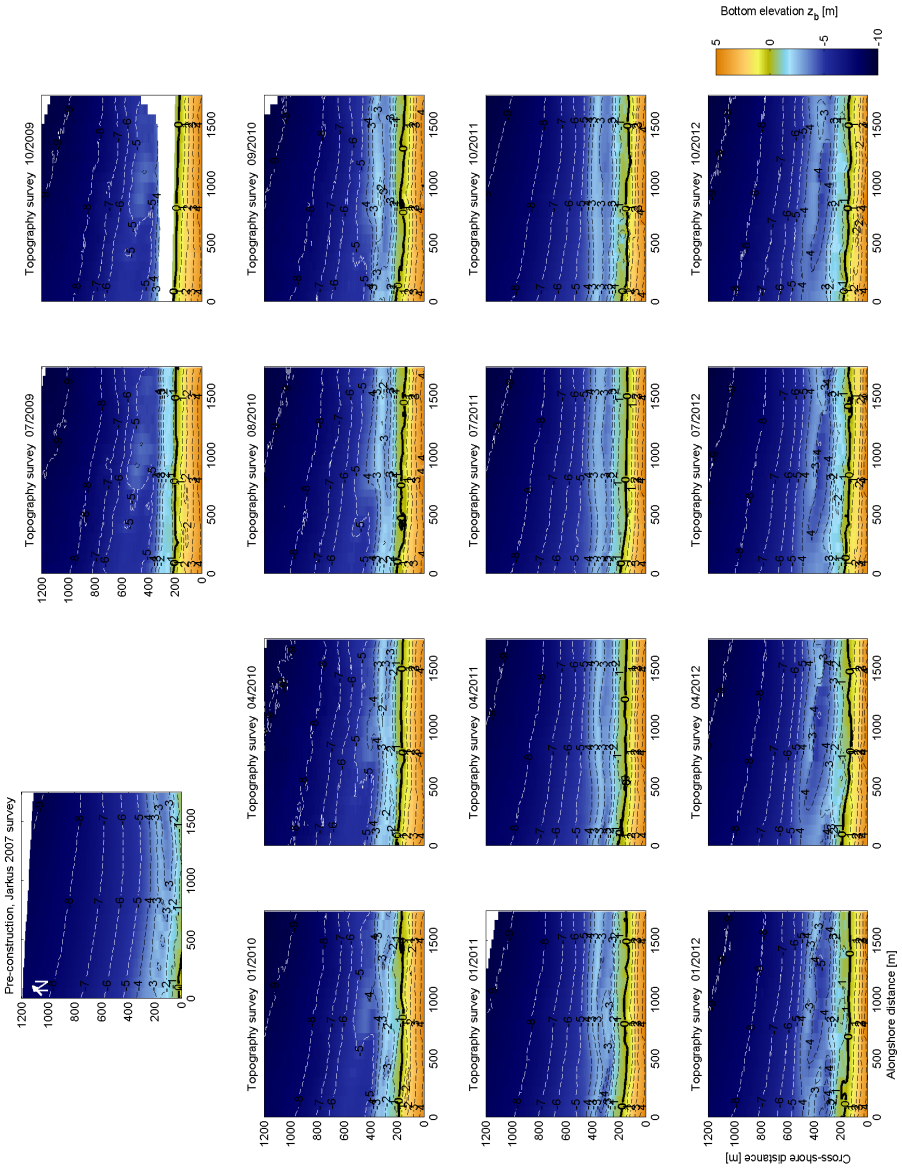

Figure 2.5: Vlugtenburg beach topographies, panels approximately every 3 months. Colors indicate bed level in meters NAP (Dutch datum at approx. MSL). Surveys sorted in columns from left to right for years 2009-2012. Rows show the different seasons from mid autumn (top of page) to mid winter (bottom of page). The survey of October 2009 contained a data gap between the sub-aerial and sub-aqueous surveys.
Lower left corner shows the pre-construction topography based on the Jarkus transects (250 m alongshore transect separation) of 2007.

2.3.2 Hydrodynamic conditions

Concurrent wave conditions offshore $H_{s,0}$, $T_{m02,0}$ and direction θ_0 were obtained from a wave station ('Europlatform') located 40 km offshore at a water depth of 32 m. Wave height showed a strong seasonal signal with largest waves occurring in the months September to December (Northern Hemisphere autumn). The maximum recorded wave height $H_{s,0}$ over the entire 3.5 year period was 6.8 m during the December 2011 storm. During summer months low wave heights were recorded, and the lowest average wave height $H_{s,0}$ in a period between two surveys was 65 cm.

To combine the effect of wave height and period, the wave forcing is expressed as wave power. Offshore values were converted into wave power P_0 as follows:

$$P_0 = E_0 c_{g,0}, \tag{2.1}$$

where subscript $_0$ denotes offshore. Wave power P_0 values are computed using the data measured at 32 m water depth, and as the largest mean wave period recorded during the 3.5 year period equals 7.8 seconds, wave conditions at the wave station can be considered mostly as deep water. Wave energy E_0 is taken as $E_0 = 1/16\rho g H_{s,0}^2$. The group velocity $c_{g,0}$ is calculated using the wave period, water depth and the wavenumber as given by the linear dispersion relation.

Secondly, a proxy for the alongshore wave power available for alongshore transport was examined, incorporating the effect of wave angle. The wave power available for alongshore sediment transport was approximated by $P_{y,\mathrm{sed}}$ (*Komar*, 1998), similar to *van Enckevort and Ruessink* (2003b) and *Price and Ruessink* (2011):

$$P_{y,\mathrm{sed}} = P_b \sin(\theta - \theta_\perp)\cos(\theta - \theta_\perp), \tag{2.2}$$

where $\theta_\perp$ is the wave angle of shore-normal incidence (310 deg with respect to North). $P_{y,\mathrm{sed}}$ is to be evaluated at breakpoint, and therefore offshore wave data are translated inshore using the dispersion relationship for linear water waves and Snell's Law for straight and parallel offshore contours. Breakpoint values are taken at the water depth where the wave height exceeds 0.5 times the water depth. Sheltering by nearby (4 km) harbor moles for southerly waves or possible wave current interaction due to river outflow near the harbor entrance are not included in this transformation.

Mean and maximum values of both P_0 and $P_{y,\mathrm{sed}}$ for each time period between consecutive surveys were examined to investigate whether primarily

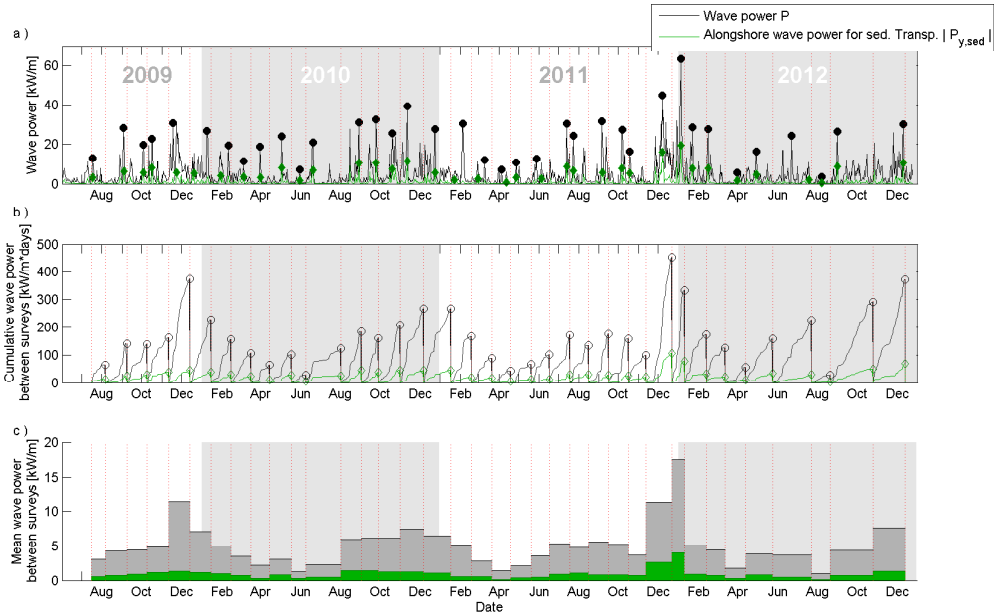

Figure 2.6: Wave power in the months after construction of the nourishment. Red vertical lines represent the survey dates. a) Timeseries of wave power P and absolute alongshore wave power available for sediment transport $P_{y,\mathrm{sed}}$ (in green). Peak wave power events for each survey period are highlighted by the symbols. b) Cumulative wave power in each period between two surveys. c) Mean wave power for each period between two surveys.

high wave events or monthly wave climate properties are responsible for the observed morphodynamic response (Figure 2.6). A seasonal fluctuation can be observed in the wave power signals, where the smallest wave power is generally observed around April (Northern Hemisphere spring). Although storms are usually stronger in fall and winter, high wave power events can be observed across all seasons (Figure 2.6 a). Typically, one or two intermediate to high wave power events can be discerned in between two surveys. These storms are often obliquely incident, and consequently times with maximum wave power P_0 coincide with maxima in $|P_{y,\mathrm{sed}}|$.

A particular aspect of this region of the Dutch coast is the large angle of wave incidence with respect to shore (Figure 2.7). The mean angle of wave incidence offshore is quantified separately as it affects the generation

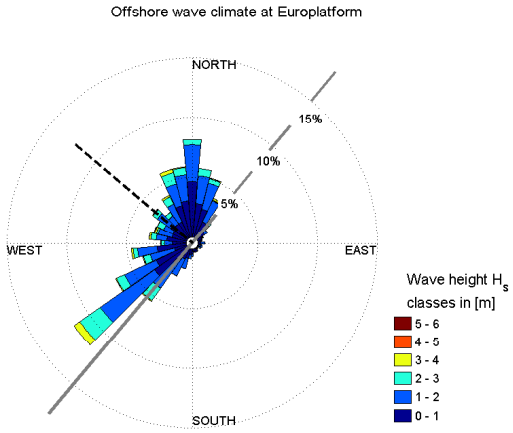

Figure 2.7: Offshore wave conditions as measured at Europlatform in the period 07/2009 to 01/2013. The shoreline orientation and shore-normal at Vlugtenburg beach are indicated with the gray solid and black dashed line respectively.

and removal of alongshore variability (e.g. *Calvete et al.*, 2005; *Thiebot et al.*, 2011; *Smit et al.*, 2008; *Price*, 2013). It is to be related later to the alongshore variability observed in the surveys (§ 2.5.2). The mean angle of wave incidence offshore is computed for each period between two surveys and weighted by wave power P_0 as follows:

$$\overline{|\theta_{0,\text{s.n.}}|} = \frac{\sum_{t=T_i}^{t=T_j} P_0 \, |\theta_0 - \theta_\perp|}{\sum_{t=T_i}^{t=T_j} P_0}, \tag{2.3}$$

with T_i and T_j being the dates of successive surveys.
Values of mean angle of wave incidence $\overline{|\theta_{0,\text{s.n.}}|}$ reflect the large angle of wave incidence offshore at this part of the coast; smallest $\overline{|\theta_{0,\text{s.n.}}|}$ value over a period between two surveys was 33 degrees, the largest value 77 degrees.

2.4 Results

The topographic surveys after completion of the project show an adaptation of the beach and foreshore morphology. The largest bed level changes can be observed 200 m on either side the 0 m NAP (∼MSL) isobath (Figure 2.8). Bed level changes landward of the ∼ 3.5 m NAP elevation ($x \approx 50$ m) are limited and only subject to aeolian transport (*de Vries et al.*, 2010). Below this elevation the shape of the sub-aerial profile has changed over the 3.5 years from a more linear (man-made) to a concave upward (erosional) profile (Figure 2.8) and consequently the sub-aerial beach width has reduced. Towards the lower shoreface the morphological changes decrease and the lowest part ($x \approx$ 1200 m) of the profile shows little change in bed level over the time period of the surveys.

In the following sections the post-nourishment morphological evolution is examined in more detail, addressing the following aspects:

- Overall sediment budget of the beach and shoreface (§ 2.4.1).
- Shoreline position (§ 2.4.2).
- Redistribution of the nourished sand in the cross-shore profiles (§ 2.4.3).
- Emergence and migration of the subtidal bar (§ 2.4.4), and
- Alongshore topographic variability (§ 2.4.5).

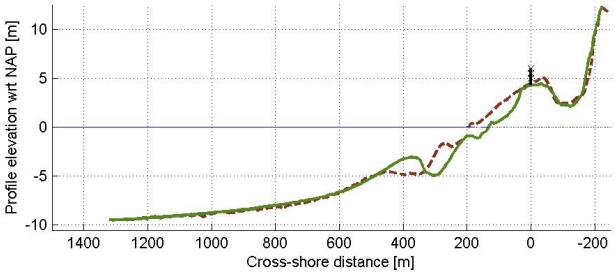

Figure 2.8: Profile elevation just after completion of the project in July 2009 (dashed line) and after 3.5 years (solid line) for an arbitrary profile (Transect 7). Cross-shore location $x = 0$ m is located at the dunefence of the new dune. The old dune is visible around $x = -200$ m.

2.4.1 Overall sediment budget of the beach and shoreface

To obtain a measure of the overall sediment budget at the site, sediment volume is examined for the beach and shoreface across the alongshore stretch

of 1.75 km covered by the surveys. Sediment volume for individual transects is computed by cross-shore integration of the transect elevation data (Figure 2.9). Landward border is taken as the 0 m cross-shore location, where the bed level elevation is about 4 m NAP (elevation slightly varying between transects) and no marine activity was observed either visually or in the profile data. Seaward border is the 1200 m cross-shore location at about -9 m NAP.

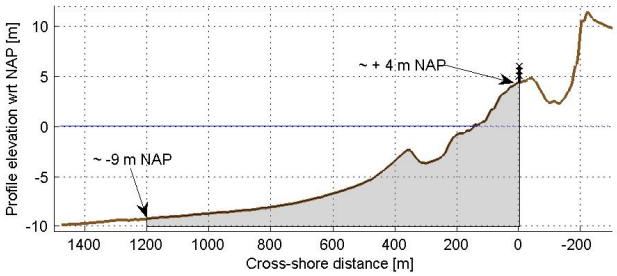

Figure 2.9: Methodology for the calculation of the sediment volume per transect. Shaded area indicates the volume per meter alongshore used to determine sediment balance.

Sediment volumes per profile are averaged over all profiles and compared to the first survey after construction, to show the evolution of the sediment budget over all surveys (Figure 2.10). Monthly timeseries of sediment volume show slight variability on a monthly time scale (Figure 2.10, black line). Part of this variability can originate from small survey inaccuracies of O (0.5 %) in the sound speed used in the depth soundings, as discussed in Appendix A. A 3-survey moving average is therefore applied to the data to remove small fluctuations while retaining the seasonality in the computed signal (Figure 2.10, red line).

Over the 3.5 years investigated, the sediment volume in the area decreases by over 100 m^3/m (i.e. 0.18 Mm^3 in total over the area). The first months after construction show a rapid decrease in sediment volume, accounting for the majority ($\sim$70 %) of the losses in nourished volume up to present. In the following years the volume fluctuates but a shows small downward trend of approx. 15 $m^3/m/yr$. Yearly changes of 1, 2, and 3 years after construction are given in Table 2.1. Annual volume losses in the last year are very small. Apart from the annual trend in sediment volume, a small interannual fluctuation can be observed. In general, the last quarter of the year shows a decrease in sediment volume, and constant (or slightly increasing) volume in the spring

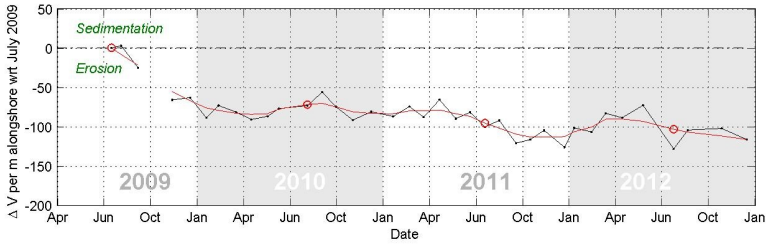

Figure 2.10: Sediment budget after implementation of the nourishment. Monthly averaged sediment budget from the new dune foot to deep water given by the black line. Red line depicts the moving average over 3 surveys. Survey of October 2009 is omitted due to a data gap between the sub-aerial and sub-aqueous surveys.

months. The data do not reveal large episodic behaviour and individual stormy months (e.g. the December 2011 storm) do not have an evident impact on total sediment volume.

Table 2.1: Alongshore averaged yearly volume changes in the profiles on the beach and shoreface (Figure 2.10, red 'o' symbols).

	1^{st} year	2^{nd} year	3^{rd} year	Total after 3 years
Total volume change -9 tot +5 m	-72 m^3/m/yr	-23 m^3/m/yr	-8 m^3/m/yr	-103 m^3/m

2.4.2 Shoreline Position

The shoreline position is of importance as it controls the beach width and therefore the recreational use of the beach. Shoreline position over all measured profiles was determined with a similar approach as used in the annual assessment of coastal safety in the Netherlands (see *van Koningsveld and Mulder*, 2004). The cross-shore position x_s is calculated as the area (or volume per unit length) in horizontal slice in the profile between -0.5 and 0.5 m NAP divided by the 1 m height of this slice (Figure 2.11). This volume-based definition of the shoreline position is less sensitive to intertidal features (e.g. ridge runnel morphology) or survey inaccuracies than selecting the profile crossing with the 0 m NAP isobath. The landward reference line is the fence between the dune and beach and as such the value for shoreline position x_s also directly provides a measure of beach width available at mid tide for recreational use.

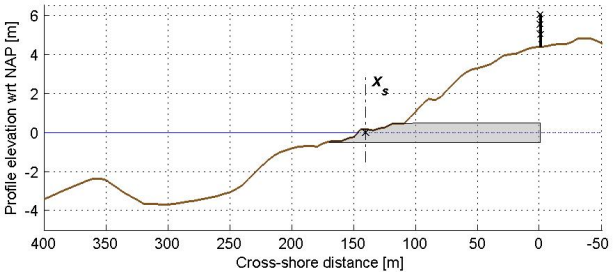

Figure 2.11: Methodology to determine shoreline location per transect. Shaded area indicates the horizontal slice between +0.5 and -0.5 m NAP which is used to determine the weighted shoreline position x_s.

After the nourishment is implemented in 2009, the shoreline is located around 200 m from the dunefence (Figure 2.12). The initial steep construction profile resulted in a strong redistribution of sand over the profile and consequently a change in shoreline position. Over the years the shoreline migrates landward and in the last surveys a shoreline retreat of approximately 50 m is observed, reducing the beach width by one quarter of its original width.

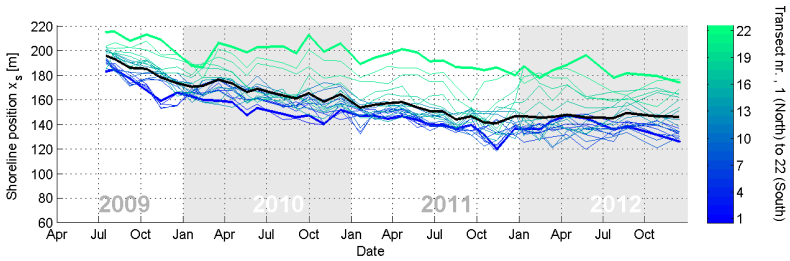

Figure 2.12: Evolution of the shoreline position over time. Colored lines represent the shoreline position for the 38 surveys per profile, thick black line the mean position of all profiles. Most northern (blue) and southern (green) transects highlighted by the thick lines.

The landward migration rate is largest in the initial response and reduces towards the end of the investigated period, similar to the observations in the total sediment budget. Changes in x_s are however more gradual than the rapid response observed in the first 6 months on the total sediment volume. In the last year the alongshore averaged shoreline position remains nearly stable.

A small difference in behaviour between individual profiles can be observed. Southern profiles with a shallower shoreface (see Figure 2.5) show a smaller shoreline retreat ($\sim$ 40 m) than northern profiles ($\sim$ 60 m). Individual storms have little impact on x_s and high energy periods (i.e. surrounding the December 2011 storm) do not result in a an apparent[3] setback.

2.4.3 Redistribution of nourished sand over the profile

The construction of the nourishment resulted in a steep profile ($\sim$ 1:20) between the -1 and the -4.5m NAP (Figure 2.13, blue line), partly originating from the construction method of using bulldozers to push sediment seaward from the beach. On the seaward side of the profile the nourished sediment was dumped and sprayed over the dredging vessel bow on the shoreface creating a terrace-like foreshore at cross-shore distance x=400 to 600 m. This initial man-made profile has changed over time into a more natural profile with a concave shape and a single subtidal bar. The strong gradient in the profile at the seaward edge of the foreshore nourishment terrace (at x =600 m, Figure 2.13) is reduced, resulting in a monotonously sloping lower shoreface below -4.5 m NAP. By spring of 2011, after a period of 2 years, the profile shows no sign of the shape of the foreshore nourishment terrace in the profile (Figure 2.13, green lines). Higher up the profile, above the -1 m NAP ($\sim$ MLW line) beach erosion is observed and the initial beach profile is transformed to a concave profile. The supra-tidal beach profiles are changing episodically as maxima of high water level during storms affect the maximum influence level of marine processes.

The redistribution of the sediment over the profile is expressed in two approaches, firstly examining when profiles are most active and secondly by calculating the volume changes for different zones in the profile.

The changes in bed level between consecutive surveys are quantified by a morphological activity index *MAI*, expressing the net result of migration of sediment between two surveys. Morphological activity of a single transect *MAI* is defined as:

$$MAI = \frac{\sum |z_i(x) - z_{i-1}(x)| \Delta x}{n_{\text{days}}}, \tag{2.4}$$

[3]A linear regression analysis on the shoreline migration and mean incident wave power between consecutive surveys did not show a significant correlation between both diagnostics (see Table 2.3, p.55).

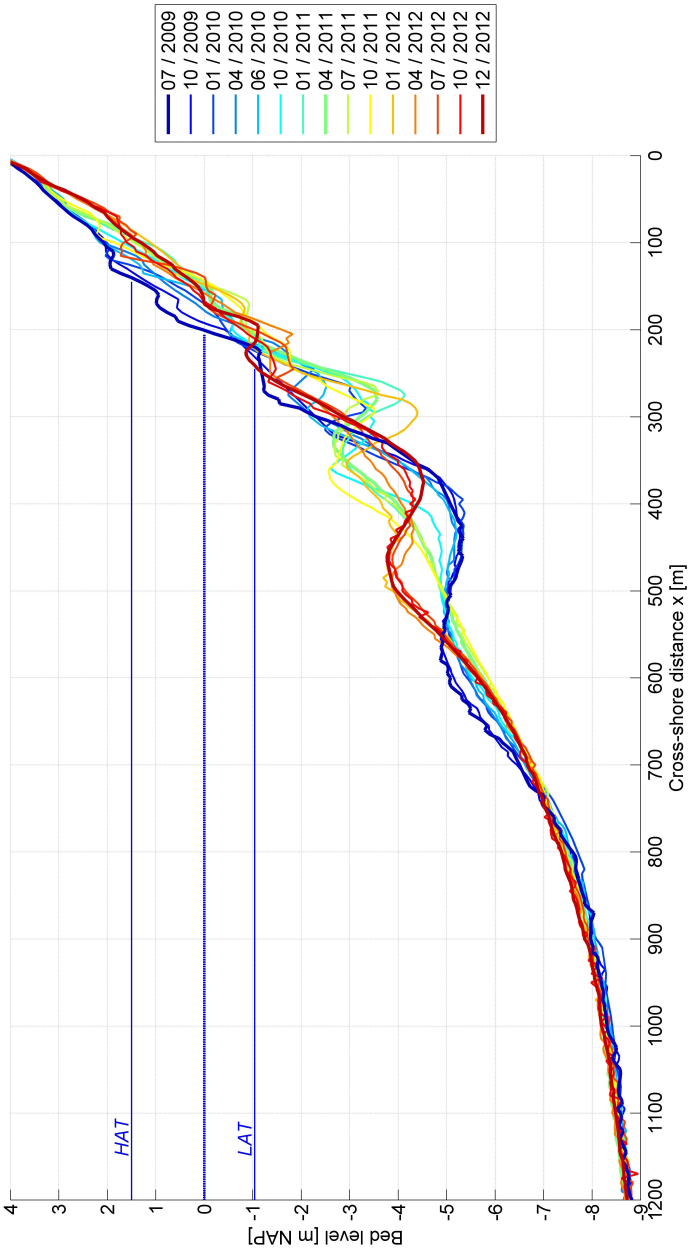

Figure 2.13: Cross-shore profile evolution for an arbitrary transect (# 17). A selection of surveys is shown, approximately 3 months apart. Colors indicate the survey dates.

Where $z_i(x)$ is the transect data and index i indicates the survey number. Δx is the cross-shore spacing of transect data, 5 m. Morphological activity is scaled by the number of days between consecutive surveys, n_{days}, to compensate for the irregularity in survey intervals. Bed level changes between consecutive surveys are summed as absolute values in Eq. 2.4, such that both erosion and accretion are accounted for. A displacement of a sediment body within the profile (e.g. migration of a subtidal bar) is therefore accounted for twice, as both erosion and sedimentation are added. On the contrary, erosion (or sedimentation) of sediment that is not deposited (eroded) within the profile is only accounted for once. *MAI* values give an lower limit to the activity in a period, comparing only consecutive surveys about a month apart. Revolving bedlevel changes and activity within the time period between surveys are not taken into account.

MAI values confirm the large displacements of sediment in the profile during the fall and winter (storm) seasons, as *MAI* is 2 to 3 times as large during survey period surrounding the December 2011 and January 2012 storm (Figure 2.14) compared to the other months. Generally speaking all transects show similar behaviour.

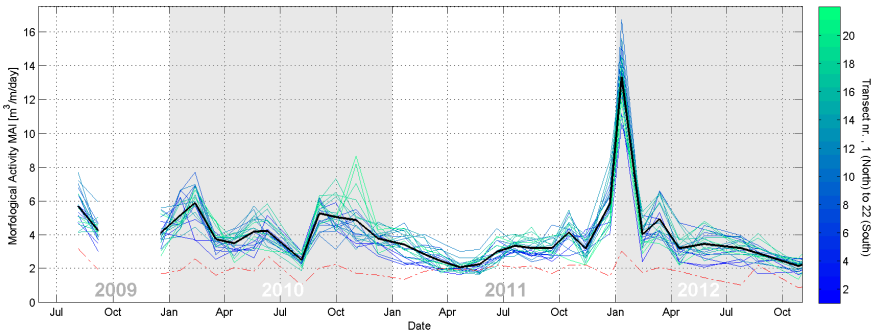

Figure 2.14: Morphological activity over time. Colored lines represent the 22 individual transects, thick black line represents the mean value over all profiles. Red line gives the value for random ± 10 cm survey noise. *MAI* values for October and November 2009 are omitted due to a data gap between the sub-aerial and sub-aqueous surveys in the October 2009 survey.

Periods with very minimal morphological activity can be observed throughout the investigated period, yet the first 1.5 years visually appear to be slightly more active.

It is noted that small survey noise can influence *MAI* values due to the addition of absolute bed level deviations from one survey to another. An estimate of the potential contribution of noise due to survey errors on *MAI* values is obtained by replacing $z_i(x) - z_{i-1}(x)$ in Eq. 2.4 with random noise of $\pm$ 10 cm (uniformly distributed) and computing the resulting spurious morphological activity. Profile averaged morphological activity values of O (2 $m^3/m/day$) can be expected, based on this conservative assumption of random noise of $\pm$ 10 cm. (Figure 2.14, red line). Although during most of the study period the morphological activity is larger than the noise level, survey inaccuracies could potentially contribute to a substantial part of the computed *MAI* for the quiet periods (e.g. Spring 2011).

Next, the monthly redistribution of sediment within the profile is further elaborated upon by investigating the volumetric changes in discrete elevation zones. Transects are subdivided in sections based on elevation yielding volume estimates for different horizontal slices of the profile. The profile is subdivided into the following sections:

- Upper supra-tidal, Beach volume above +3 m NAP to the dunefence.
- Lower supra-tidal, Beach volume above MHW to +3 m NAP.
- Intertidal, Beach volume between MLW and MHW.
- Surf zone, Volume between MLW and -4.3 m NAP.
- Upper shoreface, Volume between -4.3 and -7 m NAP.
- Lower shoreface, Volume below -7 m NAP.

Divisions between sections are at the +3, +1, -0.65, -4.3 and -7 m NAP isobaths. The +3 m NAP is the general definition of the dune foot at the Dutch coast (see *de Vries et al.*, 2012, and references therein). Divisions of +1 and -0.65 m NAP are the approximate mean high water (MHW) and mean low water (MLW) at the site respectively. The -4.3 m NAP division is chosen equal to the lower boundary of the momentary coastline (MKL) zone used for coastal policy at this location. For Dutch coastal policy the volume in the the horizontal section of the profile between +3 m and -4.3 m NAP is used to determine the MKL position (see *van Koningsveld and Mulder*, 2004), and to evaluate the necessity of nourishments in the near future. The three sections 'Lower supra-tidal', 'Intertidal' and 'Surf zone' defined here together form a horizontal section equal to the MKL zone definition. The -7 m NAP division is selected arbitrary to divide the shoreface in two sections. Volumes in the six horizontal sections are examined per profile, after which the results of the 22 profiles are alongshore averaged.

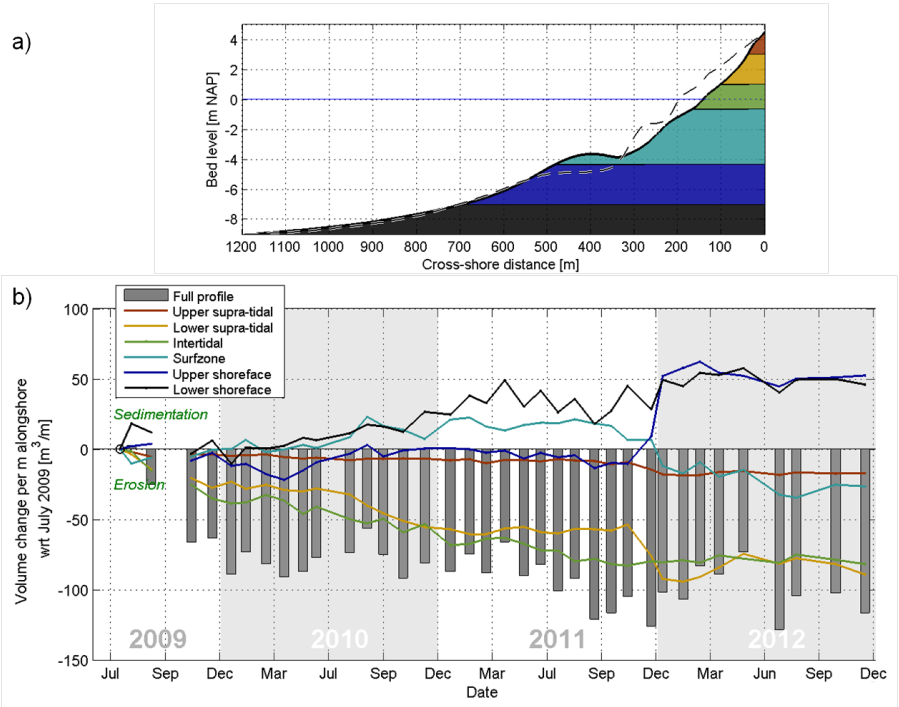

Figure 2.15: Alongshore averaged volume changes since the start of the monitoring in July 2009, subdivided to different elevation zones. a) Alongshore averaged profile in December 2012 with the different elevation zones given in colors. Initial profile in July 2009 given by the dashed line. b) Volume changes per elevation slice (colored lines). Bar graphs show the total volume change over the profile, as already shown in Figure 2.10.

Sediment balances for different elevations show different behaviour for each elevation section. The intertidal and lower supra-tidal beach each show a volumetric loss of O (80 m^3/m) after 3.5 years, such that their combined loss is nearly twice as large as the loss over the full profile (Figure 2.15b, green and yellow lines vs the bar graph). The lower sections of the profile (Upper and Lower shoreface) are acquiring sediment, suggesting a large redistribution of sediment within the profile in downward direction (Figure 2.15b, black and dark-blue lines). If this sediment indeed originates from the upper profile, about 40-50 % of the sand lost on the upper profile accretes on the shoreface. The accretion in the shoreface below -7 m NAP is substantial of O (50 m^3/m)

which is confirmed by profile data showing a bed level increase of about 10 cm at -8 m NAP (see Figure 2.13). The gradual accretion in this zone suggests it being either the result of the diffusion of the foreshore nourishment itself or a continuous net onshore flux as suggested by (*Stive and Eysink*, 1989; *van Rijn*, 2011, amongst others) rather than the effect of single storms. Detailed month to month comparisons of volume in this zone are however difficult as sound speed errors in this area close to the river plume introduce small scatter in the most seaward / deepest sections (for details see Appendix A).
The zones used for the MKL evaluation of coastal management (the surf zone to lower supra-tidal sections) show a total loss of about O (200 m^3/m) by December 2012 (Figure 2.15b; yellow, green and light-blue lines combined), approximately twice as large as the overall loss volume in the total profile.[4] Evaluation of the profile on these zones alone underestimates the lifetime of the nourished sediment.

Contrary to the total sediment budget (Figure 2.8) and the shoreline evolution (Figure 2.12) which show gradual changes over time, the changes in individual sections can be very episodic. A large downward shift in volume is found during the stormy December 2011 and January 2012 months, with a large gain in sediment in the upper shoreface section and large loss in the lower supra-tidal beach. Only small changes are observed in the intertidal volume during these months, suggesting that the intertidal area may be a 'pivot-zone' in the profile for these storm events. The volume of the surf zone section shows no large month to month variations, but an interesting shift in trend from slightly accretive in the first two years to erosive in following period.
A small seasonality is seen in the erosion of the supra-tidal beach, showing larger erosion rates during the autumn months (October-December) when wave forcing is strong. In the last year of the investigated period, the changes of shoreface volume are small, possibly as seaward slope of the subtidal bar is less active once it has arrived at deeper water. The majority of the losses observed in profiles in the last year are attributed to the zones next to the intertidal zone (surf zone and lower supra-tidal beach), again suggesting that the zone around the shoreline may act as a pivot between both.

[4]Based on this reduction in volume in the MKL section, the Dutch Ministry of Infrastructure and the Environment decided to re-nourish the shoreface at Vlugtenburg beach in summer 2013 with an additional $\sim$ 400 m^3/m.

2.4.4 Subtidal bar characteristics and migration

Shortly after completion of the nourishment a subtidal bar was formed. Initially, in the first bathymetric surveys, this bar was small and located close to the shoreline, while the last surveys show a larger bar located further offshore (see Figures 2.8 and 2.13). The following section investigates the location and dimensions of the subtidal bar over the 3.5 years which show, in essence, the initiation of a cyclic subtidal bar system.

Evolution and position of the subtidal bar are investigated by tracking the bar crest position x_c, bar crest bed level d_c, and bar volume V_{bar} for the 22 transects in 38 surveys (Figure 2.16). A subtidal bar is defined to be present in case the bed elevation profile below -1 m NAP (the approximate LW elevation) is not monotonously decreasing, but contains a secondary maximum. The bar crest position for such instances is taken as the position of the secondary maximum and can be traced with a cross-shore resolution of 5 m (cross-shore spacing of the transects). Bar crest depth is the profile height at this location with respect to 0 m NAP. Secondary maxima in the profiles were selected manually and rigorously checked for survey errors. In case profile data contained a small gap near the bar crest, no bar crest was picked for the analysis.

The cross-sectional volume of the bar, V_{bar} (in m^3 per m alongshore), was defined as the cross-sectional area between the transect and a line between the bar trough and the bar toe (Figure 2.16)[5]. The trough position x_{tr}, z_{tr} between the bar and the shoreline is picked similar to bar crest, using the deepest point between the bar crest and the shore.

Selecting the seaward bar toe position x_{toe}, z_{toe} for the determination of the bar volume is more complicated as the seaward slope of the bar can merge smoothly with the slope of the shoreface (see Figure 2.16). However, in the first 1.5 years after completion the profile contains a clear transition in the profile curvature and the local maximum in dz_b^2/dx^2 is used to detect the bar toe location. Around January 2011, the seaward edge of the bar starts to gently merge with the rest of the profile. Hence small depth variations in the profiles (e.g. due to survey inaccuracies) dominate the gradients in the profile

[5]Various methods have been suggested in previous literature to discern subtidal bars from measured profile data. These are mostly based on either 1) subtracting a long term time-averaged profile or 2) subtracting a fitted (exponential) equilibrium profile from the measured transect data (e.g. *Wijnberg and Terwindt*, 1995; *Larson and Kraus*, 1994; *Ruessink et al.*, 2003; *Grunnet and Ruessink*, 2005). Both methods are slightly problematic for the transect data measured at Vlugtenburg, the former due to the limited amount of data in years compared to the bar cycle and the latter due to the erosional upper profile and the large retreat of the shoreline. After testing several approaches a more pragmatic methodology is adopted for the analysis of the Vlugtenburg profiles.

and dz_b^2/dx^2. To avoid unphysical large variations in bar volume due to large changes in the bar toe estimation, for profiles after January 2011, the bar toe was selected equal to the crossing of the profile with the -5 m level. Near January 2011 both methods provide similar values for the bar volume securing a smooth transition between methods. Visual inspection of all profile images (similar to Figure 2.16) show that the methodology outlined above provides a reasonable value of the bar volume.

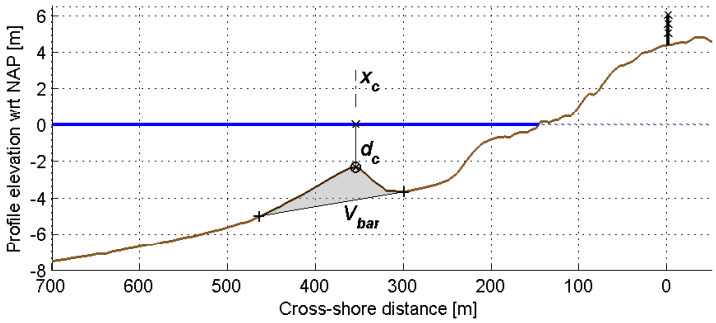

Figure 2.16: Definition of subtidal bar parameters.

Extracted bar characteristics are given for the full 3.5 year period in Figure 2.17. From the first surveys onwards the bar migrates offshore and the bar crest level decreases[6]. After the first year the bar volume is of O (150 m^3/m), using the bar volume definition outlined above. This is of the same order as the values reported for Katwijk 30 km north of the site (*Shand et al.*, 1999), but smaller than the typical bar size observed further north on the Dutch coast at Egmond ($\sim$ 215 m^3/m) or Terschelling ($\sim$ 575 m^3/m) (*Shand et al.*, 1999).

On an annual timescale a net offshore migration rate the bar of O (50 m/yr or 0.14 m/day) is observed, similar to the cyclic migration rate observed 30 km north at Katwijk (*van Enckevort and Ruessink*, 2003a). The first year shows a slightly larger migration offshore with respect of the shoreline, which possibly could be related to the smaller bar volume in this period as proposed by *Shand et al.* (1999), but this can also be related to the bar position closer to shore.

[6]Although it is beyond the main scope of this work, the bar location from shore and respectively the bar crest depth and bar volume are found to be significant and strongly correlated (r values of -0.94 and 0.92, see Table 2.3, p. 55).

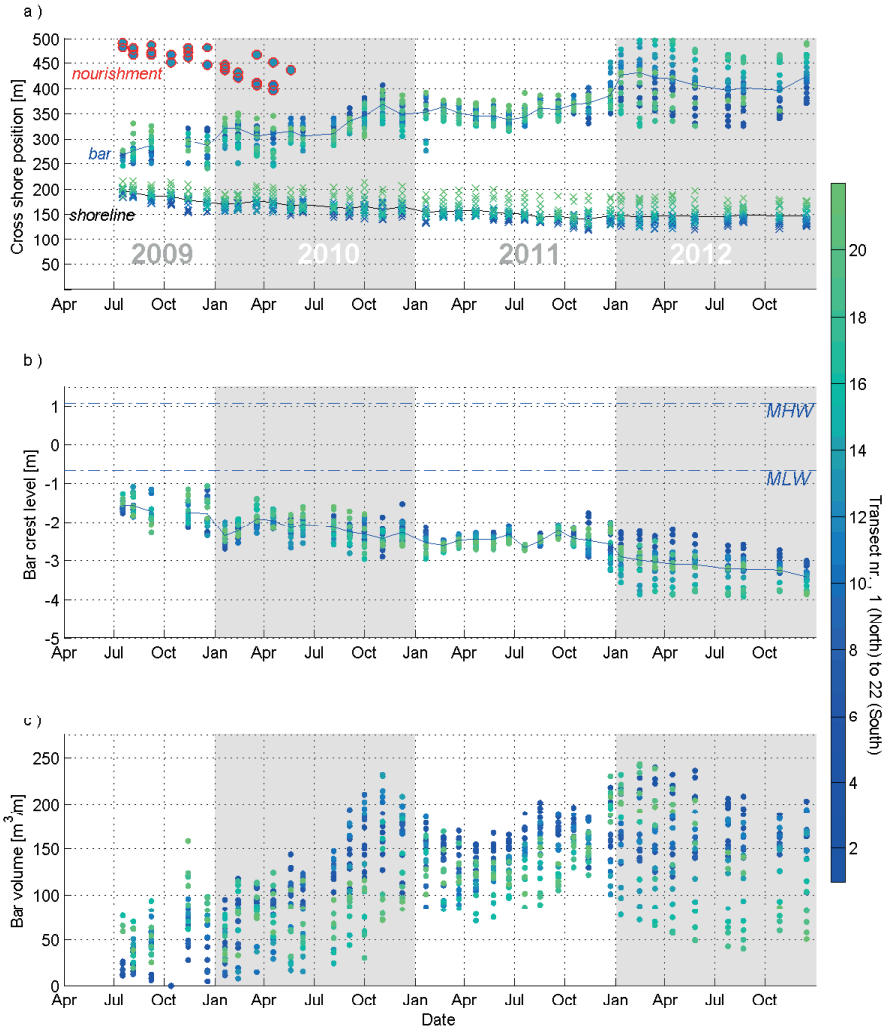

Figure 2.17: Time series of cross-shore bar crest position (a), bar crest level (b) and cross-sectional volume of the bar (c). Colors indicate the different alongshore transects 1 to 22 from north (blue) to south (green), and median positions given by the solid lines. Position of the mound in the foreshore nourishment indicated by the red circles (only when present in the profiles).

On a seasonal scale both on- and offshore behaviour can be observed, which is linked to the seasonality in forcing[7]. A rapid offshore and downslope migration of the subtidal bar is observed in fall and winter, which are the most energetic months of the year. Onshore migration of the bar is milder and observed in spring (Figure 2.18). Since the bathymetry was nearly alongshore uniform during these periods the observed seasonal effect is predominantly due to cross-shore motions rather than 2-D effects. Onshore motion of the bar was also observed to coincide with a slight steepening of the landward slope of the bar, resembling a landward roll-over of the bar crest.

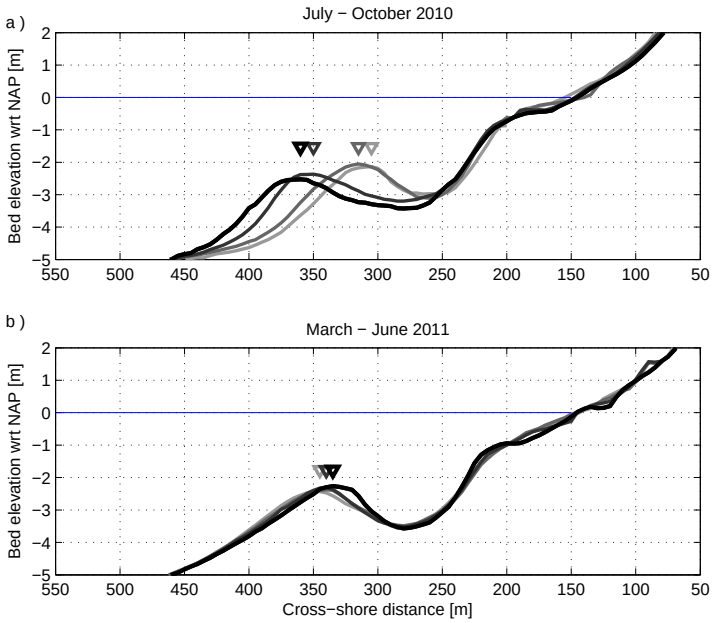

Figure 2.18: Seasonal cross-shore migration of the bar. a) Offshore migration in the beginning of autumn; profiles of July (light gray) to October (black) 2010. b) Onshore migration in following spring; profiles from March (light gray) to June 2011 (black). Profiles are alongshore averaged profiles of transects 1 to 4. Symbols indicate the cross-shore bar crest location.

[7]Monthly cross-shore bar migration between consecutive surveys is found to be correlated to both mean incident wave power between surveys $\overline{P_0}$ ($r = 0.52$, see Table 2.3, p. 55) and the alongshore wave power available for sediment transport $\overline{|P_{y,\mathrm{sed}}|}$ ($r = 0.63$).

2.4.5 Alongshore topographic variability

Alongshore variability in bed level is quantified as the deviation of the bed level in individual transects with an alongshore averaged (uniform) topography. The height of the bed level variability alone, z_{var}, can be separated by subtracting the alongshore averaged cross-shore profile $z_{b,\text{mean}}$ from the surveyed bed level along individual cross-shore profiles z_b as follows:

$$z_{\text{var}} = z_b - z_{b,\text{mean}} \tag{2.5}$$

At this particular field site the lower depth contours are slightly oblique with respect to the shoreline (Figure 2.19, *left*), making the construction of an alongshore uniform topography more complicated. If the alongshore uniform topography $z_{b,\text{mean}}$ is constructed from merely the alongshore averaged profile, it would result in large values of bed level variability z_{var} in the deeper zones (Figure 2.19, *center panels*). An alternative alongshore averaged topography, $z^*_{b,\text{mean}}$, including an ambient slope is used to overcome this issue, constructed from an alongshore averaged profile in combination with a linear alongshore slope:

$$z^*_{b,\text{mean}}(x,y) = p_2(x)\ y + p_1(x); \tag{2.6}$$

where x and y are the cross- and alongshore directions. Coefficients $p_1(x)$ and $p_2(x)$ are respectively the alongshore averaged cross-shore profile and an alongshore slope per cross-shore location, chosen such that $z^*_{b,\text{mean}}$ had the best (least squares) fit with the measured profiles. The resulting profile is nearly alongshore uniform in the surf zone but matches the overall contour orientation of the measurements at deeper water (Figure 2.19, *top right*).

Using the procedure outlined above, an alongshore averaged profile was constructed and removed from the profile for each survey, leaving only the medium scale alongshore variability for further analysis (Figure 2.20).

An overview of topographic variability after implementation of the nourishment (Figure 2.20) shows that some alongshore variability is present just after construction. Alongshore variability reduces over time and by summer 2011 the topography shows minimal variability. Patterns in the alongshore variability show only limited migration alongshore and change in length scales.The majority of the alongshore variability in topography was found to be located around -3 m water depth on the subtidal bar (cross-shore location x of $\sim$400 m).

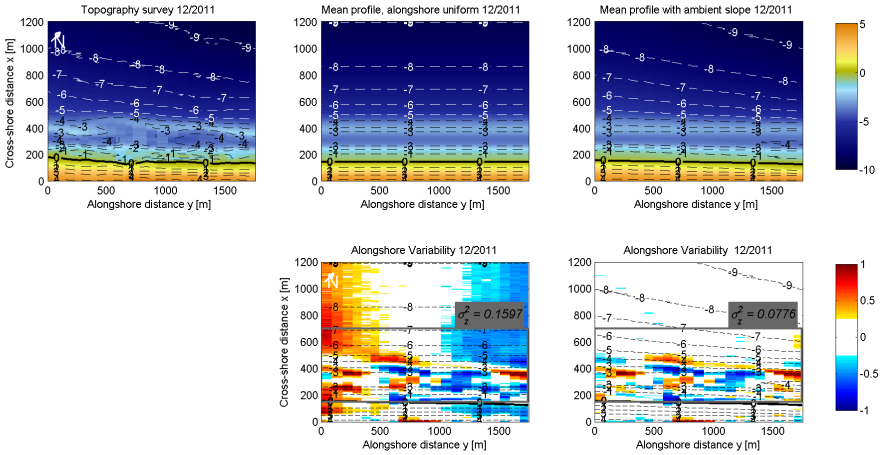

Figure 2.19: Alongshore variability at Vlugtenburg beach on December 2011. Top panels show (from left to right) the profile data z_b, the alongshore uniform topography based on the mean cross shore profile $z_{b,\text{mean}}$ and the alongshore uniform topography $z^*_{b,\text{mean}}$ including an ambient alongshore slope. Bottom panels show the alongshore variability z_{var} extracted using the expressions for the alongshore uniform topography above and Eq. 2.5.

Total alongshore topography variability was quantified per survey in a single value using a bulk alongshore variability metric σ_z^2. Parameter σ_z^2 expresses the depth variations between the individual profiles and the mean profile as follows[8]:

$$\sigma_z^2 = \frac{1}{L_x L_y} \int_{x_{\text{onshore}}}^{x_{\text{offshore}}} \int_{y_{\text{north}}}^{y_{\text{south}}} \left(z_{\text{var}}(x,y)\right)^2 dydx, \tag{2.8}$$

with parameters x_{offshore}, x_{onshore}, y_{north} and y_{south} marking the domain used for the evaluation of the variability and L_x, L_y being the resulting size of the domain. For the results here onwards a seaward limit of 700 m (at approx. -7 m) is used to minimise the impact of survey noise in deep water and a

[8] σ_z^2 proposed in this thesis is based on the alongshore variability parameter χ^2 suggested by *Ruessink et al.* (2001):

$$\chi^2 = \frac{1}{L_x L_y} \int_{x_{\text{onshore}}}^{x_{\text{offshore}}} \int_{y_{\text{north}}}^{y_{\text{south}}} \left(\frac{z_{\text{var}}(x,y)}{z_{b,\text{mean}}(x,y)}\right)^2 dydx \tag{2.7}$$

To avoid asymptotic behaviour near the waterline in case $z_{b,\text{mean}}(x,y)$ becomes small, the denominator is removed from the original χ^2 expression, to obtain Eq. 2.8.

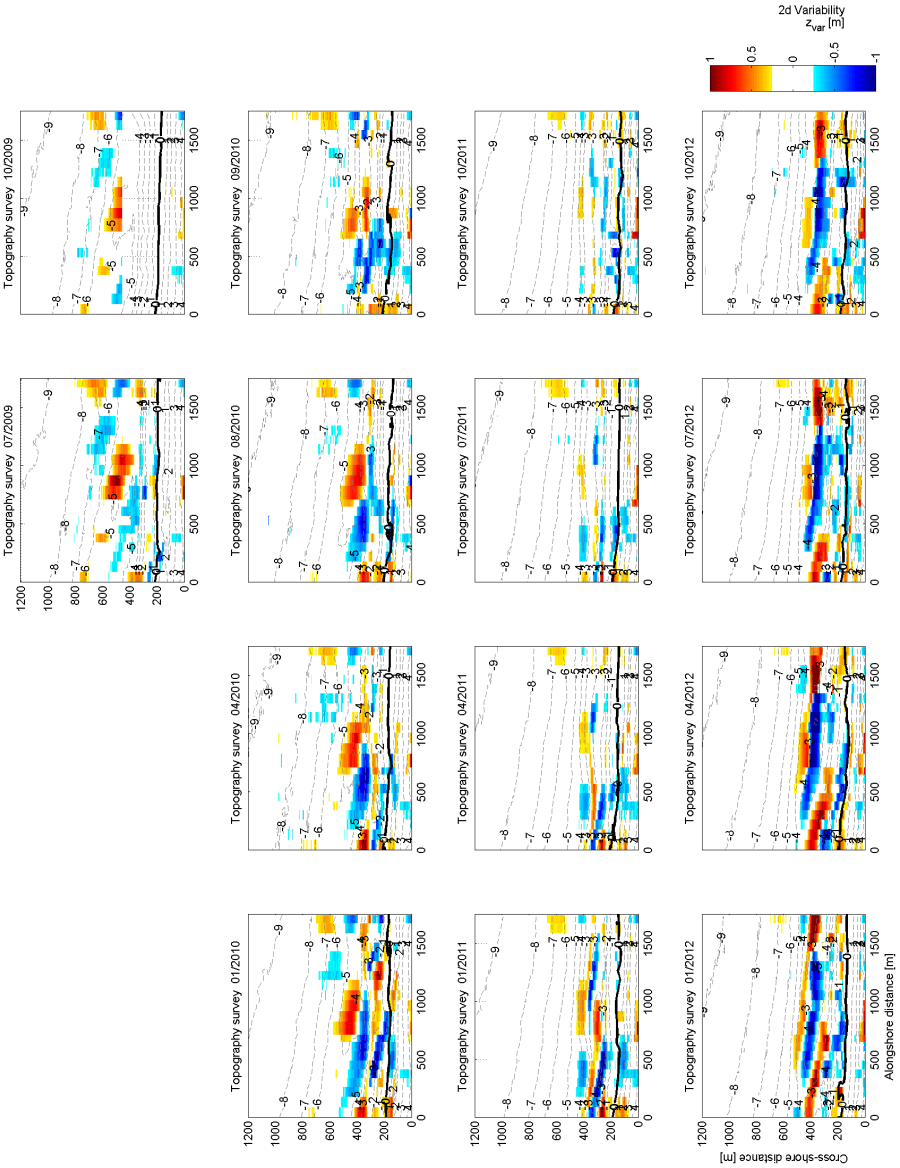

Figure 2.20: Overview of alongshore variability in topography z_{var} in panels approximately every 3 months for 2009 to 2012. Contourlines give the isobaths of the measured topography.

shoreward limit of 150 m (at approx. MSL) is used to ensure σ_z^2 contains all variability in the surf zone (Figure 2.20). Following results are however not significantly altered if slightly different boundaries are selected because the majority of the variability is in the midst of this domain. Further investigation of the effect of survey inaccuracies and the transect spacing at Vlugtenburg beach show that these have only a limited effect on the calculated values of σ_z^2 (Appendix 2.A, p. 60)

Temporal evolution of alongshore topographic variability

The bulk alongshore variability quantified using Equation 2.8 is displayed in Figure 2.21 for all surveys. Some variability was found in the first survey after completion of the nourishment, which remained from the construction. Overall, the variability appears to fluctuate on an inter-annual timescale, with a strong change in variability magnitude observed in the December 2011 to February 2012. Annually, no strong trend is visible as the values of σ_z^2 in the last surveys (after 3.5 years) are similar to the values half year after implementation of the nourishment in December 2009. Furthermore, the time series of σ_z^2 show a large auto correlation (auto correlation coefficients r for a lag of 1, 2 and 3 surveys are 0.88, 0.66, and 0.42) signifying that the magnitude of the alongshore variability is only slightly altered from month to month, as also observed visually in monthly topography plots (Figure 2.20).

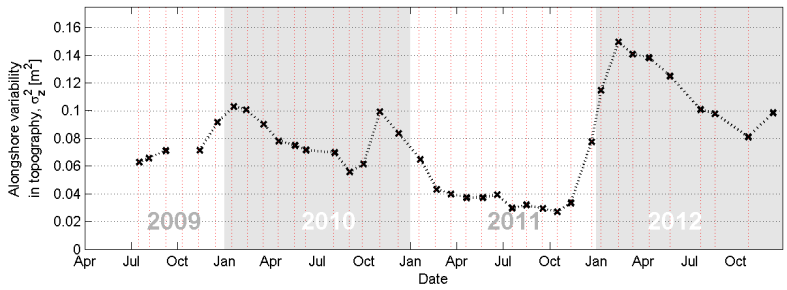

Figure 2.21: Bulk alongshore variability σ_z^2 for the 3.5 years after completion of the nourishment. Red lines indicate the survey dates. Survey of October 2009 contained a data gap between the sub-aerial and sub-aqueous surveys and was therefore not used in the analysis.

Variability σ_z^2 was found to increase in jumps, generally in the period October to January. Decreases in variability were more gradual and mostly during

spring and summer. These observations are in contrast to previous observations of bar variability at the US and Australian coast (e.g *Lippmann and Holman*, 1990; *Ranasinghe et al.*, 2004; *Holman et al.*, 2006) showing faster changes in variability (timescales of days to weeks) as well as inverse development rates; a rapid episodic removal of variability during storms followed by a slower increase in variability in subtidal bars under milder wave conditions. Time series of the variability (Figure 2.21) do not show an apparent signature of different development of variability in the first period after completion compared to the rest of the time series. No effect of the multi-annual profile adaptation of the nourishment on alongshore topographic variability can therefore be discerned.

The monthly timescale of the surveys do not contain any information on behaviour of variability on shorter timescales. Thus variability could well be removed and regenerated between two surveys, such that a morphological reset[9] would have taken place or the signal of the magnitude of variability could be aliased. Hereto the spatial patterns in the nearshore are compared, to examine whether the alongshore variability pattern varies much between months, indicating that variability might be removed and new variability emerged in between to surveys.

An alongshore transect of the alongshore variability z_{var} is extracted on an arbitrary cross-shore location (x=325m) in the sub-tidal zone where depth is of O (2.5 m). The alongshore pattern in the variability on this transect is -if compared to surrounding months- very stationary (see Figure 2.22). The major pattern on this alongshore transect has a length scale of about 1200-1500 m, and migrates on average to the south. A morphological reset would appear in a timestack diagram like Figure 2.22 as an abrupt division between the horizontal alternating patterns of red and blue colors from one period to another (see *van Enckevort et al.* (2004): Figures 3, 4 and 5). The similarity in the pattern and pattern location between consecutive surveys as observed in Figure 2.22 at Vlugtenburg however suggests that either 1) patterns -if removed between to surveys- are regenerated rapidly at the nearly same locations with the same length scale, or that 2) patterns persist over long timescales and no patterns reformation occurs between surveys. Based on earlier reports on rare occurrence of resets at the Dutch coast (*van Enckevort et al.*, 2004) the latter explanation is far more likely, and although the evidence on this behaviour is only circumstantial, the author concludes that the Vlugtenburg beach did

[9] A morphological reset is defined here as a (high-wave) event that removes the alongshore variability in topography and where the patterns emerging in the post-event topography are unrelated to the patterns prior to the event (Following the definition of *Holman et al.* (2006) and *van Enckevort and Ruessink* (2003b)).

not experience a morphological reset during the 3.5 years investigated here[10]. This absence of resets at Vlugtenburg beach over the 3.5 years period is in line with earlier findings at the Dutch coast by *van Enckevort and Ruessink* (2003b); *van Enckevort et al.* (2004). The former propose that the relative slow reaction could well be related to the characteristics of the 'natural' profile at the Dutch coast such as the large volume of the (multiple) bars. As the profile at Vlugtenburg beach shows only single subtidal bar with volumes similar to sites abroad, the absence of resets at this site is suggested to be not only related to the profile but possibly also the Dutch wave climate characteristics (e.g. the large angles of wave incidence; see Figure 2.7).

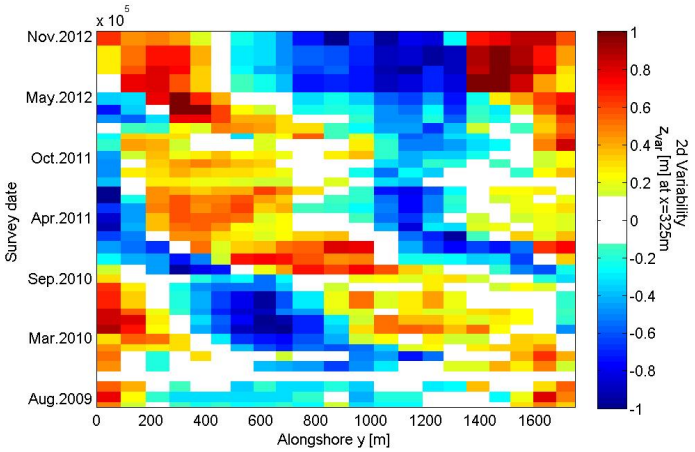

Figure 2.22: Height of the bed level variability z_{var} on an alongshore transect in the subtidal zone (at cross-shore x=325 m) over all surveys. Blue (red) spots show alongshore locations where the bed level is lower (higher) than the alongshore averaged bed level.

[10]This is further confirmed by daily Argus imagery data presented by *van der Grinten and Ruessink* (2012), which show that during part of the investigated period (2011 and 2012) no resets were observed at Noordwijk either (35 km north of Vlugtenburg).

2.5 Discussion

2.5.1 Overall sediment balance with the surveyed domain

An overall reduction in sediment volume was observed when bed level changes were integrated over the surveyed area (Figure 2.10). The reduction is largest in the first months after implementation of the nourishment, of O (70 m^3 / m alongshore / year) followed by a small downward trend of approx. 15 m^3/m/yr in the next years (see § 2.4.1). This sediment deficit can in essence be attributed to a combination of four different factors; 1) Compaction and consolidation of the soil within the domain, 2) A net flux across the landward boundary of the domain, 3) A net flux across the seaward boundary at deep water and 4) a gradient in alongshore sediment fluxes on the lateral boundaries. Although none of these four aspects were (or can possibly be accurately) measured in-situ, their contribution to the sediment deficit is discussed based on previous (sediment budget) studies.

Consolidation and compaction. Soil volume change (and consequently bed level reduction) is theoretically possible within the measured domain due to compaction and consolidation. Compaction is the decrease in air void volume in the soil body, which leads to a densification. This densification occurs almost instantaneous and can be stimulated by applying vibration and rolling over the soil. Most likely the maximum compaction of the nourishment has been reached during construction by the use of heavy mechanical equipment. Consolidation on the other hand is the expulsion of excess pore water from a saturated soil body and is time-dependent. Because the beach consists of granular material (i.e. medium size sand, rather than peat or clay) this dewatering is fast, on the timescale of days or less. Moreover, no extra load is applied on the subsoil after construction, and therefore consolidation, if any, is expected to have taken place prior to the first survey. Based on this reasoning consolidation and compaction are not proposed to be a significant factor in the measured volume loss over the 3.5 years.

Landward flux. The net landward flux across the landward boundary (across the crest of the new dune at +4 to +5 m NAP into the artificial dune valley) is very plausible, yet difficult to quantify. Profile data show no significant bed level changes at landward part of the analysed profiles (at $\sim$ +4 m NAP). However, it is well possible that sand is transported by wind beyond this boundary with little gradient in sediment transport and consequently no bed level change on the artificial dune is observed. Visual inspection of the area reveals indeed accretion landward of the artificial dune row near the old dune

Table 2.2: Estimates of sediment fluxes at Vlugtenburg in m^3/m alongshore/yr.

Reference	net sediment flux [$m^3/m/yr$]
Reported total yearly volume change in the profile	
Stive and Eysink (1989)[3]	-3
van Rijn (1997)[4]	-7.5
Transport across dune foot (+3m NAP), positive seaward	
de Vries et al. (2012)[1]	-20 to -30
van der Wal (2004)[2]	-14
Stive and Eysink (1989)[3]	-1
van Rijn (1997)[4]	-5
Transport across -8 m NAP isobath, positive seaward	
Stive and Eysink (1989)[3]	-10
van Rijn (1997)[4]	-15
Derived alongshore gradient in alongshore transport (-8 to +3 m NAP)	
Stive and Eysink (1989)[3]	-12
van Rijn (1997)[4]	-17.5

[1] Based on 25 yearly profiles near Vlugtenburg, flux taken equal to the observed mean annual dune volume change.
[2] Average value based on 12 nourished sites along the Dutch coast.
[3] Based on sediment volume of a 15 km coastal section (Hoek van Holland to Kijkduin) evaluated for the period 1850-1985.
[4] Based on sediment volume of a 10 km coastal section (Hoek van Holland to Ter Heijde) evaluated for the period 1964-1992.

row, but it cannot be determined whether this deposited sediment originates from the beach, the bare dune valley or neighboring alongshore sections (see Figure 2.2 for an overview of the area). Based on long term sediment budget studies of the coastal cell fairly low rates of net transport of 1-5 m^3/m from the beach into the dunes are expected (see Table 2.2).However, these data also incorporate locations and time periods when sediment has been eroded from the dune.

However, focussing on a transect at Vlugtenburg that has shown only dune growth over the last decades, *de Vries et al.* (2012) observe a substantially larger net sediment flux of 20-30 $m^3/m/yr$ towards the dunes. *de Vries et al.* (2012) further note that the rate is correlated to the beach slope. Considering the beach slope has increased compared to prior to the nourishment a more moderate rate of O (15 $m^3/m/yr$) at Vlugtenburg is proposed following the relations of *de Vries et al.* (2012). In the first year after the installation of a nourishment, rates towards the dunes can be slightly larger (*van der Wal*, 2004), which could be related to aeolian sorting blowing the fine fragments

from the supra-tidal beach and leaving a shell pavement. A similar enhanced aeolian transport in the first year could well be the case at Vlugtenburg, as the nourishment grain size on the upper beach was selected to be slightly smaller (180 μm) than the natural material to promote aeolian transport into the dunes. It is therefore estimated that the losses from the beach to the dunes are $\sim$ 25 m^3/m/yr in the first year and $\sim$ 15 m^3/m/yr in the following years.

Offshore flux. Previous literature suggest a net onshore sediment flux across the offshore boundary due to wave boundary layer effects (*Stive and Eysink*, 1989) as well as tidal and density driven net flows near the bottom (*van Rijn*, 1997). Estimated values for the onshore flux in this area are 10-15 m^3/m/yr (Table 2.2). Clear evidence for this onshore flux could not be derived from the profile data, but the seaward side of the profiles (at -8 m NAP) show a small bed level increase, a sign of sediment transport at these deeper waters. Whether the observed accretion is the result of onshore or offshore transport is undetermined. Since the sedimentation in the lower shoreface in the first phase after implementation of the nourishment is limited (Figure 2.15, black line) when overall volume losses are highest (72 m^3/m/yr, Table 2.1), the data rather suggests that the observed accretion of the lower shoreface is connected to down slope transport following the evolution of the upper profile (and bar migration) than to onshore sediment flux at deep water. However, analogous to previous studies a net onshore flux of 12.5 m^3/m/yr is assumed here.

Alongshore gradients in transport. Alongshore gradients in net alongshore sediment transport are thought to be an important factor in the sediment budget at the Dutch coast. In the coastal sections near Vlugtenburg the net gradient in alongshore transport is attributed mostly to the presence of the harbourmoles, yielding an increase in the net annual alongshore sediment transport in northward direction (see *van de Rest*, 2004, for an overview of multiple studies). *Stive and Eysink* (1989) and *van Rijn* (2011) suggest that losses due to this gradient are respectively 6 or 17 m^3/m per year.

Sediment budget. Based on the budget studies a volume change of -7.5 m^3/m/yr (*van Rijn*, 1997) to -3 m^3/m/yr (*Stive and Eysink*, 1989) can be expected in the area. Larger sediment losses ($\sim$ -20 m^3/m/yr) can be expected if the proposed fluxes for landward sediment transport are replaced with the values of *de Vries et al.* (2012) and *van der Wal* (2004). Above values for total annual volume change over the entire profile (-8 to +3 m NAP) are of similar order as the values observed in the 3^{rd} year after completion at Vlugtenburg, but the large losses in the first year of O (70 m^3/m/yr) are substantially larger.

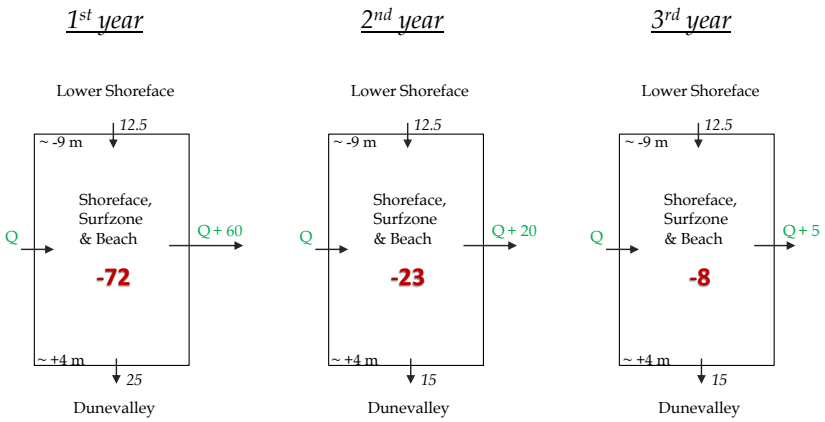

Figure 2.23: Sediment budget and fluxes for the Vlugtenburg domain. Red bold values give the measured annual volume deficit per meter alongshore, italic values are the estimated fluxes in m^3 per meter alongshore per year based on literature. Green values show the resulting net alongshore sediment transport fluxes derived from the volume deficit and the cross-shore fluxes.

An estimate of the sediment balance is conceived based on the fluxes at the landward and seaward boundaries proposed in earlier studies and the observed volume losses. These provide a conceptual figure of the net sedimentary fluxes per year (Figure 2.23). As both cross-shore fluxes towards the dunes and lower shoreface are envisioned to have only limited variation from year to year, most of the yearly differences in volume balance are related to changes in net alongshore sediment transport gradients. The yearly changes in net alongshore sediment transport gradients can originate from multiple sources, such as variations in sediment budget in adjacent sections or year-to-year variations in the wave climate. One of the reasons, specifically causing the observed decrease in alongshore sediment gradient from the first year onward, could be the cross-shore profile shape.

The variation of alongshore gradients in littoral transport due to cross-shore profile shape

The large losses in the first period are postulated to be partly due to the steepness of the initial profile. The profile in the first surveys contain a steep slope, especially below the low water line from -2 to -4 m NAP (see Figure 2.13). This section of the profile accommodates part of the wave-driven alongshore sediment transport during intermediate to energetic wave conditions. The alongshore wave-driven sediment transport integrated over the surf zone, Q_y, can be quantified by e.g. the *Kamphuis* (1991) formulation:

$$Q_y = K \left(\frac{g}{2\pi}\right)^{1.25} D^{-0.25} \rho H^2 T^{1.5} \sin^{0.6}(2\alpha_b) m_b^{0.75} \tag{2.9}$$

with K being an empirical constant, D the nominal grainsize, ρ the fluid density, H and T the wave height and period, α_b the breaking wave angle and m_b the beach slope in the breaking zone. As the profile is simplified in Eq. 2.9 to a single slope parameter, it does not specifically account for the presence of subtidal bars.

Given that this profile-integrated wave-driven alongshore sediment transport Q_y is dependent on the profile slope m_b, as proposed by Eq. 2.9, a steeper surf zone slope results in a larger sediment transport Q_y under equal wave forcing. For coastal areas with structural retreat due to alongshore gradients in transport, for instance due to the presence of harbourmoles, an increase of the slope m_b results in a multiplication of both incoming ($Q_{y,1}$) and outgoing sediment fluxes ($Q_{y,2}$) and hence also yields a larger gradient in sediment transport dQ_y/dy as illustrated in Figure 2.24.

This enhanced gradient in alongshore sediment transport ultimately results in a larger volume loss and bed level reduction in the steeper coastal section. Note that this effect is specifically of importance for nourished beaches where only the slope of the beach is altered. For natural beaches the causality between beach slopes and sediment transport is less clear as beach slope m_b itself is also is dependent on grain size D and wave forcing parameters H, T and α_b.

The postulated initial increase in the losses due to a steeper profile is elaborated upon by observing temporal evolution of profile slope between +1 to -4.3 m NAP; the intertidal and surf zone sections (based on the MKL definition, see § 2.4.3). Starting from the first survey, the slope changes from a slope of ∼1:40 to a milder ∼1:60 (Figure 2.25), while in the period 1965-2007 prior to the project the mean slope was 1:73 ± 7.5 (possibly also due to the presence

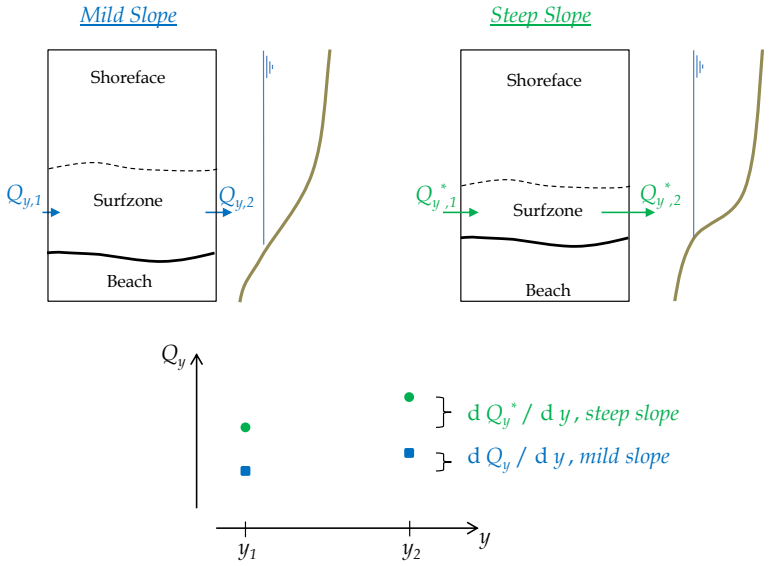

Figure 2.24: Schematic on the effect of a change in profile slope in the surf zone on a coast with an alongshore gradient in alongshore sediment transport Q_y (for instance due to the presence of harbour moles). Top left panel shows (in blue) the case of a coast with a (natural) mild cross-shore slope in the surf zone, top right panel shows (in green) the case after steepening of the profile. The topography with a steep surf zone slope yields larger cross-shore integrated wave driven alongshore sediment fluxes Q_y(indicated by the size of the arrows) and consequently a larger alongshore gradient in transport Q_y/dy.

of groynes during the this period). In the surveyed 3.5 years, the first time period with strong losses coincides with the period with the steep slopes, which supports the earlier hypothesis on the enhancement of alongshore losses after construction.

An estimate of the importance of the slope effect can be obtained when the observed profile steepness changes are combined with Eq. 2.9. For a given sediment transport Q_y an increase in the bed slope from 1:75 to 1:45 results a 47 % increase in predicted alongshore sediment transport. Altough this does not account for the all observed differences in derived alongshore sediment gradients shown in Figure 2.23, it reveals that recently nourished coasts can show a larger sediment deficit in the period when the profile is still adjusting than the long term average annual sand deficit.

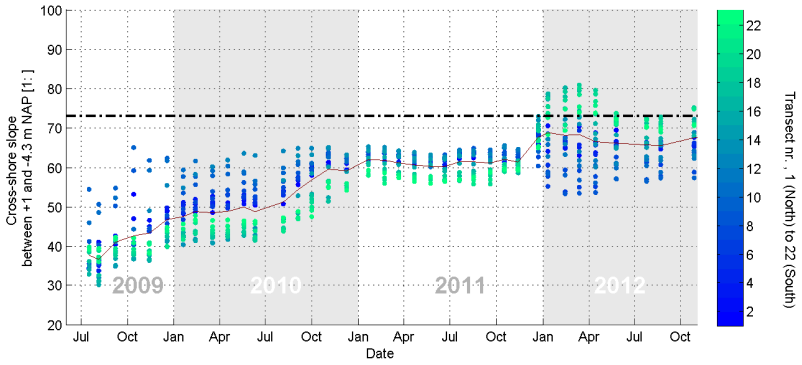

Figure 2.25: Evolution of the cross-shore slope of the profile in the intertidal and surf zone area. Colored dots give the slope for each of the different alongshore transects 1 to 22 from north (blue) to south (green). Solid line indicates the alongshore mean slope averaged over all transects. Dashed horizontal line indicates the mean slope for the period 1965-2007.

Based on these findings at Vlugtenburg, the steepness of the constructed profile is likely to be an important parameter for nourishment design. Especially at coasts with alongshore gradients in transport, it affects the initial alongshore losses. Likewise, a steepening of the man made profile can also be used to enhance the feeding property of a nourishment to the adjacent coast if desired.

2.5.2 Controls on alongshore variability in topography

The observed variability σ_z^2 is compared to profile parameters and wave forcing parameters previously suggested as governing processes in published literature. Similarly the temporal change in σ_z^2 over a period between two surveys, $\Delta\sigma_z^2/\Delta t$, (with Δt being the number of days between two surveys) is correlated. Relationships among variables are investigated with a least squares linear regression analysis. Resulting correlation coefficient r (i.e. Pearson coefficient ρ) for each cross-correlation is given in Table 2.3. Coefficient r is used rather than the more common r^2 to show the direction of the relationship (positive or negative). Parameters are tested in pairs, testing individual relationships. Due to the large interconnectivity between parameters (e.g. bar volume, crest location and depth) the values indicate similar changes in parameter space rather than direct dependency. A relationship is taken to be significant if the null hypothesis (no relationship between parameters) could

be rejected with 95 % confidence. The residuals of the linear regression (i.e. errors between linear model and the data) occasionally showed signs of autocorrelation, due to for instance the slow evolution of variability or the net seaward trend in bar position. For such observations, regression residuals were -by definition- not independent and the number of independent observations to determine the 95 % significance threshold had to be adjusted based on the correlogram of the residuals. Furthermore, on some occasions outliers dominated a (significant) relationship. For these cases, correlation was recomputed without the outliers and significance was re-evaluated. Only if a significant relationship remained after the criteria above, it is listed in Table 2.3.

Table 2.3: Correlation coefficients r of instantaneous variability σ_z^2 and evolution of variability $\Delta\sigma_z^2/\Delta t$ with profile and wave forcing characteristics. Only significant values (95% confidence interval) are given, non-significant relationships denoted as '-'.

	σ_z^2	$\frac{\Delta\sigma_z^2}{\Delta t}$	$\frac{\Delta x_s}{\Delta t}$	$\frac{\Delta V_{\text{supra}}}{\Delta t}$	$x_c - x_s$	$\frac{\Delta x_c}{\Delta t}$	d_c	V_{bar}	$\overline{P_0}$	$\frac{P_0}{max}$	$\overline{\lvert P_{y,\text{sed}}\rvert}$	$\frac{\lvert P_{y,\text{sed}}\rvert}{max}$	$\overline{\lvert\theta_{0,\text{s.n.}}\rvert}$
σ_z^2	1	-	-	-	-	-	-	-	-	-	-	-	-
$\frac{\Delta\sigma_z^2}{\Delta t}$		1	-	-0.62	-	0.52	-	-	0.67	-	0.73	0.58	-
$\frac{\Delta x_s}{\Delta t}$			1	-	-	-0.34	-	-	-	-	-	-	-
$\frac{\Delta V_{\text{supra}}}{\Delta t}$				1	-	-	-	-	-0.75	-0.76	-0.79	-0.71	-
$x_c - x_s$					1	-	-0.94	0.92	-	-	-	-	-
$\frac{\Delta x_c}{\Delta t}$						1	-	-	0.52	0.54	0.63	0.57	-0.42
d_c							1	-0.79	-	-	-	-	-
V_{bar}								1	-	-	-	-	-
$\overline{P_0}$									1	0.89	0.94	0.81	-
max P_0										1	0.86	0.88	-
$\overline{\lvert P_{y,\text{sed}}\rvert}$											1	0.89	-0.42
max $\lvert P_{y,\text{sed}}\rvert$												1	-0.49
$\overline{\lvert\theta_{0,\text{s.n.}}\rvert}$													1

Topographic controls

A number of topographic parameters were examined:

1. Change in cross-shore shoreline position $\Delta x_s/\Delta t$. Where x_s is calculated from the weighted mean position of the profile between - 0.5 and 0.5 m NAP (see § 2.4.2) and Δt is the number of days between the two surveys.
2. Change in supra-tidal beach volume between two consecutive surveys, $\Delta V_{\text{supra}}/\Delta t$. The volume of the supra-tidal beach (in m^3 per m alongshore) was obtained using the zone above + 1 m NAP.
3. Bar crest distance with respect to the shoreline (x_c-x_s).
4. Bar crest movement, $\Delta x_c/\Delta t$.
5. Water depth over the bar crest, d_c and
6. Bar volume V_{bar} (in m^3 per m alongshore).

The first two parameters are expected to provide a measure for the adjustment of the artificial construction profile to a more natural slope. $\Delta x_s/\Delta t$ and $\Delta V_{\text{supra}}/\Delta t$ are hypothesised to give an indication whether variability is related to the sediment redistribution from the upper beach towards lower profile changing the post construction profile to a more natural profile.[11] Remaining parameters 3-6 represent cross-shore subtidal bar characteristics previously associated with the growth rate or length scales of topographic variability. Bar crest locations further from shore (i.e. large x_c-x_s) are thought to generally result in larger alongshore spacing (*van Enckevort et al.*, 2004, and references therein) but the effect on the magnitude of variability is unclear.

The movement of the cross-shore bar crest is a proxy for the imbalance of the cross-shore bar position with respect to its equilibrium position based on the instantaneous wave forcing. Based on a simple empirical model, *Plant et al.* (2006) show that bar crest movement and alongshore variability are interrelated state variables and cross-shore migration of the crest can also incite a change in alongshore variability. Water depth over the bar crest controls partly the activity of the bar as deep bar crests are only inside or close to the surf zone during extreme wave events. Conceptual modelling of the emerging variability has confirmed that different crest levels result in changes in growth rate of variability (e.g *Calvete et al.*, 2007). Similarly, the bar volume is suggested to be related to the response time of the system (*van Enckevort et al.*, 2004; *Smit et al.*, 2008) as bar volume is a measure for the amount of sediment that has to be displaced to create the variability.

[11] Attempts to extract topographic variability on the supra-tidal beach and to correlate it with the subtidal variability σ_z^2 have met with difficulties, as part of the upper beach is reworked during the summer season for lifeguard access and placement of beach restaurants.

Correlation results

None of the topographic parameters give a significant correlation with the alongshore variability observed in the topography at a single moment in time (σ_z^2). This implies that the magnitude of the variability is not significantly larger when the subtidal bar is further off(on)shore or differs in volume. However, a moderate relationship is found between the changes in variability ($\Delta\sigma_z^2/\Delta t$) and both the reduction in the supra-tidal beach volume and the bar crest movement. This signal was mostly determined by the winter months where variability was increasing while the beach was eroding and the bar crest moves offshore. No relation is found with the bar crest level or bar volume, which is remarkable as in the 3.5 years a nearshore subtidal bar is formed and migrates offshore, resulting in a wide range of crest levels (d_c from -1.6 to -3.4 m) and bar volumes (V_{bar} from 50 to 150 m^3/m) over time. These trends are however not reflected in a significant relationship as alongshore variability was very low in the midst of the migration mid 2011 (see also Figure 2.20).

Environmental / Hydrodynamic controls

Wave forcing parameters discussed in § 2.3.2 are correlated to the (temporal variation in) variability. Mean values of incoming wave power P_0 and wave power available for sediment transport $|P_{y,\text{sed}}|$ are examined as well as their maxima in a period between surveys. The weighted mean wave angle $\overline{|\theta_{0,\text{s.n.}}|}$ in a period between surveys is also tested.

Correlation results

Similarly to the topographic controls, none of forcing parameters are significantly correlated to instantaneous observed variability. Nevertheless a moderate relationship is found between the changes in variability ($\Delta\sigma_z^2/\Delta t$) and wave power variables $\overline{P_0}$, $\overline{|P_{y,\text{sed}}|}$ and the monthly maxima of $|P_{y,\text{sed}}|$.

Correlation coefficient with incident wave power parameters is positive, indicating that increases in variability often coincide with time periods with large incident wave power (Figure 2.26). This is in contrast to traditional conceptual models of cyclic behaviour of bar states, which prescribe that high wave events coincide with a decrease and removal of variability and less energetic conditions during the following period result in the formation of variability (*Wright and Short*, 1984; *Ranasinghe et al.*, 2004; *Lippmann and Holman*, 1990). These models are confirmed by observations at Duck, NC, USA (*Lippmann and Holman*, 1990), Palm Beach (*Holman et al.*, 2006) and the Gold Coast, Australia (*Price*, 2013) amongst others, but such relation between forcing and variability is less clear at the Dutch coast as previously reported by (*van Enckevort*

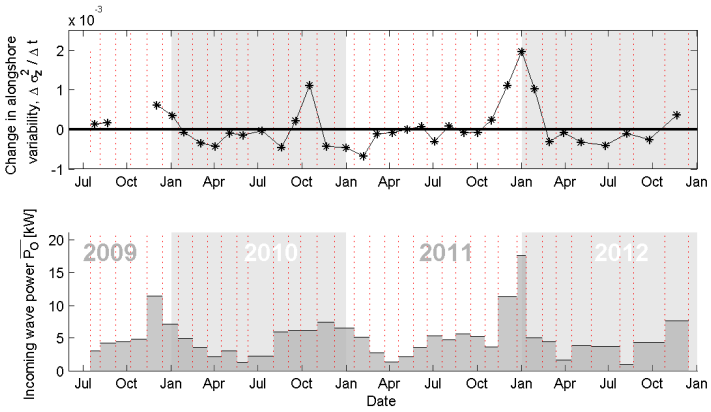

Figure 2.26: a) Change in alongshore variability between two consecutive surveys. b) Mean wave power offshore $\overline{P_0}$ in the period between two surveys. Red vertical lines indicate the survey dates.

and Ruessink, 2003b). The Vlugtenburg observations, contrasting the traditional model of removal of variability during storms, underline their earlier observation. A possible hypothesis for the different behaviour was suggested to be the large bar volume at the Dutch coast (*van Enckevort and Ruessink*, 2003b). Based on our data however, this argument does not provide a complete explanation as the subtidal bar volume of O (50-150 m^3/m) (see § 2.4.4) at Vlugtenburg is not significantly larger than than bar volumes in France (*Castelle et al.*, 2007) or Australia (*Price*, 2013) that have been reported to straighten during storm events. Possibly the 'counter-intuitive' behaviour at the Dutch coast can also be partly explained by the different environmental setting, such as the short-crested sea states or the large angles of wave incidence and variations therein.

The magnitudes and evolution rates of the topographic variability in the first period just after completion of the nourishment are not substantially different than for the total period investigated. It is therefore difficult to distinguish the effect of specifically the nourishment on the changing variability, especially as the bar behaviour resembles the values reported on unnourished beaches closeby. Whether the emergence and evolution of variability can be significantly affected by selecting a different nourishment design (e.g. by applying a milder construction slope) remains therefore unresolved. It would

be essential to perform a similar analysis at different nourishment projects to conclude whether above findings are generic.

2.6 Conclusions

The objective of the present chapter was to examine the morphodynamic evolution of a beach after implementation of a beach and shoreface nourishment. Over 3 years of monthly surveys (38 in total) have been acquired using a jet-ski equipped with single beam echosounder and a RTK-GPS backpack. This monthly timescale of surveys is essential to capture the absorption of the nourishment into the profile, the creation of a subtidal bar and the emergence of alongshore variability in the topography. The topographic data have been examined to investigate 1) the adaptation of the constructed profile towards a more natural profile and 2) the generation and evolution of alongshore variability in topography.

Redistribution of the nourished material

Morphodynamic evolution is analysed first in terms of nourishment volume, shoreline changes and redistribution of sand in the cross-shore. The analysis indicates that the initially steep construction profile resulted in a large redistribution of nourished sand from high up the profile down and seaward to the subtidal zone, resulting in a retreat of the shoreline of ∼50 m in 36 months. About 50 % of the sediment volume eroded from the upper beach (intertidal and supra-tidal beach) was compensated for by sedimentation in the lower shoreface, suggesting a downslope transport of (nourished) sand even to deep water (beyond the - 8 m isobath).

The overall morphological evolution is characterised by two periods, a first period of 6 to 12 months in which the largest losses of sediment volume of O (70 m^3 / m alongshore / yr) are observed, the steep foreshore slope is readjusting and a subtidal bar is formed. The following 2.5 to 3 years show a slower evolution and sediment losses in the area are limited, of O (15 m^3/m/year). The initial increase in volume losses after the implementation of the nourishment is found to be in part a result of the construction profile. It is shown that steeper profiles yield an increase in alongshore losses at coastal stretches where alongshore gradients in transport are present.

Alongshore variability in topography

The emergence of a cyclic subtidal bar system is observed and its emerging alongshore variability is compared to environmental and topographic controls previously suggested as governing processes. The analysis shows that the alongshore variability at Vlugtenburg beach is primarily found in the subtidal

bar and is evolving on a monthly timescale. This is slower than previous observations at the US east coast (Duck, NC) or Australian coasts (Palm Beach, Gold Coast). The first period just after completion of the nourishment shows no different magnitudes or evolution rates of variability than the total period investigated, such that an apparent effect of the nourishment on the variability cannot be discerned.
Neither geometry of the subtidal bar or parameters describing the average monthly wave forcing give a direct correlation with the alongshore variability observed in the topography at a given time. However, the temporal change in the magnitude of the alongshore topographic variability (the change with respect to the previous month) is found to be related to the incoming wave power and erosion on the upper beach. The relation is found to be positive, such that storms do not remove the alongshore variability at Vlugtenburg beach, which is in contrast to other beaches. Instead, energetic storm events during late autumn and winter months (October to January) resulted in a rapid increase in variability, which was then followed by a gradual decrease in alongshore variability during milder spring and summer wave conditions.

Appendix 2.A. Performance of the topographic variability parameter σ_z^2

In this appendix the proposed σ_z^2 parameter is examined for several synthetic topographies to test whether σ_z^2 can correctly represent the variability on the expected length scales of 200-1500 m using the transect distances of the Vlugtenburg dataset. Hereto, the measured alongshore mean profile of December 2011 (Figure 2.19) is used on which an synthetic rip-bar alongshore variability is imposed:

$$z_b(x,y) = z_{b,\text{mean}}(x,y) + h_{\text{2dVar}}(x,y) \text{ , with} \tag{2.10}$$

$$h_{\text{2dVar}}(x,y) = a_r \cos(\frac{2\pi}{\lambda_r} y) \cos(\frac{2\pi}{300}(x - x_c)) \exp^{-\frac{|x-x_c|}{45}} + \text{noise}, \tag{2.11}$$

where a_r is the amplitude of the alongshore variability (half the height difference between shoal and rip channel bed level) and λ_r represents the rip channel spacing controlled by the first cosine term. The noise term is random noise varied between 0 to $\pm$15 cm (uniformly distributed) to asses the effect of

survey inaccuracies. An example of a synthetic topography is shown in Figure 2.27.

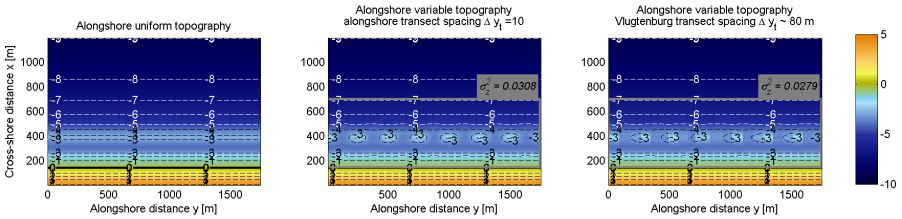

Figure 2.27: Synthetic topography based on the mean profile measured at Vlugtenburg in December 2011 (Figure 2.19). Left panel shows the mean profile, middle and right panels show the mean profile with alongshore variability (a_r=1 m, λ_r= 150 m) imposed with very fine transect spacing of 10 m and the coarse Vlugtenburg survey spacing respectively.

Different synthetic topographies have been constructed to examine a) which length scales can be resolved by the used transect spacing and b) to what extent survey noise affects σ_z^2 variability estimates.
The O (80 m) spacing at Vlugtenburg in between transects provides an lower limit of the alongshore length scale of features that can be correctly represented with σ_z^2. Synthetic bathymetries with alongshore variability with various length scale λ_r have been constructed on both a fine grid and resampled the Vlugtenburg spacing and subsequently expressed in a σ_z^2 value. The analysis shows that features with typical length scales of about twice the transect spacing can be well represented by σ_z^2. For the Vlugtenburg surveys this means that variability of O (200 m) and larger is captured. A typical alongshore length scale of subtidal features is of 500 m or larger for several Dutch sites (*van Enckevort and Ruessink*, 2003a) and these scales can be well resolved. The effect of survey inaccuracy (noise) of alongshore variability estimates is found to be limited. Some surveys contain slightly more noise as they are surveyed in rougher seas. Random noise of variable magnitude was imposed on the alongshore variable topography to examined how this affects the σ_z^2 value. For a Vlugtenburg bathymetry with a typical σ_z^2 value of O (0.07 m^2) (a_r=1.5 m, λ_r= 250 m) the noise has little contribution in the computed σ_z^2 value. If the (survey) noise increases to $\pm$ 0.15 m the variation in σ_z^2 is of O (10 %).
In summary, the topographic variability parameter σ_z^2 was found to be suitable to quantify the variability in the Vlugtenburg surveys on a length scale of 200 m and larger.

The emergence of topographic variability at the Dutch nourished beach revealed a slow development compared to other sites. As postulated in the introduction this is potentially related to the type of wave conditions. In the next chapter it is investigated whether the speed at which the variability develops is indeed dependent on the wave conditions. Unique data at Palm Beach, Australia, is examined for this part of the study since the variability at this site evolves rapidly (on the timescale of days) while the variability is removed several times a year by storms and subsequently regenerated. Also, Palm Beach is a single barred beach, enabling to circumnavigate the complexity of bar coupling that may be present at multiple barred coasts.

Abstract Chapter 3
Post-storm re-emergence of alongshore morphological variability is an intriguing phenomenon that has been studied for decades, albeit predominantly with numerical models. Here, for the first time, this phenomenon is investigated exclusively using field data. Four years of Argus video images and wave data obtained at Palm Beach, Australia are analysed with the primary objective of investigating the impact of wave height, period, angle and frequency bandwidth on the formation time T_v of post-reset alongshore variability.

The results of the analysis show that (a) there is no clear dependency of T_v on wave height or wave period for the periods investigated, and (b) large T_v's coincide with very oblique wave angles, which verifies previous model derived observations. The data analysis also suggests a previously unknown relationship between T_v and frequency bandwidth of the incoming wavefield such that large (small) T_v's coincide with the prevalence of wide (narrow) banded sea (swell) wave conditions after resetting storms. Thus, the data show that shore-normal or moderately obliquely incident, narrow banded swell waves are conducive for the rapid post-reset emergence of alongshore topographic variability.

Novel items in Chapter 3 are:

- The use of field data to link formation times T_v to concurrent wave conditions.
- The broad range of forcing conditions under which alongshore variability is observed to be removed and was found to re-emerge.
- The shown dependency of formation time on wave angle (consistent with previous conceptual model analyses), and the potential relationship with frequency bandwidth (introduced here for the first time).

3

Post-storm emergence of alongshore topographic variability in nearshore bars: a field data analysis

3.1 Introduction

The nearshore sub-aqueous zone is the most active part of the coastal profile. Often this part is characterised by the presence of one or more subtidal bars. These bars are frequently found to be alongshore variable; i.e. both the cross shore location of the bar as well as the crest height are non-uniform in alongshore direction. Such a topography is typically denoted as a rip-bar topography (*Wright and Short*, 1984). The hydrodynamic circulations and rip currents associated with this alongshore topographic variability play a major role in the distribution of nutrients, pollutants, sediments in the nearshore zone and can be hazardous for swimmers (e.g. *Dalrymple et al.*, 2011).

It has been long recognised that the alongshore variability in nearshore topography varies over time in a cyclic fashion. This cyclic behaviour is described by a conceptual model of discrete beach states (*Wright and Short*, 1984; *Lippmann and Holman*, 1990). In this model, alongshore variability is

generally removed during high energy (storm) events (*Wright and Short*, 1984; *Ranasinghe et al.*, 2004; *Holman et al.*, 2006; *Price and Ruessink*, 2011). The resulting alongshore uniform topography is referred to as the Longshore Bar Trough (LBT) beach state. In the period after the storm, waves become milder and alongshore variability reemerges on the subtidal sand bar. Typically, the first alongshore variability that can be seen is (rhythmic) alongshore undulations in the planform shape of the bar (Rhythmic Bar and Beach (RBB) state). Under continued mild wave conditions, sections of the bar can elongate in a transverse direction and eventually weld onto the shore, forming a Transverse Bar and Rip (TBR) beach. If the mild wave conditions persist for weeks, the entire bar will weld onto the beach resulting in a Low Tide Terrace (LTT) topography. However, a high energy storm can interrupt the above sequential beach state transition, and 'reset' the morphology to the LBT state. The alongshore morphological variability (characterised by rip/bar locations) that re-emerges after such a 'resetting storm' is, by definition, substantially different to that in the pre-storm morphology (*van Enckevort et al.*, 2004; *Holman et al.*, 2006).

Generally the alongshore uniform LBT phase after a resetting storm is short lived (on the order of 1-5 days, (*Lippmann and Holman*, 1990; *Ranasinghe et al.*, 2004)). The residence time of the LBT state however varies substantially from one post-resetting-storm period to another (at a given site), and between sites. Based on observations at Duck, *Lippmann and Holman* (1990) report a standard deviation of about 2 days (around the mean residence time of 2.1 days) while at Palm beach, Sydney, *Ranasinghe et al.* (2004) report a standard deviation of almost 4 days. This storm-to-storm variation in the formation of alongshore variability is amply illustrated in Figure **??** which shows two different reset events at Palm Beach, Australia.

The post-reset re-emergence of alongshore variability in nearshore morphology has intrigued scientists for decades. To date, almost all studies focusing on this phenomenon have adopted some sort of numerical modelling approach to gain insights, albeit with minimal field validation. In essence, these modelling studies have shown that the time period between the reset event and the first re-emergence of alongshore variability (hereafter referred to as formation time of alongshore variability, T_v) can be influenced by both hydrodynamic and topographic factors. A wide range of computed T_v values are reported, ranging from O (25 days) (*Damgaard et al.*, 2002; *Klein et al.*, 2002) to O (0.5 days) (*Deigaard et al.*, 1999). The hydrodynamic/morphological phenomena that have been found to influence the magnitude of T_v in these studies are also quite different, with the conclusions of some studies directly contradicting those of others. A brief summary of the major findings of these modelling

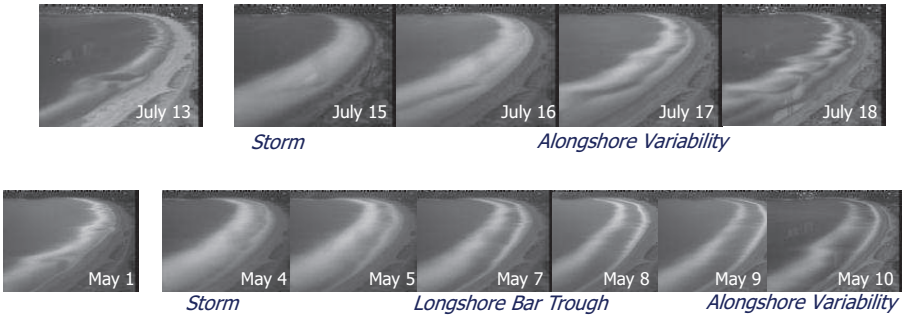

Figure 3.1: Daily time averaged Argus video images overlooking Palm beach, Australia for several days around two resetting storms, of July 1996 (*top*) and May 1996 (*bottom*). White bands in the images indicate areas of predominant wave breaking, and provide a proxy for the plan shape of the shallow subtidal bar.

studies is given below.

3.1.1 Previous modelling results

Previous modelling studies are based on different numerical model concepts to obtain insight in the formation time or growth rate of alongshore variability. Distinction can be made into three types of model concepts: 1) Linear stability models (e.g. *MORPHO60*, *Calvete et al.* (2005, 2007)), computing the initial growth rate of the fastest growing pattern in the topography. As the analysis is linear, the amplitude of the topographic disturbance is arbitrary (*Falqués et al.*, 2000) and growth is expressed as an e-folding time, the time it takes for the perturbation to attain an amplitude equal to e times the initial perturbation amplitude. 2) Non-linear models (e.g. *Morfo55*, *Caballeria et al.* (2002); *Garnier et al.* (2008); *Thiebot et al.* (2011)) calculating the time evolution of bed level change, computing only the effect of changed wave forcing and sediment transport due to the variability rather than the entire hydrodynamics and sediment transport fluxes. And, 3) 2DH coastal area models simulating the time evolution of the complete flow, sediment transport and bed level (e.g. *PISCES*, *Damgaard et al.* (2002); *MORPHODYN*, *Castelle* (2004); *Mike 21*, *Drønen and Deigaard* (2007); *Delft3D*, *Smit et al.* (2008)).
The three model concepts provide different proxies for the formation time of alongshore variability and therefore a direct comparison in terms of T_v cannot be really made. Instead the relative impact of tested parameters on (the proxy

for) T_v will be discussed hereafter.

Calvete et al. (2007); *Smit et al.* (2008); *Drønen and Deigaard* (2007) have shown that the seaward slope of the bar or the active cross-sectional volume of the bar is one of the main topographic aspects affecting the formation time of the emerging alongshore variability. When the seaward slope is doubled, T_v doubled (*Calvete et al.*, 2007), possibly due to the increased quantity of sediment that needs to be displaced to create the alongshore variability (*van Enckevort et al.*, 2004; *Smit et al.*, 2008).

Cross-shore bar distance from shore, if varied independently in numerical models by moving the shoreline with respect to a fixed bar shape, was found to have only little influence on T_v (*Deigaard et al.*, 1999; *Calvete et al.*, 2007). This contradicts the data driven empirical model results of *Plant et al.* (2006) and *Splinter et al.* (2011) which showed that bar position and amplitude of the alongshore variability are codependent. Yet, comparison between both findings are difficult as *Plant et al.* (2006) and *Splinter et al.* (2011) used bar positions derived from video imagery, with no information on bar crest level, bar slopes and cross-sectional volume that might be varying simultaneous.

The ratio of wave height over water depth (H/d) on the bar is another parameter that is commonly believed to govern T_v. Small wave heights or deep bar crests result in barely breaking waves on the bar and consequently very long formation times T_v (e.g. *Calvete et al.*, 2005; *Garnier et al.*, 2008). For wave heights in the order of the water depth on the bar crest or larger ($H/d_c \geq 1$) predictions are not consistent. While some studies report a decrease in T_v when wave heights increase beyond this threshold (e.g. *Calvete et al.*, 2007), others show no such inverse relationship (e.g. *Calvete et al.*, 2005, their Figure 5).

Predictions of T_v under varying wave periods are also inconsistent. *Calvete et al.* (2005) reported a decrease in T_v (based on e-folding time) of O(20 times) when the wave period increases from 4 to 18 seconds, larger than the impact of any other external parameter investigated in that study (provided that waves are breaking on the bar). Yet *Garnier et al.* (2008) found a nearly constant T_v for different wave periods ranging between 6 and 9 seconds.

An increase in the wave angle has generally been found to result in higher T_v. For waves arriving with an offshore angle of 30 degrees with respect to shore-normal, T_v is predicted to increase by a factor of 3 to 5 compared to T_v for shore-normal wave incidence (*Calvete et al.*, 2005; *Drønen and Deigaard*, 2007; *Smit et al.*, 2008). *Garnier et al.* (2008) report an even larger increase of formation time T_v, where a 6 degree wave angle (at 4.5 m water depth) is shown to result in an increase of O (30 times) relative to that when waves are shore-normal, while no variability was found to form for wave angles greater

than 7 degrees. Recently, *Thiebot et al.* (2011) investigated the emergence of variability under a very wide range of wave angles for a double barred system. Similar to *Garnier et al.* (2008), their simulations show a higher T_v under increasing wave angle and no emergence of variability for medium to high wave angles. However, for extreme wave angles of $\geq$ 20 degrees at the outer bar crest (water depth of 3.5 m), variability was found to be emerging again in the form of shore-oblique bars.

Potential linkages between T_v and frequency and directional spread of the incident wave field have so far received little attention. The frequency and directional spread of the incident wave field is largely responsible for spatial and temporal variations in the wave forcing, which in turn affect wave breaking, wave forcing and mixing properties in the nearshore (e.g. *Feddersen*, 2004; *Spydell and Feddersen*, 2009). Therefore, it is highly likely that frequency and directional spread of incident waves do have a significant effect on T_v. The only study to date that investigates the effect of directional spreading on the development of alongshore morphological variability is reported in the process-based model study by *Reniers et al.* (2004). Although model results presented by *Reniers et al.* (2004) showed a clear effect of directional spreading on the hydrodynamics and the fully developed rip spacing there was no attempt therein to directly investigate potential links between directional spread and T_v.

While the above modelling studies have significantly improved our understanding on the post-reset re-emergence of alongshore morphological variability, the lack of field validation of the results introduces some uncertainty regarding the conclusions drawn therein. For a basic validation of these model-based conclusions, what is required is a single study comparing field observations of T_v for several reset events at a single subtidal bar, resembling the simplified cases tested in the aforementioned numerical (process-based or stability model) studies. The present study, for the first time, aims to address this need using a 4 year long, daily beach state and wave data series.

The specific aim of the present study is to investigate the impact of wave height, period, direction and frequency bandwidth on the formation time T_v of post-reset alongshore variability using 4 years of Argus video and concurrent wave data at Palm Beach, Australia. Several post-reset periods are investigated to identify linkages between the above forcing conditions and T_v. As the time exposure video images analysed here do not directly provide information on the vertical dimension, this study is by necessity limited to an investigation of the impact of hydrodynamic forcing conditions (rather than profile parameters, such as beach slope etc.) on T_v. Specific attention is paid to the potential linkages between wave period/frequency spread (bandwidth) of the

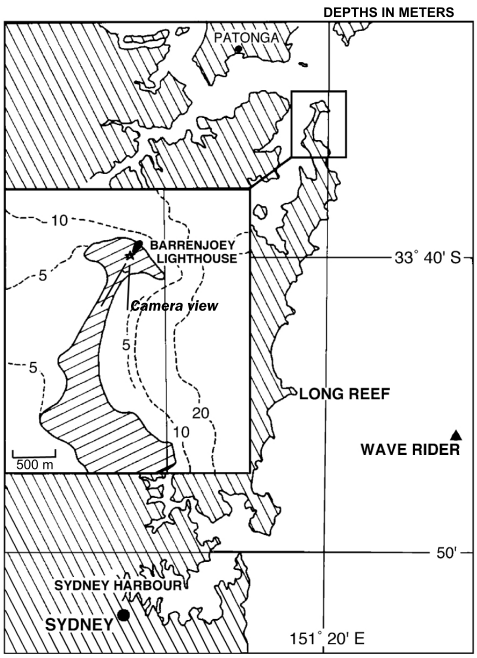

Figure 3.2: Location of Palm beach, Australia. Nearby wave rider buoy is indicated by the triangle. *Modified from: Ranasinghe et al.* (1999)

incident waves, to test the hypothesis that long crested swell waves enable a quicker formation of variability than short crested wind sea waves.

3.2 Observations

3.2.1 Study site

Palm Beach, Australia, a 2 km long embayed beach located 30 km north of Sydney (Figure 3.2), was selected for this study. It provides a unique field site for the objective of this study due to the presence of a single subtidal bar, which makes it analogous to the schematised modelling studies described in section 3.1.1. The field site is equipped with an Argus imaging station and a nearby offshore wave buoy, which provides information on bar morphology and wave conditions at an hourly temporal resolution. The wave climate at Palm

Beach is characterised as a combination of a highly variable wind wave climate superimposed on persistent south-easterly swell. Mean deep water significant wave height is 1.59 m and the mean wave period is 10 s. The surf zone bed slope is 0.02 flattening to 0.005 1 km seaward of the shore (*Brander*, 1999) providing a platform for the waves to refract inshore before they reach the surf zone.

Palm Beach experiences all intermediate beach states described in *Wright and Short* (1984), going through the full cycle of an alongshore uniform bar (LBT) just after a storm, evolving into a Rhythmic Bar Beach (RBB), a Transverse Bar Rip (TBR), and finally arriving at a Low Tide Terrace (LTT). Annually, around 5 resetting storms erase the existing alongshore variability, after which new post-storm bar variability is initiated (*Ranasinghe et al.*, 2004; *Holman et al.*, 2006).

3.2.2 Image processing

Daily averaged Argus time exposure images (daytimex images) of the beach were used to determine the initiation of alongshore variability in the bar. The Argus video images were taken from the Barrenjoey Lighthouse at 115 m above mean sea level looking southwards towards the bay (Figure 3.2). The present data analysis was based on the images collected at Palm Beach during the period 1996 to 1999. These 4 years of daily image data were used as the beach state and reset classifications obtained from these images have been rigorously quality controlled via sample classifications obtained from a panel of coastal experts/non-experts (*Ranasinghe et al.*, 2004; *Holman et al.*, 2006).

The station collects time-exposure (timex) images every daylight hour. These timex images were created by averaging the first 10 minutes of continuous 1 Hz snap shot images. To minimise the influence of the varying water level over the tidal cycle the hourly timex images obtained during daylight hours were averaged to obtain the daily averaged timex image (daytimex image). A plan view image of the bar location was created by rectifying the daytimex images and converting these into real world coordinates using the technique described in *Holland et al.* (1997) (Figure 3.3 b).

Areas with consistent wave breaking appear in these daytimex images as high intensity (white) bands (*Lippmann and Holman*, 1989). Wave breaking is mostly determined by water depth, and therefore the areas with consistent wave breaking are indicative of the location of the sand bar. The maximum intensity in the white band indicating the sand bar corresponds with the location of maximum wave breaking, which can be presumed to be at or close to the bar crest location. Using simultaneous bathymetric surveys and Argus

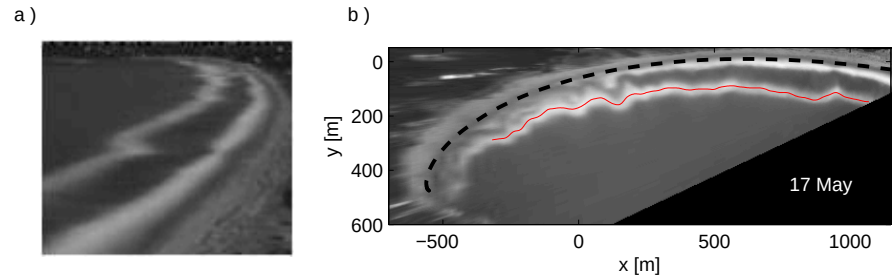

Figure 3.3: Argus daily time exposure image (a) and rectified image (b) of 17 May 1997. Bar intensity line is indicated by the thin red line, approx. shoreline location is given by the thick dashed line. Axis labels are given in meters with respect to the local coordinate system.

video observations, *van Enckevort and Ruessink* (2001) showed that bar positions derived from the images provide a reliable estimate of actual bar crest position with an accuracy of O (10 m) in the cross-shore direction.

The bar crest location in real world coordinates was derived from the rectified daytimex images. Maximum intensity in the white band in the images was computed semi-automatically using the BarLine Intensity Mapper (BLIM) toolbox developed at Utrecht University (*Pape*, 2008). Since the bar was more visible in the northern half of the embayment and the pixel resolution decreases towards the south, the southern 500 m of the bay was excluded from this analysis, leaving approximately 1100 m of bar crest line to be analysed. The bar crest line location was subtracted from the shoreline location to obtain the cross shore distance of the bar x_c with respect to the beach. Shoreline position was approximated by a log spiral (*Ranasinghe et al.*, 2004) indicating its approximate position. The alongshore averaged bar position $< x_c >$ was subtracted from the alongshore varying bar crest distance, leaving only the variability of the bar crest with respect to the alongshore averaged bar position (Figure 3.4).

The alongshore variability of the bar was quantified by the alongshore variability amplitude, a, similar to *Plant et al.* (2006); *Splinter et al.* (2011). Variability amplitude a was calculated by performing a Fourier decomposition of the relative alongshore bar crest line as depicted in Figure 3.4, and taking the root mean variance in the 100 to 550 m band. The 100 m threshold used here was chosen to remove variations with small alongshore length scales and the 550 m upperlimit was selected equal to half of the analysed bar crest line,

thus providing a measure of the magnitude of the medium scale alongshore variability in the bar. The typical length scale of the topographic variability (rip spacing) is of O (180 m) at Palm Beach (*Holman et al.*, 2006) and is hence well captured by these limits. For reference, if one considers a bar with a crest distance varying sinusoidally with respect to the shoreline with an alongshore wave length L^*=250 m and an amplitude $A^* = 14$ m, the calculated variability amplitude a is $\sim$ 10 m (Note that for a sine wave a is by definition equal to $A^*/\sqrt{2}$). A hypothetical straight alongshore uniform bar would result in an a value equal to 0 m.

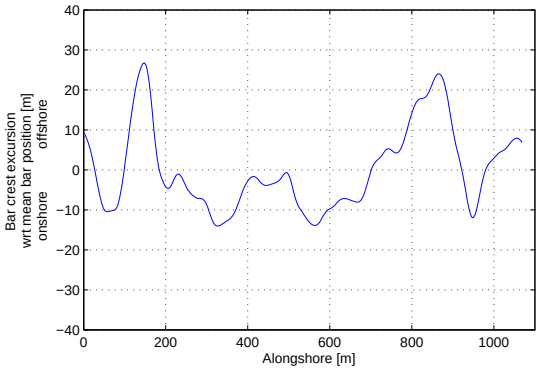

Figure 3.4: Argus derived planform bar crest excursion with respect to the mean bar location on 17 May 1997 (Figure 3.3).

3.2.3 Wave data

Offshore wave conditions were obtained from the Long Reef wave buoy (Figure 3.2). This directional wave buoy is located 20 km south of the site in a water depth of 87 m. Hourly significant wave height H_s and one dimensional frequency spectra $E(f)$ were obtained for the resetting storms identified by *Holman et al.* (2006). The one dimensional frequency spectra provide information on the distribution of wave energy in 64 frequency bands of 0.005 Hz ranging from 0.005 Hz to 0.32 Hz. Measured spectra were moving averaged over a time span of 3 hours to provide smoother spectra. Wave period from the spectra was expressed in mean period T_{m01} rather than a peak period T_p. Because T_p is derived only from the peak of the spectrum it is sensitive to small variations in the frequency spectrum while T_{m01} is determined from

the full spectral shape and therefore provides a more robust value of the wave period. T_{m01} is derived as follows:

$$T_{m01} = \frac{m_0}{m_1}, \tag{3.1}$$

where m_n is the n-th order moment of the spectrum.

The frequency bandwidth of the spectra is expressed by parameter κ (*van Vledder*, 1992). Bandwidth parameter κ used here is little influenced by high frequency errors in the spectrum and calculated from the short wave spectrum $E(f)$ using:

$$\begin{aligned} \kappa^2 &= \frac{1}{m_0^2}\left[\int_{0.005}^{0.32} E(f)\cos(\frac{2\pi f}{\bar{f}_0})df\right]^2 + \\ &\quad \frac{1}{m_0^2}\left[\int_{0.005}^{0.32} E(f)\sin(\frac{2\pi f}{\bar{f}_0})df\right]^2, \end{aligned} \tag{3.2}$$

where $\bar{f}_0$ is the zero crossing frequency ($\sqrt{m_2/m_0}$).

High κ values are obtained when incident wave spectra have wave energy concentrated close to the peak frequency of the spectrum (i.e. narrow frequency bandwidth) as commonly found with swell waves. Strictly speaking κ represents a value of the narrowness in frequency spread rather than the width, as wide banded spectra as found in wind seas or double peaked spectra result in low κ values and narrow banded swell conditions yield to high κ values, nevertheless it will be referred to as a bandwidth parameter from hereon. As a reference, commonly used Jonswap spectra and wider Pierson-Moskowitz spectral shapes (*Holthuijsen*, 2007) yield κ values of 0.57 and 0.42 respectively. In this study, typical spectral bandwidth values κ calculated from the wave buoy data were in the range 0.3 to 0.6. Generally, bandwidth and period of the short wave spectrum are not independent, with narrow frequency spreads coinciding with long period swell. However, in the days from the peak of the storm until the emergence of alongshore variability analysed here, the period and bandwidth κ did not show a significant correlation (r^2=0.11, p=0.08). Data related to the directional spreading of the wave field were not available for this study and therefore effects of directional spreading were not examined. Wave direction measurements obtained from the wave buoy are the principal wave direction which is the direction corresponding to the peak period of the energy spectrum. Wave angles with respect to shore during and after the storms vary from shore-normal incidence to oblique. The height of

oblique waves recorded at the offshore wave buoy are reduced significantly due to refraction when propagating shoreward. To effectively compare post-storm periods with obliquely and near normal incident waves, the offshore wave data were therefore translated inshore to shallower water depths with the linear dispersion relation including refraction and shoaling. Breakpoint values of wave height H_b, direction θ_b and depth h_b are determined such that H/h equals the breaker criterion γ. The breaker criterion γ used herein was based on the formulation by *Battjes and Stive* (1985), which includes the effect of wave steepness.

3.3 Results

Fifteen (15) resetting storms are reported in total at Palm Beach during the period 1996 to 1999 (*Holman et al.*, 2006). To be identified as a resetting storm the imagery data was thoroughly checked for 1) removal of the alongshore variability in topography during the storm and 2) that patterns emerging in the post-event topography are unlike to the patterns prior to the event (*Holman et al.*, 2006). The severe weather conditions during storms occasionally led to either malfunctioning of the wave buoy or unclear Argus images, making 6 of these events unsuitable for the present analysis. The remaining 9 post-storm periods show a rapid (less than a week) emergence of the first alongshore variability. The moment at which the first patterns emerged was determined by using a threshold value of a equal to 4 m combined with a visual assessment of the images by a classification panel. Threshold a=4 m used here was slightly more stringent than the threshold $a \sim$6 m used in *Price and Ruessink* (2011) to separate LBT and RBB beach states.

T_v values subsequently obtained for these events ranged from one to six days. The observed post-storm morphological responses fell into two distinct categories: one where the storm was followed by short T_v ($<$ 2 days after the peak of the storm) and another where the nearshore bar stayed alongshore uniform for more than 2 days.

Two post-storm periods, typical for a fast and delayed initiation of alongshore variability in the subtidal bar are shown in Figures 3.5 and 3.6 respectively. Six post-storm periods fall in the first category. Figure 3.5 shows the morphological evolution after the storm of 15/16 July 1996. The Argus images show that the subtidal bar experiences only a day of alongshore uniformity on the day of the peak of the storm, whereafter the first alongshore variability in bar crest position can be observed. These patterns grew quickly and 3 to 4 days after the peak of the storm a cresentic bar (RBB) morphology was

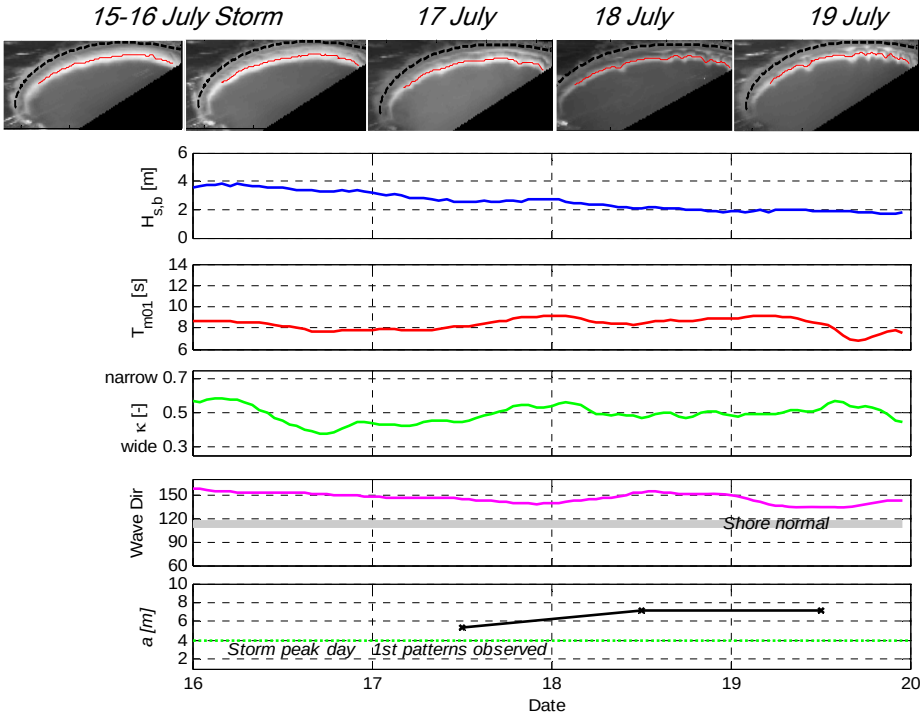

Figure 3.5: Post-storm development of alongshore variability in the subtidal bar at Palm Beach. Fast emergence of alongshore variability after the storm of July 1996. Rectified Argus images (*top*) show alongshore variability emerging one day after the peak of the storm on 16 July 1996. The bar crest line is shown in red in the images. Concurrent wave data (*middle*) show offshore wave height at breakpoint, wave period, bandwidth and offshore wave angle. Bottom panel shows the alongshore bar crest variability a [m] as derived from the Argus images.

observed. During this storm the wave height offshore H_s attained 3.6 m which is relatively mild compared to the other resetting storms. The wave period during the storm was about 9 seconds and the wave field was narrow-banded with κ values up to 0.6. In the days after the storm the wave height slowly decreased while wave period and bandwidth remained relatively constant.

Figure 3.6 shows the morphological evolution after the storm of 9-11 May

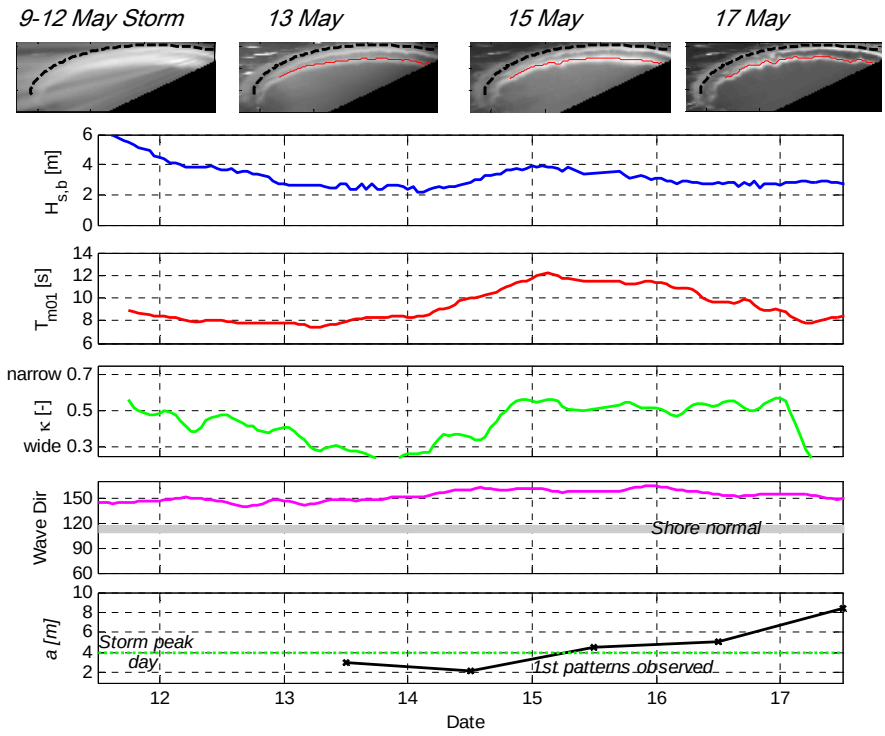

Figure 3.6: Post-storm development of alongshore variability in the subtidal bar at Palm Beach. Delayed emergence of alongshore variability after the storm of May 1997. Rectified Argus images (*top*) show alongshore variability emerging 4 days after the storm on 11 May 1997. The bar crest line is shown in red. Concurrent wave data (*middle*) show two days (15 - 17 May) of long period, narrow banded waves associated with the morphological transition. Graphs show wave height at breakpoint, wave period, bandwidth and offshore wave angle. Bottom panel shows the alongshore bar crest variability a [m] as derived from the Argus images. During the storm no bar crest position could be extracted from the image.

1997 where alongshore variability emerged much more slowly. Two days after the storm (13 May 1997) the bar was still alongshore uniform, and the first variability in the bar emerged 4 days after the peak of the storm on 15 May 1997. Note that during this entire period waves were breaking on the bar, as

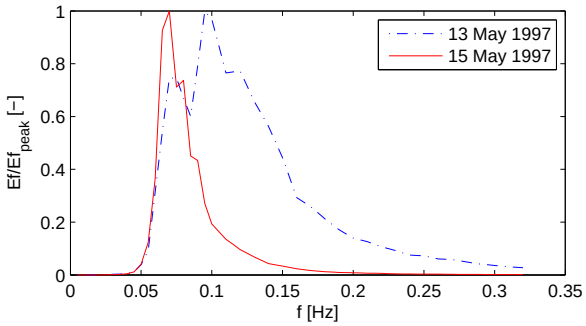

Figure 3.7: Normalised daily averaged incident wave spectra for the May 1997 post-storm period.

all images show a white band of dissipation over the bar. Wave heights during the May 1997 storm were large with a daily averaged $H_s = 6$ m (and hourly peaks of $H_s > 8$ m). In the time period after the storm, wave heights reduced rapidly and wave conditions were very wide banded ($\kappa = 0.3$-0.4). After 3 to 4 days a new south-easterly swell reached Palm Beach, wave period increased while frequency spread decreased. Simultaneous to the arrival of the new swell on May 15^{th}, the morphology turned from alongshore uniform into alongshore variable. The shift in wave conditions is further illustrated by the wave spectra for 13 and 15 May 1997 (Figure 3.7), showing significant lowering of the peak frequency and narrowing of the spectrum from 13 to 15 May. The short wave spectrum as recorded on 15 May 1997 corresponds to typical narrow-banded swell conditions. During the whole period (9 to 17 May), wave incidence was strongly oblique with offshore wave angles of around 40 degrees with respect to shore-normal.

Wave data for the 9 post-storm periods are presented in Figure 3.8. Wave height, period, wave angle and frequency bandwidth are shown for the days from the peak of the storm to the day the first alongshore variability in the bar emerged. The data are presented as daily averaged values, on a similar timescale to the daytimex Argus images. Wave conditions both within the storm and the period afterwards vary substantially among the different events. The resetting storms had peak wave heights $H_{s,b}$ ranging from 2.6 m to 6 m (red diamonds in Figure 3.8). The three resetting storms with the lowest peak wave heights are associated with narrowbanded (high κ) frequency spectra. Peak wave heights for some storms were lower than the wave heights that prevailed at the time of emergence of alongshore variability after other storms,

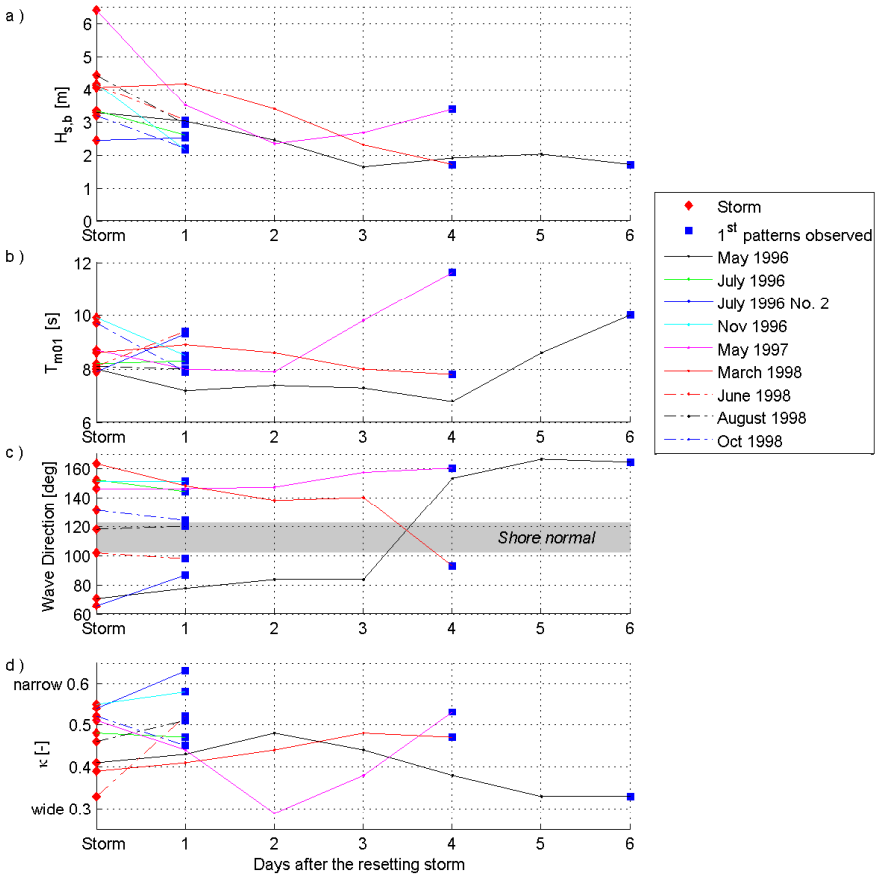

Figure 3.8: Post-storm wave conditions between the day of the peak of the resetting storm and the day the first alongshore variability was observed. Daily averaged values of significant wave height at breakpoint (a), wave period (b), wave angle offshore (c) and frequency bandwidth (d). Approximate shore-normal incidence is indicated by the shaded area.

indicating that resetting and post-reset behaviour is not purely a function of wave height. Resetting storms had different angles ranging from oblique to near shore-normal. Interestingly, these data show that waves do not necessarily need to be obliquely incident for a reset to occur (Figure 3.8, June 1998 and August 1998 resets). Figure 3.8 indicates that the emergence of alongshore variability is not linked to a single specific type of wave condition and high to low values for wave height, period and bandwidth as well as oblique and shore-normal wave angles are observed on the day the first alongshore variability was identified (squares in Figure 3.8).

The data show no consistent dependency between wave height and T_v, which is qualitatively in line with the inconsistent model derived conclusions on this dependency. Generally, the first patterns are observed when wave heights decrease to the 2-3 m range. However, the data do not substantiate previous model findings that larger wave heights (with respect to the bar crest) result in smaller (*Calvete et al.*, 2007) or constant (*Calvete et al.*, 2005) formation times. In fact, post-reset periods with long T_v show relatively large wave heights on the day after the storm.

Wave period does not provide consistent justification for the observed variations in formation time among resets. Except for the May 1996 reset event, wave period data are all in the 8 - 10 seconds range and post reset periods with large T_v values do not show substantially different wave periods from those with small T_v values. The first identification of variability together with the arrival of waves with large wave periods for the May 1996 and May 1997 resets (Figure 3.8 and 3.6) suggests an acceleration of the formation of variability. This quantitatively agrees with the numerical model findings of *Castelle* (2004) and *Calvete et al.* (2005), which predict a decrease in formation time T_v for larger wave periods. The limited amount of observations at Palm Beach and the lack of topographic data, however, preclude any firmer conclusion.

Post-storm periods with near normal incident waves coincide with small T_v while those with large T_v coincide with strongly oblique waves. This increase in T_v as waves become more oblique is likely because the strong alongshore currents generated by strongly oblique waves would have an overriding effect on the small (time/space varying) cross-shore flows that contribute to the initial formation of small alongshore variability in the bar (e.g. *Wilson*, 2009; *Castelle*, 2004). Initial variability, which evolves into rip channels and shoals via positive feedback mechanisms, is thus reduced or grows slower (e.g. *Price and Ruessink*, 2011; *Smit et al.*, 2008). It is however also noted that that eventual emergence of variability was observed even under high angles of wave incidence ($\sim$ 45 degrees offshore). The longer formation times T_v observed in the present study for post storm periods with large wave angles qualitatively

validates similar predictions by both stability and process based type models (e.g. *Calvete et al.*, 2005; *Drønen and Deigaard*, 2007; *Smit et al.*, 2008). However, a possible maximum wave angle under which the topography remains alongshore uniform and no variability is formed as found by *Castelle* (2004) and *Garnier et al.* (2008) is not confirmed, as observations showed the emergence of initial variability even when wave angles remained highly oblique (O 40 degrees with respect to shore-normal) from the storm onward. Wave angles at 3.5 m water depth are determined using Snell's law, similar to *Thiebot et al.* (2011), to verify a possible generation of variability under extremely oblique wave incidence. However, even under offshore wave angles of 45 degrees with respect to shore-normal, the nearshore wave angle remains below the threshold of O (20 degrees) for the formation of shore-oblique bars suggested by *Thiebot et al.* (2011).

The spectral bandwidth parameter κ compares favorably with the formation time of alongshore variability. Post reset periods with large T_v show relatively lower κ values the day after the storm (Figure 3.8 d) indicating wider frequency spread in the waves, while most of the reset periods where $T_v \leq 2$ days coincide with relatively narrow frequency spreads (high κ values).

The incident wave conditions preceding the emergence of alongshore variability (Figure 3.8), underline the diversity of the formation of variability in nature. Nevertheless, the data suggest a relationship between the post-storm emergence of alongshore variability in bars and the characteristics of the incoming wave forcing, where wide banded wind sea conditions and high angle waves appear to result in larger T_v values.

As anticipated, the number of post-storm periods in the 4 years data series is insufficient to define clear threshold criteria for the emergence of variability based on the data alone. The number of resets is too little to be able to cluster data and isolate parameters one by one. The observed relationship of frequency bandwidth could therefore well be biased by concurrent changes in the other parameters. Moreover, the observed scatter post-reset behaviour are most likely due to the inevitable variations in the cross-shore profile amongst storms. It is recognised that the approach, which is based on estimations of topography using video observations, may lead to underestimation of the effect of changing topography. More detailed conceptual modelling therefore needed, to rigorously test the suggested relationships.

3.4 Bulk wave parameters and the development of alongshore variability

Simultaneous variations in wave height, period and direction make the extraction of robust trends that are applicable to all post-reset periods difficult, if not impossible. Lumping the various wave parameters together in a bulk parameter is a way to circumnavigate this problem. Therefore, further analysis was undertaken by investigating the evolution of two bulk wave parameters (Surf similarity parameter ξ_b and beach profile parameter Ω) during the period between the peak of the storm and the emergence of alongshore variability in the nearshore bar for the resetting storms discussed above. The surf similarity parameter ξ_b provides a proxy for changes in the intensity of wave breaking in the nearshore. The evolution of the beach profile parameter Ω (besides its common use to determine beach states) is an indicator of overall (cross-shore) erosive/accretive behaviour of the profile. Although both parameters are mostly cross-shore oriented, the observed coupling between the alongshore variability and the cross-shore profile topography of subtidal bars (e.g. *Plant et al.*, 2006; *Splinter et al.*, 2011) provides justification for the use of these two bulk parameters to investigate the emergence of alongshore variability.

3.4.1 Surf similarity parameter

The surf similarity parameter ξ_b given by *Battjes* (1974) is commonly used as a proxy for the type of wave breaking (spilling-plunging-collapsing-surging):

$$\xi_b = \frac{\tan\alpha}{\sqrt{H_b/L_0}} = \frac{\tan\alpha}{\sqrt{\frac{2\pi H_b}{gT^2}}}, \tag{3.3}$$

where $\tan\alpha$ is the slope of bottom and H_b is the breaker height. Spilling breakers are typically obtained for ξ_b smaller than 0.4, plunging breakers for $0.4 < \xi_b < 2$. Observations have shown that plunging waves result in more wave breaking induced turbulence and sediment suspension (*Ting and Kirby*, 1995, 1996; *Aagaard and Hughes*, 2010). Two dimensional large scale flume observations confirm that this can result in an accelerated morphological response (*van Thiel de Vries et al.*, 2008).

The evolution of the surf similarity parameter from the peak of the storm to the first emergence of alongshore variability is shown for the 9 reset events in Figure 3.9. As no topography data is available from the post storm periods, the bottom slope $\tan\alpha$ was taken as 1:25, representative of the outer slope of the bar and similar to the slope during the RDEX experiment at the site

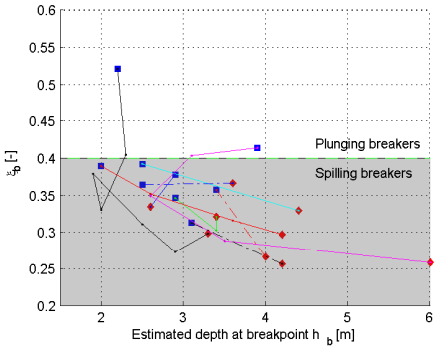

Figure 3.9: Estimated water depth at breakpoint and breaker type in the days after the resetting storms at Palm Beach. Filled '◇' symbols represent the wave conditions on the days of the peak of the storm, squares represent the conditions on the days the first alongshore variability was observed. Legend similar to Figure 3.8.

(*Reniers et al.*, 2001). Figure 3.9 shows that during storm conditions the waves were breaking at large water depths and ξ values fall in the spilling breaker range. In the days after the storm, wave breaking intensified (as shown by the upward shift of ξ_b) as wave heights decreased and wave period increased. Mean surf similarity values are higher on the day the first alongshore variability was observed (ξ_b =0.39) compared to that (ξ_b =0.3) on preceding days where no variability was observed. However, there appears to be no clear ξ_b threshold that can be associated with the post-reset emergence of alongshore variability.

3.4.2 Beach profile parameter Ω

Dimensionless parameter Ω (also referred to as dimensionless fall velocity or Dean number, *Dalrymple and Thompson* (1976); *Wright and Short* (1984); *Dean and Dalrymple* (2002)) incorporates wave height and period as well as sediment characteristics. Ω is frequently used to classify beach profiles and beach states and is given by:

$$\Omega = \frac{H_{s,b}}{w_s T_p}, \tag{3.4}$$

where w_s is the sediment fall velocity and T_p the peak wave period (*Wright and Short*, 1984).

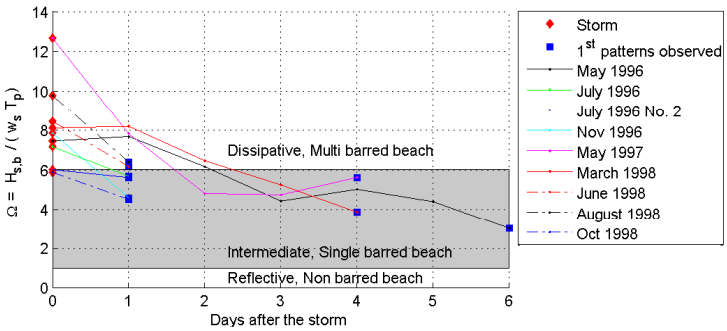

Figure 3.10: Post-storm wave conditions expressed as Ω with the *Wright and Short* (1984) thresholds for beach classification. Filled '◇' symbols represent the wave conditions on the days of the peak of the storm, squares represent the conditions on the days the first alongshore variability was observed.

A value of Ω equal to 1 is commonly adopted as the threshold between reflective beaches (Ω <1) and intermediate "barred" beaches (1 < Ω <6). Dissipative conditions are expected for Ω values higher than 6 (*Wright and Short*, 1984).

Daily averaged Ω values for the post-resetting storm periods are shown in Figure 3.10. In these estimates, a fall velocity w_s of 0.042 m/s was used, based on the grain size of 300 μm at Palm Beach (*van Rijn* (1993) equation for fall velocity), while wave height was taken as the significant breaker height $H_{s,b}$, following *Wright and Short* (1984).

At the peak of the storm, Ω values are high due to the large wave heights. In the period after the storm, Ω values decrease and conditions move from the dissipative regime towards the intermediate regime, which is generally associated with alongshore non-uniform (especially the RBB and TBR) beach states. In general, $\Omega < 7$ appears to be a necessary condition for the emergence of alongshore variability in the bar (Figure 3.10). It is noted, however, that Ω values are traditionally calculated using long term average values (i.e. yearly, seasonally or weekly averaged wave climate) reflecting quasi equilibrium beach behaviour. On shorter time scales the beach is more out of equilibrium making the use of Ω as an indicator of short term beach state less robust. Therefore, more investigation is required to verify whether the above $\Omega < 7$ threshold is universally applicable as a necessary condition for the emergence of alongshore variability in the bar. In addition to Ω, the absolute magnitude of the offshore forcing (i.e. incoming wave power) is proposed to be equally important for

the formation of alongshore variability on these shorter timescales (e.g. *Allen*, 1985; *Jiménez et al.*, 2008; *Smit et al.*, 2008). Post-reset periods with large T_v values are however observed to coincide with low as well as high incoming wave power conditions, such that no specific combination for T_v and incoming wave power could be found for the emergence of alongshore variability (not shown).

Besides being an indicator of beach state, Ω is also previously proposed as an indicator of accretive (onshore sediment transport) or erosive (offshore sediment transport) conditions over the active profile (e.g. *Larson and Kraus*, 1989). As alongshore variable morphology (RBB/TBR) is more likely to be associated with accretive conditions (*Lippmann and Holman*, 1990; *Ranasinghe et al.*, 2004), in the context of the present study, an Ω threshold for the emergence of post-reset alongshore variability may well exist. The threshold separating offshore and onshore transport has been investigated extensively. Several different Ω-like parameters and thresholds have been proposed (e.g. *Larson and Kraus*, 1989; *Dalrymple*, 1992; *Seymour and King*, 1982), based on ratios among wave height, period and a profile slope or fall velocity. Multiple methods were tested in the present study, giving similar results and thus the analysis related to only one of the Ω-like thresholds is described below.

Larson and Kraus (1989) reported that erosive profiles are found if $S_0 < 0.0007\Omega^3$. Here, wave steepness offshore $S_0 = H_0/L_0$ was calculated using deep water wave length $L_0 = g/(2\pi)T^2$. The threshold $S_0 < 0.0007\Omega^3$ was obtained by using numerous erosive and accretive profiles, either from 2-dimensional wave tank experiments (*Larson and Kraus*, 1989) or field measurements under predominantly shore-normal wave conditions (e.g. *Hattori*, 1982). To compare the observations at Palm Beach under mostly obliquely incident waves with the threshold determined from these studies with shore-normal waves, the measured offshore wave height H_0 was translated to a representative shore-normally incident 'offshore' wave height $H_{0s.n.}$. Thus, offshore wave heights were scaled with a refraction factor, compensating for the loss of wave height due to refraction from the wave buoy to the edge of the surf zone:

$$H_{0s.n.} = \frac{1}{K_r} H_0 = \sqrt{\frac{\cos\theta_0}{\cos\theta_b}} H_0, \tag{3.5}$$

where K_r is the refraction factor based on the wave angle θ and subscript 0 and b denote offshore and breakpoint values respectively. Offshore wave height H_0 was taken as the mean wave height H_m as suggested by *Larson and Kraus* (1989) for field data. The evolution of this parameter from the day of the storm to the day alongshore variability first emerged is shown in Figure 3.11

for the 9 events. The erosion/accretion threshold proposed by *Larson and Kraus* (1989) is also shown.

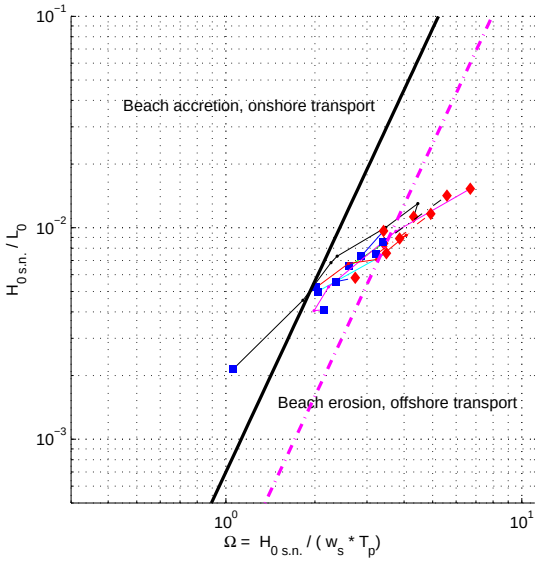

Figure 3.11: Wave steepness vs dimensionless fall velocity Ω. Filled '$\diamond$' symbols represent the days of the storm, squares represent the day the first alongshore variability was observed. Thick line shows the empirically determined threshold between erosive and accretive profiles $S_0 = 0.0007\Omega^3$. Magenta dashed line shows the newly proposed threshold $S_0 = 0.0002\Omega^3$. Legend similar to Figure 3.10.

Figure 3.11 shows that the storm days and most of the post-storm days are in the beach erosion zone of the graph. This indicates that the first alongshore variability emerged under energetic and erosive wave conditions. This is to be expected as the wave heights in the days immediately following the storms were well above the yearly mean wave height of 1.59 m at Palm Beach. The threshold criterion $S_0 = 0.0007\Omega^3$ therefore cannot be used to differentiate between storm days and days when the first patterns were emerging. Other thresholds of accretive and erosive profiles proposed by *Larson and Kraus* (1989) and *Dalrymple* (1992) gave similar results (not shown). Days of erasure and re-emergence of variability are however clearly clustered and therefore a different threshold, $S_0 = 0.0002\Omega^3$, is proposed which delineates these conditions. Storm days and days when the first patterns were observed are well separated by the new threshold. The scatter between different storm events is likely due

to the antecedent morphology and post-storm profile which varies from one post-storm period to the other.

3.5 Conclusions

Previous numerical modelling studies have significantly improved our understanding of post-storm re-emergence of alongshore morphological variability. However, the lack of field validation of the results obtained in these modelling studies leaves some uncertainty regarding the conclusions drawn therein. The study in this chapter exclusively used field data to investigate the complex phenomenon of post-storm re-emergence of alongshore morphological variability and provides new insights and qualitative validation of the conclusions drawn in previous modelling studies. In this study, four years of Argus video images and wave data obtained at Palm Beach, Australia were analysed with the primary objective of investigating the impact of wave height, wave period, wave angle and frequency bandwidth on the formation time T_v of post-reset alongshore variability.

Analysis of the reset events for which high quality data were available during the 4 year study period confirmed the previous model derived observations that (a) there is no clear dependency of T_v on wave height or wave period, and (b) there is a clear dependency of T_v on wave angle such that large T_v's coincide with very oblique wave angles. The data also suggested a dependency of T_v on frequency bandwidth such that large (small) T_v's coincide with the prevalence of wide (narrow) banded sea (swell) wave conditions after the resetting storm, a phenomenon that has not been reported to date. These observations indicate that shore-normal or moderately obliquely incident, narrow banded swell waves represent preferential conditions for the rapid post-reset emergence of alongshore topographic variability.

Analysis of the post-storm temporal evolution of two commonly used bulk parameters; surf similarity parameter ξ_b and beach profile parameter Ω, indicated that both of these parameters maybe useful in predicting the emergence of post-storm emergence of alongshore variability. ξ_b shows a shift from spilling breakers (during the storm) to plunging breakers when alongshore variability emerges. The data analysis also indicated that $\Omega < 7$ appears to be a necessary condition for the post-reset re-emergence of alongshore variability, and suggested a new criterion of $[S_0 \leq 0.0002\Omega^3]$ to predict conditions favoring the post-storm emergence of alongshore variability.

Acknowledgements

The author would like to thank Graham Symonds (CSIRO, AU) for collecting the Palm Beach images and Leo Pape / Gerben Ruessink (Utrecht University, NL) for developing the BLIM toolbox. The NSW Office of Environment and Heritage and Manly Hydraulics Laboratory are acknowledged for providing the Sydney wave buoy data. Furthermore the anonymous reviewers are thanked, their comments on a submitted version of this manuscript improved its quality greatly.

Large scale very low frequency (VLF) surf zone eddies are previously hypothesised to be important for the formation of alongshore topographic variability. Moreover, these VLF motions are of importance for the presence and strength of transient circulations and rip currents. The next chapter examines what determines the magnitude of VLF motions, and investigates their presence at the Dutch coast. The effect of VLF motions of different magnitudes on the emerging topographic variability will be discussed in Chapter 5.

Abstract Chapter 4
Very low frequency surf zone (VLF) motions are thought to be important for redistribution of nutrients and sediment as well as swimmer safety. Moreover, these motions are previously hypothesised to be related to the initiation of topographic variability. Traditionally, these motions have been observed in the presence of strong alongshore currents, at swell dominated open-ocean beaches (e.g. US west coast, West Australia), or both. There is no evidence of the existence of such motions at marginal seas with wind-sea wave fields in absence of a strong current.
Results of a field experiment at Vlugtenburg beach are presented, showing the presence VLF motions also at a Dutch beach with its short period wind-sea climate. To examine the effect of the type of wave climate in more detail, VLF observations acquired during an extensive field campaign at Duck, NC, USA are re-analysed. Results from the Duck data analysis show that VLF motions are indeed stronger under longer period, narrow frequency spread (swell) waves as found at open-ocean beaches.
These findings are confirmed with conceptual model simulations where the characteristics of the offshore wave forcing are varied independently. Additional computations also reveal that the slope of the surf zone near the breakpoint largely determines the magnitude of the wave group driven VLF motions. This provides an explanation for the presence of VLF motions observed at Vlugtenburg beach under wind sea conditions, as the beach slope at the time of the campaign was steep.
Overall, the findings imply that VLF motions are generally weak at a wind sea dominated coasts. Substantial VLF motions can however still be found when the profile is very steep, for instance after installation of a nourishment.

Novel items in Chapter 4 are:

- The observation of VLF surf zone motions at the Dutch coast in absence of a strong mean longshore current.
- The discovered dependency of vortical VLF motions on wave period and frequency spread of the incoming wave field.
- The discovered dependency of vortical VLF motions on the cross-shore slope of the beach near the breakpoint.
- The clarification for part of the spread in observed VLF magnitude at a given wave height.

4

Surf zone velocity fluctuations on the very low frequency timescale

4.1 Introduction

Very low frequency (VLF) motions are slowly varying current fluctuations with timescales larger than 250 seconds ($f < 0.004$ Hz). Substantial current fluctuations on this VLF timescale have been observed mostly inside and close the surf zone (e.g *Vos*, 1976; *Smith and Largier*, 1995; *Brander and Short*, 2001; *Johnson and Pattiaratchi*, 2004; *MacMahan et al.*, 2004, 2010b). The presence of these surf zone velocity fluctuations can pose a risk to ocean bathers as offshore velocities can vary with as much as 0.5 m/s on the timescale of minutes, resulting in amplification of existing rip currents or the generation of temporal 'transient' rip currents (*Vos*, 1976; *Johnson and Pattiaratchi*, 2004; *MacMahan et al.*, 2006).
Typical spatial and temporal scales of VLF motions are of O (100 m) and O (10 minutes). Because for most of the velocity fluctuations in the VLF frequencies the ratio between observed alongshore length scale k_y and frequency f falls outside the free surface gravity wave range (based on linear dispersion), these motions are assumed to be vortical (eddy-like) motions rather than propagat-

ing wave like motions (*MacMahan et al.*, 2010b). This eddy-like behaviour of VLF velocity fluctuations is found to affect the mixing of material such as larvae, nutrients and pollutants inside the surf zone (*Spydell et al.*, 2007; *Spydell and Feddersen*, 2009) as well as the exchange of material between the surf zone and the shelf (*Reniers et al.*, 2009, 2010).

VLF velocity fluctuations have been attributed to 2 different mechanisms: current instabilities and temporal variations in wave forcing.
Current instabilities are in general observed under oblique incident waves, which generate a wave driven alongshore current in the surf zone. The strong cross-shore shear in alongshore flow can result in meandering of the current and eddy shedding on the VLF timescale (e.g. *Bowen and Holman*, 1989; *Oltman-Shay et al.*, 1989; *Aagaard and Greenwood*, 1995; *Dodd et al.*, 2000; *Miles et al.*, 2002; *Noyes et al.*, 2005). Similarly, strong cross-shore flows in rip channeled bathymetries can show energetic low-frequency oscillations, a mechanism referred to as rip current instability (*Haller and Dalrymple*, 2001). For shore-normal incident waves and in the absence of an alongshore current, VLF velocity fluctuations are thought to be primarily generated by temporal variations in wave height, yielding oscillation of existing 2D horizontal circulations (ripcells) (*MacMahan et al.*, 2004) and finite crest length wave breaking (generating turbulence which cascades to larger length scales) (*Peregrine*, 1998; *Spydell and Feddersen*, 2009). The latter mechanism of variations in wave forcing is however not restricted to normal-incident waves only and *Long and Özkan-Haller* (2009) recently suggested that VLF motions observed under oblique incident waves are a combination of both mechanisms.
The origin of mechanism first discussed above, the temporal and spatial variability in wave forcing, is the directional and frequency spread in the incoming wavefield. As this spread is present in all natural wave fields to some degree, *MacMahan et al.* (2010b) hypothesise surf zone VLF motions to be ubiquitous even for conditions without strong mean currents.

There is however only limited knowledge on what determines the magnitude of these VLF velocity fluctuations for periods without longshore current. Observations show that the magnitude of such vortical VLF velocity fluctuations can vary significantly from day to day (*MacMahan et al.*, 2004, 2010b). Maximum observed root mean squared magnitude for the VLF velocity fluctuations is of O (0.5 m/s) (*MacMahan et al.*, 2004) and magnitude of the VLF motions was found to increase under higher incident waves. Yet, for a given offshore wave height at a single beach, the existing observations of VLF magnitude show a large scatter (*MacMahan et al.*, 2010b, their Figure 4).

Reported strong VLF observations in the absence of a mean alongshore current are from open ocean beaches with medium to long wave periods (US

east coast, *Smith and Largier* (1995); *MacMahan et al.* (2004), US west coast, *MacMahan et al.* (2010b) and Australia, *Johnson and Pattiaratchi* (2004)). However, at a beach with short wave periods (T of 3-6 s) on the Israeli Mediterranean coast, *Bowman et al.* (1988) find no pulsations in their observations.

As the presence of VLF motions has been explained from the (directional) spread in the wave field it is hypothesised here that the type of wave conditions, swell or wind sea, affects the magnitude of the VLF velocity fluctuations in absence of strong longshore current. Long crested swell is expected to yield to stronger VLF motions than wind sea with short-crested, peaky waves. A similar hypothesis was hinted at by *Vos* (1976), reporting apparently stronger VLF flow pulsations under moderate swells based on his visual observations (from a surfboard). This was however never further substantiated with measurements.

The hypothesis however also implies that VLF motions due to temporal variations in wave forcing might not be very large at the Dutch coast due to the mostly wide banded, short period wave conditions[1]. What is needed is a study investigating what factors affect the magnitude of VLF velocity fluctuations in absence of strong alongshore currents and examining whether strong VLF motions are restricted to open ocean beaches.

The objectives of the current chapter are therefore twofold:

- To examine whether VLF motions are also present at the Dutch coast in absence of strong longshore currents, and more generally,
- to investigate to what extent the magnitude of VLF motions in absence of longshore currents is affected by the type of wave conditions.

These objectives are addressed in the following sections.

4.2 Observations of VLF motions at the Dutch coast

The aim of the measurement campaign reported in this section was to investigate surf zone VLF motions at the Dutch coast, and especially for conditions without strong longshore current.

In the experiment campaign the opportunity is taken to examine the capabilities of a horizontal looking Acoustic Doppler Current Profiler (hADCP hereafter) in the surf zone. Similar to a regular ACDP, the Doppler effect is

[1]VLF motions generated by longshore current instability are not regarded here. The presence and magnitude of VLF motions at the Dutch coast generated by this mechanism were reported by *Miles et al.* (2002).

used to measure current velocity in bins along separate beams. Velocity is measured parallel to the beam and by using 2 (or more) beams pointing in different directions it is possible to combine beam-parallel velocities to a profile of 2D or 3D orthogonal velocities. Horizontal looking ADCPs typically have all beams aligned in a horizontal plane, thus providing a profile of 2D velocities in the horizontal plane. Velocity profile length ranges between 20 m and 100 m, depending on the instrument and settings. Since the velocities of spatially separated beams are combined to compute the orthogonal velocity vectors, it is assumed that the velocity is more or less uniform across the beams. Therefore hADCPs are typically applied in river situations (e.g. *Kamminga et al.*, 1998; *Hoitink et al.*, 2009). One of the recent field campaigns experimenting with a hADCP in the coastal region by *Castelle et al.* (2009) showed promising results especially for the mean flow velocities, revealing strong shear in flow in the vicinity of a rip channel. In the present study it will be tested if a hADCP is also capable to measure signals with timescales smaller than 30 minutes.

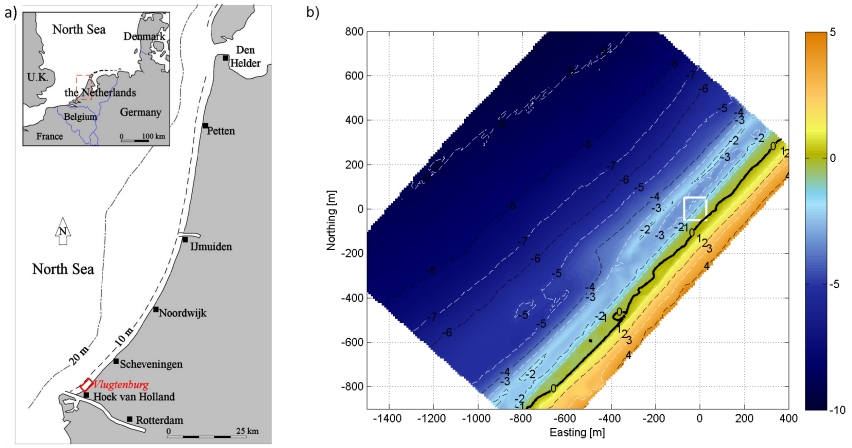

Figure 4.1: a) Location map of Vlugtenburg beach and b) Bottom topography at Vlugtenburg beach during the experiment. Colors indicate elevation in meters with respect to NAP. Local coordinate system (0,0) at the instrument frame. White box is the measurement area (Figure 4.2 a).

4.2.1 Field experiment

Field site

The measurements are obtained at Vlugtenburg beach, as part of the UNESCO-IHE field campaign *'REDNEX2010'* in June 2010. The field site, Vlugtenburg beach, is close to the town of Hoek van Holland on the west part of the Dutch coast (Figure 4.1) and discussed in more detail in Chapter 2. The topography in the area near the instruments is surveyed during the field campaign on a fine transect spacing of 10 m. The larger 'meso-scale' topography is measured as part of the nourishment monitoring study using 22 transects about 80 m apart (see Figure 2.4). Topography measurements are executed with a jetski-based survey system for the subaqueous zone, complemented with RTK-GPS backpack surveys on the sub-aerial beach (see Appendix A). The bottom topography at the time of the experiment was characterised by a single subtidal bar with a barcrest at -2 m NAP and an offshore location of approximately 70 m from the low water line (Figure 4.1 b). NAP indicates here the Dutch Ordnance Datum, which is close to mean sea level. Mean slope of the beachface below the low water line (-3 to -1 m NAP) is around 1:20. The topography is mostly alongshore uniform with small alongshore variability in the beach slope present around the -2.5 m NAP isobath (Figure 4.2 a).

Instrumentation

Waves and currents are measured during the experiment using a *Nortek* 600 kHz hADCP and a *Nortek* 2000 kHz High Resolution upward looking ADCP (HR profiler hereafter) on a single measurement frame installed near the low water line (Figure 4.2).

The *Nortek* hADCP records velocities in 9 bins along the beam axis with a bin size d_{bin} set at 5 m. The two transducer beams have a separation angle of 50 degrees (Figure 4.2, red lines). Velocities measurements per bin i are hence obtained at the following horizontal coordinates ($x_{\text{hADCP}i}$,$y_{\text{hADCP}i}$) with respect to the instrument:

$$x_{\text{hADCP}i} = \pm\{(i-0.5)d_{\text{bin}} + d_{bl}\}\sin(\theta/2), \tag{4.1}$$

$$y_{\text{hADCP}i} = \{(i-0.5)d_{\text{bin}} + d_{bl}\}\cos(\theta/2), \tag{4.2}$$

where ($x_{\text{hADCP}i}$, $y_{\text{hADCP}i}$) are defined from the transducer head, and direction y is the viewing direction of the instrument (exactly in between the 2 beams). Blanking distance d_{bl} equals 0.5 m. As can be seen from Eqns. 4.1 and 4.2, the farthest velocity points ($i = 9$) are located at points (+/- 18.2, 39.0) meters

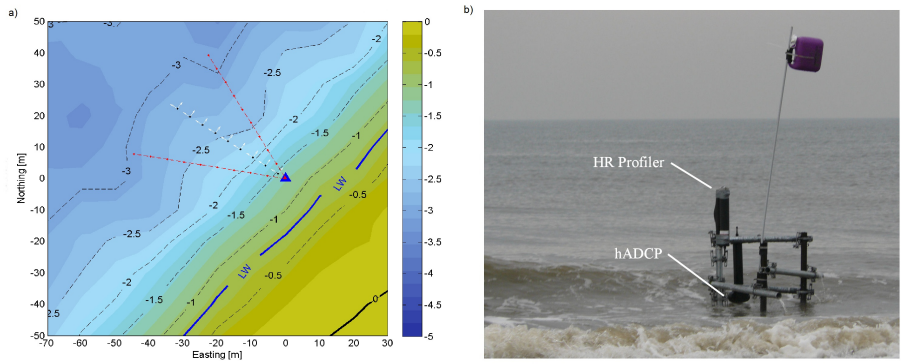

Figure 4.2: a) Detailed bottom topography near the measurement frame (blue triangle) with the sensors on June 8^{th}. Colors and contours show elevation in meters NAP, approximate low water elevation given by the thick blue line. Red lines indicate the two individual beams of the hADCP, black dots show the location of computed cross and alongshore velocity points. b) Measurement frame at low tide on Tuesday June 8^{th}. The purple can serves as a buoy, mounted slightly outside the beams of the HR profiler.

from the instrument. Velocity measurements are obtained at these points and only parallel to the beam direction. Orthogonal velocities $(u_{\mathrm{hADCP}}, v_{\mathrm{hADCP}})$ are then obtained by combining the along beam velocity measurements in both beams, creating a 'virtual' velocity observation in between the two beams (Figure 4.2, black dots). Consequently, as cross and alongshore velocities are derived from the beam velocities, relatively uniform conditions are required in direction parallel to the instrument especially for the furthest bins.

The two individual beams fan out with a total beam angle of 4 degrees. As a consequence of this beam angle, positioning of the instrument close to the water surface or bottom results in beams intersecting the water surface or bottom and the best range is found when the instrument is positioned at mid-water depth. As a reference, if the transducer is mounted 1 m under the water level, the beams will intersect the water level when the profile exceeds 28 m.

The HR profiler was set up to measure in 44 bins of 1 cm in the upper part of the water column around high tide. The blanking distance is set at 10 cm. Its internal pressure sensor was used to record the water level above the instrument. All instruments recorded at 1 Hz.

Selected field days

The field campaign spanned 6 days in total, of which two selected field days are discussed hereafter. The offshore wave and wind conditions as well as the position of the instruments are listed in Table 4.1. The first day of observations presented is Tuesday June 8^{th}. The offshore wave station recorded waves with a significant wave height H_s of 0.60 m arriving from the north (40 degrees oblique with respect to shore-normal). The measurement frame was installed close to the -1.5 m NAP isobath (Figure 4.2 a). As such, at high water on June 8^{th}, the instrument frame was positioned in a water depth of over 2 meters. Based on the water depth and small wave height (as well as visual observations), the instruments were positioned outside the surf zone. The hADCP was oriented approximately cross-shore, and its profile spanned 39 m between the beach and the subtidal bar (towards the -3 m NAP depth contour, Figure 4.2 a). On the second day presented here, Sunday June 13^{th}, waves were larger (H_s of 1.4 m) and instrument frame is placed higher up the profile in the intertidal zone. As a result the measurements are inside the surf zone. The hADCP was mounted looking alongshore across a small rip channel.
Surf zone width was small on June 8^{th} and located close to the shoreline (i.e. no breaking on an offshore bar), whereas the larger wave heights on June 13^{th} resulted in a wider surf zone (see Figure 4.3 for snapshots of the local beach camera).

Table 4.1: Instrument setup and offshore conditions

	Selected days	
	June 8^{th}	June 13^{th}
High water at Scheveningen	12:20, +0.92 m NAP	16:40, +1.08 m NAP
Bottom level at frame	-1.30 m NAP	-0.61 m NAP
Transducer height hADCP	-0.75 m NAP	0.30 m NAP
hADCP orientation	Looking cross-shore	Looking alongshore
Transducer height HR	0.09 m NAP	0.48 m NAP
Offshore wave height H_s	0.60 m	1.4m
Offshore wave period T_{m02}	5 s	6 s
Offshore wave direction	North	North
Wind at Hoek van Holland	Up to 15:00 5 m/s South, after 15:00 2 m/s North	3 m/s Northwest
Position	*Outside the surf zone*	*Inside the surf zone*

Figure 4.3: Beach camera snapshots during low tide on June 8^{th}(left) and on June 13^{th} (right). Two persons near the waterline in the right image are installing the measurement frame.

4.2.2 Processing the timeseries

The recorded time series of the hADCP are first transformed from the beam coordinate system (v_1,v_2) to the orthogonal instrument coordinate system (u_{hADCP}, v_{hADCP}), including a compensation for the pitch and roll of the instrument. Velocities in the instrument coordinate system are then rotated to a coordinate system perpendicular to the coastline giving cross and alongshore velocity timeseries (u,v). HR profiler velocities were rotated in the horizontal plane to match the coordinate system of the hADCP. In this shore perpendicular coordinate system alongshore velocities are positive to the south and cross-shore velocities are positive offshore. Next, the data are quality controlled on two aspects. Since the instruments are in the very nearshore, measurements can be corrupted by bubbles and the instrument transducer and beams intersecting with the water surface. The returned signal strength (or amplitude) of the signals is used to eliminate bad observations. Good velocity measurements are typically characterised by a high signal strength which monotonously decreases in the bins further from the instrument. Points are removed with: 1) low signal strength or 2) non-decreasing (i.e. increasing) signal strength with respect to the bin closer to the instrument. To avoid a bias (towards low velocity periods), velocity data within 10 seconds of a corrupted velocity measurement are also removed.

Movement of the instruments during the experiment is checked with the internal heading and tilt data. During the last day of the experiment, June 13^{th}, the instruments were subject to heavy wave impact at mid tide while being partly submerged. Recordings show a slight rotation of the instrument during this mid tide period. Since the data during this period are already removed due to bubbles, no extra filtering is performed using the heading

and tilt data. Other than this period at mid tide, changes in tilt or heading remained in the order of 0.1 degrees.

Quality controlled velocity signals of both instruments are then separated into 4 different timescales:

1. Mean flow velocity patterns (tide), timescale T > 30 minutes,
2. Very low frequency (VLF) motions, 30 min > T > 250 seconds,
3. Infragravity (IG) velocities, 250 s > T > 25 s, and
4. Short wave (SW) orbital motion. T < 25 s.

Separate velocity signals are acquired by filtering the data with cutoff frequencies at 0.00055, 0.004 and 0.04 Hz corresponding to the timescales mentioned above. Short wave motion is expressed with velocity spectra obtained by performing a Fast Fourier Transform for the wind wave frequencies. Non-grassy spectra are obtained by calculating and averaging over 24 spectra, each representing 5 minutes, where the 5 minute input is first detrended to remove the influence of the mean flow on the velocity spectra. Since the waves are not traveling exactly shore-normal, total velocity spectra are computed using both cross and alongshore velocities and then combined.

4.2.3 Results

Results are shown for the two selected days of the field campaign, the first with small waves, causing the instruments to be just outside the surf zone. Next, a day is shown with high energy wave conditions with the instruments inside the surf zone.

A. Outside the surf zone

On Tuesday June 8^{th} the instruments are mounted well under the high tide level (Table 4.1), resulting in observations over a large part of the high tide period. The maximum water level over the transducer was over 1.5 m at high tide and a full profile (39 m) with good signal strength was obtained at this time. At mid tide water level was lower, and the furthest hADCP bins reflected against the water level. The HR profiler recorded 4 hours of velocities and pressure observations. The low passed measurements are shown in Figure 4.4. In these results all high frequency velocity and pressure signals due to waves and infragravity waves are filtered out, leaving only observations with periods of 250 s and larger (i.e. mean flow and VLF motions). Figure 4.4a shows the water level as calculated from the low passed HR pressure signal. Tidal amplitude corresponds well with the tidal gauge recordings at Scheveningen harbor. High water is slightly earlier in time in the observations at Vlugtenburg than

at Scheveningen, which can be attributed to the northward propagation of the tidal wave along the coast and the 13 km distance between the sites. The low passed alongshore hADCP velocities for closest, middle and farthest bin (resp. 3, 16 and 39 m from the instrument, Figure 4.2) are shown in Figure 4.4b. Alongshore velocities are negative (northward) during high tide, caused by the northward tidal current. During ebb, the direction of the tidal current reverses and becomes southward oriented. In the bins farther from the instrument alongshore velocities are larger as the tidal flow becomes more important in the trough between the beach and the subtidal bar. The shear in the alongshore current is substantial; flood current at the end of the profile (at -3 NAP) is up to 0.39 m/s, while close to the instrument (at -1.5 m NAP) the velocity is at maximum 0.2 m/s. Cross-shore velocities in both instruments (Figure 4.4 c) are very limited (< 0.05 m/s), indicating that the coordinate system is aligned well with the local alongshore flow. Although both instruments measure at different locations in the horizontal (2.7 m apart) and vertical (0.95 m apart), low frequency flow observations of the first bin of the hADCP correspond well with measurements of the HR profiler if compared visually (Figure 4.4).

The low pass velocities presented in Figure 4.4 show small velocity fluctuations with periods larger than 250 s. At high tide the low passed velocities show no oscillations, and at mid tide (before 11:00 and after 14:00) small oscillations can be observed in the velocity signal. The magnitude of these fluctuations on the VLF timescale (250 s $<$ T $<$ 30 min) is however very limited ($u_{\mathrm{VLF,rms}} <$ 0.05 m/s). The oscillations could well be wave group induced VLF motions or instabilities of the longshore current as the magnitude increases once the instruments are located closer to the surfzone at mid tide, but due to the limited magnitude of the signal other explanations such as wind fluctuations cannot be excluded.

B. Inside the surf zone

On Sunday June 13^{th} the instruments are mounted higher in the water column (see Table 4.1). The hADCP was oriented looking alongshore, across a small rip channel. This alongshore orientation of the hADCP proved not beneficial within the surf zone. As the water depth is limited, only the first bin of the profile contained good quality data. For bins further away from the instrument, beams intersected with the water surface (under the wave troughs) or the bottom. The intended alongshore profile over the rip channel was therefore not obtained.
Pressure signal of the HR profiler showed 1 hour undisturbed measurements around high tide with wave heights of approximately 1 m at the frame. Outside

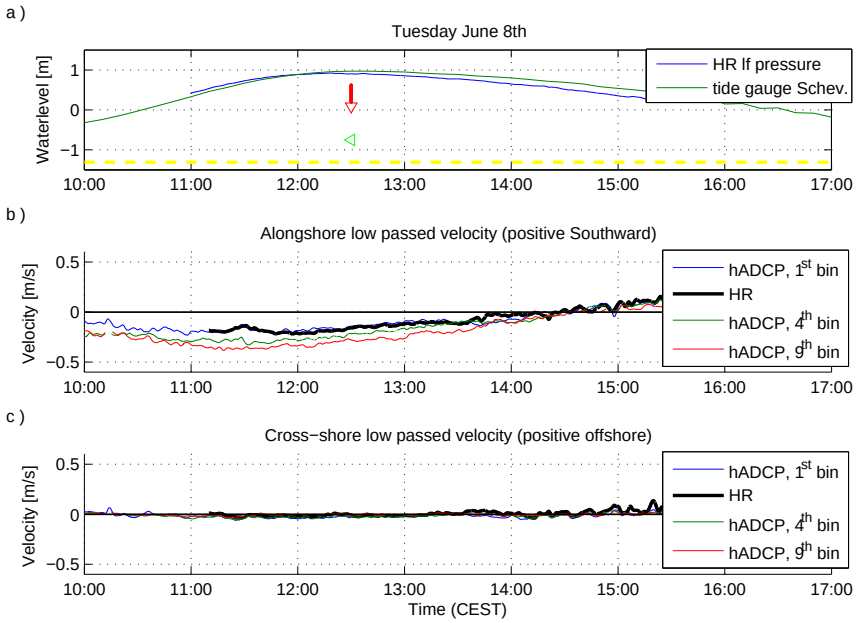

Figure 4.4: Low passed (T > 250s) measurements outside the surf zone on Tuesday June 8^{th}. a) Water level recorded at the frame (blue line) and the water level recording at the nearby harbor of Scheveningen (green). Position of the instruments given at high water; HR profile is given in red, hADCP transducer given by the green triangle. Approximate bottom level given by the yellow dashed line. b) Alongshore and c) cross-shore velocities of the 1^{st},4^{th} and 9^{th} bins of the hADCP (blue, green and red) and HR profiler (black).

this period wave troughs were occasionally reaching the transducer level, and corrupting the measurements. Overall, the best quality data was measured in the first (lowest) bins of the HR profile. Low passed signals (T > 250 s) for both instruments are shown in Figure 4.5.

During the high tide the alongshore velocity fluctuates around zero as the southward wave induced current in the surf zone and northward flood tidal flow are in balance (Figure 4.5). As the tide level and flood current decrease, the southward wave driven current becomes dominant resulting in positive (southward) alongshore velocities. Measurements of alongshore currents of the HR profiler and the hADCP show a very good visual correspondence.

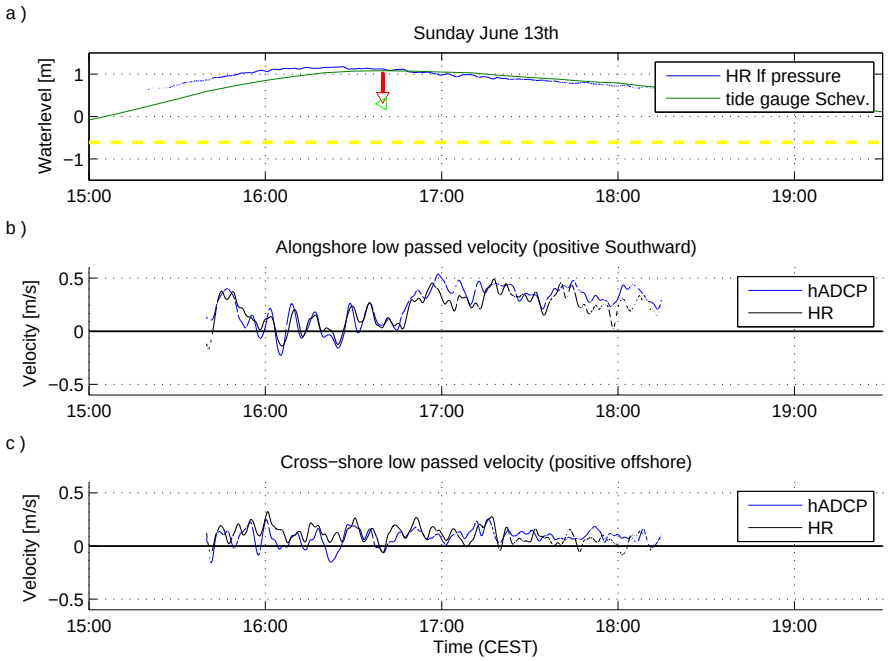

Figure 4.5: Low passed (T > 250s) measurements inside the surf zone on Sunday June 13^{th}. a) Water level recorded at the frame (blue line) and the water level recording at the nearby harbor of Scheveningen (green). Position of the instruments given at high water; HR profile is given in red, hADCP transducer given by the green triangle. Approximate bottom level given by the yellow dashed line. b) Alongshore and c) cross-shore velocities of the 1^{st} bin of the hADCP (blue) and HR profiler (black). Note that measurements with poor quality are removed, causing the signal gaps towards the beginning and end of the recording.

Cross-shore velocity signals show similar oscillations, yet there is some deviation between the data from both instruments. The orientation of the hADCP (looking alongshore) leads to a mismatch in cross-shore velocities as the two transducer beams fan out in the cross-shore and the derived cross-shore velocity (based on vector addition of two beam velocities) is measured at different water depths. Alongshore flow is believed to be more uniform, yielding to a better comparison of both instruments.

The velocity signals reveal substantial oscillations with timescales of O (10

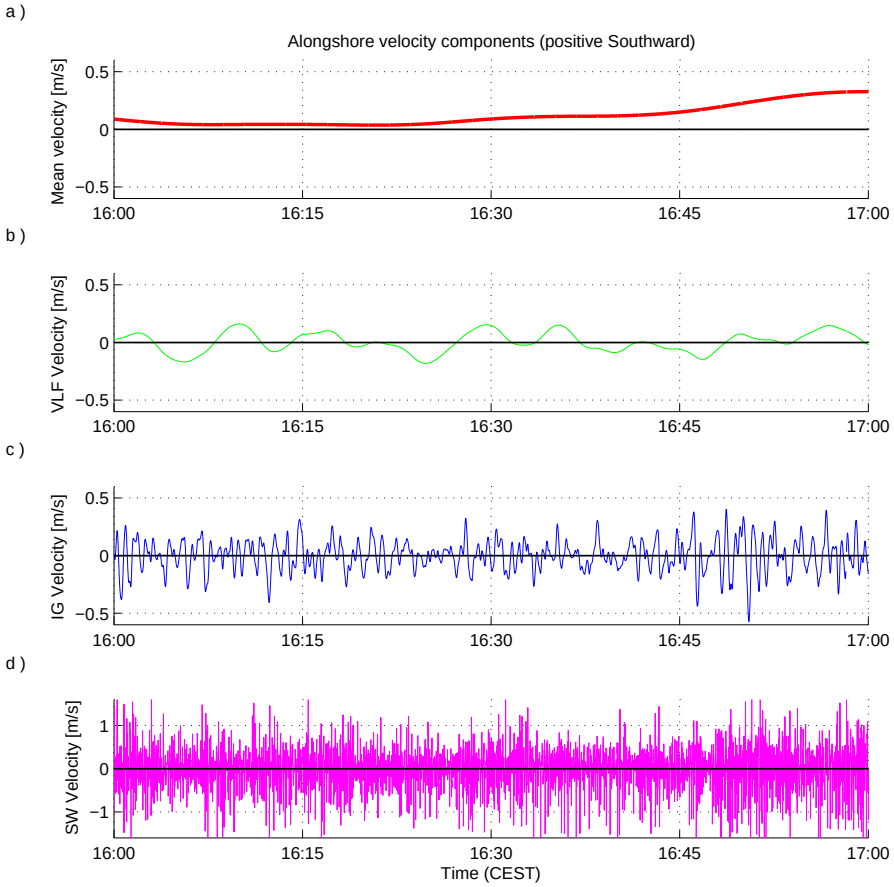

Figure 4.6: Alongshore flow measured with the HR profiler on Sunday June 13^{th} separated in four different velocity bands. a) mean flow (T > 30 min) b) VLF flow (30 min > T > 250 s) c) Infragravity flow (250 s > T > 25 s) and d) short wave (orbital) flow (T < 25 s).

min). To assess the magnitude of these oscillations with respect to the short wave energy, the velocity signals for the period around high tide (16:00 to 17:00) are depicted for the four different frequency bands in Figure 4.6. The root-mean-square (rms) velocities in the time period 16:00 to 17:00 for the VLF, infragravity and short wave band are 0.09, 0.13 and 0.49 m/s respectively

(Figure 4.6). Very low frequency velocity fluctuations were thus of similar order of magnitude as the infragravity fluctuations. The observed magnitude in the VLF band of O (0.1 m/s) is similar to the values reported at Duck, USA (see *MacMahan et al.*, 2010b). As both instruments show similar velocity fluctuations and the data is thoroughly quality checked, the observed fluctuations are thought to be physical rather than instrument errors.
VLF motions were found under minimal mean alongshore current, and could therefore well be forced be wave group action, as hypothesised by (*MacMahan et al.*, 2010b). However, since measurements are from a single point, it cannot be determined whether fluctuations also (partly) originate from strong shear in an alongshore current onshore (at the beach face) or offshore (at the sub-tidal bar crest) of the measurement frame.

C. Comparison hADCP vs HR profiler

The quality of the hADCP in the nearshore coastal region is quantified by comparing the hADCP data with the HR data. Since the velocity measurements from the instruments are obtained at slightly different locations, a direct comparison of the recorded timeseries of both instruments is not possible. Instead, measured velocities are compared on slow and fast timescales separately.

First the difference in low pass filtered (T > 250 s) results of both instruments is quantified for both days (Figure 4.4 and 4.5). Hereto the HR signal and the first bin of the hADCP are compared. Two values are computed, the mean difference between the two instruments and the Signal to Noise (SNR) ratio (e.g. *Castelle et al.*, 2009), given by:

$$SNR = \{\sigma(u_{j,\mathrm{HR}})/\sigma(u_{j,\mathrm{HR}} - u_{j,\mathrm{hADCP}})\}^2 , \tag{4.3}$$

where subscript j denotes either the cross-shore or alongshore direction. Mean deviation and signal to noise values for the low passed signals are given in Table 4.2. Mean deviation between measurements of both instruments is very low compared to the flow velocity. The measurements inside (June 13^{th}) and outside (June 8^{th}) the surf zone show mean deviations and SNR values of the same magnitude. Inside the surf zone the SNR values are slightly lower, possibly due to the large spatial variations in velocity in this zone. Cross-shore motions are less accurate.

On short wave timescale (T < 25 s) the quality of the hADCP data is investigated using the measured velocity spectra. Only the observations of June 8^{th} outside the surf zone are used, for alongshore looking hADCP measurements on June 13^{th} cannot result in good velocity observations on the short wave

Table 4.2: Comparison instruments, mean and low frequency ($f < 0.004$ Hz) velocity

	Alongshore	**Cross-shore**
Tuesday June 8^{th} 12:00 to 15:00		
Mean deviation, $\mu(u_{j,\mathrm{hADCP}} - u_{j,\mathrm{HR}})$	0.002 m/s	-0.020 m/s
Signal to Noise ratio, SNR	5.5	1.6
Sunday June 13^{th} 16:00 to 17:00		
Mean deviation, $\mu(u_{j,\mathrm{hADCP}} - u_{j,\mathrm{HR}})$	-0.001 m/s	-0.065 m/s
Signal to Noise ratio, SNR	4.7	1.1

timescale due to the beam separation. The vertical offset between instruments makes direct comparison of the velocity spectra impossible. Therefore the velocity spectra are transformed into variance density spectra of the surface elevation using linear wave theory. Combined velocity spectra U_{f_i} are multiplied with a transfer function to attain surface elevation per frequency bin f_i, similar to *Guza and Thornton* (1980):

$$\eta_{f_i} = 2\pi f_i \sinh(k_i h)/\cosh(k_i(h - z_{td}))U_{f_i} \tag{4.4}$$

Where k_i is the wave number corresponding to each frequency f_i, h the water depth at the velocity point (as extracted from the topographic survey) and z_{td} the height of the transducer with respect to the water level. Calculated surface elevation spectra from the velocity measurements are shown in Figure 4.7.

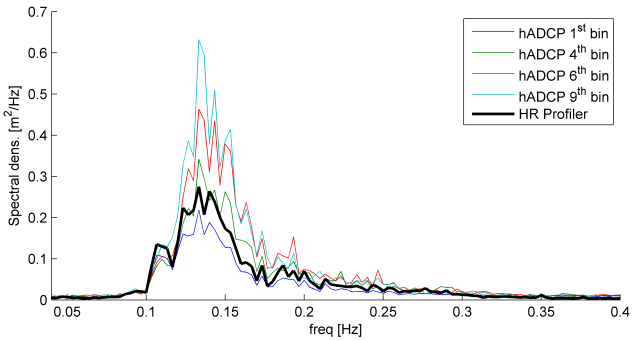

Figure 4.7: Variance density spectra of the short wave surface elevation spectra as measured on Tuesday June 8^{th} between 12:00 and 14:00 by different hADCP bins (colored lines) and the HR profiler (thick black line).

Spectra from all hADCP bins show a similar shape and distribution. Spectral density increases in the bins further from the hADCP, indicating a larger wave height measurement further offshore, as can be expected due to the refraction of waves. Results are quantified using wave height H_s calculated from the surface elevation spectra as:

$$H_s = 4\sqrt{m_0}, \tag{4.5}$$

where m_0 is the zeroth-order spectral moment of the spectrum. Significant wave heights computed from the spectrum are shown in Table 4.3.

The spectrum derived for the first bin of the hADCP is slightly smaller than the spectrum obtained from the HR profiler (Figure 4.7). Consequently the first bin value of the hADCP shows a small (6%) underestimation of the wave height, assuming wave height obtained with HR profiler at the frame is near correct. An underestimation could well be due of the large bin size (5 m) relative to the wave length of O (20 m) in this region. Mean period T_{m02} based on the measurements of the hADCP and HR profiler are 5.0 and 5.4 s respectively, resembling the wave period measured offshore (Table 4.1)

Table 4.3: Comparison instruments, wave height derived from high frequency velocity

Tuesday June 8th 12:00 to 14:00						
	HR Profiler	hADCP 1^{st} bin	hADCP 4^{th} bin	hADCP 6^{th} bin	hADCP 9^{th} bin	Offshore Station
Wave height H_s [m]	0.52	0.49	0.58	0.66	0.69	0.68

4.2.4 Conclusion observations of VLF motions at the Dutch coast

The objective of the present section was to investigate the presence and magnitude of very low frequency (VLF) motions at the Dutch coast. Secondly the opportunity was taken to test the potential of a horizontal ADCP in the nearshore.

Measurements of two separate instruments showed the presence of substantial VLF oscillations on one of the field days. The observed root-mean-squared velocity of the oscillations in the VLF frequencies was 0.09 m/s, which is of similar order of magnitude as values reported by *MacMahan et al.* (2010b) at Duck, USA. This finding implies that the VLF oscillations in absence of strong alongshore current are not only reserved to ocean coasts with medium to long

period (T > 10 s) waves. On the field day when VLF motions were observed, waves were well aligned and long crested for Dutch standards. Future research will have to show if the VLF velocities are of equal magnitude under the more common shorter crested wind sea conditions.

Observations of the hADCP close to the instrument corresponded well with measurements using the upward looking HR profiler, especially for the low frequency part of the observations. The profiling capacity was found to be limited in the very nearshore as the large separation angle between the beams restricts the use to situations with uniformity in flow in the across profile direction perpendicular to the instrument. Similarly, horizontal vortical motions with a radius similar to the profile length of O (50 m) will be poorly reproduced by the furthest cells of the profile, since the conversion from beam parallel velocities to a profile of alongshore and cross-shore velocities will become troublesome. In general, a horizontal looking ADCP has shown to be of most value when deployed outside the surf zone, where 1) the flow is more uniform and 2) the beams intersect less with the water or bottom. In this region a hADCP can be an asset revealing both the shear in alongshore current as well as wave height transformation with a single instrument.

4.3 Magnitude of VLF motions under shore-normal waves, field observations at Duck, NC, USA

Surf zone VLF velocity fluctuations in absence of a strong longshore current have been observed at a few locations around the globe, mostly on open ocean coasts. Observations however show a large scatter in observed VLF motion magnitude, even for a single wave height at a given site (see *MacMahan et al.*, 2010b, their Figure 4). Little investigation has been executed to define which parameters affect the magnitude of these motions. The objective of the current section is therefore to investigate the magnitude of VLF velocity fluctuations using field data for various incident wave conditions and examine whether the magnitude is dependent on the type of wave conditions. Hereto the observations reported by *MacMahan et al.* (2010b) are re-analysed and separated into different incoming wave conditions. A restriction is made here for shore-normal incident waves to prevent the presence of large current related VLF motions.

4.3.1 Dataset description

The dataset used for the analysis was obtained during the 4 month SandyDuck '97 field campaign at Duck, NC, USA. During the experiment an extensive array of instruments was deployed in the nearshore, capable of capturing both the wave transformation as well as the surf zone hydrodynamics (*Elgar et al.*, 2001). The instrument data used for the forthcoming analysis was obtained from five alongshore arrays (A1 to A5) and a large cross-shore array (C1) of SPUV (collocated Sonar altimetry, Pressure and EM flow velocity u and v) sensors (Figure 4.8). The instruments recorded data in runs of 3 hours, sufficiently long to investigate motions on the VLF timescale.

Offshore wave conditions were recorded during the campaign by an array at approximately 8 m water depth and converted to two dimensional frequency-directional spectra by the Field Research Facility (FRF) (*Long and Atmadja*, 1994). The water depth at the SPUV gauges was obtained using the sonar altimeter data of the SPUVs combined with the tidal elevation recorded at the National Oceanic and Atmospheric Administration (NOAA) tide station located at the seaward end of the FRF pier (500 m east of the instrument array).

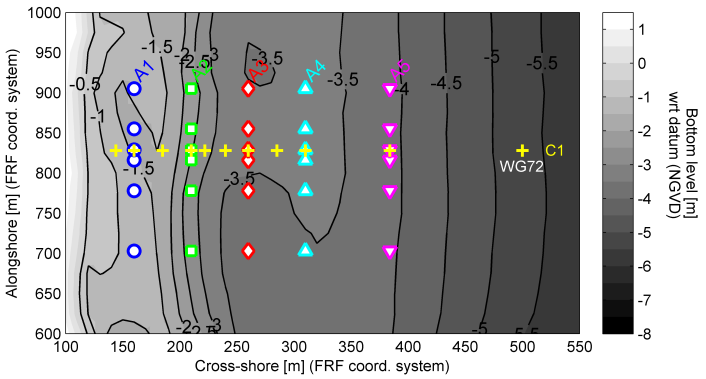

Figure 4.8: Overview of the SandyDuck instrument layout. Blue circles indicate SPUV locations of the most shoreward alongshore array A1, green squares show array A2. Large cross-shore transect of sensors C1 indicated by the yellow crosses. Bottom topography as measured on October 30^{th} 1997.

4.3.2 Data processing

The SPUV instrument data are processed as described by *MacMahan et al.* (2010b), but for completeness the methodology is briefly repeated.
During the 4 months of the SandyDuck campaign (i.e. about 950 time periods of 3 hours), a wide variety of forcing conditions passed. A first selection is made to eliminate periods with significant alongshore currents, hereby avoiding instants where VLF motions were generated and/or affected by alongshore current (shear) instabilities. Similar to *MacMahan et al.* (2010b), time periods were discarded when 0.25 m/s alongshore velocity or more was observed at any of the SPUVs in the cross-shore array C1. Approximately half of the time periods (440 bursts of 3 hours) remained after this selection.
The magnitude of the vortical VLF motions was calculated for the alongshore arrays A1 to A5. The alongshore coherent arrays used at SandyDuck enable an estimate of the alongshore length scale k_y of (low frequency) motions. In a 2 dimensional spectral analysis (Maximum Likelihood Estimator; see *MacMahan et al.* (2010b) and references therein) the recorded flow velocities were separated for each alongshore array into 2D energy spectra $G_{uu}(f, k_y)$ and $G_{vv}(f, k_y)$ of the cross and alongshore velocities respectively. These velocity spectra contain a segment with energy with small alongshore wavenumbers related to predominantly cross-shore motions of waves. The regions of the f, k_y

spectra with larger alongshore wavenumbers reflect alongshore traveling waves and vortical (eddy-like) motions. Vortical motions were separated using the shallow water dispersion relation ($k_y = \sqrt{f/gh}$, with h being the local water depth) as the boundary between the free surface gravity waves and vortical motions (see also Figure 4.13). The magnitude of vortical VLF motions was then quantified by integrating the energy of both G_{uu} and G_{vv} for the vortical VLF regions outside the dispersion relation curve:

$$\begin{aligned} q^2_{\mathrm{VortVLF,rms}} &= \int_{-0.04m^{-1}}^{-k_{yg}} \int_{0.0005Hz}^{0.004Hz} [G_{uu}(f,k_y) + G_{vv}(f,k_y)]df\,dk_y \\ &+ \int_{k_{yg}}^{0.04m^{-1}} \int_{0.0005Hz}^{0.004Hz} [G_{uu}(f,k_y) + G_{vv}(f,k_y)]df\,dk_y, \end{aligned} \tag{4.6}$$

where +/- k_{yg} are the boundaries of the vortical region region, given by the shallow water dispersion relation $k_{yg} = f/\sqrt{gh}$. G_{uu} and G_{vv} are the frequency-alongshore wavenumber (f,k_y) spectra of the cross-shore and alongshore velocity respectively.

The calculated vortical VLF magnitude $q_{\mathrm{VortVLF,rms}}$, at the most shoreward array A1 is shown in Figure 4.9 for the full 4 month period. In total 235 time periods were found with both negligible alongshore current and noticeable vortical VLF motions ($q_{\mathrm{VortVLF,rms}} > 0$ m/s) (filled circles in Figure 4.9).

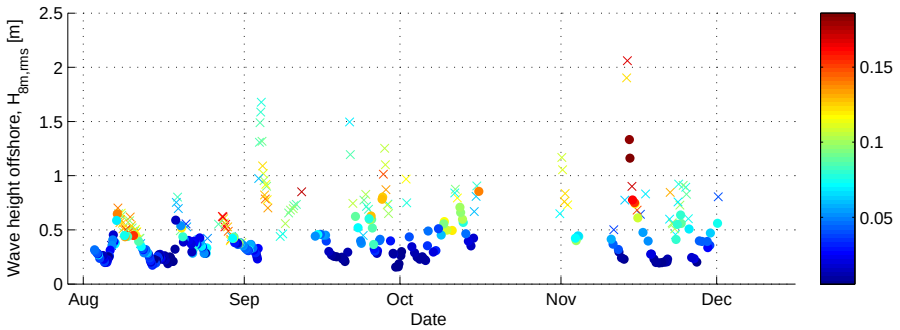

Figure 4.9: Vortical VLF magnitude as observed during 4 months of SandyDuck at array A1. Colors indicate $q_{\mathrm{VortVLF,rms}}$ values in m/s, warm (red) colors coincide with large vortical VLF motions (up to 0.18 m/s), blue colors indicate hardly any vortical VLF motions. Filled circles represent time period with negligible alongshore current, crosses are periods with alongshore current larger than 0.25 m/s.

Most of the periods when vortical VLF motions were observed the incoming wave height was small, mean $H_{\mathrm{rms,8m}}$ over all these periods equals 0.4 m. As the bottom level at the array A1 is typically around -1.3 m below datum this implies (combined with the tidal range of 1 m) that the array was located outside the surf zone for most periods vortical VLF motions were observed. A second selection was therefore made, restricting the observations only to time periods when waves were breaking at array A1. Using the large cross-shore array of sensors C1 (Figure 4.8), the wave transformation was analysed. The most shoreward alongshore array A1 was assumed to be within the surf zone if a small decrease in wave height was observed from A2 to A1 ($H_{\mathrm{rms},x=160\mathrm{m}} \leq H_{\mathrm{rms},x=210\mathrm{m}} - 0.04m$). This last selection greatly reduces the amount of data points (to only 22), but ensures that the observations are inside the surf zone. Also since time periods when A1 was outside the surf zone are rejected, more certainty is obtained that VLF motions were not generated or affected by a large wave driven alongshore current in the surf zone shoreward of the array A1. The wave height transformation along the cross-shore array C1 is shown in Figure 4.10 for the 22 retained time periods. Array A1 was located at the edge of the surf zone for all runs, except for the two time periods with the largest incident wave heights for which waves were breaking further offshore around cross-shore location $x \sim 350$ m.

Next, concurrent incident wave conditions were analysed for mean period, frequency and directional spread. Wave period was expressed in a mean period T_m, calculated as inverse of the mean frequency f_m observed at the 8 m array. The directional spread of the offshore forcing was calculated from the frequency directional spectra $E(f,\theta)$ at the 8 m array. The directional distribution (over all frequencies) was obtained following $D(\theta) = \frac{E(f,\theta)}{E(f)}$, with $E(f)$ being the one dimensional frequency spectrum. The bulk directional spread of the incident spectra was then expressed by σ_θ:

$$\sigma_\theta = \sqrt{\int_{-\pi/2}^{\pi/2} \left(2\sin(\theta - \theta_0)/2\right)^2 D(\theta) d\theta} \tag{4.7}$$

Expression σ_θ used here is similar to the bulk parameter for directional spread σ_θ^* as proposed in *Kuik et al.* (1988). Typical values for σ_θ at Duck are between 16 to 32 degrees (*Feddersen*, 2004).

The frequency spread of the spectra was expressed by parameter κ (*van Vledder*, 1992), which was calculated from the short wave spectrum $E(f)$

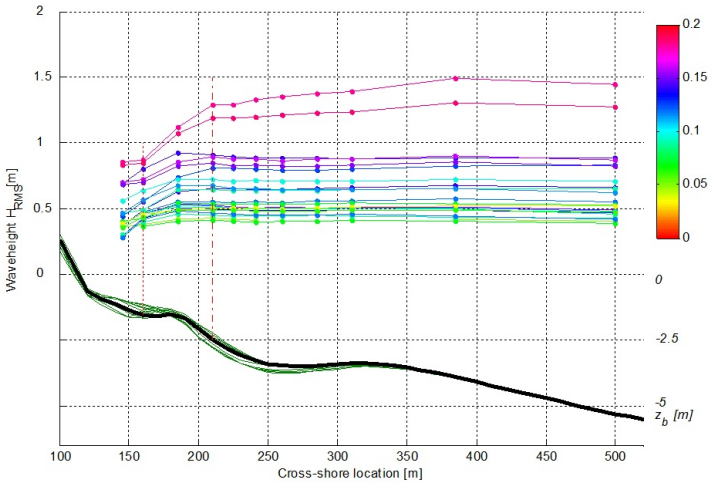

Figure 4.10: Wave transformation along cross-shore array C1 for the selected time periods with vortical VLF observations. The positions of alongshore arrays A1 and A2 are indicated by the red vertical dotted and dash-dotted lines respectively. Colors indicate $q_{\mathrm{VortVLF,rms}}$ in m/s. Topography profile as measured on October 30th 1997 at transect C1 in black, adjacent profiles in the instrumented area in dark green.

using:

$$\kappa^2 = \frac{1}{m_0^2}\left[\int_{0.044}^{0.32} E(f)\cos(\frac{2\pi f}{\bar{f}_0})df\right]^2 + \frac{1}{m_0^2}\left[\int_{0.044}^{0.32} E(f)\sin(\frac{2\pi f}{\bar{f}_0})df\right]^2, \quad (4.8)$$

where $\bar{f}_0$ is the zero crossing frequency ($\sqrt{m_2/m_0}$), m_n being the n-th order moment of the frequency spectrum $E(f)$. As spectral information of the 8 m array was not available from the 8 m array for the August and December, κ was calculated from the most seaward SPUV (WG72) at approximately 5 m water depth (Figure 4.8). Calculated values of κ are in the range 0.1 (wide) to 0.6 (narrow freq. spread). Typically, spectra were quite wide with energy spread around the peak. Theoretically, on some occasions the presence of superharmonics in the nearshore (see *Guza and Thornton*, 1980) may cause the spectra to appear wider in bulk spread parameters than they actually are. Visual inspection of the observed frequency directional spectra however

revealed that in the periods investigated here the spectra were wide rather than multiple-peaked at the harmonic frequencies.

4.3.3 Field data results

The observations of vortical VLF motion magnitude in the surf zone were compared to the characteristics of the concurrent incident wave forcing. In general, VLF motion magnitude was larger under higher incoming wave heights (Figure 4.9), as has been reported previously by (*MacMahan et al.*, 2004, 2010b). Yet, for a single incident wave height, a wide range of VLF motion magnitudes has been found. It was therefore investigated whether swell conditions (long wave period, narrow frequency and directional spread) yield to different VLF motion magnitude. Vortical VLF motion magnitude was plotted here versus two wave energy proxies:

- The incoming offshore wave height $H_{\mathrm{rms,8m}}$. The underlying hypothesis is that the total amount of wave energy dissipation in the surf zone determines the magnitude of the observed VLF motions regardless of the water level (or surf zone width) and the wave breaking intensity.
- And secondly, the local energy dissipation at A1. Using the underlying hypothesis that the magnitude of VLF motions is dependent on the local wave breaking. This is especially interesting as the water depth at the instruments is variable in the field due to the varying topography and the tide. As such an incident wave height e.g. $H_{\mathrm{rms}} = 0.8$ m at 8m offshore can lead to substantially different wave heights inshore at A1 depending on the time period and water level (see also Figure 4.10).

Figure 4.11 shows side-by-side the magnitude of vortical VLF motions against both offshore wave height (left panels) and dissipated energy (right panels). Dissipated wave energy was presented for the latter as $\sqrt{H_{A2}^2 - H_{A1}^2}$ for a comparison with the same proportionality as the other panels (in [m]).

Vortical VLF magnitude was found to be related to both incoming wave height (r^2 =0.5) as well as the dissipated energy (r^2=0.55), but the small amount of observations prevents solid statements whether any of the two is more appropriate. The slightly better correlation when using local wave energy dissipation rather than incident wave height is thought to be mostly attributed to periods with offshore wave heights of O (0.5 m) under which a wide variety of vortical VLF magnitudes and a wave height decrease over the sensors (Figure 4.10) was observed. Bulk wave characteristics of wave period, frequency spread and directional spread are shown in Figure 4.11 in colors to show their relation to the observed vortical VLF magnitude. Observations point toward a dependency of the vortical VLF magnitude on type of wave conditions, as

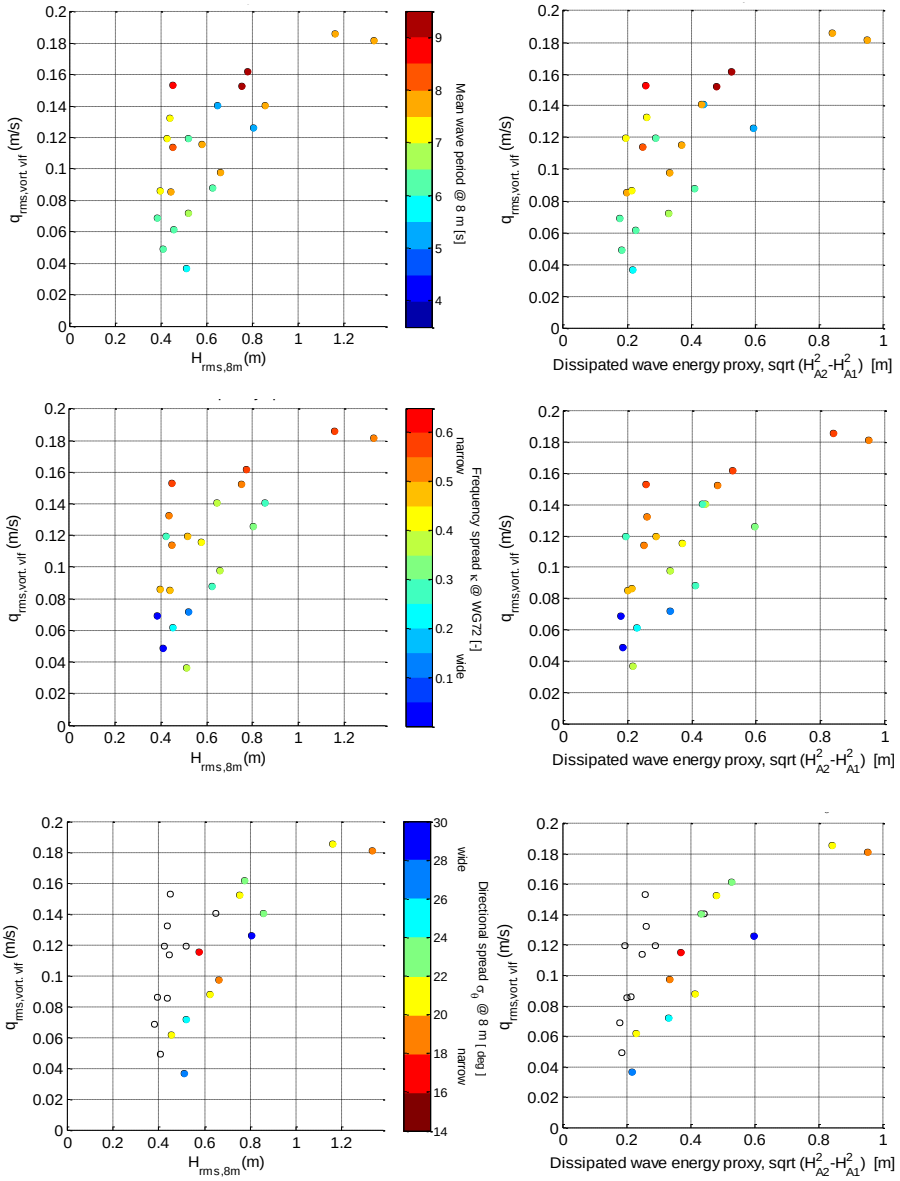

Figure 4.11: SandyDuck '97 Vortical VLF observations sorted to mean period (top), frequency spread (middle) and directional spread (bottom). Left column figures show the observations plotted against the incident wave height, right column as function of the local dissipated energy. Warm (red) colors represent narrow banded long period waves typically associated with swell waves. Open circles represent time periods with no data on σ_θ.

for both wave period and frequency spread the data clouds show sorting. Red colored data points (representing more swell like conditions) tend to be on the upper half of the data cloud. This implies that for a single wave height larger VLF motions coincide with larger wave period and/or narrow frequency spread conditions. Data points colored to directional spread did not result in a clear sorting in colors, consequently no clear effect of the directional spread was found from this dataset.
The limited amount of data, changing (3D) topography over the 4 month of velocity observations and the dependency on multiple parameters make it difficult to draw firm conclusions based on the field data alone. To investigate the effect of the short wave characteristics on VLF motion magnitude in a more isolated way, numerical model simulations were executed next. Bulk parameters of the forcing were tested independently of each other and topographic variability (in time and space) is removed.

4.4 Magnitude of wave group induced VLF motions, computations with a short wave averaged model

Variations in magnitude of vortical VLF motions under different incident wave spectra, as discussed in the previous section, are investigated in more detail using a numerical flow model. Vortical VLF motion magnitude is computed for a single barred beach with different scenarios of incident wave conditions and small variations in cross-shore profile shape. In a similar approach as previous section, the computations are restricted to the case of shore-normal incidence to avoid a mixture with VLF motions induced by alongshore current instabilities.

4.4.1 Numerical model and schematization

A 2DH (depth-averaged coastal area) model used, which is a research version of *Delft3D* and described in Appendix B. The hydrodynamic model is forced at the offshore boundary at 8 m water depth with time and alongshore varying wave group energy $E_w(x = x_{\text{offshore}}, y, t)$, resulting in hydrodynamics varying on the wave group (long wave) timescale. The synthetic timeseries of wave energy at the boundary are sampled using the two-dimensional frequency-direction short wave spectrum $E(f, \theta)$. Different wave spectra $E(f, \theta)$ are used to generate scenarios for the investigation of the effect of wave period, frequency and directional spread.

The wave forcing scenarios were tested on a schematised alongshore uniform single barred beach. The dimensions of the beach are 1.5 km in alongshore direction and almost 1.3 km in cross-shore. The beach profile is alongshore uniform with a single subtidal bar and un-erodable. The subtidal bar crest is located 115 m from the shoreline (x=190 m) and bar crest height is 1.2 m below the still water level[2]. Grid sizes are 10 m in alongshore and ranging from 4 to 25 m in the cross-shore direction depending on the water depth. Lateral boundaries are closed mimicking an embayed beach case and a weakly reflective Riemann boundary is applied at the offshore boundary to enable outgoing long waves to leave the domain (*Verboom and Slob*, 1984).

For each simulation, the hydrodynamics are modeled for a total of 180 minutes with a hydrodynamic time step of 2.4 seconds. Horizontal and vertical tides are omitted, as well as wind driven flows. Offshore wave energy boundary

[2]Figure 5.2 on page 134 shows the topography used.

conditions are sampled using random phases (see Appendix B.1) and therefore each simulation output is only a single possible realization of the nearshore flow under the imposed forcing conditions. Repetitive tests of the same scenario show that, although realizations are different, 3 hour bulk statistics of (low frequency) surf zone motions hardly changed.

Forcing Scenarios

Several wave scenarios are simulated exploring a range of natural conditions (Table 4.4). To compare different scenarios, the total offshore wave energy flux P of the spectra at a water depth of 8.1 m is identical throughout the tests. Therefore, in tests with different wave periods, offshore wave height is adjusted slightly to keep $P_{8.1}$ constant (see Table 4.4).

Table 4.4: Wave conditions used in the different forcing scenario simulations. Note that small variations in offshore wave height are made to maintain an equal offshore energy flux P(Eq. 4.9) for all simulations.

Simulation	Wave height $H_{\mathrm{rms},8.1}$ [m]	Wave period T_p [s]	Frequency spread κ [-]	Directional spread σ_θ [deg.]
Reference case				
Test R.111	1.0	10	0.57	12.2
Scenario tests				
Test T.201	1.09	**7.0**	0.57	12.2
Test T.501	0.97	**12.5**	0.57	12.2
Test T.601	0.96	**14.0**	0.57	12.2
Test K.201	1.0	10	**0.36**	12.2
Test K.301	1.0	10	**0.42**	12.2
Test K.601	1.0	10	**0.72**	12.2
Test D.001	1.0	10	0.57	**0**
Test D.101	1.0	10	0.57	**4.0**
Test D.201	1.0	10	0.57	**7.3**
Test D.401	1.0	10	0.57	**18.8**
Test D.501	1.0	10	0.57	**23.4**
Test D.601	1.0	10	0.57	**30.0**

Wave energy flux $P_{8.1}$ is computed by:

$$P_{8.1} = Ec_g = \frac{1}{8}\rho g H^2_{\mathrm{rms},8.1} c_g, \tag{4.9}$$

where group velocity c_g is calculated at the offshore boundary from the

linear dispersion relationship using the short wave period. For all other simulations with wave period T_p of 10 s, the wave height offshore H_{rms} was equal to 1.0 m at 8.1 m water depth. Frequency and directional spread are varied independently, to investigate the effect of parameters individually.

Topography Scenarios

Additionally, the effect of the slope near the breakpoint is investigated as it controls the intensity of wave breaking and is therefore related to the generation of VLF motions. The bottom topography in different scenarios is adjusted slightly seaward of the bar crest, keeping the inshore surf and the shoreline reflection zone unaltered. Slope is steepened (flattened) in the zone between the 1.2 and 4.2 m depth contour (i.e. the bar crest height and 3 m below). Seaward of the 4.2 m topography is flattened (steepened) to keep the water depth at the offshore boundary ($x = 1300$ m) equal at 8.1 m. The steepness of the slope near the breakpoint is quantified by slope between the 1.2 and 2.5 m (see Figure 4.12), where the majority of the dissipation takes place[3]. Four different slopes of the bar are tested; 1/36, 1/55 (reference case R.111), 1/74 and 1/95 (Figure 4.12). Wave forcing timeseries on the offshore boundary are identical for each topography scenario.

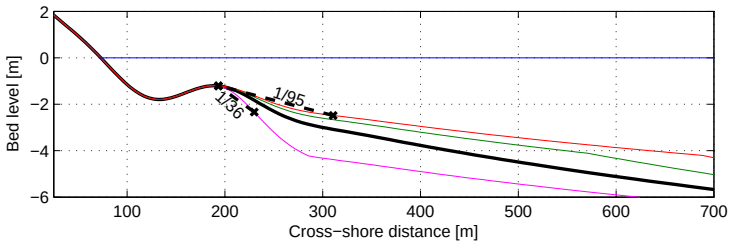

Figure 4.12: Cross-shore profiles of the different offshore bar slope scenarios.

4.4.2 Post-processing

Model results of the velocities in the domain are postprocessed to obtain the part of the velocity signal that can be attributed to low frequency motions. The first 30 minutes of each simulation contain spin up effects of the initial

[3]Figure 4.14 on page 119 shows a cross-shore distribution of the wave height. Largest decrease in wave height can be observed on the seaward flank of the bar where the depth is between 1.2 and 2.5 m.

conditions and are discarded for further analysis. Of the remaining 2h30 hours, timestacks of u and v in (y,t) are extracted at the bar crest (x = 190m). The velocity timestacks were analysed with a two dimensional FFT analysis revealing the alongshore length (k_y) and the temporal scale (f) of the surf zone velocity motions. Figure 4.13 shows the distribution of energy in f, k_y space obtained using the 2dFFT method for the model output of the reference simulation. Velocity fluctuations in the IG frequencies (0.004< f <0.04 Hz) are clearly visible in these model results around the k_y =0 axis. These are related to the incoming and reflected long waves. Very low frequency (f <0.004 Hz) velocity fluctuations appear as two distinct spots of energy off-center of the k_y =0 axis. In the reference case presented here energy is centered around k_y=±0.005 m^{-1} indicating an alongshore length scale of O (200 m). Similar to observations in the field (*MacMahan et al.*, 2004, 2010b), the majority of the VLF motions are in the vortical region of the f,k_y space.

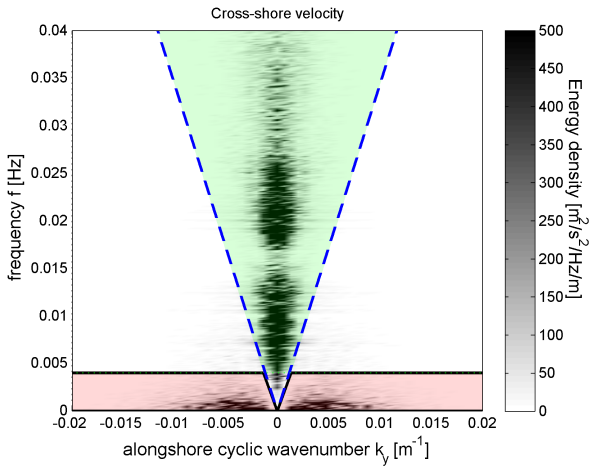

Figure 4.13: Frequency-alongshore wavenumber spectra of the computed cross-shore velocities on the bar crest. Blue dashed line shows the shallow water dispersion relation. Red and green colors mark the areas used to determine the magnitude of vortical VLF and non-vortical IG motions respectively

The velocity signals were separated into vortical (eddy-like) and non-vortical (wave-like) using a division based on the shallow water dispersion relation. Identical to the SandyDuck observations, the vortical VLF motion magnitude $q_{\mathrm{VortVLF,rms}}$ is computed by integrating the energy in the vortical energy part of the spectrum (Figure 4.13, red areas and Eq. 4.6). Energy in the non-

vortical infragravity (IG) velocity fluctuations $q_{\mathrm{Non-vort.IG,rms}}$ (Figure 4.13, green area) was calculated using a similar expression integrating over the area between the surface gravity wave dispersion curve.

4.4.3 Model simulation results

General observations

The magnitudes of vortical VLF motions and non-vortical IG velocity motions are calculated for the nearshore zone using the two dimensional FFT analysis. A cross-shore transect of the resulting velocities is shown in Figure 4.14 for the reference case R.111 (H_{rms}=1m, T_p=10s, κ=0.57 and σ_θ=12.2). Offshore wave height and water depth on the bar crest are such that the majority ($\sim$ 75 %) of the wave energy is dissipated on the (seaward side of the) subtidal bar, reducing the wave height by about 50%. Wave breaking of the largest waves is initiated at around x = 400 m.

Inshore infragravity flow fluctuations in the computational domain show a clear relation with water depth, such that large IG flow magnitudes are found near the waterline and at the crest of the bar. VLF motion magnitude shows a slightly different behaviour, with the largest velocity fluctuations predicted on the seaward flank of the bar near the point where wave height decrease is largest.

The relation between incoming wave group energy and VLF velocity fluctuations is examined in more detail by looking at the alongshore timestacks of wave energy and velocity across the bar crest. Figure 4.15a displays a time-alongshore location timestack of wave energy on seaward flank of the bar. Due to the different spectral components in the incoming wave field, the wave energy fluctuates on the time scale of wave groups, visible as the small variations in red to black in this figure. Apart from the explicit variation on the time scale of a single wave group, the sequencing of multiple large or small wave groups also leads to more subtle low frequency variation in wave energy. This is visualised in Figure 4.15 by contour levels showing the VLF low pass filtered wave energy $E_{w,\mathrm{VLF}}$. The VLF cross-shore velocity timestack (Figure 4.15 c,d) depicts the simultaneous onshore and offshore flows on the VLF time scale. Similar to findings by *Long and Özkan-Haller* (2009), instants of offshore flow are often observed following periods of low wave energy (visible in Figure 4.15c as red streaks preceded by black contours). In other words, seaward accelerating flow can be observed once a few relatively small groups arrive on the bar compared to the adjacent alongshore locations, thus generating a transient rip current. There is a slight delay between the VLF velocity response (red and

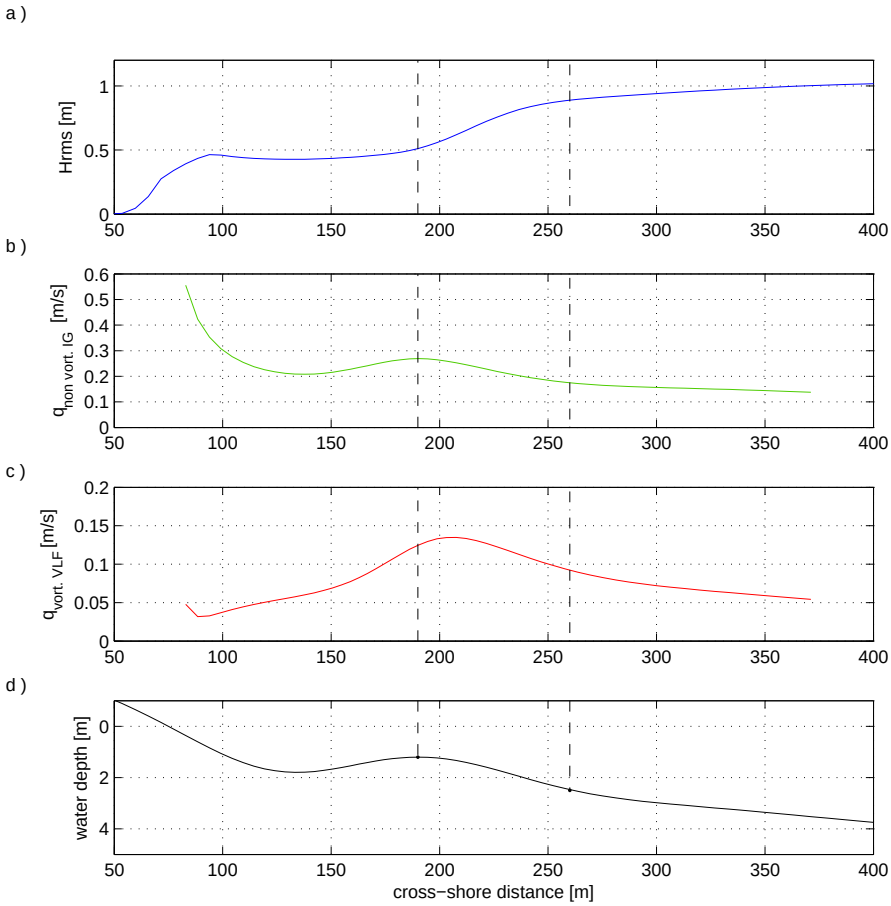

Figure 4.14: Cross-shore distribution of wave height H_{rms} (panel a), total infragravity (b) and vortical VLF (c) motion. Bottom topography given in panel d. Dashed line indicates the bar crest, dash-dotted line the location of the timestack in Figure 4.15.

blue streaks) and the wave forcing (contours), showing that the VLF motions (eddies) require time to spin up (discussed more in depth by *Reniers et al.* (2004) and *Long and Özkan-Haller* (2009)). Also, VLF motion bursts persist longer than the typical extent of the VLF wave energy contours, showing that once the motions (eddies) spin up, they can persist due to their inertia.

The cut-off frequency of the VLF motions used here ($f < 0.004Hz$) does not have a clear physical background, but is merely a frequency division. Similar relation between timestacks of low passed wave energy and low passed velocity can be found for different cut-off frequencies. The $f < 0.004Hz$ threshold however provides a clear division between mostly vortical and non-vortical motions in the computational results and is therefore used.

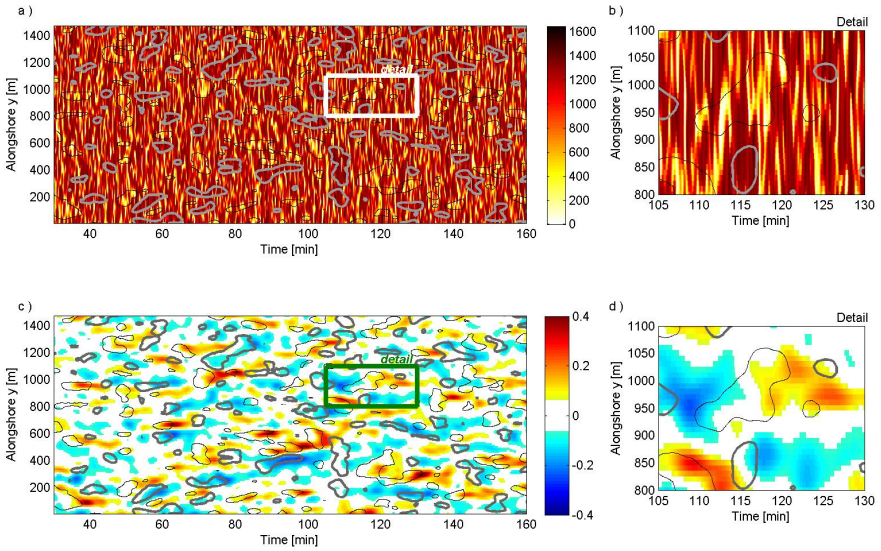

Figure 4.15: Connection between wave energy fluctuations and VLF velocities seaward of the bar crest (x=260 m). a) Wave energy timestack, c) Cross-shore velocity u_{VLF}. Contourlines in both panels show levels of the low-passed wave energy signal $E_{w,\mathrm{VLF}}$ 10 % higher (in grey) or lower (black) than the mean wave energy $\overline{E_w}$. Panels b) and d) show details of an VLF offshore velocity event.

Forcing Scenarios

Model scenarios with different offshore forcing are expected to result in a variation in VLF motion magnitude, similar to section 4.3. Frequency bandwidth and wave period of the incoming wave field determine the amount of wave energy fluctuations on the VLF timescale, which are shown to be linked to the VLF velocity fluctuations in Figure 4.15. Variation in wave period provides a linear scaling of the wave group signal, increasing the time period between wave crests, groups and sequences of large groups. Frequency spread affects the correlation between consecutive wave heights, such that narrow spreads lead to an increased number of waves per group (*Medina and Hudspeth*, 1990). The resulting effect of different offshore forcing on the observed low frequency velocity fluctuations on the bar crest is shown in Figure 4.16, with simulation results sorted by spectral parameter. The magnitude of the non-vortical IG velocity is shown here as a reference next to the vortical VLF velocity magnitude. First finding is that the vortical VLF motions do not show a similar response to changes in the wave conditions as the IG waves. The change in ratio between these two components indicates a difference in generation mechanism.

Variations in wave period T_p affected the magnitude of both IG and vortical VLF motions. Vortical VLF motions were found to increase under larger incident wave periods, similar to observations during the SandyDuck '97 field campaign (Figure 4.11). Simultaneously the infragravity flow velocity more than doubled when period T_p was increased from 7 to 14 s, which can be attributed to the generation of higher incoming bound long waves under large wave periods ($\zeta_{IG} \cong \frac{S_{xx}}{\rho f_p^2 h^2}$, *Longuet-Higgins and Stewart*, 1962) and their stronger reflection from the beach due to an increase of the relative slope of the shore (*Battjes et al.*, 2004).

Frequency spread was found to hardly affect the magnitude of IG velocity fluctuations. This can be in part understood by the incoming bound long wave part of the IG waves. An adaptation of the frequency spread changes the timescale of the wave groups and the generated long wave, yet its traveling speed and amplitude are to first order unaltered, and thus magnitude of IG flow on the bar crest shows negligible change. However, a significant increase in vortical VLF motions was found under narrower frequency spreads indicating that the shift of wave energy fluctuations towards lower frequencies stimulates the generation of VLF motions.

Directional spread has a strong connection with the magnitude of IG motions, where larger spread lead to a significant reduction in IG magnitude. This effect can be attributed to the weaker difference interaction of short wave compo-

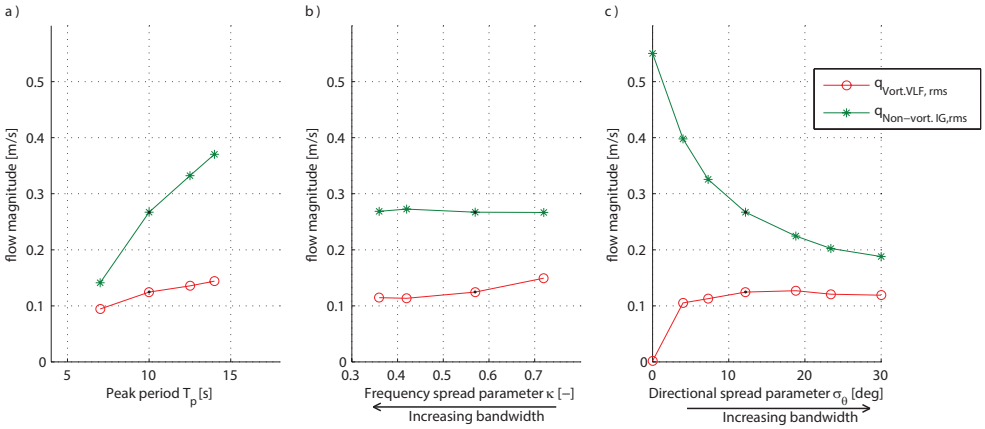

Figure 4.16: Vortical VLF (red) and non-vortical IG (green) velocity magnitude on the bar crest. Model results show how wave period (panel a), frequency spread (b) and directional spread (c) differently affect the magnitude of both components. Black dots indicate the reference scenario.

nents for increasing difference angles (e.g. *Sand*, 1982; *Herbers et al.*, 1999; *Reniers et al.*, 2002). However, such an impact of the directional spread was not found for the vortical VLF motions. Simulations with varying directional spread have nearly equal vortical VLF magnitude, apart from the case with no directional spread. For the hypothetical case of no directional spread, vortical VLF motion magnitude is nearly absent as wave group forcing becomes alongshore uniform. An optimum seems to be in place for spreads around 15 deg, which resulted in the largest VLF motions. For larger directional spreads, the vortical VLF magnitude shows a slight decrease, possibly due to the fact that for the largest directional spread the alongshore size of wave groups becomes small ($\sim$ 135 m) compared to the typical VLF eddy size of O (200 m).
In all, a variation of VLF magnitude of O (50 %) is observed if the spectral characteristics of the incoming wave field are altered. This confirms the earlier conclusions from the SandyDuck data that variations in sea state are in part responsible for the scatter in observed vortical VLF motion magnitude.

Bar slope scenarios

Seaward slope of the bar was found to have a large effect on the size of VLF motions. Simulations show an increase in vortical VLF motion magnitude on

the bar crest by 500 % if the bar is steepened locally near the breakpoint (Figure 4.17). For mild slopes the vortical VLF motions were nearly absent. Similarly, results show that bar slope only had a minor effect on IG velocity magnitude as the topography in the offshore region where for bound waves are generated and inshore where waves reflect and dissipate are unaltered.
The findings imply that large vortical VLF motions are primarily to be found at profiles with a relatively steep slope at the breakpoint. Such steep slopes were indeed present during the observations at SandyDuck '97 and RIPEX where strong vortical VLFs were measured (*MacMahan et al.*, 2004, 2010b), both locations having approximately a 1:35 slope between -2 and -4 m. The sensitivity to the slope near the breakpoint also clarified some of the scatter seen in SandyDuck '97 observations, for these observations were done under different topographies and tidal levels.

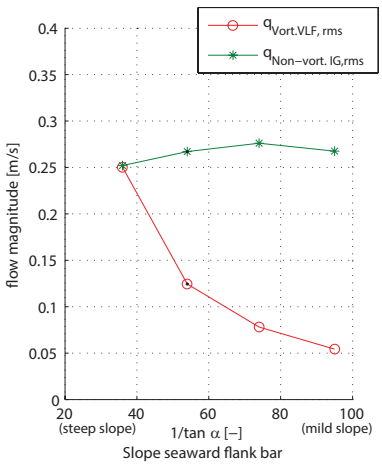

Figure 4.17: Impact of seaward slope of the bar on the vortical VLF motions (green) and non vortical IG motions (red). Black dots indicate the reference scenario with a 1:55 slope.

Moreover, from these findings it can be concluded that strong VLF velocity fluctuations could even be found at wind sea dominated coasts provided that the slope near the breakpoint is sufficiently steep. For the tested profile, the impact of the slope is larger than the wave period or any of the other spectral parameters. This is underlined by the VLF motions observed at Vlugtenburg (Section 4.2) which had a steep slope of 1:20 (around the -2m level) at the time of the experiment.

4.4.4 Discussion

In all, the numerical model scenarios indicate that wave group induced VLF motion magnitude is dependent on three aspects:

1. The timescale of wave group succession. An increase in short wave period and a decrease of frequency spread both elongate the wave group timescale, thus influence the timescale of wave group succession on the VLF timescale. Narrow frequency spread affects this timescale of groups by increasing in number of waves within a wave group. Wave period linearly scales the timescale of the wave groups.

2. The intensity of wave dissipation. As shown with the bottom slope scenarios, the dissipation rate of the wave energy is a key factor for the presence of these motions, determining if wave energy fluctuations result in large or small fluctuations in wave force. Mild bottom slopes, yielding to a more gradual wave dissipation results therefore in small wave group induced VLF motions.

3. The presence of directional spreading. Important to create alongshore variability in the forcing and therefore in the forced response. Slight alongshore variation is needed to add an alongshore component to the predominately cross-shore forcing. Once directional spreading is present, the different directional spreads only result in small variations in VLF motion magnitude.

In a first attempt, the previous model scenarios are combined using the three aspects above. Time scale of wave group succession is expressed as the mean period of wave energy fluctuations $T_{E,m01}$[4], which is around 75 s for the reference case. The slope near the breakpoint is used as a measure for the dissipation intensity, similar to Figure 4.17. And the presence of directional spread is expressed by a delta function $(1 - \delta(\sigma_\theta))$, giving a value equal to 0 for no directional spread and 1 for all other cases. Combined results of all scenarios are shown in Figure 4.18. The figure shows a clear trend, where the ratio of the wave energy fluctuations timescale and the slope near the breakpoint control the magnitude of vortical VLF motions.

[4]Mean period of wave energy $T_{E,m01}$ is evaluated at the offshore boundary at 8 m water depth. $T_{E,m01}$ follows from the first and zero'th order moment of the spectrum obtained from the timeseries of wave energy.

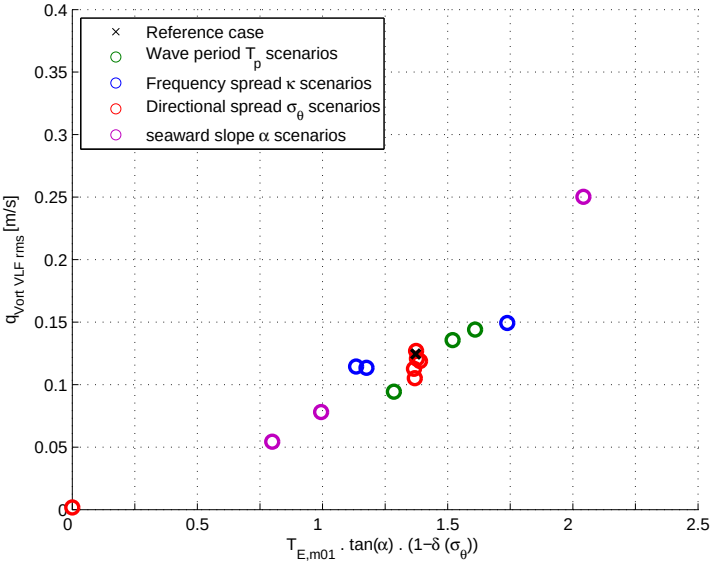

Figure 4.18: Computed vortical VLF magnitude on the bar crest as function of bulk wave forcing characteristics. Note that offshore wave height H_{rms} for all these scenarios equals 1 m.

4.5 Conclusions

The objective of the current chapter was to examine 1) whether very low frequency (VLF) velocity fluctuations can be observed at the Dutch coast in absence of alongshore current and 2) to investigate whether the magnitude of VLF motions in the surf zone are dependent on the type of wave conditions (swell or windsea).

A field campaign was conducted at Vlugtenburg beach, the Netherlands, with the intention to measure VLF velocity fluctuations. Instruments were deployed on multiple days resulting in measurements within and outside the surf zone. Observations on a day with intermediate wave height (offshore H_s of 1.4 m) showed the presence of VLF motions ($u_{\mathrm{VLF,rms}} = 0.09$ m/s) inside the surf zone in the absence of a strong mean alongshore current. As this magnitude is of similar order as values previously reported (at open ocean coasts), this demonstrated that VLF motions are not restricted to open ocean beaches with swell waves.

Next, a wide range of VLF observations of the 4 month field campaign at Duck, NC, USA were re-analysed to investigate the effect of sea state parameters on vortical VLF motion magnitude. Vortical VLF motion magnitude primarily relates to the wave height, with stronger VLF velocity fluctuations observed at instants with higher incoming waves. For a given wave height however, VLF motions were found to be stronger on times when incoming waves had long wave period, narrow frequency spread, or both. No clear trend was observed when the observations were differentiated to times when the incoming wave field had different directional spreads. Swell-like wave conditions characterised by narrow frequency spreads and long wave periods were thus concluded to promote with stronger VLF motions.

The effect of forcing parameters were experimented in a more isolated way using a numerical model on the long wave time scale. The results of conceptual model simulations with various forcing scenarios confirmed the observed effect of frequency spread and wave period on the magnitude of VLF motions. The magnitude of vortical VLF velocity fluctuations were found to vary with O (50%) when the characteristics of the incident wave spectrum changed. Additional computations with the conceptual model also indicated that the slope of the surf zone near the breakpoint largely affects the magnitude of VLF motions, at least for shore-normal incident waves. Steeper slopes near the breakpoint yielded to 500 % stronger VLF motions. The latter clarifies the presence of VLF motions under short wave periods during the Vlugtenburg beach experiment as well as the strong VLF motions found in earlier field studies, as these had steep sloping profiles near the breakpoint.

The findings also imply that VLF motions can be particularly strong after installation of a nourishment if the post-construction profile is very steep.

Acknowledgements

Nortek Netherlands is greatly acknowledged for providing the instruments and support during the REDNEX2010 field campaign. Dano Roelvink and the UNESCO-IHE students are thanked for their effort during the field campaign. Steve Elgar, Tom Herbers, Bill O'Reilly and Bob Guza are acknowledged greatly for the SandyDuck SPUV instrument data. The Field Research Facility of the U.S. Army Engineer Waterways Experiment Stations Coastal Engineering Research Center is thanked for the detailed bathymetries during SandyDuck as well as making all data publicly available. Deltares is acknowledged for the use of their *Delft3D* numerical model suite. Valuable comments by Bob Guza and Falk Feddersen following the ICCE2012 conference were

much appreciated and improved the contents of this chapter.

Analysis of measurements at the nourished beach in Chapter 2 show a slow evolution of alongshore variability. This slow evolution was hypothesised to be partly a result of the type of wave field at the Dutch coast. Subsequent field observations at a natural beach in Chapter 3 present a link between the formation speed of variability and the type of wave field, supporting this hypothesis. Yet, it is hard to generalise based on these field data alone. In the next chapter the emergence of variability and its potential dependency on the type of sea state is investigated further in a more conceptual way using a numerical model.

Abstract Chapter 5
The formation time of alongshore morphological variability has long been known to vary among beaches around the globe and from one post-storm period to another. It is investigated whether the type of wave conditions, distant swell waves or nearby generated short crested wind sea, affects the formation time of the emerging alongshore topographic variability.
A conceptual model is used to examine the emergence of alongshore variability under different shore-normal wave forcing. A research version of *Delft3D*, operating on the time-scale of wave groups, is applied to a schematised bathymetry with a single bar. The morphodynamic model is used to investigate several wave scenarios, testing the impact of peak period, frequency spread and directional spread individually. Results show that an increase in wave period has a large effect, changing the formation time up to O (250%) in case the mean wave period is changed from 5 to 10 seconds, representitive values for the Dutch and Australian east coasts respectively. In contrast, modifications in the directional and frequency spread of the wave field result only in a minor effect on the simulated formation time.
Examination of hydrodynamics and potential sediment transport shows that variations in formation time are primarily linked to changes in the magnitude of the time-averaged flow conditions. Variations in the magnitude of very low frequency ($f < 0.004Hz$) or infragravity ($0.004 < f < 0.04Hz$) surf zone velocities due to different sea states do not affect the mean sediment transport capacity in the model and result therefore in similar formation times of the topographic variability. Consequently the formation speed of patterns is primarily governed by positive feedback between mean flow and morphology, and low frequency flow fluctuations are of minor importance. The findings imply that, based on the wave period alone, swell dominated open ocean coasts may promote a faster development of topographic variability.

Novel items in Chapter 5 are:

- The examination of the effect of individual sea state parameters, i.e. wave period, directional and frequency spread, on the formation time of alongshore topographic variability.
- An evaluation of the importance of mean flow and very low frequency velocity motions for the formation time of alongshore topographic variability.

5

Emergence of alongshore topographic variability in nearshore bars: conceptual modelling

5.1 Introduction

The nearshore sub-aqueous zone is the most active part of the coastal profile and is often characterised by the presence of one or more subtidal bars. These bars are frequently found to be alongshore variable; i.e. both the cross-shore location of the bar as well as the crest height are alongshore non-uniform. The hydrodynamic circulations and rip currents associated with this alongshore topographic variability play a major role in the distribution of nutrients, pollutants and sediments in the nearshore zone and can be hazardous for swimmers (e.g. *Cook*, 1970; *Inman et al.*, 1971; *Talbot and Bate*, 1987; *Grant et al.*, 2005; *Dalrymple et al.*, 2011).

The presence and emergence of alongshore variability in nearshore morphology has intrigued scientists for decades. It has been long recognised that the alongshore variability of the nearshore topography varies over time. This behaviour is elegantly described by a conceptual model of discrete beach states

presented by *Wright and Short* (1984). In this model, alongshore variability is generally removed during high energy (storm) events (*Wright and Short*, 1984; *Ranasinghe et al.*, 2004; *Holman et al.*, 2006; *Smit*, 2010; *Price and Ruessink*, 2011). The resulting alongshore uniform topography is referred to as the Longshore Bar Trough (LBT) beach state. After the storm subsides, waves become milder and alongshore variability re-emerges in the subtidal sand bar. Typically, the first alongshore variability that can be seen is (rhythmic) alongshore undulations in the planform shape of the bar (Rhythmic Bar and Beach (RBB) state). Under continued mild wave conditions, sections of the bar can elongate in a transverse direction and eventually weld onto the shore, forming a Transverse Bar and Rip (TBR) beach. If the mild wave conditions persist for weeks, the entire bar will weld onto the beach resulting in a Low Tide Terrace (LTT) topography. However, a high energy storm can interrupt the above sequential beach state transition, and reset the morphology to the LBT state. The alongshore morphological variability (characterised by rip/bar locations) that re-emerges after such a resetting storm is, by definition, substantially different to that in the pre-storm morphology (*van Enckevort et al.*, 2004; *Holman et al.*, 2006).

The formation timescale and emerging post storm patterns of the variability vary from one location to another (e.g. *van Enckevort and Ruessink*, 2001; *Ranasinghe et al.*, 2012). Generally the alongshore uniform LBT phase after a resetting storm is short lived (on the order of 1-5 days) (*Lippmann and Holman*, 1990; *Ranasinghe et al.*, 2004). Locations at the Dutch coast react on a slower timescale (e.g. Chapter 2 and *van Enckevort et al.*, 2004). However, also at a given site, the residence time of the LBT state varies substantially from one post-resetting-storm period to another. Based on observations at Duck, *Lippmann and Holman* (1990) reported a standard deviation of about 2 days (around the mean LBT residence time of 2.1 days) while at Palm Beach, Sydney, *Ranasinghe et al.* (2004) reported a standard deviation of almost 4 days. Storm-to-storm variation in the formation of alongshore variability is illustrated in Figure 5.1 which shows two different reset events at Palm Beach, Australia, with one spanning 2 days and the other 5 days. These differences in formation time T_v are thought to originate from both profile parameters (e.g. bar distance offshore, steepness profile, bar crest height) and wave forcing (e.g. wave height, wave angle) as previously shown using conceptual modelling (see section 3.1.1 for an overview of previous modelling conclusions on the controls on the formation of variability). One aspect that has received little attention in these studies is the effect of the type of wave field on the formation time of alongshore variability, an effect hypothesised in previous chapters.

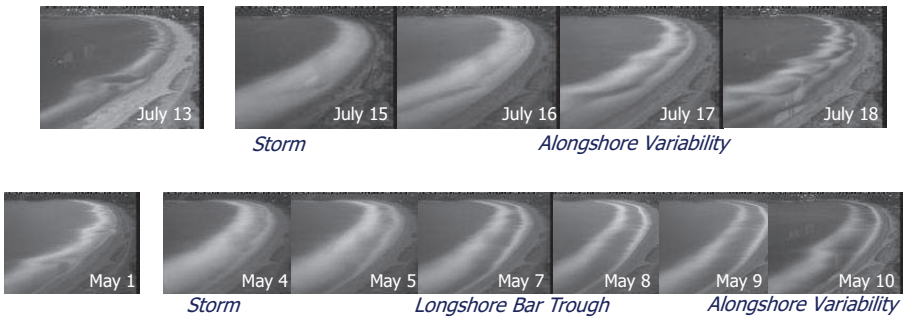

Figure 5.1: Daily time averaged Argus video images overlooking Palm beach, Australia for several days around two resetting storms, of July 1996 (*top*) and May 1996 (*bottom*). White bands in the images indicate areas of predominant wave breaking, and provide a proxy for the plan shape of the shallow subtidal bar.

Wave fields along open ocean beaches are typically different from those on marginal seas. Coasts located far from the wave generation area (i.e. storms) experience much longer crested waves (characterised as a 'swell' wave field) due to the circumferential and radial dispersion of waves propagating from the storm center than locations closer to the storm generation area which show a more shortcrested 'wind sea' type of wave field. Main parameters to express the differences in the type of wave field and its longcrestedness are the peak wave period T_p or frequency f_p, the frequency spread (about f_p) and directional spread (about the mean angle of wave incidence) which together describe the shape of the short wave spectrum. The type of wave field influences not only the longcrestedness of the waves, but also surf zone hydrodynamics. The shorter breaking wave crests associated with wide-spread wave fields are found to result in stronger vorticity and mixing in the nearshore (e.g. *Spydell and Feddersen*, 2009). Moreover, the low frequency (infragravity) waves originating from the interaction of surface wave components with different frequencies and directions, are greatly affected by the amount of spread in the wavefield (e.g. *Sand*, 1982; *Reniers et al.*, 2002). Consequently the differences in type of wave field yield also variations in resulting infragravity surf zone flow (*van Dongeren et al.*, 2003, and Section 4.4) and run-up heights near the shoreline (*Guza and Feddersen*, 2012).

Little is known on how these differences in wave field type and hydrodynamics affect the morphodynamic evolution of a beach. Only the effect of wave period on the formation time was explored previously using stability analysis, however results therein are non-conclusive. While *Calvete et al.* (2005) predict

a decrease in T_v (of over 500 %) if wave period increases from 6 to 18 s, *Garnier et al.* (2008) show hardly any change in T_v if wave period is changed from 6 to 12 s. In a first attempt, *Reniers et al.* (2004) used a process-based coastal area model to examine the impact of the directional spread on the emerging spacing of the patterns. Their results show that the spacing of emerging variability is related to the wave group spatial scale and that very low frequency motions might be related to the emergence of alongshore variability in topography. No remarks were made on the effect of directional spread on the formation time T_v therein. Chapter 3 discusses four years of Argus video data of Palm Beach Australia, investigating the relation between the growth of variability and concurrent wave conditions. It was hypothesised that the characteristics of post storm wave field affect the formation speed of the variability. While the data of Palm Beach suggest a link between the between the speed of development of alongshore variability and frequency spread, the limited amount of observations provides only partial proof. A detailed investigation using idealised numerical modelling, appears to be required to rigorously test this hypothesis.

The aim of the current chapter is to undertake strategic numerical simulations under schematised conditions to investigate the relationship between the formation time T_v of alongshore variability in nearshore bars and the type of wave field (swell vs wind sea). A long wave resolving model is used to include the effects of the incoming short wave spectrum on the low frequency (infragravity) motions. The incoming wave field is varied by systematically changing short wave peak period, frequency spread and directional spread individually, to investigate their respective effects.

5.2 Conceptual model description

The model utilised throughout this investigation is a research version of the *Delft3D* coastal area flow model which solves the depth-averaged nonlinear shallow water equations. The numerical model is short wave averaged but resolves wave energy fluctuations on a wave group scale (*Reniers et al.*, 2004). Variations in shape of the short wave spectrum due to the type of wave field can be included in this short wave averaged approach via the statistics of the incoming (non-stationary) wave group energy. Intra-wave motions linked to individual short waves are not resolved to prevent large computation times associated with computing detailed hydrodynamics for the timescale of O (5 days). Nevertheless, the short wave averaged wave group approach yields similar results as wave resolving models on the timescales of minutes, i.e. mean surf zone flow and low frequency flow associated with infragravity waves and

surf zone eddies (*Geiman et al.*, 2011). The numerical model used herein is described in detail in Appendix B and therefore only the main features of the model are discussed hereunder. Laboratory validation (*Reniers et al.*, 2004) and field validation of the model setup at the RIPEX experiment at Monterey, USA (*Reniers et al.*, 2006) show that the model is capable of resolving time-averaged short wave and infragravity motions with good skill. As the model is used with similar settings to *Reniers et al.* (2004, 2006) no further validation is undertaken here.

5.2.1 Model domain

A schematised model domain which is loosely based on Palm Beach, Australia (i.e. the study site described in Chapter 3) is used in all simulations. The dimensions of the schematised pocket beach considered are 1.5 km in alongshore direction and almost 1.3 km in cross-shore. Grid sizes are 10 m in alongshore and ranging from 4 to 25 m in the cross-shore direction depending on the water depth. The beach profile is chosen such that it corresponds to a post-reset bottom topography, alongshore uniform with a single bar (Figure 5.2). The bar crest is located 115 m from the shoreline, which is similar to the bar crest distance derived from the post-storm Argus imagery data at Palm Beach (*Splinter et al.*, 2011). Bar crest height is 1.2 m below the still water level, similar to *Reniers et al.* (2004). Lateral boundaries are closed to mimic an embayed beach and a weakly reflective Riemann boundary is applied at the offshore boundary to enable outgoing long waves to leave the domain (*Verboom and Slob*, 1984).

5.2.2 Numerical experiment

The numerical model experiments undertaken consisted of a reference simulation and several scenario tests. The purpose of the reference simulation is to test the robustness of the results and therefore was repeated ten times. The wave forcing for each of the 10 reference simulations is identical in terms of H_{rms}, T_p and shape of the incoming two-dimensional short wave spectrum. The wave group signal on the offshore boundary is however generated with random phases for each simulation. Therefore, although the mean properties of the flow are equal, the different sequencing and size of individual wave groups results in a stochastic simulation of the flow and morphological development. The wave conditions adopted in the reference simulation are shown in Table 5.1. Wave height and period were chosen close to the yearly mean conditions at Palm Beach and the selected offshore wave height H_{rms} =1 m (H_s=1.4 m)

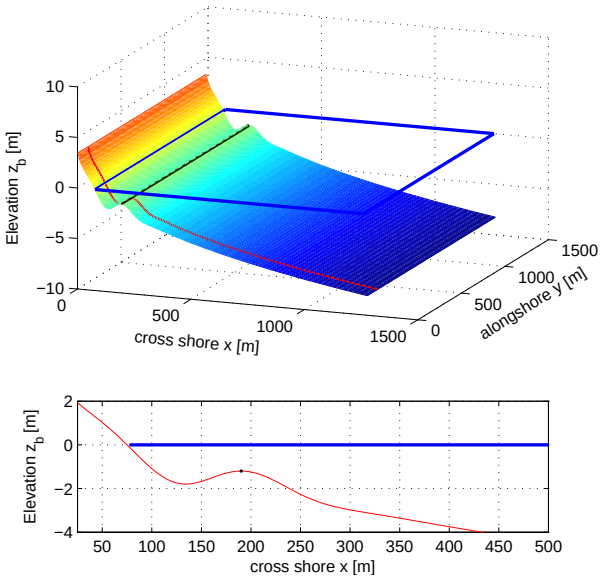

Figure 5.2: Bottom topography as used in the model. Full model domain (top panel) and a transect of the nearshore (bottom). Still water level is indicated by the blue lines, bar crest is given by the black line.

is close to the water depth on the bar resulting in wave breaking on the bar. Directional spread σ_θ is 12.2 degrees for the reference simulation (exponent s equal to 20 in Eq. B.4), to represent the predominant swell climate at Palm Beach.

Next, different scenarios are simulated for a variety of offshore wave conditions representing post-storm wave conditions, similar to the scenarios of Section 4.4. The incoming wave field is varied by short wave peak period T_p, frequency spread κ and directional spread σ_θ, where parameters are varied across a range of naturally observed values (see Table 5.1). Waves are shore-normally incident for all cases to isolate the effect of the wave field type. Parameters are tested individually by keeping other parameters constant, to separately determine the importance on the formation time of each parameter.

Hydrodynamics are simulated for a total of 7.5 hours with a hydrodynamic time step of 2.4 seconds. Courant numbers, indicating stability and accuracy of the results, are of order 2 at the bar crest.

Table 5.1: Offshore wave conditions used in the scenarios and computed formation times. Note that small variations in offshore wave height $H_{\mathrm{rms},8.1}$ are made to maintain an equal offshore energy flux $P_{8.1}$ for all simulations.

Simulation	Wave height $H_{\mathrm{rms},8.1}$ [m]	Wave period T_p [s]	Frequency spread κ [-]	Directional spread σ_θ [deg.]	Formation time T_v [h]
Reference case					
Test R.101 to 110	1.0	10	0.57	12.2	μ=38.8 (σ=1.2)
Scenario tests					
Test T.001	1.28	**5.0**	0.57	12.2	99
Test T.101	1.16	**6.0**	0.57	12.2	82
Test T.201	1.09	**7.0**	0.57	12.2	57
Test T.301	1.03	**8.5**	0.57	12.2	48
Test T.401	0.98	**11.0**	0.57	12.2	38
Test T.501	0.97	**12.5**	0.57	12.2	33
Test T.601	0.96	**14.0**	0.57	12.2	34
Test T.701	0.95	**15.5**	0.57	12.2	31
Test T.801	0.95	**17.5**	0.57	12.2	30
Test T.901	0.94	**20.0**	0.57	12.2	26
Test K.101 to 105	1.0	10	**0.31**	12.2	μ=37.6 (σ=1.5)
Test K.201 to 205	1.0	10	**0.36**	12.2	μ=38.3 (σ=0.7)
Test K.301 to 305	1.0	10	**0.42**	12.2	μ=38.9 (σ=0.9)
Test K.401 to 405	1.0	10	**0.49**	12.2	μ=38.5 (σ=0.4)
Test K.501 to 505	1.0	10	**0.65**	12.2	μ=40.0 (σ=1.1)
Test K.601 to 605	1.0	10	**0.72**	12.2	μ=40.5 (σ=1.1)
Test D.201 to 205	1.0	10	0.57	**7.3**	μ=39.4 (σ=1.3)
Test D.401 to 405	1.0	10	0.57	**18.8**	μ=38.7 (σ=1.1)
Test D.501 to 505	1.0	10	0.57	**23.4**	μ=38.3 (σ=1.2)
Test D.601 to 605	1.0	10	0.57	**30.0**	μ=38.2 (σ=1.5)

Wave propagation parameters c, c_g and θ are recomputed every 30 minutes based on the latest bathymetry computed in the morphological module. Bed level changes are multiplied using a T_{MORFAC} of 12 (Eq. B.16), resulting in an equivalent morphological simulation time of 90 hours (7.5 hours x 12), which was expected to be a sufficient simulation length to observe the emergence of alongshore variability in the post-storm nearshore bar. An exception was Test T.001 for which patterns where forming at such a slow rate that the morphological simulation time was extended to 114 hours (9.5 hours of hydrodynamics). The initial bottom topography of all tests is identical (Figure 5.2) and no morphological seeding is applied to initiate the alongshore variability. For convenience, tides as well as wind driven flows were neglected in all simulations.

5.3 Results

In this section the results from the numerical experiment are discussed as follows. First the general evolution of the emergent alongshore variability observed in all simulations is presented by taking the example of one of the reference runs. Based on these results a threshold criterion is defined for the formation time T_v. From thereon the different formation times obtained from the reference case tests and the forcing scenario tests are presented.

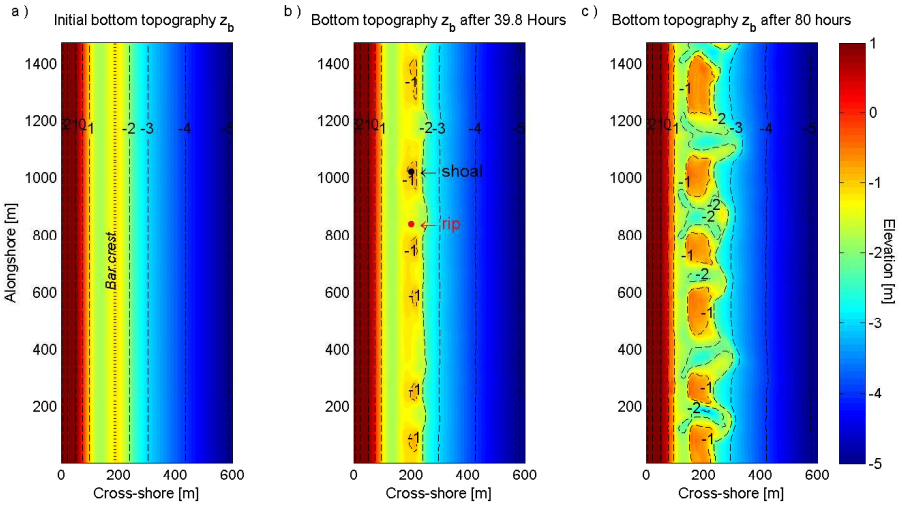

Figure 5.3: Bottom topography at the start (a), after 39.8 hours at t=T_v (b) and after 80 hours (c) of computed morphological response for a selected reference case simulation (Test R.101). Dotted line in panel (a) shows the initial bar crest at cross-shore location x = 190 m.

5.3.1 Emergence of topographic variability in the simulations

Model computations predict a development of a typical rip shoal pattern well within the 90 hours of morphological time (Figure 5.3). Starting from the beginning of the simulation, small variations in the bar position and crest height develop on the initially alongshore uniform bar after about 20 to 40 hours of simulation. Over time, the alongshore bar breaks up into shoals intersected by rip channels. The shoals extend slowly landward as sediment is deposited

at the landward side of the bar while at the same time sediment is deposited seaward of the rip channels at the rip heads. A timestack of sedimentation and erosion for an alongshore transect at the initial bar crest position $x = 190$ m (Figure 5.4) shows the gradual growth of the patterns on the bar crest.
Starting from the beginning of the computations, small O (10-20 cm) bumps and depressions are generated at some alongshore locations. These evolve with time towards shoals, while others become rip channels. During the first half of the computation (T $\approx$ 30 hours) shoals are only O (50-100 m) wide in alongshore direction. As the simulation progresses further, the horizontal flow circulations and morphodynamic feedback become more important, such that shoals increase in width to become wider than the rip channels.
Developing patterns are mostly spatially stationary. Under the shore-normal forcing conditions specified here, rip channels do not migrate significantly alongshore. Occasionally two small rips or shoals merge into a single large one. This occurs when topographic variations increase in magnitude in the latter half of the computation (40 to 90 hours). Some alongshore variations in morphological development can be observed as not all rips and shoals build up at the same rate.

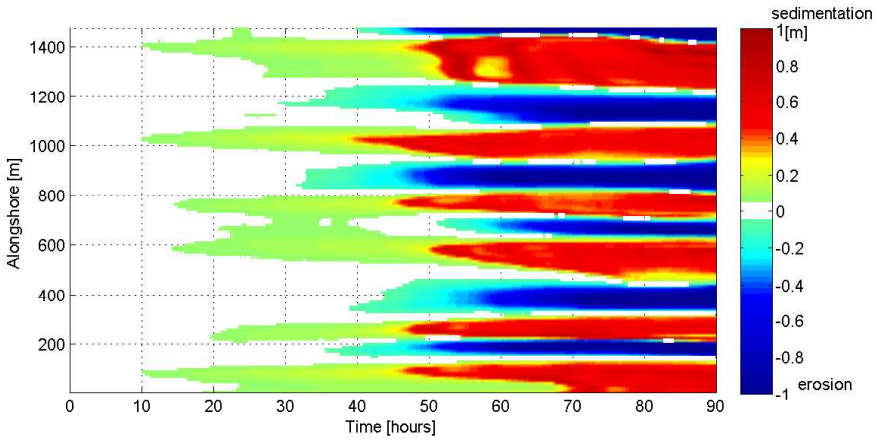

Figure 5.4: Time stack of sedimentation (red) and erosion (blue) at cross-shore location x=190 m (initial bar crest) for a reference case simulation (Test R.101).

Final mean rip spacing is in the order of 200 - 300 m but varies depending on the spectral parameters of the offshore wave forcing. The individual rip spacing (i.e. distance between two rips) varies alongshore as can be seen from Figure 5.4. Similar deviations in rip spacing around the spatially averaged rip spacing have also been observed in the field (*Ranasinghe et al.*, 1999, 2004; *Holman et al.*, 2006; *Turner et al.*, 2007).

The transformation of the nearshore bar from alongshore uniform to variable is most apparent when observing the bottom elevation changes on the bar crest over time (Figure 5.5).

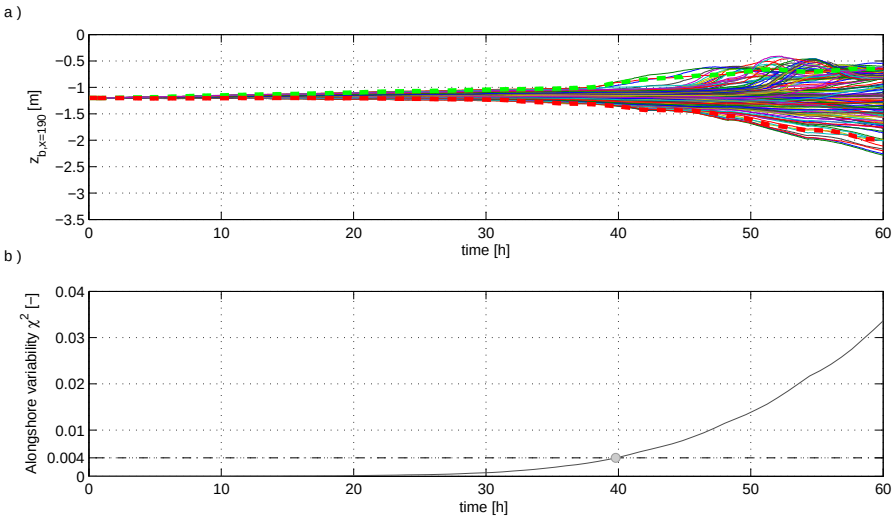

Figure 5.5: a) Bottom evolution at the initial bar crest location for a reference case run (R.101). Lines show the evolution of 150 alongshore locations on the bar each 10 meters apart. Thick dashed green and red line indicate the most pronounced rip and shoal at T=T_v (see Figure 5.3). b) Evolution of the alongshore variability χ^2 for the surf zone, including the formation time T_v for this simulation (circle) derived with the $\chi^2_{crit} = 0.004$ threshold.

All locations initially have a bottom level of $z_b = -1.2m$. As the simulation progresses shoal locations slowly accrete and rip locations erode causing the alongshore variability to increase. The first distinct alongshore variability can be observed after about 10 hours, when variations in bar crest height are of order 10 cm. In the first 30 to 40 hours a slow bottom evolution can be seen. Erosion and accretion rates of the patterns are of O (1 cm/h). For the reference

case simulations the phase with mild accretion and erosion rates lasts around 30 to 40 hours (Figure 5.5). During this time, the shoal accretes approximately 20 cm and the rip channel scours about 10 cm, resulting in alongshore depth differences of order 30 cm.

After 30 to 40 hours a shift in sedimentation/erosion behaviour is predicted. The shoals start to rapidly accrete to a level of around 0.6 m below MWL. After this, the crest height remains at a water depth of around 0.6 m and the shoal extends shoreward. Rip channels continue to erode, until a level of -2 to -2.5 m is reached at the end of the 90 hour simulation.

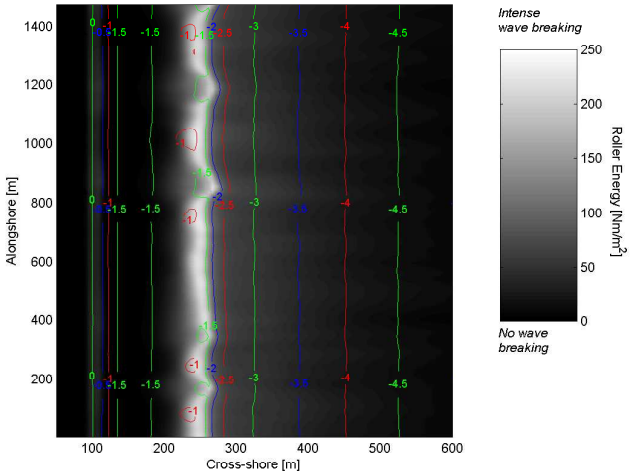

Figure 5.6: Computed mean wave dissipation pattern between T=42 and T=48 hours of morphological time for a reference case simulation (Test R.101) in grayscale. Contours show the bathymetry at T=42 h. Cross-shore scale is stretched to highlight the alongshore undulations in dissipation.

The morphology after about 40 hours is similar to a rhythmic barred beach (*Wright and Short*, 1984; *Lippmann and Holman*, 1989) (see Figure 5.3 b). This is illustrated by the computed dissipation pattern after 42 hours of simulation (Figure 5.6) showing an alongshore continuous but undulating dissipation pattern. Wave breaking on the cresentic deposition zone at the rip head connects to the wave breaking on the more landward shoal and the cross-shore extent of the planform undulations in maximum wave dissipation is of O (20m) at this stage of the computation. The planform undulations in the dissipation

patterns predicted by the numerical model compare qualitatively well with those seen in the Argus images in the days after the reset (see Figures 3.4 and 5.1).

All runs show qualitatively similar behaviour to the reference simulation discussed above and shown in Figures 5.3 to 5.6. The number of rips, individual rip locations and formation speed however vary between computations.

5.3.2 Criterion for formation time T_v

The emergence of alongshore variability is quantified for each simulation using the χ^2 metric proposed by *Ruessink et al.* (2001). χ^2 expresses the relative depth variations between the individual cross-shore profiles and the alongshore mean profile as follows:

$$\chi^2 = \frac{1}{L_x L_y} \int_{x_{\text{onshore}}}^{x_{\text{offshore}}} \int_{y_{\text{south}}}^{y_{\text{north}}} \left(\frac{z_b(x,y) - z_{b,\text{mean}}(x,y)}{z_{b,\text{mean}}(x,y)} \right)^2 dydx, \qquad (5.1)$$

where L_x, L_y represents the size of the domain where the alongshore variability is evaluated. χ^2 is calculated here for the region $x = 90$ to 400 m and $y = 0$ to 1500 m, encompassing the surf zone from the most seaward rip head to the most landward shoal over the simulations. $z_b(x,y)$ is the computed bathymetry and $z_{b,\text{mean}}(x,y)$ is the alongshore averaged profile. The evolution of χ^2 is shown in Figure 5.5b for a single reference simulation. Topographic variability is monotonically increasing within the simulated 90 hours of morphological time. Near the end of the computation shoals are still extending shoreward and growth rate is nearly linear.

Formation time T_v is defined as the time that the alongshore variability χ^2 exceeds the $\chi^2_{crit} = 0.004$ threshold. This threshold, which is reached after approximately 40 h in the reference scenario simulations, coincides with the first apparent rip shoal patterns in the topography and dissipation. Patterns at this stage resemble the first variability towards a Rhythmic Barred Beach beach state as observed at Palm Beach (Figure 5.6). After T_v is reached alongshore variability on the bar crest starts to grow rapidly in magnitude (Figure 5.5a). Results also show that after T_v is reached, the alongshore patterns remain spatially mostly stable until the end of the 90 h simulation (Figure 5.4). It is recognised that the $\chi^2_{crit} = 0.004$ threshold, although it represents the formation time of variability rather well, is arbitrary. The sensitivity of the ratios between T_v values from different simulations to several χ^2 thresholds was tested and showed little sensitivity, indicating that $\chi^2_{crit} = 0.004$ is a robust threshold.

5.3.3 Sensitivity reference case simulations

Model results vary from one simulation to the other due to the stochastic nature of the forcing. The random phases in the generation of wave energy boundary conditions, result in different sequencing and size of incoming wave groups forcing the surf zone flow. In a sensitivity test, the reference case with a standard JONSWAP spectrum is re-simulated ten times to estimate the range of the outcomes related to the randomness in the forcing. The imposed offshore wave conditions in these simulations have identical time-averaged statistical properties (H_{rms}, T_p, κ and σ_θ) but the instantaneous wave energy distributions vary. The different sequencing of wave groups leads to different morphodynamic feedback and model results show different rip channel locations and depths for each of the simulations. Bulk variability χ^2 however develops quite similar, and only slightly different growth rates of χ^2 over time are found (Figure 5.7 a, gray lines). Mean formation time derived from the ten simulations was 38.8 hours, with a standard deviation of 1.2 hours (Table 5.1)indicating that variations of O (5 %) in formation time can be expected in the results just due to the stochastic character of the wave group forcing.

5.3.4 Scenario tests

Formation time of alongshore variability T_v is calculated for model simulations with a variety of offshore wave spectra while varying a single parameter at a time. The model outcomes show a wide range of formation times T_v between 26 and 99 hours (Table 5.1, column 6) indicating that, generally, the type of wave field is of importance for the speed at which the variability in morphology develops. The absolute formation times as calculated here are however not solely a function of T_p, κ and σ_θ, but also on the initial bathymetry, model parameter settings and wave height amongst others. It is therefore more appropriate to present the formation time results of the different scenarios relative to the mean formation time of the reference case simulations (T_v = 38.8 h) so that the relative impact of the parameters varied (T_p, κ and σ_θ) can be objectively assessed.

Wave period

Simulations show a large impact of the offshore wave period on the emerging variability. Figure 5.7a shows the evolution of bulk alongshore variability χ^2 for varying wave period. Longer wave periods yield a faster development in

the first hours of the computation, but also faster development of variability after the formation time. The relative formation times with respect to the $T_p = 10$ s reference case for all wave period simulations are shown in Figure 5.7b. Results show small scatter due to the stochastic nature of the wave group forcing as examined with the reference case, but the trend in the predictions is significantly larger than the observed standard deviation of the sensitivity test. Results confirm the findings of the linear stability analysis study by *Calvete et al.* (2005), albeit showing a more moderate increase in formation time for small wave periods. Formation time T_v is approximately 2.5 times larger for shorter wave periods (T_{m01}= 5 s, characteristic for the Dutch coast) than for wave periods T_{m01} of ∼10 seconds as found at Palm beach. The observed difference in timescales of evolving alongshore topographic variability in chapter 2 and 3 can thus be potentially be in part due to the type of wave field (wind sea vs swell). However, as different beaches vary on multiple aspects (e.g. grain size, beach slope, mean wave angle) and this study only tests the wave field diagnostics it can not be stated that the wave period is the sole reason for the different formation speed between sites. Small variations in wave period in the range T_{m01} of 8-10 seconds such as observed between the different post storm periods at Palm Beach (Figure 3.8) cause only a small (∼ 10 %) difference on the formation time.

Frequency and directional spread

Simulations with different frequency or directional spread of the incoming wave field (with constant T_p) do not show large variations in formation time. Model results show T_v values within the range of values observed in the reference case simulations. To obtain more confidence in the impact of different spreads, the frequency and directional spread simulations are therefore resimulated five times with random phases . Relative formation times for different frequency and directional spreads vary in the O (10 %) range (Figure 5.8). Small trends of O 5% can be observed for both parameters, but these are too small compared to the scatter in the results to be conclusive, thus based on these computations it is concluded that the frequency and directional spreads of the wave field do not significantly affect the formation time of variability in topography.

In summary, model results show that the type of wave field is related to the growth of patterns in the nearshore, where topographic variability can develop at a wide range of speeds for a constant offshore energy flux. The primary aspect of the wave field affecting the formation speed is wave period. Directional and frequency spread appear to have a negligible effect on the formation time of alongshore variability in topography.

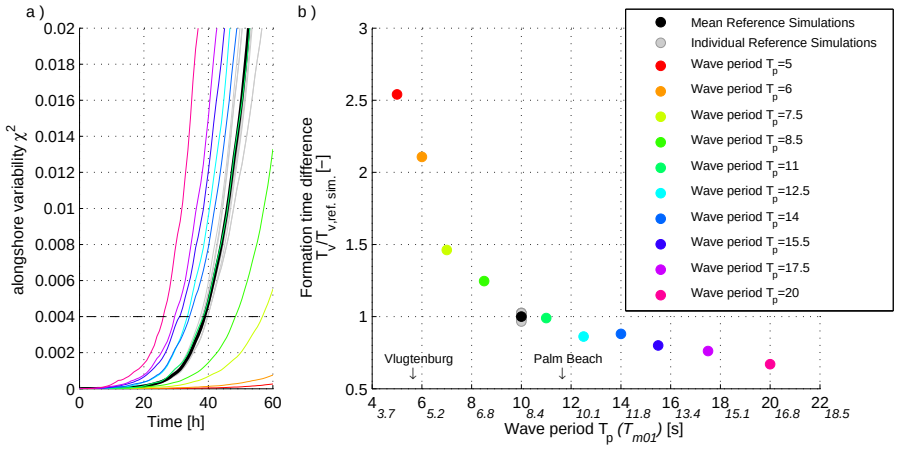

Figure 5.7: a) Development of alongshore variability for various offshore wave periods (in colors, see legend), including the threshold $\chi^2 = 0.004$ for determining the formation time T_v. b) Formation time T_v for various offshore wave periods with respect to the reference scenario with wave period $T_p = 10$s, light gray circles give the 10 individual reference case simulations, black circle gives the mean value. Mean wave period T_{m01} values consistent with the T_p values on the horizontal axis in italic.

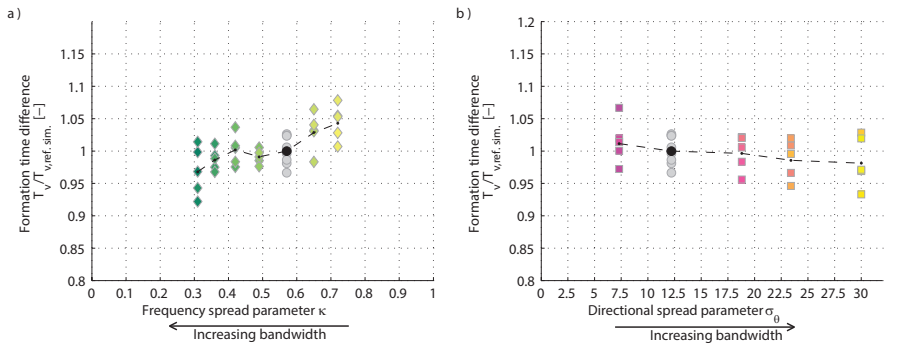

Figure 5.8: Formation time T_v for various offshore frequency spread (a) and directional spread (b) with respect to the reference scenario with a standard JONSWAP spectrum ($\kappa = 0.57$) and narrow directional spread $\sigma_\theta = 12.2$. Black dots show the mean value for each spread value. Light gray circles give the 10 individual reference simulations, black circle gives the mean value.

5.4 Discussion

Results of the morphological computations presented above show that the formation time depends on the sea state but not all parameters have a similar effect. In this section, the relationship between wave conditions and the formation time of alongshore variability are further explored to primarily investigate why frequency and directional spread have limited effect, while wave period has a large effect. To this end, the dependency between the speed of the predicted morphodynamic development and the magnitude of the surf zone motions on different timescales and their effect on the sediment transport capacity are examined in detail.

5.4.1 Flow constituents on the subtidal bar crest

Depth averaged hydrodynamic predictions were recomputed, while allowing no morphological response (i.e. fixed bed). These simulations are similar to computations in Section 4.4 and enable a clear examination of the hydrodynamics in the longshore bar trough (LBT) phase of the beach state cycle just after the storm as the initial bathymetry contains a fixed straight alongshore bar (Figure 5.2) for the full length of the computation. Model and parameter settings are identical to the morphodynamic simulations presented previously.

The offshore wave spectrum was varied for these hydrodynamic cases with input values identical to those in the morphodynamic simulations for the reference run R.101 and a selection of the scenario tests (Table 5.2). Unlike the morphodynamic simulations, where wave group chronology influences the morphological development and feedback, resulting in a scatter of the predictions, time averaged hydrodynamic diagnostics are very similar if tests are repeated. Therefore no sensitivity test is presented here. As with the previous tests, only one spectral parameter κ, σ_θ or T_p was varied at a time. The hydrodynamics were computed for a total of 3 hours only.

Timeseries of the modelled Eulerian velocity (velocity with respect to the bed) $\mathbf{u}_E$ (u_E,v_E) show surf zone flow fluctuations on various timescales (Figure 5.9). These surf zone velocity observations on a single location can separated into four different timescales, related to the origin of the motion:

$$\mathbf{u}_E = \bar{\mathbf{u}}_{\text{mean}} + \mathbf{u}_{\text{VLF}} + \mathbf{u}_{\text{IG}} + \mathbf{u}_{\text{IW}}, \tag{5.2}$$

where $\mathbf{u}_E$ is the total depth averaged Eulerian velocity at a location, $\bar{\mathbf{u}}_{\text{mean}}$ is the time averaged mean flow, $\mathbf{u}_{\text{VLF}}$ is the velocity on time scales of O (10 min) (f <0.004 Hz) associated with shear instabilities of the longshore current

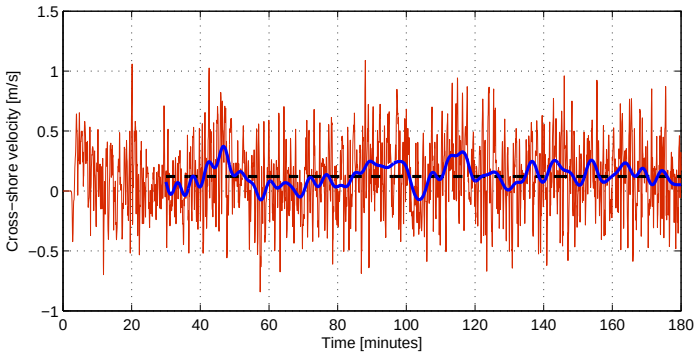

Figure 5.9: Cross-shore velocities on the bar crest (x=190m). Red line is the total short wave averaged cross-shore velocity u_E, blue thick line is the low-pass filtered velocity u_{VLF} and dashed black line the mean velocity u_{mean} on the bar. u_{VLF} and $\bar{u}_{\mathrm{mean}}$ are shown after a spin up time of half an hour.

and vortical VLF surf zone eddies (e.g. *Oltman-Shay et al.*, 1989; *MacMahan et al.*, 2010b). $\mathbf{u}_{\mathrm{IG}}$ contains the contributions of low frequency (infragravity) motions (bound, free and edge wave types) and $\mathbf{u}_{\mathrm{IW}}$ is the intra-wave velocity (orbital motions as well as turbulence). The intra-wave components (u_{IW},v_{IW}) are not resolved in the model as simulations are on the wave group timescale. The impact of intra-wave hydrodynamics (e.g. turbulence and viscosity) on morphodynamics (e.g. wave skewness related sediment transport) are therefore included in an aggregated way (short wave averaged) in the model, at the wave group timescale (see also page 180).

The timeseries of u_E show a small non-zero offshore flow $\bar{u}_{\mathrm{mean}}$ over the bar of O (0.1 m/s). This is because, although the model is depth averaged, the flow velocities obtained from the 2DH shallow water equations (Eqns. B.7 and B.8) are corrected for wave-induced (onshore) mass flux (*Walstra et al.*, 2000). Therefore, a net offshore directed mean current (undertow) is generated to balance the onshore mass flux. The mean cross-shore current on the bar crest $\bar{u}_{\mathrm{mean}}(x = 190\mathrm{m})$ is obtained from the model results by averaging the velocities on the bar $u_E(x = 190\mathrm{m}, y, t)$ in time (2.5 hours) and in the alongshore direction (1500 m) (Figure 5.9, black dashed line). Similarly, the mean alongshore velocity on the bar crest $\bar{v}_{\mathrm{mean}}(x = 190\mathrm{m})$ is computed, but as lateral boundaries are closed and waves are shore normally incident in these simulations, this velocity component is equal to zero.

Mean flow $\bar{u}_{\mathrm{mean}}(x = 190\mathrm{m})$ is subtracted from the velocity signal to ob-

Table 5.2: Numerical model input wave conditions for the hydrodynamic tests. Note that small variations in offshore wave height $H_{\mathrm{rms},8.1}$ are made to maintain an equal offshore energy flux $P_{8.1}$ for all simulations.

Simulation	Wave height $H_{\mathrm{rms},8.1}$ [m]	Wave period T_p [s]	Frequency spread κ [-]	Directional spread σ_θ [deg.]
Reference case				
Test R.101 *hydro*	1.0	10	0.57	12.2
Scenario tests				
Test T.201 *hydro*	1.09	**7.0**	0.57	12.2
Test T.501 *hydro*	0.97	**12.5**	0.57	12.2
Test T.601 *hydro*	0.96	**14.0**	0.57	12.2
Test K.201 *hydro*	1.0	10	**0.36**	12.2
Test K.301 *hydro*	1.0	10	**0.42**	12.2
Test K.601 *hydro*	1.0	10	**0.72**	12.2
Test D.201 *hydro*	1.0	10	0.57	**7.3**
Test D.401 *hydro*	1.0	10	0.57	**18.8**
Test D.501 *hydro*	1.0	10	0.57	**23.4**

tain time varying velocity on the bar crest $u'(x = 190\mathrm{m}, y, t)$. Velocity u' shows a substantial fluctuation on the timescales of O (1 minute), which is related to the intermittent arrival and breaking of individual wave groups on the bar. u' also contains a very low frequency oscillation on the timescales of 5 to 20 minutes (Figure 5.9). Low frequency $u_{\mathrm{IG}}, v_{\mathrm{IG}}$ and very low frequency motions $u_{\mathrm{VLF}}, v_{\mathrm{VLF}}$ were separated by bandpass filtering the velocity signals using $(0.004 < f < 0.04Hz)$ and $(f < 0.004Hz)$ as borders for the infragravity and VLF domain. Magnitudes of fluctuations in surf zone flow at both timescales were then expressed as the root-mean-squared values $u_{\mathrm{VLF,rms}}$ $v_{\mathrm{VLF,rms}}$ $u_{\mathrm{IG,rms}}$ and $v_{\mathrm{IG,rms}}$. These were calculated using only the last 2.5 hours of computation time to avoid the spin-up period of the model.

The mean flow velocity and fluctuating components described above were derived for each of the hydrodynamic model scenarios. Results show that the three main diagnostic parameters of the short wave field (frequency spread κ, directional spread σ_θ and short wave mean period T_p) have different effects on the mean velocity and fluctuation velocities on the bar (Figure 5.10).

As shown in Section 4.4, variations in wave period T_p show a strong positive correlation with the bulk magnitudes of low frequency velocity components (infragravity and VLF), although the mean energy flux entering the domain from offshore was identical in all simulations (Figure 5.10 a). Infragravity flow

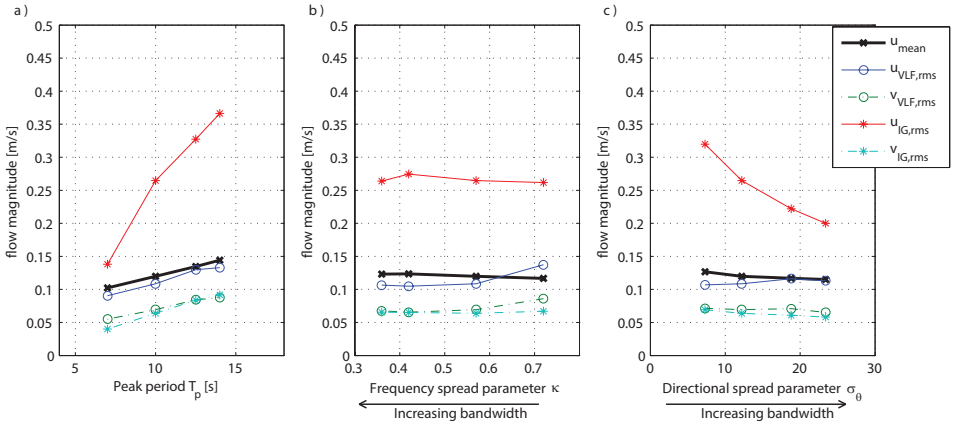

Figure 5.10: Cross-shore flow constituents on the bar vs wave period T_p (a), frequency spread κ (b) and directional spread σ_θ (c). Magnitudes are computed at the bar crest ($x = 190$m) and alongshore averaged values. Note that $\bar{u}_{\mathrm{mean}}$ is a vector and is positive offshore, $u_{\mathrm{IG,rms}}$,$v_{\mathrm{IG,rms}}$,$u_{\mathrm{VLF,rms}}$ and $v_{\mathrm{VLF,rms}}$ are scalars.

velocity magnitude more than double when the wave period T_p increases from 7 to 14 s and VLF velocity fluctuations show an increase in magnitude of O (20 %). A similar increase of O (20 %) was found in the magnitude of the mean cross-shore flow, which partly originates from the more pronounced shoaling of short waves with longer wave periods, resulting in larger wave heights on the bar, larger mass transport over the bar and consequently a larger mean offshore velocity at the bar crest.

In contrast, an increase of the frequency bandwidth or directional spread appeared to have little or no significant effect (<5 %) on the magnitude of the mean flow (Figure 5.10 b,c). Changes in frequency bandwidth however resulted in an increase of O (30 %) in magnitude of the VLF motions as the spectrum narrows, while magnitude infragravity flow remains unaltered.

Variations in spectral directional spread were found to reduce only the magnitude of IG motions significantly while no effect of directional spread was found on the magnitude of VLF motions (Figure 5.10 c). The combined hydrodynamic (Figure 5.10) and morphodynamic model results (Figure 5.7, 5.8) provide insight into the processes governing the formation time of post-reset alongshore variability in nearshore bars. Mean findings presented above are condensed in Table 5.3 for clarity.

Table 5.3: simulated effect of varying wave field characteristics.

Scenario	Hydrodynamics			Morphology
	Mean flow $\bar{u}_{\text{mean}}$	VLF motions $\mathbf{u}_{\text{IG,rms}}$	Infragravity motions $\mathbf{u}_{\text{VLF,rms}}$	Formation Time T_v
Increase in Wave period	increase	increase	increase	decrease
Narrower Frequency spread	$\sim$ no change	increase	$\sim$ no change	$\sim$ no change
Narrower Directional spread	$\sim$ no change	$\sim$ no change	increase	$\sim$ no change

5.4.2 Importance of low frequency flow fluctuations on sediment transport and formation time

As can be seen from the bottom two rows of Table 5.3, the variations in VLF and IG velocity magnitudes found under different frequency and directional spreads do not result in different formation times of topographic variability. To understand this limited influence of both IG and VLF motions, the sediment transport capacity on the subtidal bar is computed. Sediment transport capacity $\mathbf{Q}_{\text{eq}}$, being the capacity of the hydrodynamics to stir and transport sediment, is (integrated over the watercolumn) given by:

$$\mathbf{Q}_{\text{eq}} = h.\mathbf{u}_q.C_{\text{eq}} \tag{5.3}$$

Where $\mathbf{u}_q$ is the sediment transporting velocity vector (u_q,v_q) and C_{eq} is the equilibrium concentration based on the stirring by the local flow velocity and waves (for more detail on the exact sediment formulations in the model, see Appendix section B.5). To examine the importance of the infragravity and VLF motions for the sediment transport capacity four cases are examined (Table 5.4); Case 1) the 'total' flow including low frequency components as used in the previous morphodynamic computations. Case 2) where velocities used for sediment stirring and transport are filtered to remove the VLF motions from the velocity signal. Case 3) where both IG and VLF velocity fluctuations are removed as well as the wave height fluctuations due to the wave grouping, leaving only the mean (wave averaged) flow. Sediment concentrations and hydrodynamics here are constant in time, comparable to a wave averaged computation. And Case 4) a hypothetical case with only mean flow but without the aggregated intra-wave contribution for wave skewness. Table 5.4 clarifies the components included in the calculation of sediment transport capacity in the four cases. $\bar{\mathbf{u}}$ herein is the time-averaged flow (mean undertow), $\widetilde{\mathbf{u}}_{\text{VLF}}$ and $\widetilde{\mathbf{u}}_{\text{IG}}$ are the velocity fluctuations on the VLF and IG timescale respectively.

Table 5.4: Cases used for investigation of the contribution of the importance of VLF motions for the sediment transport capacity. Black squares show the parts used to calculate the sediment transport capacity for each case. Bold values represent the velocity vector(u,v).

	transport velocity components					stirring velocity components				
	$\overline{\mathbf{u}}$	$\widetilde{\mathbf{u}}_{\mathrm{VLF}}$	$\widetilde{\mathbf{u}}_{\mathrm{IG}}$	$\overline{\mathbf{u}}_{\mathrm{IW}}$	$\widetilde{\mathbf{u}_{\mathrm{IW}}}$	$\overline{\mathbf{u}}$	$\widetilde{\mathbf{u}}_{\mathrm{VLF}}$	$\widetilde{\mathbf{u}}_{\mathrm{IG}}$	$\overline{\mathbf{u}}_{\mathrm{SW,rms}}$	$\widetilde{\mathbf{u}_{\mathrm{SW,rms}}}$
Case 1. *Total flow*	■	■	■	■	■	■	■	*	■	■
Case 2. *No VLF motions*	■		■	■°	■°	■		*	■	■
Case 3. *No VLF, no IG motions, and no H_{rms} variations*	■			■°		■		*	■	
Case 4. *No VLF, no IG motions, no H_{rms} variations and no intra-wave effects*	■					■		*	■	

* In the current model setup, IG velocities are not incorporated in the stirring of sediment (see Appendix section B.5).
° Intra-wave transports are slightly affected by the removal of VLF and IG velocities.

$\overline{\mathbf{u}}_{\mathrm{IW}}$is the time-averaged contribution of wave skewness, and $\widetilde{\mathbf{u}_{\mathrm{IW}}}$the temporal variation this skewness contribution, due to variations in wave heights on the wave group timescale amongst others. Intra-wave effects are also included in the stirring of sediment and displayed as the $\overline{\mathbf{u}}_{\mathrm{SW,rms}}$ and $\widetilde{\mathbf{u}_{\mathrm{SW,rms}}}$ components (see page 179). The former is the mean stirring due to the short wave motion (orbital motions and turbulence) and latter is the temporal fluctuation of this stirring due to variations in wave height amongst others.

Inter comparison of the four cases shows the importance of IG and VLF motions for the sediment transport capacity. For the reference forcing scenario ($T_p = 10$ s, $\kappa = 0.57$, $\sigma_\theta = 12.2$ deg) the computed depth-integrated 2.5-hour-averaged transport capacity values are given in Table 5.5. Transport is split in net time-averaged parts, $\overline{Q_x}$ and $\overline{Q_y}$, and the size of fluctuations on these net values, $\widetilde{Q_{x,\mathrm{rms}}}$ and $\widetilde{Q_{y,\mathrm{rms}}}$. From the different cases it can be concluded that mean sediment transport capacity on the bar crest is negative (onshore) and mostly determined by the wave averaged components, responsible for O (70 %) of the net transport $\overline{Q_x}$ (Table 5.5, column 2). IG motions account for the remaining 29 % of net transport capacity. The onshore orientation of the transport is due to the large intra-wave contribution at this location. Without

the intra-wave transport, net transport is oriented offshore due to the mean (mass compensating) flow (Table 5.5, row 5).

Table 5.5: Sediment transport capacity on the bar crest for the four cases using the forcing of scenario R.101 (Reference scenario). Values in brackets indicate the percentages with respect to Case (1), which uses all components in the model. Values are integrated over the water column and per meter along or cross-shore $[kgm^{-1}s^{-1}]$.

	Cross-shore Q_x		Alongshore Q_y	
	mean $\overline{Q_x}$ (%) neg. = onshore	fluctuations $\widetilde{Q_{x,\mathrm{rms}}}$ (%)	mean $\overline{Q_y}$ (%)	fluctuations $\widetilde{Q_{y,\mathrm{rms}}}$ (%)
Case 1. *Total flow*	-0.048 (100)	0.094 (100)	$\sim$ 0 (-)	0.029 (100)
Case 2. *No VLF motions*	-0.048 (100)	0.088 (93)	$\sim$ 0 (-)	0.018 (63)
Case 3. *No VLF, no IG motions, and no H_{rms} variations*	-0.034 (71)	$\sim$ 0 (0)	$\sim$ 0 (-)	$\sim$ 0 ($\sim$ 0)
Case 4. *No VLF, no IG motions, no H_{rms} variations and no intra-wave effects*	+0.032 (N/A)	$\sim$ 0 (0)	$\sim$ 0 (-)	$\sim$ 0 ($\sim$ 0)

The inclusion of VLF velocity fluctuations is found to have a negligible effect on net sediment transport capacity. At the bar crest, the majority of the stirring (>90%) is due to the short wave action and the fluctuations of the flow velocity at VLF timescale yield very limited of variations in equilibrium sediment concentration. The net contribution of VLF motions on net sediment transport is nearly zero because 1. the transporting velocity of VLF motions is net zero, 2. stirring is not substantially larger under onshore than offshore motions, and 3. VLF circulation cells are not stationary.
Similar to VLF motions, the transporting velocity of IG velocity fluctuations is net zero. But, as the short wave stirring is consistently larger under onshore than under offshore infragravity motions (i.e. higher short waves coincide with onshore IG velocity waves) the net onshore contribution of 29 % is found.

Fluctuations in sediment transport capacity are primarily determined by variations in transporting part $\mathbf{u}_q$ rather than the concentration C_{eq}. The majority (93 %) of the cross-shore fluctuations can be attributed to IG flow velocities (Table 5.5, column 3). The inclusion of VLF motions accounts for only 7 % of $\widetilde{Q_{x,\mathrm{rms}}}$. In alongshore direction the fluctuations in sediment transport capacity are smaller, as waves are shore normally incident. This affects primarily the contribution of infragravity motions and consequently the VLF

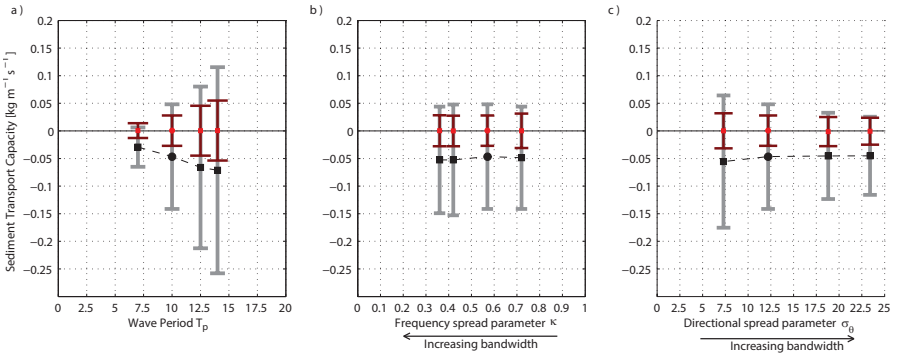

Figure 5.11: Depth integrated sediment transport capacity Q_x and Q_y vs wave period (a), frequency spread (b) and directional spread (c). Magnitudes are computed at the bar crest ($x = 190$m). Mean cross (along) shore sediment transport capacity $\overline{Q_x}$ ($\overline{Q_y}$)given by the black (red) symbols. Error bars indicate the root-mean-squared magnitude of the transport capacity fluctuations $\widetilde{Q_{x,\mathrm{rms}}}$ and $\widetilde{Q_{y,\mathrm{rms}}}$.

motions have a larger relative contribution to $\widetilde{Q_{y,\mathrm{rms}}}$ of 37 % (Table 5.5, column 5).

As a final step, the magnitudes of mean sediment transport capacity (and fluctuations) were computed for the total flow case(1) of all hydrodynamic scenarios (Fig. 5.11). Earlier findings on T_v dependencies are found to be consistent with variations in $\overline{Q_x}$ and $\widetilde{Q_{y,rms}}$. From these results it could be insinuated that the $\overline{Q_x}$ indicates the potential for morphological feedback, while the alongshore component $\widetilde{Q_{y,rms}}$ provides a dampening effect. Scenarios with changing frequency and directional bandwidth (Fig. 5.11,b and c) show no change in either $\overline{Q_x}$ or $\widetilde{Q_{y,rms}}$, in line with the negligible changes in T_v for these scenarios.

5.5 Conclusions

A series of strategic numerical model simulations were undertaken to investigate potential dependencies between the emergence of post-reset alongshore variability in nearshore bars and the type of wave field (swell vs wind sea) that prevails immediately following morphology resetting storms. A research version of *Delft3D*, which includes wave group forcing, was applied to a schematised bathymetry representing Palm Beach, Australia. The type of wave field

was varied using the three main wave field diagnostics: frequency spread, directional spread and short wave period.

Model results showed that alongshore variability can develop at a wide range of speeds for a constant offshore energy flux, depending on the characteristics of the wave field. Under the conditions tested, differences in short wave period as found between Dutch and Australian sites were able to vary the formation time of post-reset alongshore variability by a factor 2.5. Variations in frequency and directional spread of the wave field had little effect on the formation time.

These findings indicated that the development of alongshore topographic variability may be faster at swell dominated open coasts, primarily due to the occurrence of longer period swell.

Closer examination of the morphodynamic simulations, simulations of hydrodynamics only and potential sediment transport cases showed that variations in formation time were primarily linked to changes in the magnitude of the time-averaged flow conditions. Different sea state scenarios resulting in variations in the magnitude of very low frequency ($f < 0.004Hz$) or infragravity ($0.004 < f < 0.04Hz$) surf zone velocities showed similar formation times of the topographic variability. Analysis of the model results show that variation in VLF motion magnitude did not result in different mean sediment transport capacity in the model as 1. the sediment transporting velocity of VLF motions is net zero, 2. stirring is not substantially larger under onshore than offshore VLF motions, and 3. VLF circulation cells are spatially highly variable. It is therefore concluded that VLF motions have a very limited effect on the formation time of variability.

Acknowledgements

Deltares is acknowledged for the use of their *Delft3D* numerical model suite. Part of the work was executed during a short visit at the Rosenstiel School of Marine and Atmospheric Science, Miami, USA. The author thanks RSMAS and the Reniers family for their hospitality.

6 Conclusions and recommendations

6.1 Synthesis

The present study investigated the alongshore variability in topography and in particular at nourished beaches. Alongshore topographic variability and the horizontal flow circulation patterns in the surf zone are of importance for the mixing in the coastal zone and can cause distress to swimmers.
Measurements of a large nourishment case study in the current research revealed no large differences in topographic variability magnitude in the first period after implementation of a nourishment compared to the following years. Observed changes in profile shape over time did not coincide with a noticeable trend in variability magnitude. Moreover, changes in topographic variability were shown to be slow, on the timescale of months.
Further investigation of the formation of alongshore variability in topography using data of Palm Beach, Australia and model simulations, showed that the formation speed is dependent on wave angle and wave period. These findings clarified the observed slow response under typical 'wind sea' wave conditions at the Dutch coast (i.e. large wave angles and short wave periods).
Results confirmed the hypothesised impact of sea state on the formation of variability, yet only for the wave period (*Hypothesis H.1*). Frequency band-

width and directional spread did not have a large effect on formation times. Sea state diagnostics (wave period, frequency bandwidth and directional spread) were further shown to impact the very low frequency (VLF) velocity fluctuations in the surf zone. Analysis showed that swell waves as well as steep slopes yielded stronger VLF motions than nearby generated short wind seas and mild slopes. Conceptual modelling however rejected the hypothesised impact of VLF motion magnitude on the formation time of topographic variability (*Hypothesis H.2*).

Detailed conclusions of the 4 research objectives are given below.

1. Examine the morphological development and emergent alongshore topographic variability at a beach after implementation of a nourishment with frequent topographic surveys.
Over 3 years of morphodynamic data were collected at Vlugtenburg beach after implementation of a large nourishment removing all variability prior to the project. Bathymetric surveys (38 in total) were executed nearly monthly using a jetski with single beam echosounder and a RTK-GPS backpack. The morphodynamic data were examined to investigate 1) the adaptation of the constructed profile towards a more natural profile and 2) the generation and evolution of alongshore variability in topography.

The overall morphological evolution was characterised by two periods, a first period of 6 to 12 months in which the largest losses of sediment volume of O (70 m^3 / m alongshore / yr) were observed, while the steep foreshore slope was re-adjusting and a subtidal bar was formed. The following 2.5 to 3 years showed a slower evolution, and sediment losses in the area were limited of O (15 m^3/m/year). The initial increase in volume losses after the implementation of the nourishment was found to be in part a result of the construction profile. It was shown that steeper profiles yield an increase in alongshore losses at coastal stretches where alongshore gradients in transport are present.

The emergence of a migrating subtidal bar system was observed at Vlugtenburg beach and the magnitude of the alongshore variability was compared to environmental and topographic controls previously suggested. The analysis showed that the alongshore variability was evolving on a monthly timescale, slower than previous observations at the US east coasts or Australian coasts. The first period just after completion of the nourishment showed no different magnitudes or evolution rates of variability than the total period investigated, such that an apparent effect of the nourishment on the variability could not be discerned.

Neither geometry of the subtidal bar or parameters describing the wave

forcing in a month gave a direct correlation with the alongshore variability observed in the topography at a single moment in time. However, the temporal change in the magnitude of the alongshore topographic variability (the change with respect to the previous month) was found to be related to the incoming wave power, offshore migration of the subtidal bar and erosion on the upper beach; parameters that primarily changed during large storms. The relation with wave power was found to be positive, meaning that storms do not remove the alongshore variability at Vlugtenburg beach, which is in contrast to other beaches. Instead, energetic storm events during late autumn and winter months (October to January) resulted in a rapid increase in variability, which was then followed by a gradual decrease in alongshore variability during milder spring and summer wave conditions.

2. Examine the impact of wave field characteristics (wind sea vs swell) on the emergence of alongshore topographic variability.
An isolated case, of post storm re-emergence of topographic variability was investigated. In contrast to other studies, this phenomenon was investigated using field data. Several transitional periods (in which the topography evolved from nearly alongshore uniform to alongshore variable) at Palm Beach, Australia were examined with the concurrent wave conditions to observe preferential conditions for which rapid development of variability occurs.

Analysis of the storm reset events for which high quality data were available during the 4 year study period confirmed the previous model derived observations that (a) there is no clear dependency of T_v on wave height or wave period for the time periods investigated, and (b) there is a clear dependency of T_v on wave angle such that large T_v's coincided with very oblique wave angles. The data also suggested a dependency of T_v on frequency bandwidth such that large (small) T_v's coincided with the prevalence of wide (narrow) banded sea (swell) wave conditions after the resetting storm.

It was recognised that the video images used do not capture the geometric differences in topography between the reset events, and therefore findings on the relation between sea state of the incoming wave field and the formation time were explored further with a numerical morphodynamic model. A research version of *Delft3D* operating on the time-scale of wave groups, was applied to investigate the impact of peak period, frequency spread and directional spread individually. Results showed that a large increase in wave period has a strong effect, changing the formation time up to O (250%) in case the wave period was changed from typical Dutch (T_{m01}=5 s) to Australian (T_{m01}=10 s) conditions. Small variations in wave period of O (1-2 s), as observed between different post-reset periods at Palm Beach, had only a minor effect on the for-

mation time. Modifications in the other sea state parameters, the directional and frequency spread of the wave field, were shown to have a negligible effect on the predicted formation time.

In all, these findings imply that, based on the wave period and wave angle alone, open ocean coasts with shore-normal or moderately obliquely incident, swell waves represent preferential conditions for rapid development of topographic variability.

3. Examine the magnitude of Very Low Frequency surf zone motions under different sea states (wind sea vs swell) and profiles.
Another mechanism for horizontal flow circulations, the VLF motions were investigated in more detail. A field campaign was conducted at Vlugtenburg Beach, the Netherlands, and instruments were deployed on multiple days resulting in measurements within and outside the surf zone. Observations on a day with intermediate wave height (offshore H_s of 1.4 m) showed the presence of motions in the very low frequency range of O (0.1 m/s) inside the surf zone in without a strong mean alongshore current. This demonstrated that VLF motions in absence of alongshore current are not restricted to open ocean beaches with swell waves.

Next, a large dataset of VLF observations of the 4 month SandyDuck '97 field campaign at Duck, NC, USA were re-analysed to investigate the effect of wave forcing conditions on vortical VLF motion magnitude. Vortical VLF motion magnitude related primary to the wave height, with stronger VLF velocity fluctuations observed at instants with higher incoming waves. For a given wave height however, the VLF motions were found to be stronger during instants with incoming waves with long wave period, narrow frequency spread, or both. No clear trend was observed when the observations were differentiated to times when the incoming wave field had different directional spreads. Swell-like wave conditions characterised by narrow frequency spreads and long wave periods were thus concluded to promote VLF motions of large magnitude.

Furthermore, a numerical model on the long wave time scale was used to experiment with the effect of forcing parameters in a more isolated way. The results of conceptual model simulations with various forcing scenarios confirmed the observed effect of frequency spread and wave period on the magnitude of VLF motions. The magnitudes of vortical VLF velocity fluctuations were found to vary with O (50 %) when the characteristics of the incident wave spectrum changed. Additional computations with the conceptual model also indicated that the slope of the surf zone near the breakpoint largely affects the magnitude of VLF motions. Steeper slopes near the breakpoint yielded 500 % stronger VLF motions. This clarified the strong VLF motions predom-

inantly found in earlier field studies at sites with steep sloping profiles near the breakpoint. It also clarified that, despite the short wave periods, VLF motions could be observed at the Dutch coast. These findings imply that VLF motions can be particularly strong after installation of a nourishment if the post-construction profile is very steep.

4. Examine the relation between VLF motion magnitude and the formation time of topographic variability.
Closer examination of the morphodynamic simulations, simulations of hydrodynamics only and potential sediment transport cases showed that variations in formation time are primarily linked to changes in the magnitude of the time-averaged flow conditions. Different sea state scenarios resulting in variations in the magnitude of very low frequency ($f < 0.004Hz$) or infragravity ($0.004 < f < 0.04Hz$) surf zone velocities showed similar formation times of the topographic variability. Changing VLF motion magnitude did not result in different mean sediment transport capacity in the model as 1. the sediment transporting velocity of VLF motions is net zero, 2. stirring is not substantially larger under onshore than offshore VLF motions, and 3. VLF circulation cells are not stationary. It is therefore concluded that VLF motion magnitudes have only limited effect on the formation time of variability.

6.2 Recommendations

1. Prior to the present research it was unclear how a large scale nourishment may influence alongshore topographic variability on a beach. The changes in profile shape due to such nourishments could potentially change the development of alongshore topographic variability (e.g. *Damgaard et al.*, 2002; *Calvete et al.*, 2007; *Klein*, 2006). The present research showed no apparent effect of the profile such that the alongshore variability in the first phase after implementation of the nourishment (i.e. steep slope, shallow small bar close to shore) shows different behaviour than the last part of the campaign. Possibly the results are bound to the investigated coastal stretch, with predominantly large angles of wave incidence and short wave periods resulting an a slower response of variability. The results also did not provide field evidence whether the emergence and evolution of variability could be affected by selecting a different nourishment design (e.g. by applying a milder construction slope). It is therefore recommended to extend the current study with data from other nourishment projects elsewhere. Large nourishment projects are particularly of interest, as these minimise the effects of pre-existing mor-

phology and variability providing a better comparison with conceptual cases examined in modelling studies.

2. The present research underlined the difficulty in providing a prediction of the alongshore variability in the topography. Alongshore topographic variability is known to be related to both wave forcing and profile shape, and when diagnostics of both were tested individually in this thesis, a significant correlation was found for parameters describing either one (§ 2.5.2). As a result, removal and formation of alongshore variability occurs under a broad range of conditions and results in Chapter 3 even showed that variability could be either removed or generated under similar wave heights (Figure 3.8, p. 77). These field data underlined that a single blueprint of favorable conditions for removal or formation of variability is implausible.
Detailed information on hydrodynamics during post-reset events in combination with high quality topography data is essential information to further advance the knowledge of the formation of variability. Additionally, this could be attempted in a laboratory wave basin experiment. Regardless whether data is obtained from the laboratory or the field, good validation data for the formation of variability is currently lacking, and such data would provide a necessary first benchmark study to test formation characteristics and predictions by numerical models.

3. The effect of sea state parameters on the emergence of alongshore topographic variability was examined in this study using numerical model simulations on a wave group timescale. Effects of differences in wave period, frequency bandwidth and directional spread on vortical motions on smaller scales were therefore unaccounted for. To extend the current analysis, it would be of interest to re-evaluate the hypothesis using a conceptual morphodynamic model on the short wave scale (i.e. including the smaller scale vorticity effects omitted here), once such computations become computationally feasible.

4. The new findings on the effect of sea states and profile shape on large scale low frequency hydrodynamics in the surf zone (VLF and infragravity waves) could be further confirmed using a laboratory wave basin experiment with directionally spread waves. Numerical modelling studies require a parametrization for (the initiation of) wave breaking and such processes at the breakpoint govern the VLF motion magnitude. Data of a laboratory wave basin experiment with a fixed bed, different cross-shore profiles and under various sea states would be a large benefit for future research of VLF motions, providing additional data on the coupling between breakpoint processes and VLF motion generation.

References

Aagaard, T., and B. Greenwood (1995), Longshore and cross-shore suspended sediment transport at far infragravity frequencies in a barred environment, *Continental Shelf Research*, *15*(10), 1235–1249.

Aagaard, T., and M. G. Hughes (2010), Breaker turbulence and sediment suspension in the surf zone, *Marine Geology*, *271*(3-4), 250–259.

Aarninkhof, S., J. van Dalfsen, J. Mulder, and D. Rijks (2012), Sustainable development of nourished shorelines. Innovations in project design and realisation, *PIANC MMX Congress, Liverpool, UK*.

Allen, J. R. (1985), Field evaluation of beach profile response to wave steepness as predicted by the Dean model, *Coastal Engineering*, *9*(1), 71–80.

Austin, M. J., T. M. Scott, P. E. Russell, and G. Masselink (2012), Rip current prediction: Development, validation, and evaluation of an operational tool, *Journal of Coastal Research*, *29*(2), 283–300.

Battjes, J. A. (1974), Surf similarity, *Proceedings of the International Conference on Coastal Engineering; No 14*, pp. 466–480.

Battjes, J. A., and M. J. F. Stive (1985), Calibration and verification of a dissipation model for random breaking waves, *Journal of Geophysical Research*, *90(C5)*, 9159–9167.

Battjes, J. A., H. J. Bakkenes, T. T. Janssen, and A. R. van Dongeren (2004), Shoaling of subharmonic gravity waves, *Journal of Geophysical Research*, *109*(C2).

Bowen, A. J., and R. Holman (1989), Shear instabilities of the mean longshore current: 1. Theory, *Journal of Geophysical Research*.

Bowen, A. J., and D. L. Inman (1971), Edge waves and crescentic bars,, *Journal of Geophysical Research*, *76, No. 36*, 8662–8671.

Bowman, D., D. Rosen, E. Kit, D. Arad, and A. Slavicz (1988), Flow characteristics at the rip current neck under low energy conditions, *Marine geology*, *79*(1), 41–54.

Brander, R. W., and A. Short (2001), Flow kinematics of low-energy rip current systems, *Journal of Coastal Research*, pp. 468–481.

Brander, R. W. (1999), Field observations on the morphodynamic evolution of a low-energy rip current system, *Marine Geology*, *157*(3-4), 199–217.

Brander, R. W., and J. H. MacMahan (2011), Future challenges for rip current research and outreach, *Rip Currents: Beach Safety, Physical Oceanography and Wave Modeling*, pp. 1–29.

Caballeria, M., G. Coco, A. Falqués, and D. A. Huntley (2002), Self-organization mechanisms for the formation of nearshore crescentic and transverse sand bars, *Journal of Fluid Mechanics*, *465*, 379–410.

Calvete, D., N. Dodd, A. Falqués, and S. M. van Leeuwen (2005), Morphological development of rip channel systems: Normal and near-normal wave incidence, *Journal of Geophysical Research*, *110*(C10).

Calvete, D., G. Coco, A. Falqués, and N. Dodd (2007), (Un)predictability in rip channel systems, *Geophys. Res. Lett.*, *34*(5).

Castelle, B. (2004), Modélisation de l'hydrodynamique sédimentaire au-dessus des barres sableuses soumises à láction de la houle: application à la côte Aquitaine., Ph.D. thesis, Univ. Bordeaux I, Talence, France.

Castelle, B., P. Bonneton, and R. Butel (2006), Modélisation du festonnage des barres sableuses d'avant-côte : application à la côte Aquitaine, France, *Comptes Rendus Geoscience*, *338*(11), 795–801.

Castelle, B., P. Bonneton, H. Dupuis, and N. Sénéchal (2007), Double bar beach dynamics on the high-energy meso-macrotidal French Aquitanian coast: A review, *Marine Geology*, *245*(14), 141–159.

Castelle, B., et al. (2009), Rip current system over strong alongshore non-uniformities: on the use of hADCP for model validation, *Journal of Coastal Research, SI*, *56*, 1746–1750.

Castelle, B., B. G. Ruessink, P. Bonneton, V. Marieu, N. Bruneau, and T. D. Price (2010), Coupling mechanisms in double sandbar systems. Part 1: patterns and physical explanation, *Earth Surf. Process. Landforms*, *35*(4), 476–486.

Chen, C. T., and F. J. Millero (1977), Speed of sound in seawater at high pressures, *The Journal of the Acoustical Society of America*, *62*.

Clarke, L. B., D. Ackerman, and J. Largier (2007), Dye dispersion in the surf zone: Measurements and simple models, *Continental shelf research*, *27*(5), 650–669.

Coco, G., and A. B. Murray (2007), Patterns in the sand: From forcing templates to self-organization, *Geomorphology*, *91*(3-4), 271–290.

Coco, G., M. Caballeria, A. Falqués, and D. A. Huntley (2002), Cresentic bars and nearshore self-organization processes, *Proceedings of the International Conference on Coastal Engineering; No 28*, pp. 3765–3777.

Cook, D. O. (1970), The occurrence and geologic work of rip currents off southern california, *Marine Geology*, *9*(3), 173–186.

Dalrymple, R. A. (1975), A mechanism for rip current generation on an open coast, *Journal of Geophysical Research*, *80(24)*, 3485–3487.

Dalrymple, R. A. (1992), Prediction of storm normal beach profiles, *Journal of Waterway, Port, Coastal and Ocean Engineering*, *118*(2), 193–200.

Dalrymple, R. A., and W. W. Thompson (1976), Study of equilibrium beach profiles, *Proceeding of the International conference on Coastal Engineering*, pp. 1277–1296.

Dalrymple, R. A., J. H. MacMahan, A. J. H. M. Reniers, and V. Nelko (2011), Rip currents, *Annual Review of Fluid Mechanics*, *43*(1), 551–581.

Damgaard, J., N. Dodd, L. Hall, and T. Chesher (2002), Morphodynamic modelling of rip channel growth, *Coastal Engineering*, *45*(3-4), 199–221.

de Sonneville, B., and A. van der Spek (2012), Sediment-and morphodynamics of shoreface nourishments along the North-Holland coast, *Proceeding of the International conference on Coastal Engineering*, *1*(33).

de Vries, S., M. A. de Schipper, M. J. F. Stive, and R. Ranasinghe (2010), Sediment exchange between the sub-aqueous and sub-aerial coastal zones., *Proceeding of the International conference on Coastal Engineering*, *2*.

de Vries, S., H. Southgate, W. Kanning, and R. Ranasinghe (2012), Dune behavior and aeolian transport on decadal timescales, *Coastal Engineering*, *67*, 41–53.

Dean, R., and R. Dalrymple (2002), *Coastal Processes with Engineering Applications*, Cambridge University Press.

Dean, R. G. (2002), *Beach nourishment: theory and practice*, vol. 18, World Scientific Publishing Company Incorporated.

Deigaard, R., N. Drønen, J. Fredsøe, J. H. Jensen, and M. P. Jørgensen (1999), A morphological stability analysis for a long straight barred coast, *Coastal Engineering*, *36*(3), 171–195.

Dodd, N., V. Iranzo, and A. J. H. M. Reniers (2000), Shear instabilities of wave-driven alongshore currents, *Rev. Geophys*, *38*(4), 437–463.

Drønen, N., and R. Deigaard (2007), Quasi-three-dimensional modelling of the morphology of longshore bars, *Coastal Engineering*, *54*(3), 197–215.

Dugan, J., W. Morris, K. Vierra, C. Piotrowski, G. Farruggia, and D. Campion (2001), Jetski-based nearshore bathymetric and current survey system, *Journal of Coastal Research*, pp. 900–908.

Elgar, S., R. Guza, W. O'Reilly, B. Raubenheimer, and T. Herbers (2001), Wave energy and direction observed near a pier, *Journal of Waterway, Port, Coastal and Ocean Engineering*, *127*(1), 2–6.

Falqués, A., G. Coco, and D. A. Huntley (2000), A mechanism for the generation of wave-driven rhythmic patterns in the surf zone, *Journal of Geophysical Research*, *105*(C10), 24,071–24,087.

Falqués, A., N. Dodd, R. Garnier, F. Ribas, L. MacHardy, P. Larroudé, D. Calvete, and F. Sancho (2008), Rhythmic surf zone bars and morphodynamic self-organization, *Coastal Engineering*, *55*(7-8), 622–641.

Feddersen, F. (2004), Effect of wave directional spread on the radiation stress: comparing theory and observations, *Coastal Engineering*, *51*(56), 473–481.

Galappatti, R. (1983), A depth integrated model for suspended transport, *Tech. rep.*, 83-7. Delft University of Technology, Netherlands.

Garnier, R., D. Calvete, A. Falqués, and N. Dodd (2008), Modelling the formation and the long-term behavior of rip channel systems from the deformation of a longshore bar, *Journal of Geophysical Research*, *113*(C7).

Geiman, J., J. Kirby, A. J. H. M. Reniers, and J. H. MacMahan (2011), Effects of wave averaging on estimates of fluid mixing in the surf zone, *Journal of Geophysical Research*, *116*(C4).

Grant, S., J. Kim, B. Jones, S. Jenkins, J. Wasyl, and C. Cudaback (2005), Surf zone entrainment, along-shore transport, and human health implications of pollution from tidal outlets, *Journal of Geophysical Research*, *110*(C10).

Grunnet, N. M., and B. G. Ruessink (2005), Morphodynamic response of nearshore bars to a shoreface nourishment, *Coastal Engineering*, *52*(2), 119–137.

Grunnet, N. M., D.-J. R. Walstra, and B. G. Ruessink (2004), Process-based modelling of a shoreface nourishment, *Coastal Engineering*, *51*(7), 581–607.

Guza, R., and F. Feddersen (2012), Effect of wave frequency and directional spread on shoreline runup, *Geophysical Research Letters*, *39*(11).

Guza, R., and E. Thornton (1980), Local and shoaled comparisons of sea surface elevations, pressures, and velocities, *Journal of Geophysical Research*, *85*(C3), 1524–1530.

Haller, M., U. Putrevu, J. Oltman-Shay, and R. Dalrymple (1999), Wave group forcing of low frequency surf zone motion, *Coastal Engineering*, *41*(2), 121–136.

Haller, M. C., and R. A. Dalrymple (2001), Rip current instabilities, *Journal of Fluid Mechanics*, *433*, 161–192.

Hamm, L., M. Capobianco, H. Dette, A. Lechuga, R. Spanhoff, and M. J. F. Stive (2002), A summary of European experience with shore nourishment, *Coastal Engineering*, *47*(2), 237–264.

Hanson, H., A. Brampton, M. Capobianco, H. Dette, L. Hamm, C. Laustrup, A. Lechuga, and R. Spanhoff (2002), Beach nourishment projects, practices,

and objectives: a European overview, *Coastal Engineering*, *47*(2), 81–111.

Hattori, M. (1982), Field study on onshore-offshore sediment transport, *Proceedings of the International Conference on Coastal Engineering; No 18*.

Herbers, T., S. Elgar, and R. Guza (1999), Directional spreading of waves in the nearshore, *Journal of Geophysical Research*, *104*(C4), 7683–7693.

Hino, M. (1974), Theory on formation of rip-current and cuspidal coast, *Proceedings of the International Conference on Coastal Engineering; No 14*.

Hoitink, A., F. Buschman, and B. Vermeulen (2009), Continuous measurements of discharge from a horizontal acoustic doppler current profiler in a tidal river, *Water Resources Research*, *45*.

Holland, K., R. Holman, T. Lippmann, J. Stanley, and N. Plant (1997), Practical use of video imagery in nearshore oceanographic field studies, *Journal of Oceanic Engineering*, *22*(1), 81–92.

Holman, R. A., and A. J. Bowen (1982), Bars, bumps, and holes: Models for the generation of complex beach topography, *Journal of Geophysical Research*, *87*(C1), 457–468.

Holman, R. A., G. Symonds, E. B. Thornton, and R. Ranasinghe (2006), Rip spacing and persistence on an embayed beach, *Journal of Geophysical Research*, *111*(C1).

Holthuijsen, L. (2007), Waves in oceanic and coastal waters, *Cambrigde University Press*.

Holthuijsen, L., N. Booij, and T. Herbers (1989), A prediction model for stationary, short-crested waves in shallow water with ambient currents, *Coastal Engineering*, *13*(1), 23–54.

Hom-ma, M., and C. Sonu (1962), Rhythmic pattern of longshore bars related to sediment characteristics, *Proceeding of the International conference on Coastal Engineering*, *1*(8).

Hoogheemraadschap van Delfland (2007), Verbeteringsplan versterking Delflandse kust, *(In Dutch)*, *W3487-02.001/ WG-SE20060877*.

Inman, D. L., R. J. Tait, and C. E. Nordstrom (1971), Mixing in the surf zone, *Journal of Geophysical Research*, *76*(15), 3493–3514.

Jiménez, J. A., J. Guillén, and A. Falqués (2008), Comment on the article: Morphodynamic classification of sandy beaches in low energetic marine environments by Gómez-Pujol, L., Orfila, A., Cañellas, B., Alvarez-Ellacuria, A., Méndez, F.J., Medina, R. and Tintoré, *Marine Geology*, *255*(1-2), 96–101.

Johnson, D., and C. Pattiaratchi (2004), Transient rip currents and nearshore circulation on a swell-dominated beach, *Journal of Geophysical Research*, *109*(C2).

Kamminga, S., N. van Neerven, and C. Mooiman (1998), Results of a horizontally mounted acoustic doppler current profiler, in *OCEANS'98 Conference Proceedings*, vol. 1, pp. 253–256.

Kamphuis, J. (1991), Alongshore sediment transport rate, *J. Waterway, Port, Coastal, Ocean Eng.*, *117*(6), 624–640.

Klein, M. D. (2006), Modelling rhythmic morphology in the surf zone, *PhD Thesis, Delft University of Technology*.

Klein, M. D., H. Schuttelaars, and M. J. F. Stive (2002), Linear stability of a double-barred coast, *Proceeding of the International conference on Coastal Engineering*, pp. 3396–3408.

Komar, P. D. (1998), *Beach processes and sedimentation*, Prentice Hall.

Kuik, A., G. van Vledder, and L. Holthuijsen (1988), A method for the routine analysis of pitch-and-roll buoy wave data, *Journal of Physical Oceanography*, *18*(7), 1020–1034.

Larson, M., and N. C. Kraus (1989), "SBEACH: Numerical model for simulating storm-induced beach change." CERC-89-9, *Tech. rep.*, U.S. Army Corps of Engrs. Coastal Engrg. Res. Ctr., Vicksburg, Va.

Larson, M., and N. C. Kraus (1994), Temporal and spatial scales of beach profile change, Duck, North Carolina, *Marine Geology*, *117*(1), 75–94.

Lesser, G., J. Roelvink, J. van Kester, and G. Stelling (2004), Development and validation of a three-dimensional morphological model, *Coastal Engineering*, *51*(8-9), 883–915.

Lippmann, T., and R. A. Holman (1989), Quantification of sand bar morphology: a video technique based on wave dissipation, *Journal of Geophysical Research*, *94*.

Lippmann, T., and R. A. Holman (1990), The spatial and temporal variability of sand bar morphology, *Journal of Geophysical Research*, *95*, 575–590.

Long, C., and J. Atmadja (1994), Index and bulk parameters for frequency-direction spectra measured at CERC field research facility, September 1990 to August 1991, *Tech. rep.*, Field Research Facility.

Long, J. W., and H. T. Özkan-Haller (2005), Offshore controls on nearshore rip currents, *Journal of Geophysical Research*, *110*(C12).

Long, J. W., and H. T. Özkan-Haller (2009), Low-frequency characteristics of wave group-forced vortices, *Journal of Geophysical Research*, *114*(C8).

Longuet-Higgins, M. S., and R. W. Stewart (1962), Radiation stress and mass transport in gravity waves, with application to surf beats., *Journal of Fluid Mechanics*, *13*, 481–504.

MacKenzie, K. (1981), Nine-term equation for sound speed in the oceans, *The Journal of the Acoustical Society of America*, *70*.

MacMahan, J. H., et al. (2010a), Mean Lagrangian flow behavior on an open coast rip-channeled beach: A new perspective, *Marine Geology*, *268*(1), 1–15.

MacMahan, J. H. (2001), Hydrographic surveying from personal watercraft, *Journal of surveying engineering*, *127*(1), 12–24.

MacMahan, J. H., A. J. H. M. Reniers, E. B. Thornton, and T. P. Stanton (2004), Surf zone eddies coupled with rip current morphology, *Journal of Geophysical Research*, *109*(C7).

MacMahan, J. H., E. B. Thornton, and A. J. H. M. Reniers (2006), Rip current review, *Coastal Engineering*, *53*(23), 191–208.

MacMahan, J. H., A. J. H. M. Reniers, and E. B. Thornton (2010b), Vortical surf zone velocity fluctuations with O (10) min period, *Journal of Geophysical Research*, *115*(C6).

McLachlan, A., and P. Hesp (1984), Faunal response to morphology and water circulation of a sandy beach with cusps, *Marine ecology progress series. Oldendorf*, *19*(1), 133–144.

Medina, J., and R. Hudspeth (1990), A review of the analyses of ocean wave groups, *Coastal Engineering*, *14*(6), 515–542.

Miles, J., P. Russell, B. G. Ruessink, and D. Huntley (2002), Field observations of the effect of shear waves on sediment suspension and transport, *Continental Shelf Research*, *22*(4), 657–681.

New Delta Committee (2008), Working together with water. A living land builds for its future, *Findings of the New Delta Committee*.

Noyes, T. J., R. T. Guza, F. Feddersen, S. Elgar, and T. H. C. Herbers (2005), Model-data comparisons of shear waves in the nearshore, *Journal of Geophysical Research*, *110*(C5).

Ojeda, E., B. G. Ruessink, and J. Guillen (2008), Morphodynamic response of a two-barred beach to a shoreface nourishment, *Coastal Engineering*, *55*(12), 1185–1196.

Oltman-Shay, J., P. Howd, and W. Birkemeier (1989), Shear instabilities of the mean longshore current 2. Field observations, *Journal of Geophysical Research*, *94*(C12).

Pape, L. (2008), Blim toolbox manual, *IMAU report R08-02*.

Peregrine, D. (1998), Surf zone currents, *Theoretical and Computational Fluid Dynamics*, *10*(1), 295–309.

Pietrzak, J. D., G. J. de Boer, and M. A. Eleveld (2011), Mechanisms controlling the intra-annual mesoscale variability of SST and SPM in the southern North Sea, *Continental Shelf Research*, *31*(6), 594–610.

Plant, N. G., K. Todd Holland, and R. A. Holman (2006), A dynamical at-

tractor governs beach response to storms, *Geophys. Res. Lett.*, *33*(17).

Price, T. D. (2013), Morphological coupling in a double sandbar system, *Ph.D. thesis, Utrecht studies in earth sciences*.

Price, T. D., and B. G. Ruessink (2011), State dynamics of a double sandbar system, *Continental Shelf Research*, *31*(6), 659–674.

Ranasinghe, R., G. Symonds, and R. A. Holman (1999), Quantitative characterisation of rip dynamics via video imaging, *Coastal Sediments '99, Vols 1-3*, pp. 987–1002.

Ranasinghe, R., G. Symonds, K. P. Black, and R. A. Holman (2004), Morphodynamics of intermediate beaches: a video imaging and numerical modelling study, *Coastal Engineering*, *51*(7), 629–655.

Ranasinghe, R., C. Swinkels, A. Luijendijk, D. Roelvink, J. Bosboom, M. J. F. Stive, and D. Walstra (2011), Morphodynamic upscaling with the MORFAC approach: Dependencies and sensitivities, *Coastal Engineering*, *58*(8), 806–811.

Ranasinghe, R., R. A. Holman, M. A. de Schipper, T. Lippmann, J. Wehof, T. M. Duong, D. Roelvink, and M. J. F. Stive (2012), Quantifying nearshore morphological recovery timescales using Argus video imaging: Palm Beach, Sydney and Duck, North Carolina, *Proceeding of the International conference on Coastal Engineering*.

Reniers, A. J. H. M., G. Symonds, and E. Thornton (2001), Modelling of rip currents during RDEX, *Proceedings of Coastal Dynamics 2001*, pp. 493–499.

Reniers, A. J. H. M., J. H. MacMahan, E. B. Thornton, and T. Stanton (2006), Modelling infragravity motions on a rip-channel beach, *Coastal Engineering*, *53*(2), 209–222.

Reniers, A. J. H. M., J. H. MacMahan, E. B. Thornton, and T. Stanton (2007), Modeling of very low frequency motions during RIPEX, *Journal of Geophysical Research*, *112*(C7).

Reniers, A. J. H. M., J. H. MacMahan, E. B. Thornton, T. Stanton, M. Henriquez, J. Brown, J. Brown, and E. Gallagher (2009), Surf zone surface retention on a rip-channeled beach, *Journal of Geophysical Research*, *114*.

Reniers, A. J. H. M., J. H. MacMahan, F. Beron-Vera, and M. Olascoaga (2010), Rip-current pulses tied to Lagrangian coherent structures, *Geophysical Research Letters*, *37*(5).

Reniers, A. J. H. M., A. R. van Dongeren, J. A. Battjes, and E. B. Thornton (2002), Linear modeling of infragravity waves during DELILAH, *Journal of Geophysical Research*, *107*(C10).

Reniers, A. J. H. M., J. A. Roelvink, and E. B. Thornton (2004), Morphodynamic modeling of an embayed beach under wave group forcing, *Journal of*

Geophysical Research, *109*(C1).

Rienecker, M., and J. Fenton (1981), Fourier approximation method for steady water waves, *Journal of Fluid Mechanics*, *104*(119-137).

Rijkswaterstaat (1990), A new coastal defence policy for the Netherlands, *Policy report, Dutch ministry of Transport and Public Works*.

Roelse, P. (1996), Evaluatie van zandsuppleties aan de Nederlandse kust 1975-1994: een morfologische beschouwing, *RIKZ Report (in Dutch)*, *96*.

Roelse, P. (2002), Water en zand in balans: evaluatie zandsuppleties na 1990; een morfologische beschouwing, *RIKZ Report (in Dutch)*.

Roelvink, J. (1993), Dissipation in random wave groups incident on a beach, *Coastal Engineering*, *19*(1-2), 127–150.

Roelvink, J. (2006), Coastal morphodynamic evolution techniques, *Coastal Engineering*, *53*(2-3), 277–287.

Roelvink, J., and M. J. F. Stive (1989), Bar-generating cross-shore flow mechanisms on a beach, *Journal of Geophysical Research*, *94*(C4), 4785–4800.

Ruessink, B. G., J. Miles, F. Feddersen, R. Guza, and S. Elgar (2001), Modeling the alongshore current on barred beaches, *Journal of Geophysical Research*, *106*(C10).

Ruessink, B. G., K. Wijnberg, R. Holman, Y. Kuriyama, and I. Van Enckevort (2003), Intersite comparison of interannual nearshore bar behavior, *Journal of Geophysical Research*, *108*(C8).

Ruessink, B. G., R. Grinten, L. Vonhögen-Peeters, G. Ramaekers, and Q. Lodder (2012), Nearshore evolution at Noordwijk (NL) in response to nourishments, as inferred from Argus video imagery, *Proceedings of the NCK days 2012*.

Sand, S. (1982), Long waves in directional seas, *Coastal Engineering*, *6*(3), 195–208.

Seymour, R. J., and D. King (1982), Field comparisons of cross-shore transport models, *Journal of the Waterway, Port, Coastal and Ocean Division*, *108 (2)*, 163–179.

Shand, R. D., D. G. Bailey, and M. J. Shepherd (1999), An inter-site comparison of net offshore bar migration characteristics and environmental conditions, *Journal of Coastal Research*, pp. 750–765.

Shepard, F. P., K. O. Emery, and E. C. L. Fond (1941), Rip currents: A process of geological importance, *The Journal of Geology*, *49*(4), 337–369.

Short, A. (2007), Australian rip systems, friend or foe? *Journal of Coastal Research*, *50*, 7–11.

Smit, M. W. J., A. J. H. M. Reniers, and M. J. F. Stive (2010), What determines nearshore sandbar response? *Proceeding of the International confer-*

ence on Coastal Engineering.

Smit, M. W. J., A. J. H. M. Reniers, and M. J. F. Stive (2012), Role of morphological variability in the evolution of nearshore sandbars, *Coastal Engineering*, *69*, 19–28.

Smit, M. W. J. (2010), Formation and evolution of nearshore sandbar patterns, Ph.D. thesis, Delft University of Technology.

Smit, M. W. J., A. J. H. M. Reniers, B. G. Ruessink, and J. A. Roelvink (2008), The morphological response of a nearshore double sandbar system to constant wave forcing, *Coastal Engineering*, *55*(10), 761–770.

Smith, J. A., and J. L. Largier (1995), Observations of nearshore circulation: Rip currents, *Journal of Geophysical Research*, *100*(C6), 10,967–10,975.

Sonu, C. J. (1972), Field observation of nearshore circulation and meandering currents, *Journal of Geophysical Research*, *77 (18)*, 3232–3247.

Soulsby, R. L. (1997), *Dynamics of Marine Sands*, Thomas Telford, London.

Splinter, K. D., R. A. Holman, and N. G. Plant (2011), A behavior-oriented dynamic model for sandbar migration and 2DH evolution, *Journal of Geophysical Research*, *116*(C1).

Spydell, M., and F. Feddersen (2009), Lagrangian drifter dispersion in the surf zone: Directionally spread, normally incident waves, *Journal of Physical Oceanography*, *39*(4), 809–830.

Spydell, M., F. Feddersen, R. Guza, and W. Schmidt (2007), Observing surf-zone dispersion with drifters, *Journal of Physical Oceanography*, *37*(12), 2920–2939.

Stive, M. J. F., and W. D. Eysink (1989), Voorspelling ontwikkeling kustlijn 1990-2090, Deelrapport 3.1: dynamisch model van het Nederlandse kustsysteem, *Rapport H0825, WL— Delft Hydraulics (in Dutch)*.

Stive, M. J. F., et al. (2013), A new alternative to saving our beaches from sea-level rise: The Sand Engine, *Journal of Coastal Research*, *29*, 1001–1008.

Symonds, G., and R. Ranasinghe (2000), On the formation of rip currents on a plane beach, *Proceeding of the International conference on Coastal Engineering*.

Talbot, M., and G. Bate (1987), Rip current characteristics and their role in the exchange of water and surf diatoms between the surf zone and nearshore, *Estuarine, Coastal and Shelf Science*, *25*(6), 707–720.

Thiebot, J., D. Idier, R. Garnier, A. Falqués, and B. G. Ruessink (2011), The influence of wave direction on the morphological response of a double sandbar system, *Continental Shelf Research*.

Ting, F. C. K., and J. T. Kirby (1995), Dynamics of surf-zone turbulence in a strong plunging breaker, *Coastal Engineering*, *24*(3-4), 177–204.

Ting, F. C. K., and J. T. Kirby (1996), Dynamics of surf-zone turbulence in a spilling breaker, *Coastal Engineering*, *27*(3-4), 131–160.

Turner, I. L., D. Whyte, B. G. Ruessink, and R. Ranasinghe (2007), Observations of rip spacing, persistence and mobility at a long, straight coastline, *Marine Geology*, *236*(3-4), 209–221.

Valverde, H. R., A. C. Trembanis, and O. H. Pilkey (1999), Summary of beach nourishment episodes on the us east coast barrier islands, *Journal of Coastal Research*, pp. 1100–1118.

van de Rest, P. (2004), Morfodynamica en hydrodynamica van de Hollandse kust, *MSc. thesis, Technische Universiteit Delft (in Dutch)*.

van der Grinten, R., and B. G. Ruessink (2012), Evaluatie van de kustversterking bij noordwijk aan zee - de invloed van de versterking op de zandbanken, *Report commissioned by Deltares (in Dutch)*, p. 53.

van der Wal, D. (2004), Beach-dune interactions in nourishment areas along the Dutch coast, *Journal of Coastal Research*, pp. 317–325.

van Dongeren, A., A. J. H. M. Reniers, J. Battjes, and I. Svendsen (2003), Numerical modeling of infragravity wave response during DELILAH, *Journal of Geophysical Research*, *108*(C9).

van Duin, M., N. Wiersma, D. Walstra, L. Van Rijn, and M. J. F. Stive (2004), Nourishing the shoreface: observations and hindcasting of the Egmond case, the Netherlands, *Coastal Engineering*, *51*(8), 813–837.

van Enckevort, I. M. J., and B. G. Ruessink (2001), Effect of hydrodynamics and bathymetry on video estimates of nearshore sandbar position, *Journal of Geophysical Research*, *106*(C8), 16,969–16,979.

van Enckevort, I. M. J., and B. G. Ruessink (2003a), Video observations of nearshore bar behaviour. Part 1: alongshore uniform variability, *Continental Shelf Research*, *23*(5), 501–512.

van Enckevort, I. M. J., and B. G. Ruessink (2003b), Video observations of nearshore bar behaviour. Part 2: alongshore non-uniform variability, *Continental Shelf Research*, *23*(5), 513–532.

van Enckevort, I. M. J., B. G. Ruessink, G. Coco, K. Suzuki, I. L. Turner, N. G. Plant, and R. A. Holman (2004), Observations of nearshore crescentic sandbars, *Journal of Geophysical Research*, *109*(C6).

van Koningsveld, M., and J. P. M. Mulder (2004), Sustainable coastal policy developments in the Netherlands. a systematic approach revealed, *Journal of Coastal Research*, pp. 375–385.

van Rijn, L. C. (2011), Coastal erosion and control, *Ocean & Coastal Management*, *54*(12), 867–887.

van Rijn, L. C. (1993), *Principles of sediment transport in rivers, estuaries,*

and coastal seas, Aqua Publications, Amsterdam, The Netherlands.

van Rijn, L. C. (1997), Sediment transport and budget of the central coastal zone of Holland, *Coastal Engineering*, *32*(1), 61–90.

van Son, S., R. C. Lindenbergh, M. A. De Schipper, S. De Vries, and K. Duijnmayer (2010), Monitoring bathymetric changes at storm scale, *PositionIT*, *Nov/Dec*, 59–65.

van Thiel de Vries, J. S. M., M. R. A. van Gent, D. J. R. Walstra, and A. J. H. M. Reniers (2008), Analysis of dune erosion processes in large-scale flume experiments, *Coastal Engineering*, *55*(12), 1028–1040.

van Vledder, G. P. (1992), Statistics of wave group parameters, *Proceedings of the International Conference on Coastal Engineering; No 23*, pp. 946–959.

van Wiechen, J. (2011), Modelling the wind-driven motions in the Rhine ROFI, *MSc. Thesis. Delft University of Technology.*

Verboom, G., and A. Slob (1984), Weakly reflective boundary conditions for two-dimensional water flow problems., *5th International Conference on Finite Elements in Water Resources, June 1984, Vermont, Adv. Water Resources vol. 7. Delft Hydraulics, The Netherlands.*

Vos, R. (1976), Observations on the formation and location of transient rip currents, *Sedimentary Geology*, *16*(1), 15–19.

Walstra, D., J. Roelvink, and J. Groeneweg (2000), Calculation of wave-driven currents in a 3d mean flow model, *Proceedings of 27th International Conference on Coastal Engineering , ASCE*, pp. 1050–1063.

Waterman, R. E. (2010), *Integrated coastal policy via Building with Nature*, Ministry of Transport and Public Works.

Wijnberg, K. M., and J. Terwindt (1995), Extracting decadal morphological behaviour from high-resolution, long-term bathymetric surveys along the Holland coast using eigenfunction analysis, *Marine Geology*, *126*(1), 301–330.

Wijnberg, K. M. (2002), Environmental controls on decadal morphologic behaviour of the Holland coast, *Marine Geology*, *189*(3), 227–247.

Wilson, G. W. (2009), Field validation of a nearshore circulation model for alongshore non-uniform flows, *MSc. Thesis. Oreg. State Univ., Corvallis.*

Winter, G. W., M. A. de Schipper, and J. v. T. de Vries (2012), A field and numerical study into rip currents in wind-sea dominated environments, *Proceeding of the International conference on Coastal Engineering*, *1*(33).

Wright, L. D., and A. D. Short (1984), Morphodynamic variability of surf zones and beaches: A synthesis, *Marine Geology*, *56*(1-4), 93 – 118.

Yates, M., R. Guza, W. O'Reilly, and R. Seymour (2009), Seasonal persistence of a small southern California beach fill, *Coastal Engineering*, *56*, 559–564.

A. Field observation techniques

Topographic surveys discussed in Chapters 2 and 4 are executed using a combination of different equipment. This appendix elaborates on the instrumentation used in these field campaigns.

A.1 Sub-aerial topographic measurements

The bed elevation of the sub-aerial part of the topography was measured by walking along transects with a GPS backpack (Figure A.1). The precision of the 1 Hz GPS positions is enhanced using a reference base station. A local GPS base station of the *LNR Globalcom* commercial network is used as reference base station, positioned at Hoek van Holland (2.6 km from the site). Prior to November 2010 the GPS backpack contained a *Septentrio PolaRx2e* receiver. The raw GPS (RINEX) data were processed after the survey with the reference base station data using the *Leica Geo Office* package. Vertical accuracy of the obtained post-processed kinematic GPS data is 2 cm + 2 ppm[1], where parts per million indicates the separation of the backpack from the base station. Given that the base station is located at 2.6 km for the site, the vertical accuracy is of O (2.5 cm). From November 2010 onwards the GPS backpack contained a *Leica ViVa GS10* receiver with GSM modem and 1 Hz base station corrections were sent through during the survey via the GSM modem. The resulting Real time Kinematic GPS (RTK-GPS) positions have a vertical accuracy of 2 cm + 1 ppm[1] or O (2.3 cm). Errors due to the walking motion of the surveyor are estimated to be the largest source of error, of O (5 cm).

[1] 1 σ values, manufacturer specifications.

Figure A.1: Equipment used to survey the topography. Septentrio GPS backpack (*left*) and survey jetski *NEMO* (*right*).

A.2 Sub-aqueous topographic measurements

The sub-aqueous part of the profiles was measured using a jetski-based survey system (Figure A.1). Jetski-based survey systems have proven to provide good quality bathymetric data (*MacMahan*, 2001; *Dugan et al.*, 2001; *van Son et al.*, 2010) but the main advantage of the jetski-based system is the rapid deployment and maneuverability in the surf zone. The jetski survey system of Delft University of Technology, baptised NEMO, consists of a *Yamaha VX deluxe* jetski with hydrographic equipment mounted. Accurate positioning in 3 dimensions is obtained using a *Septentrio PolaRx2e* receiver in RTK-GPS mode. Water depth below the jetski is measured using a *SyQwest HydroBox* with a 210 kHz transducer. Beam width of the transducer is 8 degrees[2] providing some tolerance on pitch and roll of the jetski before depth measurements become biased (*van Son et al.*, 2010; *MacMahan*, 2001). Nevertheless, jetski surveys are ideally performed with light to no wind to reduce short wind sea and rolling of the jetski. Measured water depth is subtracted the measured GPS elevation of the jetski to obtain bed level elevation points in global coordinates. As changes in tide or the passage of a wave results in an equal change in both the measured elevation of the jetski and water depth beneath it, no special measures need to be taken to correct for wave and tidal motions. Both GPS and echo sounder data are recorded on a *Panasonic Toughbook* laptop

[2]Between the both -3 dB points on either side of the main lobe of the transducer signal.

using the *HYPACK* hydrographic software package. Latency, the O (0.5s) time delay between the recording of GPS and echosounder, is corrected for by cross correlating both signals and finding the maximum correlation. Vertical accuracy of the total system is of O (10 cm) (*van Son et al.*, 2010; *MacMahan*, 2001).

A substantial part of the systematic error in a jetski survey is the estimation of the speed of sound in water, which is required for the water depth estimation of the echosounder (*van Son et al.*, 2010). Water depth d beneath the transducer is computed from the recorded time interval Δt between a transmitted echo sounding pulse and the received pulse; $d = SS\ \Delta t$. SS herein is the speed of sound in water, which is dependent on salinity, temperature and density of the water. Small inaccuracies (e.g. 1 %) in sound speed can yield to substantial errors (10 cm) larger water depths. Altough these errors are hardly visible in the cross-shore transects, they account for large volumes when integrated over large areas.

Errors in sound speed are particularly of importance at the Vlugtenburg field site (Chapter 2). The nearby Rotterdam Waterway discharges part of the Rhine-Meuse river which is regulated to discharges around 1500 m^3/s (*Pietrzak et al.*, 2011). The differences in salinity and temperature between the river discharge and the North Sea water in combination with the oscillating tidal motion yield to fluctuations in the sound speed over time and space. Moreover the orientation of the fresh water plume is dependent on the tide and the wind conditions (*van Wiechen*, 2011). Finally this stratification also results in sound speed values that vary over depth as the system is stratified or well-mixed, depending on the lunar phase, discharge etc.

A.3 Sound velocity estimates

Prior to August 2011 the sound speed in water is estimated, using the seawater temperature as measured offshore, with the *MacKenzie* (1981) formula:

$$\begin{aligned} SS =& 1448.96 + 4.591T - 5.304 \times 10^{-2}T^2 + 2.374 \times 10^{-4}T^3 \\ &+ 1.340(s-35) + 1.630 \times 10^{-2}d + 1.675 \times 10^{-7}d^2 \\ &- 1.025 \times 10^{-2}T(s-35) - 7.139 \times 10^{-13}Td^3, \end{aligned} \tag{A.1}$$

where T is the temperature in degrees Celcius, taken equal to the average temperature measured at Europlatform during the time of survey, s is the salinity in parts-per-thousand (taken constant as 28.5 ppt) and d is depth in meters, which was taken as 5 m. Europlatform is located 40 km offshore

of the surveyed area in a water depth of 32 m. Since the surveyed area is situated differently in the Rhine river plume than Europlatform, some spatial fluctuations of seawater temperature and salinity may exist that affect the accuracy of the sound speed estimates. Theoretically, variations in seawater temperature of O (1 °C) and salinity of O (4 *ppt*) influence the soundspeed in the order of 0.5%, yielding to a systematic error of 2.5 cm in a water depth of 5 m. Therefore, starting from January 2010, the sound velocity was adjusted with ±0.5% for several (12) surveys based on the large variation observed in the bed level in the zone -8 to -10m.

From August 2011 onwards, sound speed is measured during the jetski survey with multiple sound velocity profiler casts. The profiler (*YSI Castaway*) derives a sound speed profile based on the measured values of conductivity, temperature and depth using the *Chen and Millero* (1977) equation. The use of the sound velocity profiler enables to also include the salinity effects on the sound speed estimates, thus reducing the error. The profiles occasionally show strong temperature fluctuations as well as shear in salinity of 15 to 27 ppt over depth (Figure A.2). Consequently sound speed is varying not only spatially and temporally but also over depth, even within a single survey. In the framework of this thesis a single average sound speed value was calculated from the multiple casts, representative of the entire survey. It is noted that even with a sound velocity measurement each survey, the spatial and temporal variation of the sound velocity in this region prevents a high accuracy in depth soundings, particularly when small changes of volumes on the lower shoreface are of interest.

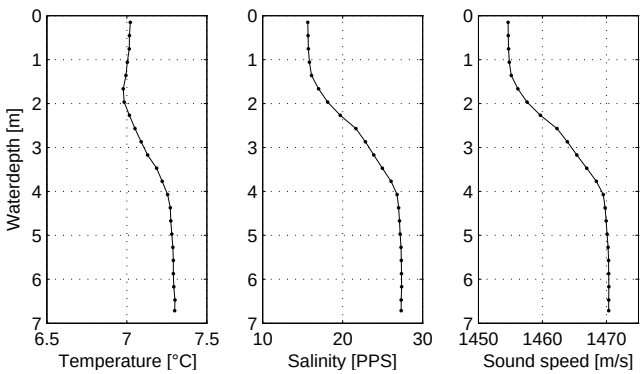

Figure A.2: Profiles of temperature (left panel), salinity (middle) and sound speed (right) measured within the Vlugtenburg survey domain during the January 2012 survey.

B. Numerical model of flow and sediment transport

Simulations of nearshore hydro and morphodynamics are made using a research version of *Delft3D* including the roller contribution and sediment transport on the long wave timescale. The model concept used is identical to the version discussed in *Reniers et al.* (2004) and no adaptations were made. The main features, assumptions and equations of the model are discussed here to support the results presented throughout the thesis.
Model configuration can be separated into six parts (Figure B.1), each to be discussed in separate sections: 1. the construction of the time and spatially varying offshore boundary conditions of wave energy, 2. a wave refraction model calculating the mean wave propagation direction, 3. wave propagation and dissipation of wave energy and 4. the 2DH hydrodynamics. And, for the morphodynamic computations, sections 5. the sediment stirring and transport and 6. bottom level update.

B.1 Offshore wave energy boundary conditions

The model is forced at the offshore boundary with time and alongshore varying wave group energy $E_w(x = x_{\text{offshore}}, y, t)$. These synthetic timeseries of wave energy are sampled using the two dimensional frequency-direction short wave spectrum. As this part is used to generate scenarios for the investigation of the effect of wave period, frequency and directional spread, it will be elaborated hereunder. The two-dimensional frequency-direction short wave spectrum was constructed from the Cartesian product of the frequency and directional distributions:

$$E(f, \theta) = D(\theta) \times E(f) \tag{B.2}$$

The frequency short wave spectrum $E(f)$ herein was based on a JONSWAP

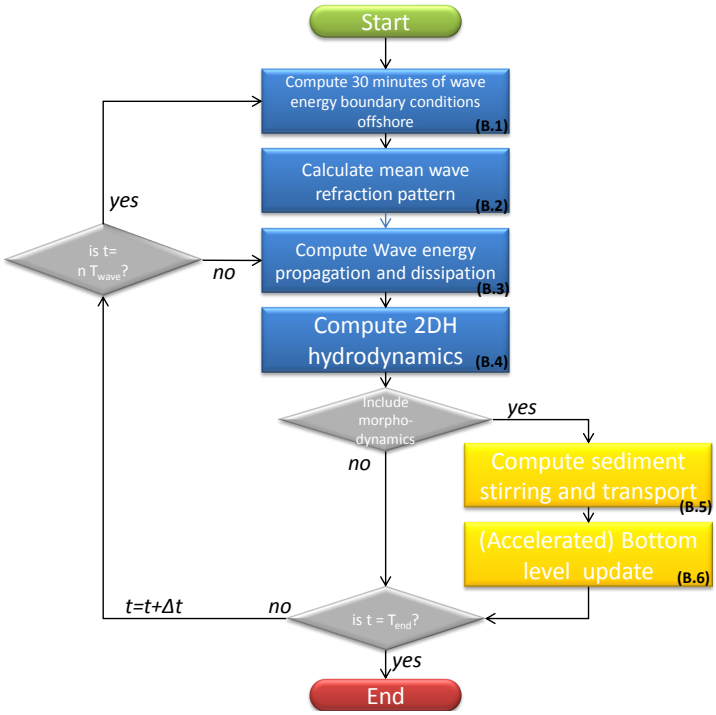

Figure B.1: Flow chart of the numerical model simulation.

formulation (Holthuijsen, 2007):

$$E(f) = \alpha g^2 (2\pi)^{-4} f^{-5} \exp\left[-\frac{5}{4}\left(\frac{f}{f_p}\right)^{-4}\right] \gamma^{\exp\left[-\frac{1}{2}\left(\frac{f/f_p-1}{\sigma}\right)^2\right]}, \tag{B.3}$$

where g is the gravitational acceleration, α is a scale parameter and σ is the peak enhancement width parameter. The most right hand term of Eq. B.3 is a peak enhancement function $\gamma^{\exp\left[-\frac{1}{2}\left(\frac{f/f_p-1}{\sigma}\right)^2\right]}$ where γ is usually chosen to be equal to 3.3 (*Holthuijsen*, 2007). Varying γ makes it possible to adapt the frequency spread of the spectrum while keeping the total amount of wave energy constant. Using γ equal to 1.0 in the JONSWAP formulation results in a standard Pierson-Moskowitz spectrum which is relatively wide (bandwidth parameter κ =0.42). Larger values of γ lead to an increase of the peak enhancement function and consequently to more narrow-banded spectra

(higher κ values). The normalised directional distribution $D(\theta)$ in Eq. B.2 was calculated as follows:

$$D(\theta) = A^* \cos^s(\theta), \tag{B.4}$$

where exponent s controls the directional width of the spectrum and parameter A^* is chosen such that the total amount of energy is conserved.

Short wave spectra of different sea states, ranging from swell to wind sea, were generated by varying f_p, γ , and s in Eq. B.3 and B.4. The resulting two-dimensional frequency-direction spectra $E(f, \theta)$ were used to generate synthetic short wave surface elevation $\eta(y, t)$ timeseries with a single summation random phase approach (*van Dongeren et al.*, 2003). The envelope of the surface elevation $A_{\text{env}}(y, t)$ follows the fluctuation of the wave energy on wave group scale and is computed using a Hilbert transform followed by a low-pass filter (f_{cutoff} =0.04 Hz). Finally, this wave group envelope is transformed into wave group energy using:

$$E_w(y, t) = \frac{1}{2}\rho g A_{\text{env}}(y, t)^2, \tag{B.5}$$

where ρ is the density of water. This time and spatially varying wave group energy is imposed along the offshore boundary as $E_w(x = x_{\text{offshore}}, y, t)$.

B.2 Wave energy refraction

Mean angle $\bar{\theta_w}(x, y)$ of wave energy propagation throughout the domain is calculated using a wave refraction model HISWA (*Holthuijsen et al.*, 1989). With the HISWA model, the wave action balance is solved for the time-averaged wave field. The model is therefore used in a stationary way, without flow interaction and a constant water level. This mean wave energy refraction is computed on a large time interval T_{wave} (typically 30 minutes) to account for changes in the refraction pattern due to bed level changes (Figure B.1).

B.3 Wave energy propagation and dissipation

Next, the wave energy at the boundary $E_w(x = x_{\text{offshore}}, y, t)$ and wave angle $\bar{\theta_w}(x, y)$ are used to propagate energy shoreward in the hydrodynamic flow module. In the module the dissipation of wave energy due to breaking (including roller lag effects) and the resulting radiation stress forces are calculated.

These forces F_x, F_y are imposed on the 2D nonlinear shallow water equations Eqs. B.7 and B.8.

The wave group energy $E_w(x = x_{\text{offshore}}, y, t)$ is imposed at the offshore boundary. Wave energy is then further propagated through the domain using a wave energy balance:

$$\frac{\partial E_w}{\partial t} + \frac{\partial E_w c_g \cos(\bar{\theta_w})}{\partial x} + \frac{\partial E_w c_g \sin(\bar{\theta_w})}{\partial y} = -D_w, \tag{B.6}$$

where the wave group speed c_g is calculated with the peak period and mean wave propagation direction $\bar{\theta_w}$ is obtained from the HISWA computation. Wave energy dissipation D_w is computed using the dissipation formulation of *Roelvink* (1993). Wave energy dissipation is then further transformed into roller energy E_r with a roller energy balance. The use of roller energy is important for a correct representation of the lateral mixing by eddy viscosity as well as the wave breaking induced mass flux.
The wave and roller energy balances are used to compute the radiation stresses throughout the domain (*Reniers et al.*, 2002). Spatial gradients in the radiation stresses determine the wave forces F_x and F_y.

B.4 Depth averaged hydrodynamics

Using the wave forcing, the resulting in surface elevation $\eta(x, y, t)$ and flow velocities $u(x, y, t)$, $v(x, y, t)$ throughout the domain can be computed. The *Delft3D* hydrodynamic solver (*Reniers et al.*, 2004; *Lesser et al.*, 2004) uses the following discretized 2D nonlinear shallow water equations:

$$\frac{\partial u}{\partial t} + u\frac{\partial u}{\partial x} + v\frac{\partial u}{\partial y} + g\frac{\partial \eta}{\partial x} - \tau_{b,x} + \nu_t\left(\frac{\partial^2 u}{\partial x^2} + \frac{\partial^2 u}{\partial y^2}\right) = -F_x, \tag{B.7}$$

$$\frac{\partial v}{\partial t} + v\frac{\partial v}{\partial y} + u\frac{\partial v}{\partial x} + g\frac{\partial \eta}{\partial y} - \tau_{b,y} + \nu_t\left(\frac{\partial^2 v}{\partial x^2} + \frac{\partial^2 v}{\partial y^2}\right) = -F_y, \tag{B.8}$$

where η is the surface elevation, τ_b denotes the bottom shear stress and ν_t is the horizontal viscosity governed by the wave breaking intensity (more detail in *Reniers et al.* (2004)). Wave forcing F_x, F_y is varying on the wave group scale, and as a result the hydrodynamics (u, v and η) vary on similar timescale and longer.

B.5 Sediment stirring and transport

Instantaneous sediment transport $\mathbf{q}$ (or $hC\mathbf{u}_q$) throughout the domain is calculated using a depth averaged, short wave averaged, advection equation for sediment transport with a source/sink term based on the equilibrium concentration C_{eq} and the sediment adaptation time T_s (*Galappatti*, 1983).

$$\frac{\partial hC}{\partial t} + \frac{\partial hCu_q}{\partial x} + \frac{\partial hCv_q}{\partial y} = \frac{h(C_{\text{eq}} - C)}{T_s}, \tag{B.9}$$

where u_q and v_q are the sediment transport velocities. The source/sink term on the RHS is driven by the equilibrium concentration C_{eq} and is obtained using the Soulsby-Van Rijn formulation for sediment stirring under combined waves and currents (*Soulsby*, 1997):

$$C_{\text{eq}} = \frac{\rho(A_{sb} + A_{ss})}{h}\left(\left(\mathbf{u}_{\text{stir}}^2 + \frac{0.018u_{\text{SW,rms}}^2}{Cd}\right)^{1/2} - u_{cr}\right)^{2.4}(1-3.5\beta) \tag{B.10}$$

The first fraction $\frac{\rho(A_{sb}+Ass)}{h}$ controls the suspended and near bed transported sediment volume by the two coefficients A_{ss} and A_{sb}. Suspended load coefficient A_{ss} is independent of the hydrodynamics, and only a function of grain size (see *Soulsby*, 1997). Bed load coefficient A_{sb} is mostly determined by grain size, but has a small dependency on local water depth of $h^{0.2}$.
The second term describes the stirring by the local hydrodynamics. Current stirring is given by $\mathbf{u}_{\text{stir}}$. Current stirring is taken as the 10 minute moving average of the Eulerian (depth averaged, compensating for mass transport in waves and rollers) flow. This moving average is, by necessity, only computed using the previously computed velocity fields (backward filtering) and it therefore has a slight offset in time. Short wave stirring is calculated (on a long wave timescale) from the local wave height and wave dissipation:

$$u_{\text{SW,rms}} = \sqrt{\frac{\pi H_{\text{rms}}}{\sqrt{2}T_p h}^2 + turb} \tag{B.11}$$

Main contribution herein is the orbital motion stirring given by the root mean square value of the bottom orbital velocities (linear wave theory) based on the instantaneous local wave height (H_{rms} term). Second RHS term is an

addition due to wave breaking induced turbulence (more on this term in *Reniers et al.*, 2004; *Roelvink and Stive*, 1989). Threshold stirring velocity u_{cr} is of O (0.3 m/s) and is calculated using the *van Rijn* (1993) equation and slightly dependent on water depth.

Final term on the RHS of the equilibrium concentration equation (Eq. B.10) is the bed slope term, with the local (maximum downstream) bed slope given as β. The slope coefficient value 3.5 varies from the 1.6 in the original *Soulsby* (1997) formulation, based on hindcast findings of the LIP Delta flume experiments (A. Reniers, pers. comm.; *Reniers et al.*, 2004).

Concentration adaptation timescale T_s is set by:

$$T_s = \max\left(0.05\frac{h}{w_s}, 1\right), \tag{B.12}$$

where coefficient 0.05 is determined from the LIP flume tests (A. Reniers, pers. comm.). Fall velocity w_s is user defined and equal to 0.014 m/s.

Sediment transport velocities $\mathbf{u}_q$ are based on the Eulerian velocity $\mathbf{u}_E$ and augmented with a representative intra-wave transport velocity $\mathbf{u}_{\mathrm{IW}}$.

$$u_q = u_E + u_{\mathrm{IW}}, v_q = v_E + v_{\mathrm{IW}} \tag{B.13}$$

The motivation for the inclusion the intra-wave velocity term is that the skewness in intra-wave orbital velocity results in net onshore transport over a wave period. Intra-wave representative transport velocities, $u_{\mathrm{IW}}, v_{\mathrm{IW}}$, are calculated such that the resulting transport over a wave period using the concentration on wavegroup scale is equal to the integrated intra wave transport:

$$u_{\mathrm{IW}} = \alpha_{\mathrm{IW}} \frac{\int_{t_i=0}^{t_i=T_p} u_{iw}(t_i).C_{\mathrm{IW}}(u_{\mathrm{iw}}(t_i))dt_i}{\int_{t_i=0}^{t_i=T_p} C_{\mathrm{IW}}(u_{\mathrm{iw}}(t_i))dt_i} \cos(\bar{\theta_w}), \tag{B.14}$$

in which α_{IW} is a tuning parameter, set to 0.5, see *Reniers et al.* (2004), and $\bar{\theta_w}$ is the mean wave angle. The intra-wave velocity signal $u_{\mathrm{iw}}(t_i)$ is calculated using a approximation of wave shape based on superposition of cosine functions (truncated fourier series). The wave shape can therefore vary in skewness, asymmetry is kept zero. Amplitude of superharmonics, determining the skewness of the total intra-wave signal are calculated using the method of *Rienecker and Fenton* (1981).

Intra-wave sediment concentration $C_{\mathrm{IW}}(t_i)$ is assumed to react instantaneously

to changes in the near bed intra-wave velocity (i.e. that the process is quasi-steady) using a *Soulsby* (1997) formulation similar to Eq. B.10:

$$C_{\mathrm{IW}}(t_i) = \frac{\rho(A_{sb} + A_{ss})}{h} \left(\left(\mathbf{u}_{\mathrm{stir}}^2 + \frac{0.018 u_{\mathrm{iw}}(t_i)^2}{Cd} \right)^{1/2} \right)^{2.4} \tag{B.15}$$

The resulting intra-wave representative transport velocity u_{IW} is variable on the wavegroup timescale due to two mechanisms: 1) wave heights are varying and therefore the magnitude of the intra-wave velocity signal u_{iw} and 2) the stirring by the background flow ($\mathbf{u}_{\mathrm{stir}}$ in Eq. B.15) fluctuates, which also influences the magnitude of C_{IW}. The resulting equivalent intra-wave transport velocity u_{IW} has an inverse relationship with the mean flow; in case of large mean current stirring, intra-wave velocities are a only a small percentage of the total stirring, and the intra-wave velocity u_{iw} yields less variation in transport over a wave period.

The intra-wave representative transport makes the time-averaged transport velocity switch sign from offshore directed (due to the mass flux compensation offshore transport in u_E) to onshore. As a reference, in the single barred case discussed in Chapter 5, u_{IW} (using α_{IW} =0.5) is about twice as large as u_{mean}, switching the flow from O (0.1 m/s) offshore to O (0.1 m/s) onshore. The inclusion of this intra-wave component is essential to maintain the subtidal bar in the profile. Without the inclusion of the intra-wave transport term the sediment transporting velocity on the bar would be offshore and increasing from the landward side of the bar towards the seaward side at breakpoint. Assuming for simplicity a constant sediment concentration this results in an increasingly offshore transports in the offshore direction over the bar and thus a diffusion of the shape.

It is noted that current velocities on timescales smaller than 10 minutes do not contribute to the stirring, as the current stirring is done using the 10-minute averaged u_E and v_E. Temporal variations in sediment stirring on the wave group (i.e. infragravity wave) timescale are solely taken into account via the variations in wave height (time-varying H_{rms} in Eq. B.11) rather than the long wave velocities. Prior tests with the inclusion of infragravity flow in the current stirring resulted in large offshore transports and to obtain a good skill in the hindcast of the LIP experiments the 10-minute moving average filter was introduced (A. Reniers, pers. comm.; *Reniers et al.*, 2004).

B.6 Bed level update

After computing sediment concentrations, the bed elevation z_b is updated. A surplus of sediment in the water column beyond the equilibrium concentration is stored in the bed and likewise a deficit (i.e. $C > C_{\text{eq}}$) yields an erosion of the bed, following the source/sink term of the sediment transport equation (Eq. B.9):

$$\frac{\partial z_b}{\partial t} = \frac{1}{\rho_s(1-n_p)} \frac{h(C-C_{\text{eq}})}{T_s} T_{\text{MORFAC}}, \tag{B.16}$$

where ρ_s and n_p are the mass density and the porosity of the bottom material, set as respectively 2650 kg/m^3 and 0.4.
Morphological evolution of the topography is accelerated by a factor T_{MORFAC} to reduce computational time (*Roelvink*, 2006; *Ranasinghe et al.*, 2011). In the present study it is set to 12, similar to *Reniers et al.* (2004).

About the author

Matthieu Andréas de Schipper was born to a French mother and Dutch father in Rotterdam on August 10, 1983. He obtained his secondary education at Marnix Gymnasium in Rotterdam, and graduated in July 2001. The following September he commenced his studies in Civil Engineering and Geosciences at Delft University of Technology. After acquiring his BSc. degree in 2004, he specialised in Hydraulic Engineering, taking courses in fluid mechanics, hydraulic constructions and coastal engineering. He obtained his MSc. degree (cum laude) in September 2007 after writing a thesis 'On the generation of surfable waves using ship hulls' at the section Fluid Mechanics under combined supervision of Prof. Guus Stelling and Prof. Marcel Stive. This thesis was rewarded with awards for best graduate of the faculty Civil Engineering and Geosciences and the 'Bataafsch Genootschap der Proefondervindelijke Wijsbegeerte', a society promoting science based on experiments. Inspired by research in nearshore hydro- and morphodynamics, he joined the coastal engineering group of Prof. Marcel Stive in search of a PhD research topic. In little over a year he and his colleague Sierd de Vries constructed a jetski based survey system, contributed to an ERC grant proposal *NEMO* and participated in a large field campaign in France (ECORS) amongst others. He also wrote a proposal for his doctorate research which was granted by January 2009. Since then he worked on the effects of anthropogenic interventions (i.e. nourishments) in the coastal zone and the effect of these interventions on swimmer safety. During the 4 years that passed, he encouraged students to explore coastal field work by supporting the yearly UNESCO-IHE field campaigns and (co-)supervising 13 MSc. thesis projects.
Simultaneously, he co-founded a small engineering company *Shore Monitoring and Research* in 2009, specializing in coastal consultancy based on field measurements. Together with partners Roeland de Zeeuw and Sierd de Vries the company grew steadily over the years and is at present involved in several large nourishment projects, such as the Sand Engine. From January 2013 onwards he works at Delft University of Technology on the *NEMO* project investigating the large scale morphodynamics of the Delfland coastal cell.

Publications

First author publications

- Schipper, M.A. de, S. de Vries, M. Henriquez, A.J.H.M. Reniers, H.J. de Koning-Gans, R.J. Labeur and M.J.F. Stive (2008) Surfing waves generated by a hull. Proceedings of the International Conference on Coastal Engineering, Hamburg.
- Schipper, M.A. de, R. Ranasinghe, A.J.H.M. Reniers and M.J.F. Stive (2010) On the initiation of nearshore morphological rhythmicity. Proceedings of the International Conference on Coastal Engineering, Shanghai.
- Schipper, M.A. de, R.C. de Zeeuw, S. de Vries, J. Terwindt and M.J.F. Stive (2011) Horizontal ADCP measurements of waves and currents in the very nearshore. Proceedings of the Current, Wave and Turbulence Measurement workshop, Monterey.
- Schipper, M.A. de, S. de Vries, R. Ranasinghe, A.J.H.M. Reniers and M.J.F. Stive (2012) Morphological developments after a beach and shoreface nourishment at Vlugtenburg beach. Conference proceedings of the NCK days 2013.
- Schipper, M.A. de, A.J.H.M. Reniers, J.H. MacMahan, R. Ranasinghe and M.J.F. Stive (2012) Vortical VLF motions under shore-normal incident waves. Proceedings of the International Conference on Coastal Engineering, Santander.
- Schipper, M.A. de, S. de Vries, R. Ranasinghe, A.J.H.M. Reniers and M.J.F. Stive (2013) Alongshore topographic variability at a nourished beach, Proceedings of Coastal Dynamics 2013.
- Schipper, M.A. de, A.J.H.M. Reniers, R. Ranasinghe and M.J.F. Stive (submitted) The influence of sea state on formation speed of alongshore variability in subtidal sand bars. Coastal Engineering.

Co-authored publications

- Lindenbergh, R.C., S.S. Soudarissanane, S. de Vries, M. Coquet, M.A. de Schipper, K.A. Hejbudzka, K. Duijnmayer, B. van Goor, and A.B. Cohen (2010) Eolian sand transport monitored by terrestrial laser scanning. Close range image measurement techniques Vol. XXXVIII. International archives of photogrammetry, remote sensing and spatial information sciences, 1-6.
- Lindenbergh, R.C., S.S. Soudarissanane, S. de Vries, B.G.H. Gorte and M.A. de Schipper (2011). Aeolian beach sand transport monitored by terrestrial laser scanning. The Photogrammetric Record: an international journal of photogrammetry, 26(136), 384-399.
- Ranasinghe, R., R. Holman, M.A. de Schipper, T. Lippmann, J. Wehof, T.M. Duong, D. Roelvink and M.J.F. Stive (2012) Quantifying nearshore morphological recovery time scales using Argus video imaging: Palm Beach Sydney and Duck, North Carolina. Proceedings of the International Conference on Coastal Engineering, Santander.
- Sénéchal, N., et al. (2008). ECORS-Truc Vert08 : Qualification des modèles de houle et de morphodynamique. Xèmes Journées Nationales Génie Côtier - Génie Civil, Sophia Antipolis, France.
- Son, S.T.J. van, R.C. Lindenbergh, M.A. de Schipper, S. de Vries and K. Duijnmayer (2009) Using a personal watercraft for monitoring bathymetric changes at storm scale. Proceedings of the International Hydrographic Conference.
- Son, S.T.J. van, R.C. Lindenbergh, M.A. de Schipper, S. de Vries and K. Duijnmayer (2010) Using a personal watercraft for monitoring bathymetric changes at storm scale. PositionIT, EE publishers Nov / Dec.
- Stive, M.J.F., M.A. de Schipper, A.P. Luijendijk, R. Ranasinghe, J.S.M. van Thiel de Vries, S.G.J. Aarninkhof, C. van Gelder-Maas, S. de Vries, M. Henriquez and S. Marx (2013) The Sand Engine: A solution for vulnerable deltas in the 21st century? Proceedings of Coastal Dynamics 2013.
- Stive, M.J.F., M.A. de Schipper, A.P. Luijendijk, S.G.J. Aarninkhof, C. van Gelder-Maas, J.S.M. van Thiel de Vries, S. de Vries, M. Henriquez, S. Marx, and R. Ranasinghe (2013) A new alternative to saving our beaches from local sea-level rise: the Sand Engine. Journal of Coastal Research, 29(5), 1001-1008.
- Vries, S. de, D.F. Hill, M.A. de Schipper and M.J.F Stive (2009) Using Stereo Photogrammetry to Measure Coastal Waves. Journal of Coastal Research, SI 56, 1484-1488.

- Vries, S. de, M.A. de Schipper, M.J.F. Stive and R. Ranasinghe (2010) Sediment exchange between the sub-aqueous and sub-aerial coastal zones Proceedings of the International Conference on Coastal Engineering,
- Vries, S. de, D.F. Hill, M.A. de Schipper and M.J.F Stive (2011) Remote sensing of surf zone waves using stereo imaging. Coastal Engineering, Volume 58, Issue 3, Pages 239-250.
- Wengrove, M.E., M. Henriquez, M.A. de Schipper, R. Holman and M.J.F. Stive (2013) Monitoring morphology of the Sand Engine leeside using Argus' CBathy. Proceedings of Coastal Dynamics 2013.
- Winter G., A.R. van Dongeren, M.A. de Schipper and J.S.M. van Thiel de Vries (2012) Rip Current Observations at Egmond aan Zee. Conference proceedings of the NCK days 2013.
- Winter G., A.R. van Dongeren, M.A. de Schipper and J.S.M. van Thiel de Vries (2012) A field and numerical study into rip currents in windsea dominated environments. Proceedings of the International Conference on Coastal Engineering, Santander.
- Winter G., A.R. van Dongeren, M.A. de Schipper and J.S.M. van Thiel de Vries (submitted) Rip Currents under Obliquely Incident Wind Waves and Tidal Longshore Currents. Coastal Engineering.
- Zeeuw, R.C. de, M.A. de Schipper, D. Roelvink, S. de Vries and M.J.F. Stive (2012) Impact of nourishments on nearshore currents and swimmer safety on the Dutch coast. Proceedings of the International Conference on Coastal Engineering, Santander.

Acknowledgements

The last years have been a great experience for which I'm very grateful. I would like to express my gratitude to the Building with Nature funding program for supporting the project over the years. The program and the biannual meetings gave me a broad multi-disciplinary view on coastal science.
Marcel Stive, thank you for the unlimited faith and trust over all these years. You always gave the impression that it would all work out in the end, which is a blessing during periods with slow progress. I'm also thankful for providing incredible freedom to pursue new ideas and go down beaten and unbeaten tracks. Some ideas turned out to be dead alleys, but your optimism taught me that one day even these will become of use.
Rosh Ranasinghe and Ad Reniers, I thank you both for guiding me these years, urging me to finish, bringing order in chaotic thoughts as well as providing inspiration. I have been very fortunate to have both of you as supervisors, and the final thesis contains clear evidence of our collaboration. I have good memories on our formal progress meetings but also the less formal heart-to-heart meetings, discussions on the best Michael Jackson song ever and cooking Italian food until midnight.
To the personnel of the Fluid Mechanics lab and workshop (especially Sander de Vree), thank you for the endless patience. Over the last years I often ran into your office with requests for rapid support or with equipment that was broken in during field campaigns. Thanks for helping out on these occasions.
This thesis is the result of over 4 years of thoughts, work and inspiring conversations at the Hydraulic Engineering department of Delft University of Technology, but also during conferences and visits in the Netherlands or abroad. Office mates, department members and colleagues in the coastal community, thanks for sharing your enthusiasm for coastal processes with me.
The last few years I (co-)supervised students during field campaigns, internships and MSc. thesis projects. There is something special about a student that just had his 'Eureka' moment, and enters your office. Thanks for sharing these moments with me.

And finally, friends, family and in particular Martijn, Roeland, Sierd and Ilhame; thank you in so many ways. Thanks for keeping up with impossible working schedules and providing the necessary distraction from time to time. I would not have been able to do this without you, and it certainly would not have been as much fun.

Matthieu A. de Schipper
November 2013

STELLINGEN BEHOREND BIJ HET PROEFSCHRIFT

'KUSTLANGSE VARIABILITEIT OP GESUPPLEERDE EN NATUURLIJKE STRANDEN'

M.A. DE SCHIPPER

1. Door een versteiling van het strandprofiel kan een suppletie op een structureel eroderende kust initieel tot extra verliezen leiden. -dit proefschrift

2. Alleen bij een perfect kustlangs uniforme begintoestand kunnen zeer laagfrequente brandingstromen verantwoordelijk worden gehouden voor het ontstaan van kustlangse variabiliteit in zandbanken.

3. De stroomsnelheid in een muistroom is geen goede indicator voor zwemveiligheid aan de Nederlandse kust.

4. Experimenten waarbij de kust ver uit natuurlijk evenwicht is gebracht zijn het beste instrument om kennis over de natuurlijke kustprocessen te vergroten.

5. De wijze waarop morfologische berekeningen worden gepresenteerd en geïnterpreteerd heeft veel weg van het voorspellen van de sneeuwhoogte over vijf jaar op 26 december om 16h00. De kennis in deze modellen verdient een betere presentatie.

6. De realisatie en evaluatie van het nut van de Zandmotor zijn voornamelijk een sociaal experiment; de morfologische ontwikkeling een kustwaterbouwkundig experiment.

7. Fondsen, marktpartijen en wetenschap treffen elkaar op het snijvlak van duidelijk beantwoordbare en onbeantwoordbare vragen. Alleen de nagenoeg onbeantwoordbare vragen op dit snijvlak zijn stof voor promovendi.

8. Er is een toename van de 'black box' benadering op een groot aantal vlakken van de samenleving, van spellingscontroles tot doorberekeningen van verkiezingsprogramma's en van auto's tot morfologische modellen. Hierdoor kunnen en willen mensen minder eigen verantwoordelijkheid nemen.

9. Creativiteit ontstaat waar ruimte voor falen is.

10. 'Wetenschap is het geloof in de onwetendheid van deskundigen'[1]. Dit betekent ook dat het wiel opnieuw uitvinden niet zinloos is, en vaker aangemoedigd zou moeten worden.

[1]Feynman, Richard P, (1969), What Is Science?, The Physics Teacher, 7, 313-320

Deze stellingen worden opponeerbaar en verdedigbaar geacht en zijn als zodanig goedgekeurd door de promotoren, prof. dr. ir. M.J.F. Stive en prof. dr. ir. A.J.H.M. Reniers.

PROPOSITIONS PERTAINING TO THE THESIS

'ALONGSHORE VARIABILITY OF NOURISHED AND NATURAL BEACHES'

M.A. DE SCHIPPER

1. A nourishment can lead to increased losses on a structurally eroding coast due to the steepening of the coastal profile. -this thesis

2. Very low frequency surfzone velocity fluctuations can create alongshore variability in sandbars only if the initial condition is perfectly uniform alongshore.

3. The magnitude of the rip current velocity is not a good indicator for swimmer safety on the Dutch coast.

4. Experiments where the coast is far out of natural equilibrium are the best tool to acquire knowledge on natural coastal processes.

5. The way morphological models are presented and interpreted has a lot in common with predictions of snow depth in five years on December 26th at 4 pm. The knowledge in these models deserves a better presentation.

6. The implementation and evaluation of the usefulness of the Sand Engine nourishment is mostly an experiment in social sciences; its morphological development an experiment in coastal engineering.

7. Funding agencies, private parties and science meet at the intersection of the clearly answerable and unanswerable questions. Only the nearly unanswerable questions on this intersection are of interest for doctorate candidates.

8. There is an increase in the 'black box' approach on many sides of our society, from spelling checks and the evaluation of election programs, to cars and morphological models. Because of this, people (want to) take less own responsibility.

9. Creativity flourishes with room for failure.

10. 'Science is the belief in the ignorance of experts'[1]. This also means that re-inventing the wheel is not useless and should be encouraged more often.

[1]Feynman, Richard P, (1969), What Is Science?, The Physics Teacher, 7, 313-320

These propositions are regarded as opposable and defendable, and have been approved as such by the supervisors, prof. dr. ir. M.J.F. Stive and prof. dr. ir. A.J.H.M. Reniers.